

BOSTON UNIVERSITY
COLLEGE OF ENGINEERING

Dissertation

**METHODS AND ALGORITHMS FOR QUANTITATIVE
ANALYSIS OF METALLOMIC IMAGES TO ASSESS
TRAUMATIC BRAIN INJURY**

by

AMANDA GAUDREAU-BALDERRAMA

B.Sci., Massachusetts Institute of Technology, 2009
M.Eng., Massachusetts Institute of Technology, 2010

Submitted in partial fulfillment of the
requirements for the degree of
Doctor of Philosophy

2017

© 2017 by
AMANDA GAUDREAU-BALDERRAMA
All rights reserved

Approved by

First Reader

Janusz Konrad, Ph.D.
Professor of Electrical and Computer Engineering

Second Reader

Lee Goldstein, M.D., Ph.D.
Associate Professor of Psychiatry
Associate Professor of Neurology
Associate Professor of Pathology and Laboratory Medicine
Boston University, School of Medicine

Associate Professor of Electrical and Computer Engineering
Associate Professor of Biomedical Engineering
Boston University, College of Engineering

Third Reader

Howard Eichenbaum, Ph.D.
University Professor of Psychological and Brain Sciences

Fourth Reader

W. Clem Karl, Ph.D.
Professor and Chair of Electrical and Computer Engineering
Professor of Biomedical Engineering
Professor of Systems Engineering

Fifth Reader

Prakash Ishwar, Ph.D.
Professor of Electrical and Computer Engineering
Professor of Systems Engineering

Success consists of getting up just one more time than you fall.

– Oliver Goldsmith

Acknowledgments

My time as a graduate student at Boston University was a period of immense growth. A period made possible by the support and guidance of my two advisors, Lee Golstein and Janusz Konrad. I would like to thank Janusz for the many hours he devoted to ensuring the technical integrity of the years of work that went into this thesis. Janusz's ability to be both a friend and a critic motivated me to persevere through many periods of doubt and confusion. I would like to thank Lee for always reminding me to take a step back and look at the bigger picture. It is because of Lee that I am able to finish my doctorate with such a diverse set of experiences and expertise, and an invaluable perspective on what it takes to conduct research at the frontier of medicine. Of course, this project would not have been possible without Lee's tireless commitment to investigating issues that are vitally important to public health.

I would like to thank the many collaborators who made this work possible. I'm extremely grateful for the Molecular Aging and Development Laboratory members. I'd like to thank Noel Casey for teaching me about LA-ICP-MS and for producing the MIMS, Andrew Fisher and Chad Tagge for their support with the mouse neurotrauma models and engineering insights, Olga Minaeva for her practical and rigorous perspective which I will truly miss, Mark Wojnarowicz for his thoughtfulness, patience training and working with me on wet-lab experiments, and most of all, for his friendship, Juliet Moncaster for supporting every aspect of the group's operation, and Srikant Sarangi for always being available to talk, whether about research or life. I would also like to thank Bo Yan for being such an enjoyable collaborator and for his support generating MIMS, Prakash Ishwar for offering thoughtful theoretical suggestions on this project and beyond, and David Castañón for his patient guidance through optimal filtering. I would also like to thank Polina Golland for letting me

learn from the best in the field, and Adrian Dalca for going out of his way to help.

So many individuals made the 4-th floor of Photonics feel like so much more than just an office. Jonathan Wu, thank you for keeping me company in 401E. I'll always remember your unique blend of self-deprecating quirky genius which made every day at the office interesting. My rival hipster office-mate Andrew Cutler, thank you for the philosophical conversations and for the SAGE companionship. I will also remember fondly the various food and seminar field trips with Tolga Bolukbasi, Theodora Brisimi and Wenbo He. Parisa Babaheidarian, our tea times were both the fuel and refuge I needed to get me through the day.

My ability to make it though my doctorate would not have been possible without my friends, my family, and most of all, my husband. To the APR Boston crew, I will always remember our weekend hangouts as some of the most loving, carefree and fun days of my life. Thank you for helping me hold onto my sanity. To my Tia Sylvia and Uncle John, thank you for providing a home away from home. To the Balderrama-Durbins, thank you for keeping my heart whole, and for always being there to listen and to guide when I needed it. I owe all my accomplishments to my mom, Irma Balderrama, for her tireless encouragement, love, and wisdom. Finally, to David He, who supported me through the most difficult days and gave me so many of my happiest, I am so grateful I was able to go through this part of my life with you, because "I came here with a load and it feels so much lighter now I met you". I'm eager to venture into post-PhD life with you by my side.

Disclaimers and Funding Support

This material is based upon work supported by the National Institute of Neurological Disorders & Stroke (NINDS) under Grant No. 1F31NS080564 (Aug 2012 – July 2015).

Any opinions, findings, and conclusions, or recommendations expressed in this publication are those of the author(s) and do not necessarily reflect the views of the National Institute of Neurological Disorders & Stroke or NIH.

**METHODS AND ALGORITHMS FOR QUANTITATIVE
ANALYSIS OF METALLOMIC IMAGES TO ASSESS
TRAUMATIC BRAIN INJURY**

AMANDA GAUDREAU-BALDERRAMA

Boston University, College of Engineering, 2017

Major Professors: Janusz Konrad, Ph.D.
Professor of Electrical and Computer Engineering

Lee Goldstein, M.D., Ph.D.
Associate Professor of Psychiatry, Neurology,
Pathology & Laboratory Medicine
Associate Professor of Biomedical Engineering
Associate Professor of Electrical and Computer
Engineering

ABSTRACT

The primary aim of this thesis is to develop image processing algorithms to quantitatively determine the link between traumatic brain injury (TBI) severity and chronic traumatic encephalopathy (CTE) neuropathology, specifically looking into the role of blood-brain barrier disruption following TBI. In order to causally investigate the relationship between the tau protein neurodegenerative disease CTE and TBI, mouse models of blast neurotrauma (BNT) and impact neurotrauma (INT) are investigated. First, a high-speed video tracking algorithm is developed based on K-means clustering, active contours and Kalman filtering to comparatively study the head kinematics in blast and impact experiments. Then, to compare BNT and INT neuropathology,

methods for quantitative analysis of macroscopic optical images and fluorescent images are described. The secondary aim of this thesis focuses on developing methods for a novel application of metallomic imaging mass spectrometry (MIMS) to biological tissue. Unlike traditional modalities used to assess neuropathology, that suffer from limited sensitivity and analytical capacity, MIMS uses a mass spectrometer – an analytical instrument for measuring elements and isotopes with high dynamic range, sensitivity and specificity – as the imaging sensor to generate spatial maps with spectral (vector-valued) data per pixel. Given the vector nature of MIMS data, a unique end-to-end processing pipeline is designed to support data acquisition, visualization and interpretation. A novel multi-modal and multi-channel image registration (MMMCIR) method using multi-variate mutual information as a similarity metric is developed in order to establish correspondence between two images of arbitrary modality. The MMCIR method is then used to automatically segment MIMS images of the mouse brain and systematically evaluate the levels of relevant elements and isotopes after experimental closed-head impact injury on the impact side (ipsilateral) and opposing side (contralateral) of the brain. This method quantifiably confirms observed differences in gadolinium levels for a cohort of images. Finally, MIMS images of human lacrimal sac biopsy samples are used for preliminary clinicopathological assessments, supporting the utility of the unique insights MIMS provides by correlating areas of inflammation to areas of elevated toxic metals. The image processing methods developed in this work demonstrate the significant capabilities of MIMS and its role in enhancing our understanding of the underlying pathological mechanisms of TBI and other medical conditions.

Contents

1	Introduction	1
1.1	Traumatic Brain Injury	1
1.2	Animal Models of Blast- and Impact-Induced Neurotrauma	3
1.3	Assessment of Blood-Brain Barrier Disruption	3
1.4	Specific Aims of this Thesis	5
1.5	Thesis Organization	7
2	Traumatic Brain Injury Mouse Models and Assessments	9
2.1	Traumatic Brain Injury Mouse Models	9
2.2	Neuropathological & Behavioral Deficits in TBI	11
2.2.1	Injury Severity Assessments (BUCS)	13
2.3	Introduction to Imaging Modalities Utilized	16
2.3.1	Evans Blue Extravasation with Fluorescent Imaging	16
2.3.2	Metallomic Imaging Mass Spectrometry for Biological Samples	17
2.4	Current Biomedical Image Registration Methods	22
3	Assessment of TBI via Traditional Imaging Modalities	25
3.1	High-Speed Video for Tracking Head Movement	25
3.2	Semi-supervised Segmentation for Gross Pathological Assessment . .	37
3.3	Evans Blue Fluorescent Imaging for Evaluating Blood-Brain Barrier Dysfunction	45
3.4	Summary of Contributions	46

4	Algorithms for Metallomic Imaging Mass Spectrometry (MIMS)	
	Data Processing	48
4.1	MIMS Data Acquisition, Pre-Processing and Rendering	49
4.1.1	MIMS Acquisition Protocol	49
4.1.2	Raw Data Extraction	51
4.1.3	Image Rendering Tools	55
4.2	MIMS Region Segmentation	57
4.3	MIMS Calibration	64
4.4	MIMS Channel Equalization	67
4.5	Multi-modal Image Registration	75
4.5.1	Problem Formulation & Assumptions	76
4.5.2	Affine Transformation Model	77
4.5.3	Mutual Information Similarity Metric	78
4.5.4	Optimization	83
4.5.5	Results	86
4.5.6	Discussion	97
4.6	Summary of Contributions	97
5	Analysis of Metallomic Brain Images of Nanoparticle-Injected Mice	101
5.1	Experimental Objective	101
5.2	Experimental Methods	102
5.2.1	Gadolinium-Injected Cohort (iGd)	102
5.2.2	Nanoparticle-Injected Cohort (iNP)	104
5.2.3	Tissue Fixation and Paraffin Embedding	105
5.2.4	Input Image Information	105
5.3	Processing Pipeline	109
5.3.1	Image Preparation	115

5.3.2	Registration Initialization	115
5.3.3	Image Registration Procedure	120
5.4	Results and Discussion	121
5.4.1	Assessment of Gadolinium-Injected Cohort	122
5.4.2	Assessment of Nanoparticle-Injected Cohort	130
5.4.3	Mask Registration for MIMS Spatial Corrections	133
5.4.4	Factors Affecting Image Registration Outcome	137
5.5	Summary of Contributions	142
6	Analysis of Metallomic Images of Human Lacrimal Sac Biopsy Sam- ples	144
6.1	Background	144
6.2	Experimental Objective	145
6.3	Experimental Methods	146
6.4	Processing Pipeline	148
6.5	Results and Discussion	149
6.5.1	Comparison of MIMS Using Different Instrument Modes	149
6.5.2	Calibration Curve Characteristics	162
6.5.3	Clinicopathological case studies	163
6.6	Summary of Contributions	177
7	Conclusions	178
7.1	Summary of Contributions	178
7.2	Future Work	180
	Appendices	182
A	Experimental Protocols	183
A.1	Tissue Preparation	183
A.2	Evans Blue Dye Injection and Imaging Method	183

A.3	Matrix-Match Calibration Standards for MIMS	184
B	Overview of MATLAB Tools Developed for MIMS	185
B.1	MIMS Raw Data Files and Resulting MATLAB Data Structures . . .	185
B.2	List of MATLAB Functions	189
B.2.1	Chapter 3 Functions	189
B.2.2	MIMS Functions	189
B.2.3	MMMCIR Functions	190
B.2.4	Image Visualization Functions	190
C	Derivation of Physical Parameters for Inverse Affine Transformation	191

List of Tables

2.1	Metallomic imaging mass spectrometry acquisition parameter trade-offs	20
3.1	Parameter values used for Chan-Vese algorithm	31
3.2	Kalman filter variable definitions. Definitions with a “*” indicate that in this application, these values are constant and do not change, but in general may be defined as a function of k	34
3.3	Kalman filter prediction and update steps	35
4.1	Per line parameters used by DigiLaz III software to generate *. lzs files for the CETAC LSX-213 laser ablation instrument	50
4.3	Representative kernels and their relevant parameters for KDE	82
4.4	Summary of image pairs used for image registration	88
4.5	Experimental parameters used	88
4.6	Depiction of images used in the image registration experiments	89
4.7	Parameters and results for registration between a photograph of a copper grid with itself	90
4.8	Parameters and results for registration between a photograph of a copper grid with a MIMS of a copper grid	90
4.9	Parameters and results for registration between MIMS of the mouse brain with an atlas image	90
5.1	Gadolinium-injected (iGd) experiment information	111
5.2	Nanoparticle injected (iNP) experiment cohort information	112

5.3	Regional structure abbreviations and full names for atlas images used for registration	114
5.4	Specification of MIMS brain image registration parameters	116
5.5	Experimental outcomes for registration using true-MI versus summed- MI on iNP-30 with 30 bins per dimension and an Epanechnikov kernel.	140
6.1	Demographic information for lacrimal sac biopsy samples (LSBS) . . .	146
6.2	LSBS MIMS analysis summary.	150
6.3	Summary of calibration data characteristics from calibration experiments	167

List of Figures

1.1	Experimental set-ups for prominent animal models of TBI (from (Xiong et al., 2013))	4
1.2	Probing blood-brain barrier compromise using exogenous compounds	6
2.1	Schematic of the blast tube set up (from Goldstein et al. (2012)) . . .	10
2.2	Schematic of momentum transfer instrument (from Tagge et al. (2017))	12
2.3	Schematic of structure of the blood-brain barrier from Winkler et al. (2011))	14
2.4	Boston University concussion scale scoring rubric	15
2.5	Example of a spectrograph output from an inductively coupled plasma mass spectrometer	18
2.6	Metallomic imaging mass spectrometry system overview	19
2.7	Diagram of spatial parameters affecting final image resolution	21
3.1	Blast tube high-speed video frame	27
3.2	High-speed video segmentation procedure using k-means	29
3.3	High-speed video segmentation using Chan-Vese after failure of k-means	30
3.4	Evolution of Chan-Vese segmentation	32
3.5	Mouse nose position results from segmentation, Butterworth filtering, and Kalman filtering.	36
3.6	Comparison of Butterworth filtering and Kalman filtering for estimating higher-order position derivatives.	37

3·7	Exemplary images from brain surface pathology of Evans blue-injected mice	38
3·8	Examples of characteristic pathologies in a left surface RGB photographic image.	39
3·9	Steps to define the tissue segmentation mask for macroscopic photo images	42
3·10	Selection of exemplary pathology in RGB images	43
3·11	Procedure used to determine per pixel label of gross pathology surface images	43
3·12	Example results obtained using the proposed pathology classification method	44
3·13	Fluorescent imaging masking, left and right side identification, and results	47
4·1	DigiLaz III graphical user interface	52
4·2	MATLAB graphical user interface for constructing laser ablation routines	53
4·3	Example of manufacturer’s graphical user interface for the specification of parameters of the Element ICP-MS instrument.	53
4·4	MIMS raw data acquisition timing diagram.	54
4·5	Depiction of a MIMS sequence	55
4·6	MIMS calibration and spatial coordinate mapping	56
4·7	Unwrapping raw data from the optical emission spectrometer	58
4·8	Examples of select image processing and rendering tools	59
4·9	MIMS sequence notation	61
4·10	Examples of the channel categorization routine used by the segmentation algorithm	63
4·11	Intermediate images used to define a <i>laser on</i> mask	63

4.12	Intermediate images used to define the final MIMS segmentation mask	64
4.13	Calibration curve data screening and selection	68
4.14	Images and histograms of raw log-normal MIMS data and their transformations	72
4.15	Channel equalization for comparing different channels within one MIMS image \vec{I}_τ in a normalized intensity domain.	73
4.16	Channel equalization for comparing images between subjects.	74
4.17	Overview of functions and parameters required to perform image registration	76
4.18	Construction of joint observations variable for computing the probability function	80
4.19	Visualization of KDE notation	81
4.20	Functional block diagram of image registration function	85
4.21	Image registration using simulated annealing	86
4.22	Exp. 1 registration result: Cu grid photo registered to Cu grid photo	91
4.23	Exp. 2 registration result: Cu grid photo registered to multi-channel Cu grid MIMS	92
4.24	RGB colored schematic atlas of the approximate sagittal section corresponding to the MIMS data (from Atlas (2013))	93
4.25	Exp 3 registration results: hippocampus segmentation image registered to MIMS	94
4.26	Display of mapping experimental results onto original image dimensions.	95
4.27	MI projection onto transformation parameter axes for various Exp. 3 inputs	96
4.28	Projections of MI onto transformation parameter axes for MMMCIR experiments	98

4.29	Assessing MI of sum-of-scalar RVs versus MI of multi-dimensional RVs	99
5.1	^{157}Gd MIMS brain image for BBB compromise proof of concept (from Tagge et al. (2017))	103
5.2	Timing diagram for gadolinium-based MRI contrast agent injected cohort (Figure courtesy of Andrew Fisher).	104
5.3	Thick section positions cut using the brain-slicing matrix.	105
5.4	Allen mouse brain atlas CVR-coordinate system	107
5.5	Tilted tissue sectioning views	108
5.6	Allen Mouse Brain Atlas images used for MIMS registration procedure	110
5.7	Labeled atlas images used in MIMS brain image registration experiments	113
5.8	Brain tissue masks for registration initialization	117
5.9	Mask registration exemplary inputs and results	118
5.10	Multi-modal, multi-channel image registration procure for MIMS brain image	119
5.11	Anatomical subgroup image derived from atlas	123
5.12	Explanation of visualization of registration results	123
5.13	Gadolinium-injected MIMS brain images for relevant isotopes	124
5.14	Pseudo-colored iGd MIMS brain images with outlines from manual subgroup segmentations	125
5.15	Pseudo-colored iGd MIMS brain images with outlines from image registration subgroup segmentations	126
5.16	iGd-12 comparison between manual- and registration-derived anatomical subgroups	127
5.17	iGd-10 comparison between manual- and registration-derived anatomical subgroups	128
5.18	Nanoparticle-injected MIMS brain images for relevant isotopes	131

5·19	Pseudo-colored iNP MIMS brain images with outlines from registered atlas image	132
5·20	Isotope levels in MMMCIR segmented subgroups for iNP experiment	134
5·21	Levels of ^{31}P and ^{64}Zn in each anatomical subgroup for iNP samples	135
5·22	Inverse transformations derived from mask registration for MIMS spatial corrections	136
5·23	Comparison of registration results when including versus excluding background pixels	141
5·24	Comparison of true-MI versus summed-MI values for small perturbations	143
6·1	Anatomical diagram of lacrimal sac and nasolacrimal duct.	144
6·2	Paraffin-embedded lacrimal sac biopsy samples.	147
6·3	^{64}Zn raw sequences from STD1 experiments	151
6·4	^{66}Zn raw sequences from STD2 experiments	152
6·5	^{66}Zn raw sequences from KED2 experiments	153
6·6	Various image modalities of LSBS 3733-2	153
6·7	Raw LSBS MIMS tissue images from select endogenous biometals . .	154
6·8	Raw MIMS from select toxic metal isotopes for all lacrimal sac biopsy samples	155
6·9	Comparison of Zn isotope signal distributions in tissue regions from all LSBS MIMS experiments	157
6·10	Comparison of ^{137}Ba signal distributions in tissue regions from all LSBS MIMS experiments	158
6·11	MVE-MIMS from select endogenous biometals for LSBS 3733-2 . . .	159
6·12	MVE-MIMS from select toxic metal isotopes for LSBS 3733-2	160
6·13	Intensity co-occurrence characteristics for correlated and uncorrelated images	161

6·14	Cross-correlation between MIMS from different experiments for LSBS 3733-2	162
6·15	^{66}Zn calibration curve comparison	164
6·16	^{60}Ni calibration curve comparison	165
6·17	^{44}Ca calibration curve comparison	166
6·18	Comparison of ^{66}Zn LSBS represented in <i>ppm</i>	168
6·19	Comparison of ^{60}Ni LSBS represented in <i>ppm</i>	169
6·20	MVE-MIMS from select isotopes for LSBS 14391	171
6·21	Images used for clinicopathological case study of LSBS 14391	172
6·22	Segmentation of LSBS 14391 immunohistochemical image	173
6·23	Visualization and analysis of immunohistochemical image derived seg- ments for LSBS 14391 shown on MIMS image	174
6·24	Images used for clinicopathological case study of LSBS 3733-2	175
6·25	Median signal levels within MIMS-derived clusters for LSBS 3733-2	176
B·1	Raw data structure in txt files from the optical emissions spectrometer.	186
B·2	Raw data structure in fin2 files from the magnetic sector field MS.	186
B·3	Raw data structure in csv files from the quadrupole MS.	187
B·4	Data structure provided by <code>readfiles.m</code> in MATLAB workspace.	187
B·5	Quadrupole header file information provided by <code>readfiles.m</code> in MAT- LAB workspace.	188

List of Abbreviations

AMBA	Allen Mouse Brain Atlas
amu	atomic mass units
BBB	Blood Brain Barrier
BF	Butterworth Filter
BNT	Blast Neurotrauma
BUCS	Boston University Concussion Scale
BUSM	Boston University School of Medicine
CBM	Center for Biometals & Metallomics
CC	Correlation-Coefficient
CDF	Cumulative Distribution Function
<i>cps</i>	Counts per Seconds
CTE	Chronic Traumatic Encephelopathy
CV	Chan-Vese
CVR	Caudal-Ventral-Right Coordinate System
DCR	Dacryocystorhinostomy
EBD	Evans Blue Dye
ELISA	Enzyme-linked Immunosorbent Assays

GAC	Geodesic Active Contours
GUI	Graphical User Interface
H&E	Hematoxylin and Eosin (IHC stain)
HSV	High Speed Video
ICP	Inductively-Coupled Plasma
IHC	Immunohistochemical
IHF	Immunohistofluorescence
INT	Impact Neurotrauma
iGd	Gadolinium-Injected Experiment
iNP	Nanoparticle Cocktail Injected Experiment
IQR	Interquartile Range
IR	Image Registration
JDF	Joint Density Function
KDE	Kernel Density Estimation
KED	Kinetic Energy Discrimination
KF	Kalman Filter
LA	Laser Ablation
LSBS	Lacrimal Sac Biopsy Samples
m/z	Mass to Charge Ratio
MS	Mass Spectrometer
MI	Mutual Information

MIND	Modality-Independent Neighborhood Descriptor (from (Heinrich et al., 2012))
MIMS	Metallomic Imaging Mass Spectrometry
MMMCIR.....	Multi-Modal, Multi-Channel Image Tegration
MRI	Magnetic Resonance Imaging
MVE	Mean-Variance Equalized (or equalization)
NIST	National Institute of Standards and Technology
NFT	Neurofibrillary Tangles
NLD	Nasolacrimal Duct
OES	Optical Emission Spectrometer
p-tau	Phosphorolated Tauopathy
PI	Photographic Image
PBS	Phosphate-Buffered Saline
pdf	Probability Density Function
<i>ppm</i>	Parts per Million
SA	Simulated Annealing
TBI	Traumatic Brain Injury

Endogenous Elements Considered (natural abundance %)

⁴⁴ <i>Ca</i>	Calcium (2.1)
⁶³ <i>Cu</i>	Copper (69.1)
⁶⁵ <i>Cu</i>	Copper (30.8)
⁵⁶ <i>Fe</i>	Iron (2.1)

^{57}Fe	Iron (91.8)
^{31}P	Phosphorus (100)
^{64}Zn	Zinc (48.3)
^{66}Zn	Zinc (27.9)

Exogenous Elements Considered (natural abundance %)

^{27}Al	Aluminum (100)
^{137}Ba	Barium (11.2)
^{157}Gd	Gadolinium (15.7)
^{60}Ni	Nickel (26.2)
^{208}Pb	Lead (52.4)
^{48}Ti	Titanium (73.7)

List of Variable Definitions

Variable	Section	Definition
γ_0	3.1	intensity threshold for HSV
p	3.1	pixel search area for HSV
$\phi(t, x, y)$	3.1	Lipschitz level-set function used in CV
C	3.1	Zero-level set (contour defining boundary in CV)
F	3.1	Energy functional for minimization in CV
c_1, c_2	3.1	mean intensities inside and outside C respectively
\vec{P}	3.2	RGB gross pathology surface image
G	3.2	Gradient magnitude image of \vec{P}
L	3.2	Maximum intensity scalar image
γ	3.2	Threshold for initial mask
φ_s	3.2	Down-sampling factor for \vec{P} hierarchical segmentation
\vec{p}	3.2	$\{R, G, B\}$ triplet value of a pixel
c	3.2	$\in \{1 \text{ (blood)}, 2 \text{ (Evans Blue)}, 3 \text{ (contusion)}, 4 \text{ (tissue)}\}$, Class labels in \vec{P} images
\mathcal{P}	3.2	$\{\vec{P}^{(n)}\}_{n=1}^N$, Set of gross pathology images
$\vec{\mathcal{I}}$	4	MIMS sequence

τ	4	$\in \{1, \dots, T\}$, indicator of sample “type”
d	4	Number of MIMS channels (dimensionality of each pixel)
\vec{I}_τ	4	Vector-pixel MIMS image of a single sample “type” τ
$I_\tau^{(i)}$	4	i -th channel MIMS image of a single sample “type” τ
g	4.3	$\in \{laser\ on, sample\}$, MIMS categories
M_τ	4.3	$\subseteq \{1\ (blank), 2\ (washout), 3\ (background), 4\ (sample)\}$, label mask of MIMS for sample type τ
$K_\tau^{(i)}$	4.3	$\subseteq \{0, 1\}$, binary mask derived from bimodal histogram threshold from i -th channel and type τ
$S_\tau^g(p)$	4.3	Segmentation image for group g and type τ
$\alpha^{(i)}, \beta^{(i)}$	4.3	Coefficients of line of best fit for i -th channel
x_j	4.3	$j = \{1, \dots, n_{std}\}$, standard calibration value in <i>ppm</i>
$y_j^{(i)}$	4.3	Median of the data in the <i>laser on</i> portion of the calibration image $I_j^{(i)}$
$\vec{x} = \text{vec}(I_\tau^{(i)})$	4.4	Vector of log-normal raw pixel values from MIMS
$\vec{y} = \ln \vec{x}$	4.4	Log of raw data having a Gaussian distribution
\vec{t}	4.4	Transformed \vec{y} data having a Gaussian distribution with specified target mean and variance
$g_{\vec{\mu}}$	4.5	Transformation function parametrized by the affine transformation parameters $\vec{\mu}$
$\vec{\mu}$	4.5	Parameters of transformation model g

$\mathcal{F}(\vec{p})$	4.5	Fixed image defined on grid \vec{p}
$\mathcal{M}(\vec{q})$	4.5	Moving image defined on grid \vec{q}
$\mathcal{M}^r(\vec{p})$	4.5	Moving image transformed into fixed image space
ϕ	4.5	Interpolation function used to compute $\mathcal{M}^r(\vec{p})$
$A_{\vec{\mu}}$	4.5	Affine transformation matrix
\mathcal{N}	5	ABMA Nissl-stain image
\mathcal{A}	5	ABMA atlas image
$M_{\mathcal{N}}$	5	Foreground/Background Nissl mask
$M_{\mathcal{A}}$	5	Foreground/Background atlas mask
$M_{\vec{T}}$	5	Foreground/Background MIMS brain mask
L	5	Left-side
R	5	Right-side
$\bar{\partial}^{(L-R)}$	5	normalized side difference metric used for left-versus-right MIMS signal analysis

Chapter 1

Introduction

1.1 Traumatic Brain Injury

Traumatic brain injury (TBI) has garnered significant attention in the United States, particularly in the past decade. It has been estimated that approximately 2.5 million emergency department visits yearly are for TBIs (Frieden et al., 2015) with nearly 84% of these injuries being classified as mild TBIs (Meaney et al., 2014; Frieden et al., 2015; VA and DoD, 2016). Recent US government work groups have provided definitions and guidelines to address TBI in the civilian and military populations. This group defined traumatic brain injury as follows (VA and DoD, 2016):

“a traumatically induced structural injury and/or physiological disruption of brain function as a result of an external force and is indicated by new onset or worsening of at least one of the following clinical signs immediately following the event:

- Any period of loss of or a decreased level of consciousness
- Any loss of memory for events immediately before or after the injury (post-traumatic amnesia)
- Any alteration in mental state at the time of the injury (e.g., confusion, disorientation, slowed thinking, alteration of consciousness/mental state)

- Neurological deficits (e.g., weakness, loss of balance, change in vision, praxis, paresis/plegia, sensory loss, aphasia) that may or may not be transient
- Intracranial lesion”

Two distinct types of TBIs eliciting substantial media attention include those caused by exposure to blast from conventional and improvised explosive devices and sports related head-injuries. The relationship between repetitive concussion in athletes and the neurodegenerative disease chronic traumatic encephalopathy (CTE) was first identified by Bennet Omalu and colleagues (Omalu et al., 2005, 2006). Like Alzheimer’s disease, one of the most identifiable features of CTE is the aggregation of hypophosphorylated tau, markedly at the depths of the sulci and around blood-vessels in the brain. The discovery of this distinctive neuropathology along with debilitating behavioral deficits in US National Football League players was highly controversial. The drama of this finding was even featured in the 2015 mainstream movie Concussion. Coincidentally in those same years, US soldiers began returning from the Iraq and Afghanistan wars with unprecedented rates of TBIs, earning it the name of “signature injury” of the Iraq war in the media (Zoroya, 2005; Robertson, 2006; Benzinger et al., 2009). Assessment of injury severity and the long-term deficits associated with TBI remain ongoing areas of research.

Blast-exposed individuals have been documented to suffer from significant neuropsychiatric symptoms, cognitive deficits, and neurological sequelae (Tanielian et al., 2008; Hoge et al., 2008; Ling et al., 2009; Vasterling et al., 2009; Cernak and Noble-Haeusslein, 2010; Hicks et al., 2010; Brenner et al., 2010; Peskind et al., 2011; Mac Donald et al., 2011) that resemble the clinical signs and symptoms of head-injured athletes diagnosed with chronic traumatic encephalopathy (CTE), a chronic neurodegenera-

tive condition (McKee et al., 2009, 2010; Cantu, 2007). Neuropathological abnormalities associated with CTE suggest a pathogenic mechanism involving blood-brain barrier (BBB) disruption induced by the shearing forces associated with the inciting trauma. This vasocentric hypothesis postulates a secondary neuroinflammatory cascade which leads to abnormal perivascular protein (tau) accumulation and cerebrovasculature abnormalities that define CTE neuropathology.

The pathogenic cascade by which mechanical head trauma (concussive injury) and blast exposure (percussive injury) lead to the irreparable brain damage and cognitive dysfunction is poorly understood. Available treatment is limited to supportive measures. Development of new clinically useful diagnostic technology, disease biomarkers, prophylactic countermeasures, and therapeutic interventions is critically dependent on elucidating the primary pathogenesis and mechanistic details of the underlying disease. Large knowledge gaps in our understanding of TBI and CTE pathophysiology will continue to impede efforts toward developing new diagnostics and treatments for improving TBI outcome. This interdisciplinary translational research is designed to meet this urgent need by developing and implementing new analytical technology for disease-driven mechanistic discovery.

1.2 Animal Models of Blast- and Impact-Induced Neurotrauma

While a number of observational studies have looked at the effects of traumatic and concussive head-injuries in humans (Terrio et al., 2009; Gavett et al., 2011; Barkhoudarian et al., 2011), these studies cannot establish a causal link between injury and outcome. In addition, patient history may not be complete and the parameters of the injury are nearly impossible to establish. For these reasons, an injury

realistic animal model is essential to a more complete understanding and characterization of the primary and secondary effects of TBI.

A variety of animal models have been developed to mimic different types of TBIs. Figure 1.1 shows several predominant models (Xiong et al., 2013), many of which require a craniotomy or impede movement of the head altogether. Needless to say, these types of TBIs are not representative of the typical closed-head, nonlethal blast neurotrauma (BNT) and impact neurotrauma (INT) injuries experienced in combat or contact sports, respectively. This work is focused on supporting the development of an injury-realistic animal model of BNT and INT. By designing a clinically-relevant mouse model of these types of TBIs, the pathological developments associated with TBI and progression of CTE-like neuropathology can be better understood. This knowledge may inform our understanding of the mechanisms of injury and guide the ultimate development of therapeutic measures. Ongoing research on the measurable effects of TBI has also motivated promising avenues for biomarkers which may indicate injury severity (Weissberg et al., 2014).

1.3 Assessment of Blood-Brain Barrier Disruption

Most imaging methods used to assess BBB disruption are qualitative, requiring either neurobiological expertise to identify abnormalities (as with electron microscopy) or which may elicit non-specific/non-graded activation responses (as with immunohistochemistry). The few methods which are (semi-)quantitative tend to provide a single number as an output, such as measuring gene expression level or brain edema. To determine the role of BBB dysfunction in the development of CTE and the cytoarchitectural comorbidities associated with the neuropathology, spatial information is essential. The objective of this work will be to develop methods for identification of

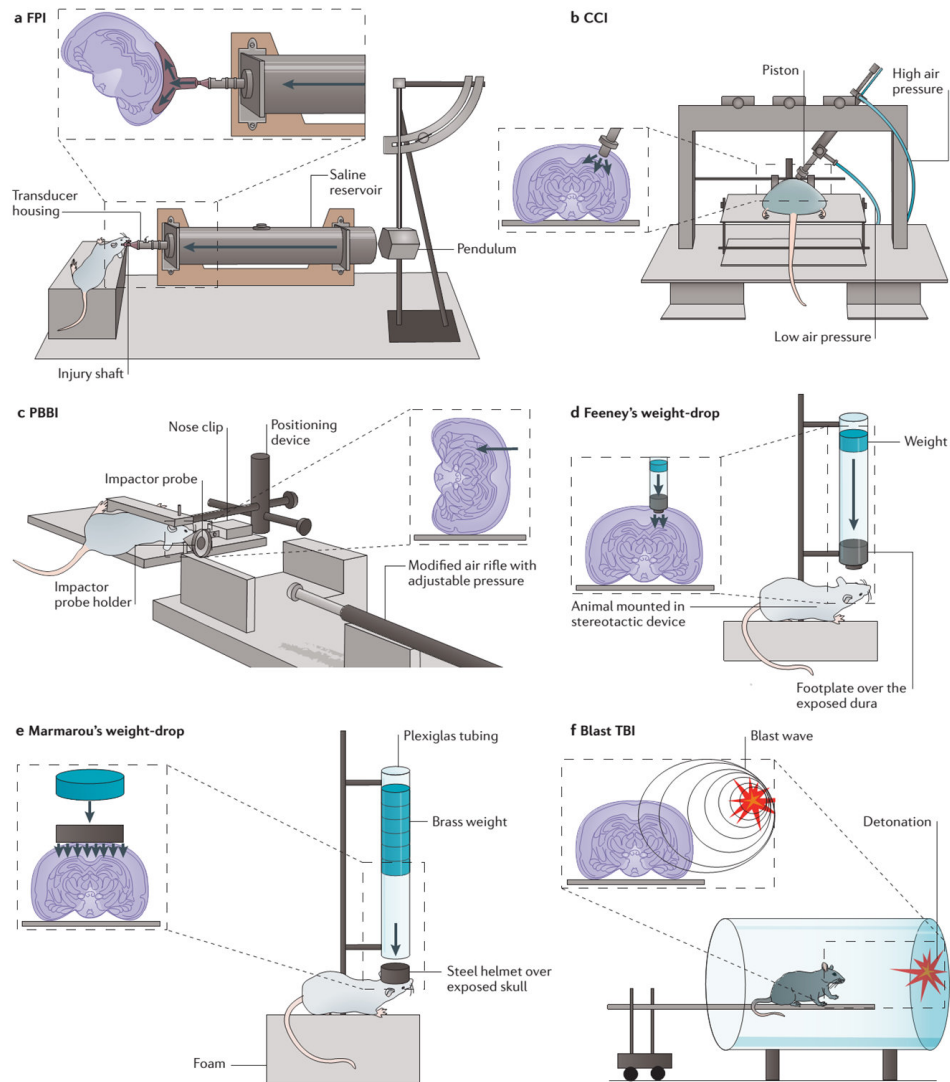
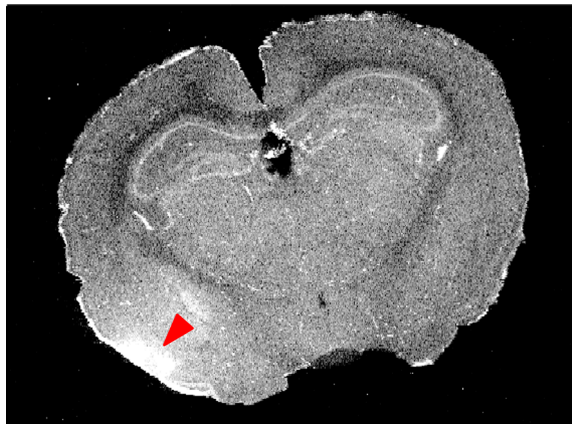
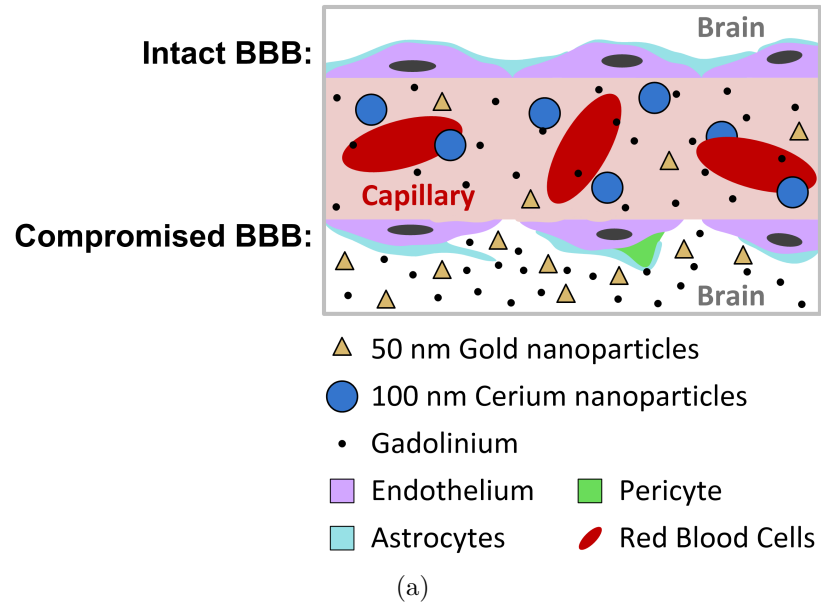


Figure 1.1: Experimental set-ups for the animal models of TBI. **(a)** The fluid percussion injury device uses rapid injection of a fluid pulse into the epidural space. **(b)** The controlled cortical impact injury model uses an air or electromagnetic driven piston to penetrate the brain at a known distance and velocity. **(c)** The penetrating ballistic-like brain injury involves the transmission of projectiles with high energy. **(d)** In Feeney's weight-drop model, a free weight is released directly onto the exposed dura. **(e)** In Marmarou's weight-drop model, a metal disk is placed over the skull to prevent bone fracture. **(f)** Blast brain injury. (Figure and caption from copied from (Xiong et al., 2013), Figure 1)

BBB dysfunction in-situ and to quantitatively associate these measures with experimental parameters to aid in our understanding of the progression of neuropathology resulting from TBI.

Metallomic imaging mass spectrometry (MIMS) is a novel application of analytical chemistry instrumentation typically used to determine the purity or metallomic content of a solution or gaseous sample. MIMS enables quantitative imaging which may be utilized to overcome the issues of sensitivity and specificity associated with classical BBB evaluation modalities. Through the use of isotopic ratio characterization and injection of elemental cocktails as tracers, MIMS may be used to probe specific neural processes in the brain, such as localization and quantification of BBB disruption. More details describing the acquisition of MIMS for biological tissue are given in Section 2.3.2. In summary, MIMS are quantitative maps which quantify the elemental composition of the sample being imaged.

Figure 1.2 conveys the concept of using MIMS to image tissue from an animal injected with nanoparticles and metallomic tracers of known size and composition as a means to identify the extent of BBB compromise. The size and density of nanoparticles extravasated indicate the severity of the BBB compromise. Fluorescent nanoparticles have been used in this way to study BBB compromise as a result of foreign body response in a mouse model (Sawyer and Kyriakides, 2013). These results support the concept of using nanoparticle size and quantity in brain parenchyma to serve as an indicator of BBB compromise. As opposed to fluorescent imaging or electron microscopy for nanoparticle identification, as was used in the aforementioned study, MIMS provides a more robust method for quantification and localization of nanoparticles with respect to brain anatomy.



(b) ^{157}Gd MIMS of TBI sample

Figure 1·2: Microvascular disruption in traumatic brain injury. (a) schematic showing the rationale for assessing blood-brain barrier (BBB) compromise using injected nanoparticles combined with metallomic imaging mass spectrometry (MIMS). (b) Preliminary MIMS detecting elevated ^{157}Gd signal in the left ipsilateral cortex following impact neurotrauma indicating BBB compromise.

1.4 Specific Aims of this Thesis

The focus of this work is on development of image processing algorithms for facilitating the comparison of behavioral and neuropathological outcomes in mouse models of blast- and impact-neurotrauma. Using both novel and traditional neuropathological imaging methods, quantitative assessments are developed to test the hypothesis that biomechanical forces transmitted to structures in the brain during BNT and INT disrupt BBB functional integrity and activate secondary neuroinflammatory responses leading to progressive CTE neuropathology. While many of the methods developed for data collected to elucidate the mechanisms of TBI are applications of traditional techniques in computer vision and machine learning, these methods have not been used to inform TBI in the ways described in this work. The image processing and analytical contributions of this thesis have furthered our understanding of the factors involved in TBI outcomes in mouse models of blast- and impact-neurotrauma. The image analysis schemes presented are used to investigate the effect of key injury parameters (dose, fractionation, post-exposure interval) on brain microvascular structure and function in relationship to regional CTE neuropathology and supported key findings in our recently submitted publication (Tagge et al., 2017).

The primary contribution of the work described is the development of methods to aid in the presentation and interpretation of data from a newly-emerging analytical imaging modality, metallomic imaging mass spectrometry (MIMS). These methods address all aspects of the analytical elemental-isotopic imaging technique, from data acquisition to data analysis, for exploring hypotheses related to biospecimen pathology. The novel contributions made towards MIMS data processing and analysis are demonstrated to provide robust, quantitative insights into the underlying pathogenesis of two very different biospecimens: coronal sections of the mouse brain and human

lacrimal sac biopsy samples. Large-scale automated analysis of MIMS brain images from mice is made possible by a newly conceived multi-modal, multi-channel image registration (MMMCIR) method which maximizes multivariate mutual-information between two images to determine the optimal affine transformation parameters. The MMCIR method is applied to MIMS brain images to facilitate the automated and objective analysis of biological specimens uncommon in the field of translational medical research. The utility and robustness of the MIMS methods described are shown to provide unique analytical evidence of the pathological mechanisms of TBI and human dacryolith formation.

The aims of this work can be summarized as follows:

- To develop an algorithm for tracking mouse head motion in high-speed video footage in order to quantify injury severity and correlate relevant head kinematic metrics with measured neuropathology
- To develop quantitative methods for quantification of pathology in photomacroscopic and fluorescent images
- To create a software toolkit for MIMS aiding in the data extraction, visualization and preprocessing specific to this modality
- To develop an unsupervised approach for anatomical segmentation of rigid, stereotyped anatomical structures
- To apply the method for automatic anatomical segmentation on a cohort of MIMS brain images in order to evaluate the role of BBB integrity following impact neurotrauma in a mouse model of TBI
- To evaluate elemental-isotopic content of human lacrimal sac biopsy samples by using the methods developed for MIMS

1.5 Thesis Organization

This thesis can be divided into three main efforts: understanding the physical mechanisms of TBI through traditional imaging modalities, developing image processing methods for objective and automated analysis of MIMS, and combination of traditional imaging and MIMS modalities to assess pathology in biological tissues. The chapters are organized as follows:

- **Chapter 2** presents background information on the TBI mouse models used in this work and the traditional methods employed for neuropathological and behavioral assessment. An overview of the MIMS properties and acquisition procedure is provided, followed by a summary of the state-of-the-art methods for neuropathological image analysis and image registration .
- **Chapter 3** discusses the technical development and results of the high-speed video head tracking algorithm. Assessments of tissues from Evans blue injected mice having undergone TBI is also presented. The first method presented is a semi-supervised per-pixel classification algorithm which constructs a photometric (RGB) model of four classes of interest. This model is then used for labeling photomacroscopic images of the surface of the brain. The Chapter concludes with details on the workflow developed for processing fluorescent images of thick brain sections from Evans blue injected mice.
- **Chapter 4** details the algorithms developed specifically to address properties of the MIMS modality. Basic functions, such as those used to extract and visualize data, as well as technical details behind MIMS calibration and normalization, are presented. Finally, each aspect of the multi-modal, multi-channel image registration function is discussed in detail.
- **Chapter 5** applies the methods developed for MIMS on two TBI cohorts.

Multi-modal, multi-channel image registration is used to label anatomical regions in coronal brain MIMS. Anatomical subgroups are defined and signal levels on the left and right sides of the brain within each subgroup are compared. The results from these experiments provide preliminary evidence for local and differential BBB compromise, but also motivate the need for further improvements to MIMS acquisition.

- **Chapter 6** explores the use of MIMS for investigation of human lacrimal sac samples. Through the acquisition of samples with matrix-matched calibration standards, preliminary results indicate the presence of toxic heavy metals in the surgically removed dacryoliths and suggest that foreign substances may contribute to the development of this condition.
- **Chapter 7** summarizes the contributions made as part of this work and suggests several areas for improving and extending the research presented.

Chapter 2

Traumatic Brain Injury Mouse Models and Assessments

2.1 Traumatic Brain Injury Mouse Models

In order to understand how the parameters of a traumatic brain injury (TBI), such as severity, frequency, and head kinematics, influence acute and chronic neuropathological and behavioral outcomes, a mouse model of blast neurotrauma (BNT) and impact neurotrauma (INT) were designed and validated in the Neurotrauma Laboratory at the Boston University School of Medicine. Development and validation of these mouse neurotrauma model systems was the thesis work of two graduate students, Andrew Fisher (graduated 2017) and Chad Tagge (graduated 2015), with the help of post-doctoral researcher, Olga Minaeva, Ph.D., all of whom conducted research in Dr. Goldstein's laboratory. The validated TBI mouse models have been described in recent publications (Goldstein et al., 2012; Tagge et al., 2017). The models were designed in such a way that the physical parameters of the system, as well as the neuropathological and behavioral outcomes, closely resemble those found in combat soldiers and contact-sports athletes having suffered from mild TBIs.

For the BNT model, a shock tube was constructed in collaboration with Fraunhofer Center for Manufacturing Innovation at Boston University and operated at the Neu-

rotrauma Laboratory (part of the Dr. Goldstein's Molecular Aging and Development Laboratory). A schematic of the shock tube is shown in Fig. 2.1. The shock tube was constructed to deliver highly reproducible wave fronts of pressurized gas whose characteristics are similar to those produced by 4.5 *kg* of C4 explosives at a distance of 5.5 *m* (Goldstein et al., 2012). Helium gas accumulates in the compression chamber until the pressure causes the plastic membrane to rupture, at which point the pressurized wave-front travels along the expansion chamber towards the mouse. The shock wave front travels at a speed of approximately 150 *m/s* to the end of the shock tube where the mouse resides in a customized restraint system allowing for free motion of the head and neck. The BNT model uses a single blast to the left-lateral side. Significant measurements and analyses have been conducted to ensure the similarity of the blast-wave measured in the tube to dynamics of those measured in the field. Previous experiments have marked the similarity between the neuropathology in the mouse brain to that observed in TBI-exposed human brains (Goldstein et al., 2012). Further technical details on the design and validation of the blast shock tube can be found in Fisher (2017).

The INT model was designed with the goal of inciting a left-lateral head injury comparable to that experienced in the BNT model and which closely mimics the acute injuries observed in sports-related TBIs. Rather than being an inertial-loading injury as in the BNT case, the INT would be contrasted by direct-contact loading. Since rapid head acceleration is one of the postulated contributors of the chronic neuropathology observed in brains of individuals having a history of concussive injuries, the INT model parameters were adjusted such that the maximum head angular acceleration was approximately equal to the head accelerations observed in the BNT model. The impactor was designed by Chad Tagge of Dr. Goldstein's laboratory and its design is discussed in detail in his recent thesis (Tagge, 2016, Chapter 2). As

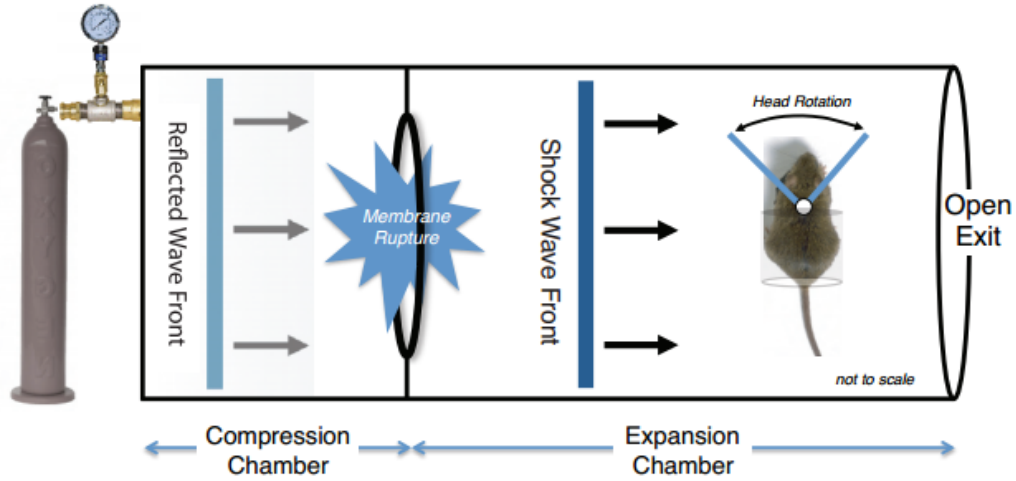
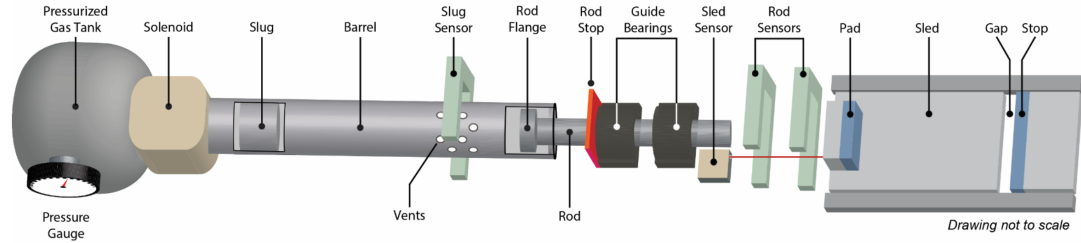


Figure 2-1: Schematic of the blast tube set up. Pressurized gas is delivered into the closed system of the pre-burst compression chamber. Abrupt rupture of a mylar membrane diaphragm separating the compression and expansion chambers initiates a blast shock wave front that traverses the long axis of the 4.5 m shock tube at supersonic velocity ($\text{Mach } 1.26 \pm 0.04$). (Figure and caption from Goldstein et al. (2012), Fig. S3)

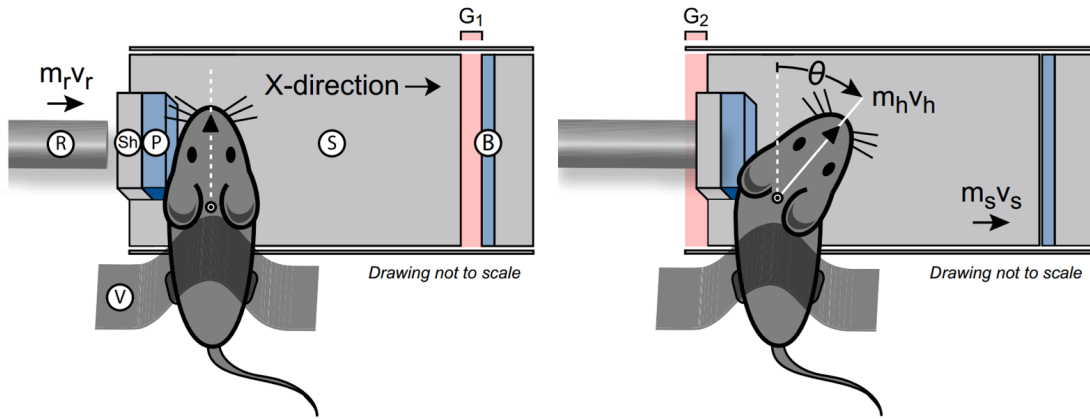
shown in Fig. 2-2(b), the mouse is secured with the left-lateral side of its head against the pad attached to the sled. The back-end architecture of the impactor, pictured in Fig. 2-2(a), uses pressurized gas to accelerate a slug. The momentum generated by the slug is transferred to a rod ($m_r v_r$), which makes contact with the sled and results in the transfer of an angular momentum to the mouse's head ($m_h v_h$, Fig. 2-2(c)).

2.2 Neuropathological & Behavioral Deficits in TBI

While the evidence causally linking TBI to behavioral and physiological deficits is difficult to establish in humans, brains acquired from adolescent donors, military personnel, and high-profile professional athletes are highly suggestive of a connection. A discussion of the link between TBI and CTE in humans is presented in Ojo et al.



(a) Impactor architecture



(b) Before impact

(c) After impact

Figure 2:2: (a) Instrument schematic for the concussive impact neurotrauma mouse model. (b & c) Schematic of momentum transfer instrument and unanesthetized C57BL/6 mouse before (b) and after (c) lateral impact injury. (b) Mouse is secured across the thorax with a Velcro strap (V) and positioned such that the head is in contact with the impactor assembly, a helmet analog comprised of an inner foam pad (P) and an outer hard shell (Sh) that is fixed to a mobile sled (S). Stainless steel rod (R) of known mass (m_r) and empirically-measured velocity (v_r) transfers momentum to the sled. (c) Sled of known mass (m_s) and empirically-measured velocity (v_s) transfers momentum to the head resulting in traumatic acceleration. Sled motion is terminated by a backstop (B). Distal sled gap, (G_1). Proximal sled gap, (G_2). (Figures and captions from Tagge et al. (2017), Fig. 2 and Fig. S2)

(2016) along with a variety of caveats and complications associated with studying the association in animal models. Nevertheless, the neuropsychiatric features including depression, cognitive impairment, and aggression, which have been reported with CTE neuropathology (DeKosky et al., 2013), demand further investigation and establishment of the connection between TBI, CTE, and development of neuropsychiatric deficits.

Despite many similarities between the neurodegenerative diseases CTE and Alzheimer's, CTE is differentiated by the accumulation of hyper-phosphorylated tauopathy (p-tau) primarily occurring at the depths of the sulci and near other micromechanical heterogeneities in the brain, such as blood vessels (Goldstein et al., 2012). The first formal definition for CTE was provided by McKee et al. (2013) suggesting its diagnosis as the presence of the following four components:

- “1. perivascular foci of p-tau immunoreactive astrocytic tangles and neurofibrillary tangles (NFT)
2. irregular cortical distribution of p-tau immunoreactive NFT and astrocytic tangles with a predilection for the depth of cerebral sulci
3. clusters of subpial and periventricular astrocytic tangles in the cerebral cortex, diencephalon, basal ganglia and brainstem
4. NFT in the cerebral cortex located preferentially in the superficial layers”

Mouse models of BNT and INT have demonstrated diffuse perivascular pathology (Goldstein et al., 2012; Tagge et al., 2017). It has been postulated that damage to local blood-brain barrier (BBB) architecture creates a hypoxic environment and results in a complex neuroinflammatory response, potentially leading to a chronic imbalance (Marchi et al., 2013; VA and DoD, 2016). Blood-brain barrier dysfunction has also been implicated in other neurodegenerative diseases such as Alzheimer's

and Parkinson's (Neuwelt et al., 2011). One of the greatest challenges associated with in-vivo detection of BBB dysfunction is the local and microscopic damage to vessels, which cannot be reliably identified using conventional imaging methods such as computed tomography or magnetic resonance imaging (Shenton et al., 2012) and is not recommended as a clinical assessment (VA and DoD, 2016). Using these validated animal models for TBI, the goal of this work is to develop the metallomic imaging mass spectrometry (MIMS) modality in order to quantitatively and spatially assess the degree of BBB compromise.

A healthy BBB consists of a blood containing lumen formed by epithelial cells. The epithelial cell layer is surrounded by pericytes which complete the barrier between the cerebrovasculature and neuronal tissue. A schematic representation of the BBB from Winkler et al. (2011) is shown in Fig. 2-3. In summary, an intact BBB is one which completely isolates the blood from brain tissue by a layer of specialized cells responsible for chaperoning nutrients and other molecules from one side of the barrier to the other.

Traumatic brain injury is believed to focally induce BBB disruption resulting in compromised microvasculature and subsequent neuronal death leading to chronic and progressive neurodegeneration. State of the art in-vivo imaging methods have not revealed any differences between the brains of mice in control and TBI groups (Mac Donald et al., 2011) likely because most modern imaging technologies do not have sufficient resolution to show the cellular level effects. Currently, neuropathological assessments of TBI are achieved through a variety of postmortem tissue imaging procedures including immunohistochemistry and electron microscopy.

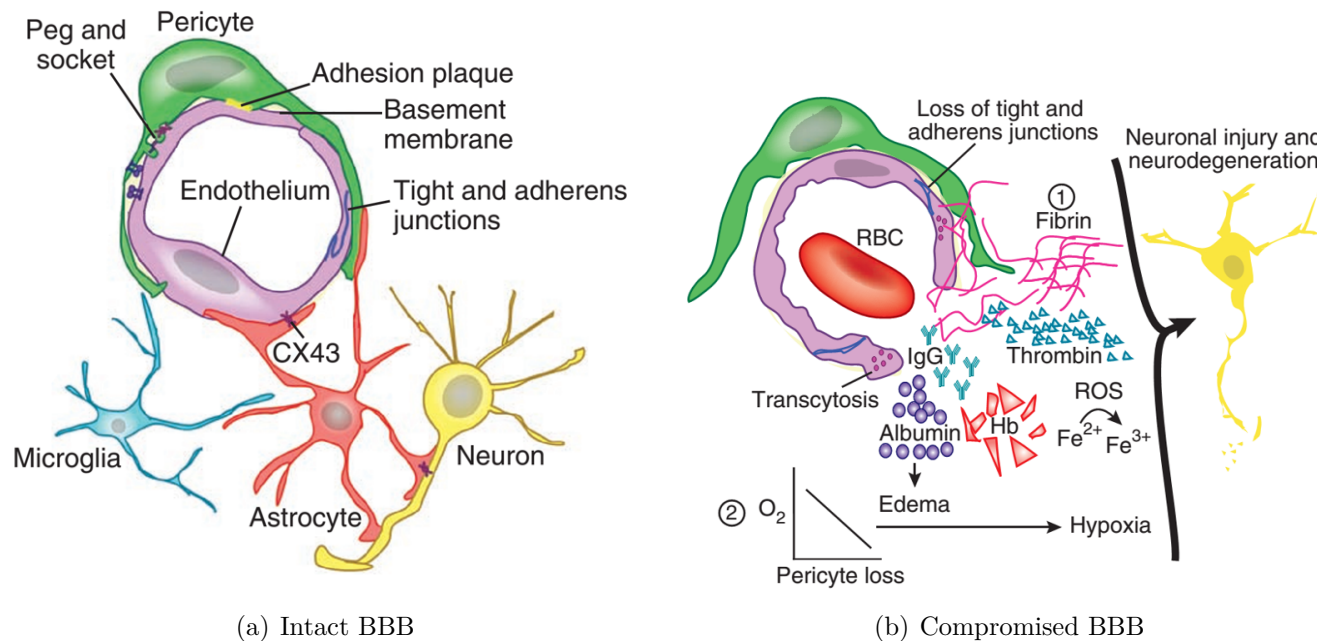


Figure 2-3: (a) Structure of a normal neurovascular unit (Figure copied from (Winkler et al., 2011), Fig. 1). (b) “(1) Blood-brain barrier (BBB) breakdown due to disrupted BBB tight and adherens junctions and increased bulk flow fluid transcytosis leads to brain influx of serum proteins (for example, albumin, immunoglobulin G (IgG)), causing edema, and of blood-derived vasculotoxic and neurotoxic macromolecules (for example, fibrin, thrombin, hemoglobin (Hb)-derived iron), causing neuronal injury and neurodegenerative changes. RBC, red blood cell; ROS, reactive oxygen species. (2) Reductions in capillary blood flow due to microvascular degeneration and pericapillary edema aggravate chronic hypoperfusion and hypoxia, depriving metabolically active neurons of oxygen and other essential nutrients, which leads to neuronal dysfunction.” (Figure and caption copied from (Winkler et al., 2011), Fig. 5a)

2.2.1 Injury Severity Assessments (BUCS)

One of the first scoring systems for assessing TBI severity was developed by Teasdale and Jennett (1974). This 15-point scale, called the Glasgow Coma Scale (GCS), is still used today as a way of grading a head injury as mild (score of 13-15), moderate (9-12) or severe (3-8) (Benzinger et al., 2009). Other common metrics which help define TBI severity include the period of altered consciousness, the period of loss of consciousness, and duration of post-traumatic amnesia (VA and DoD, 2016). While behavioral and motor function impairment measures for animal models have been proposed, such as the neurological severity score (Chen et al., 1996; Beni-Adani et al., 2001; Stahel et al., 2000), the binary scoring for achievement or failure of each of the ten tasks did not reflect the nuances associated with the motor-neurological deficits.

To fill this unmet need for a behavioral and motor function assessment which was easy to administer and captured some of the nuances associated with post-TBI motor function, such as side-specific motor neurological deficits, Tagge (2016) developed a 15-point Boston University concussion scale (BUCS). Mice perform three tasks, each carrying a score from zero to five points. Description of the tasks and their scores are explained in the scoring rubric in Fig. 2-4. Mice having undergone INT showed a statistically significant decrease in BUCS by 3.2 points compared to BNT exposed mice two minutes after TBI, with the score recovering to normal levels (mean score of 14.5) three hours after injury (Tagge et al., 2017). These scores were used to compare post-injury severity and confirm recovery of motor function, but have yet to be explored in detail for how they relate to injury parameters and neuropathology.

Domain 1 <i>OpenField</i> 30 Secs	Score = 5		Score = 4		Score = 3		Score = 2		Score = 1		Score = 0		Domain 1 <i>Open Field</i> Sub-Score Max = 5
	A	Linear locomotion	A	Linear locomotion	A	Unidirectional rotation	A	No locomotion	A	No locomotion	A	Tonic-Clonic Seizure	
	B	Explores 2 or more corners	B	Explores <2 corners	B	Note rotation direction	B	Ventral abdomen down	B	Lateral abdomen down	B	Note unilateral or general	
Domain 2 <i>Wire Mesh</i> 30 Secs	Score = 5		Score = 4		Score = 3		Score = 2		Score = 1		Score = 0		Domain 2 <i>Wire Mesh</i> Sub-Score Max = 5
	A	Multidirectional locomotion, Paw exits box at least once	A	Multidirectional locomotion, Paws remain within box	A	Unidirectional rotation	A	No Locomotion	A	No Locomotion	A	Unable to grip mesh or	
	B	Four-paw hang	B	Four-paw hang	B	Note rotation direction	B	Four-paw hang	B	<Four-paw hang	B	Falls from mesh	
Domain 3 <i>Beam Walk</i> 30 Secs	Score = 5		Score = 4		Score = 3		Score = 2		Score = 1		Score = 0		Domain 3 <i>Beam Walk</i> Sub-Score Max = 5
	A	Beam traversal	A	Beam traversal	A	Beam traversal	A	No beam traversal	A	No beam traversal	A	Unable to perform test or	
	B	Total distance > ½ beam	B	Total distance < ½, ≥ ¼ beam	B	Total distance < ¼ beam	B	Balances on beam	B	Unbalanced on beam	B	Falls from beam	
Note: BUCS-4R validated only for C57BL/6 mice following left lateral closed-head impact injury without administration of pre-injury anesthesia (injection or vapor). "A" Criteria: dominant mode of locomotion. "B" Criteria: criterion modifier. Domain scores = highest performance score during test session.												Combined BUCS Score Total Sub-Scores 1+2+3	

Figure 2·4: Boston University concussion scale scoring rubric

2.3 Introduction to Imaging Modalities Utilized

As previously discussed, validated forms of in-vivo imaging and biomarkers which reliably indicate TBI severity and pathogenesis remain in development (Marchi et al., 2013). Many common forms of assessment include western blots, enzyme-linked immunosorbent assays (ELISA), immunohistochemical (IHC) and immunofluorescent (IHF) imaging, and electron microscopy. Both western blots and ELISA require tissue homogenization and as such are not localized measures. As images, IHC and IHF do inform pathogenesis while maintaining spatial integrity, but these techniques are still largely considered qualitative and difficult to normalize. While there is promise in their utility in automated diagnosis using machine learning, particularly for carcinomas (Rizzardi et al., 2012), this approach requires a large, labeled dataset which is representative of image variability. The specifics of the two modalities used beyond the optical images (RGB) in this work are described in this Section.

2.3.1 Evans Blue Extravasation with Fluorescent Imaging

Evans blue dye (EBD) is a blue-colored fluorescent dye (excitation peaks at 470 and 540 *nm*, emission peak at 680 *nm* (Jaffer et al., 2013)) which binds to serum albumin (Rawson, 1943). The dye may be injected and allowed to circulate to serve as a marker for BBB compromise in animal models (Uyama et al., 1988; Manaenko et al., 2011). Since the dye is bound to the serum protein albumin, the presence of EBD in the brain parenchyma indicates a compromised BBB to the extent that albumin is extravasated. EBD may be detected by visible blue discoloration of the brain tissue in optical images, or more quantitatively through fluorescent imaging. Previous work has validated the ability for large-region quantification of EBD extravasation in the brains of mouse models of stroke (Jaffer et al., 2013) and blast (Kabu et al., 2015).

Staining with EBD allows for spatial localization of BBB disruption (del Valle et al., 2008; Kabu et al., 2015; Tagge et al., 2017).

This principle of marking BBB dysfunction by the presence of EBD in optical and fluorescent images was used for evaluating the effect impact neurotrauma on BBB integrity (Tagge, 2016; Tagge et al., 2017). The experimental protocol for the optical and fluorescent images of brain tissue from EBD injected mice is provided in Appendix A.2. The algorithms developed for stream-lining the analysis of these data are presented in Chapter 3. Detailed methods and results derived from these images are discussed by Tagge (2016) and are summarized in Fig. 5A-D of Tagge et al. (2017).

2.3.2 Metallomic Imaging Mass Spectrometry for Biological Samples

Mass spectrometers (MS) are an essential tool in analytical chemistry used to measure the purity of a sample. They are utilized in a number of applications including microelectronic materials research, environmental and geological assessment, and carbon dating. These instruments can be extremely sensitive (detecting parts per quadrillion), have a vast linear dynamic range (up to 10^{12} orders of magnitude, atomic mass units [*amu*]) and are capable of simultaneously measuring isotope ratios across the periodic table with mass resolution near 0.001 *amu*.

In inductively-coupled plasma mass spectrometry (ICP-MS) used in this work, a sample is sprayed into an argon plasma and ionized. While the specifics of the instrument depend on the type of mass analyzer used by the MS instrument, generally an ionic particle's movement in electric and magnetic fields is fully characterized by a differential equation and solvable given the initial conditions. By manipulating these fields, ions with a specific m/z value may be counted. The MS instrument functions

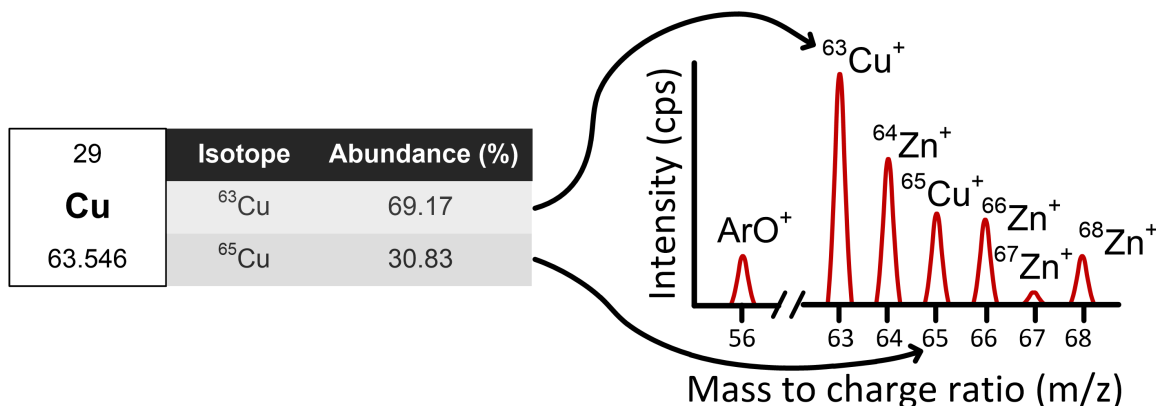


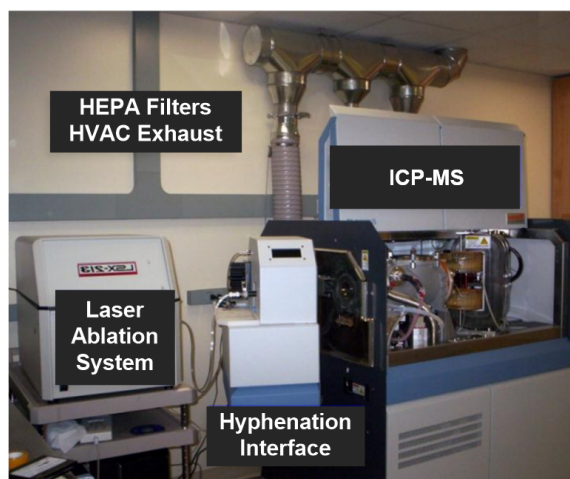
Figure 2-5: Representation of a spectrograph measured from a sample containing copper and zinc. On the left, isotope information for copper is given. The top number (29) indicates that it is the 29-th element on the periodic table of elements. The number at the bottom of the box indicates the the atomic mass of the element, which is the average mass of each of the two isotopes: for copper ^{63}Cu and ^{65}Cu . The two isotopes are found with the relative abundance indicated. The image on the right provides an example of a spectrograph for a range of the mass to charge ratio (m/z) values. For each measurement, the instrument records the intensity for each m/z -value specified.

as a transducer by translating the number of ions with known m/z -value hitting the detector into a voltage. For each time point of data, the MS output is a spectrograph (Fig. 2-5). The operator may select a range of values, such as $m/z = \{62 - 70\}$, or may select a number of specific isotopes to acquire data for. For each of these indicated m/z -values, the instrument returns the amount of the given m/z -value in counts per second (*cps*). These readings can be converted into absolute concentrations (for example, parts per million [*ppm*]) using a linear, matrix-matched calibration curve which can be used to calculate *ppm* from *cps* from the instrument. An important operational consideration is that of atomic interferences. These are mentioned by the MS instrument software, which allows for various modes of operation for minimizing these interferences (Thermo Fisher Scientific, 2010).

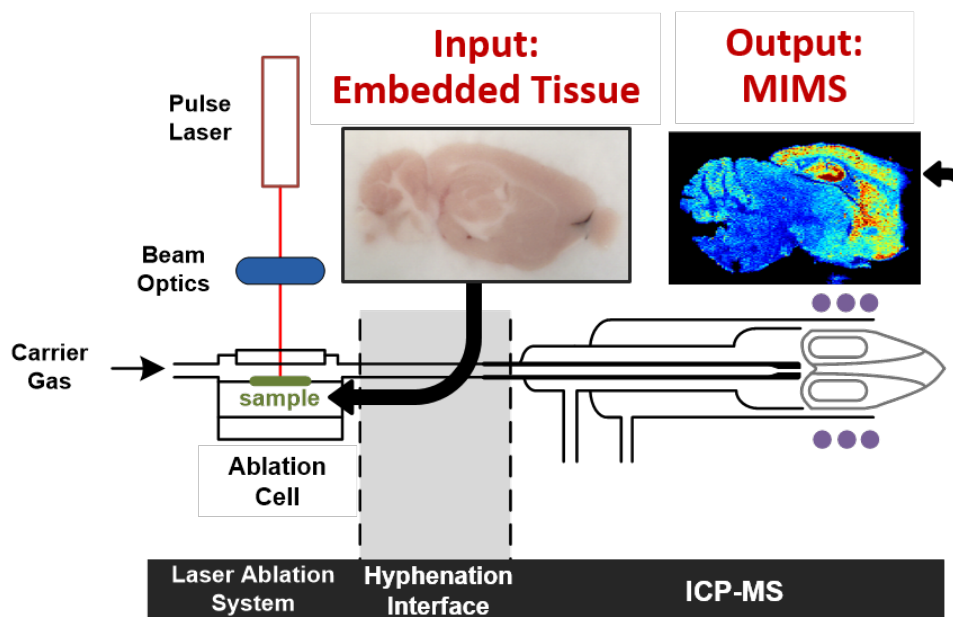
The use of MS for investigating the metallomic distribution of biological tissue is a

recent application introduced in the early 2000's (Kindness et al., 2003). To generate an isotopic distribution map of an object, a laser ablation system (LA) and hyphenation system are added to the front end of the MS (Fig. 2·6(a)). As shown in Fig. 2·6(b), the biological sample is enclosed in the ablation cell, which has a window at the top. The laser shines through the window and ablates material from the top layer of the sample, generating a plume of particles which are carried into the MS plasma by a carrier gas flowing over the sample. A metallomic image is created by continuously raster scanning (row-by-row) the laser across the tissue while the MS acquires a spectrograph at an indicated acquisition sampling rate, t_{acq} . The spectrograph for each spatial location of the sample can be thought of as a vector-valued pixel containing quantitative information about the distribution of isotopes at that particular location. A recent publication provides a detailed protocol for LA-ICP-MS (Hare et al., 2017). It should be noted that metallomic imaging mass spectrometry (MIMS) is a destructive, ex-vivo imaging technique since the surface of the sample is ablated and the sample must be enclosed in a small ablation cell. The ablation depth has not been characterized, but is understood to be on the order of tens of microns, depending on laser power and sample material properties.

The image quality and spatial resolution of the resulting MIMS are influenced by the experimental parameters and instrumentation. The specificity and detection limit of a given isotope are primarily influenced by the spectrometer used. The Center for Biometals (CBM; Boston, MA) where the data were acquired, which is part of Dr. Goldstein's Molecular Aging and Development Laboratory, has three instruments available: a Thermo Fisher iCAP 7200 (ICP-OES), a Thermo Fisher iCAP-Q (quadrupole ICP-MS), and a Thermo Fisher Element 2 (magnetic sector field ICP-MS). The images in this work were acquired under the direction of the analytic director of the CBM at the time, Noel Casey, Ph.D. The data in Chapter 5 were



(a) MIMS acquisition system



(b) LA-ICP-MS schematic

Figure 2-6: (a) Metallomic imaging mass spectrometry system comprised of a laser ablation (LA) system on the front end with an inductively-coupled plasma mass spectrometer (ICP-MS) on the back end. The two instruments are connected via a hyphenation interface. The system as a whole is known as LA-ICP-MS. (b) Schematic diagram of the LA-ICP-MS system.

Table 2.1: The arrows indicate the direction that spatial parameter needs to change (\uparrow = increase, \downarrow = decrease) in order achieve the result indicated in the column header. t_{acq} : MS sampling rate; v_{scan} : scan speed; d_{spot} : laser spot size.

MIMS parameter	Max signal	Min noise	Max spatial res.	Min total T
t_{acq} [s]	\uparrow	\uparrow	\downarrow	—
v_{scan} [$\mu\text{m}/\text{s}$]	\downarrow	\downarrow	\downarrow	\uparrow
d_{spot} [μm]	\uparrow	\downarrow	\downarrow	\uparrow

acquired using the Element XR by Dr. Casey. The data considered in Chapter 6 were acquired by Bo Yan, Ph.D., with the iCAP-Q.

The spatial resolution of each pixel is dictated by the stage movement, gas flow rate and composition, and ablation cell characteristics of the LA system. The LA instrument used in this work was the Teledyne CETAC LSX-213 G2+. The instrument’s specifications can be found on the company’s website (Teledyne CETAC Technologies, 2014). The spatial dimensions of a pixel may be calculated from the four user-defined parameters dictating stage movement and data sampling: (1) the laser spot size, d_{spot} [μm]; (2) stage scan speed, v_{scan} [$\mu\text{m}/\text{s}$]; (3) line-to-line spacing, d_{l2l} [μm]; (4) MS sampling rate, t_{acq} [s]. A diagram showing how these variables influence the spatial resolution can be found in Fig. 2-7. The laser spot size, scan speed and MS sampling rate all influence the horizontal resolution of each pixel. The vertical resolution is considered to be the line-to-line spacing indicated. There are several challenges associated with optimizing the parametrization of MIMS to acquire the highest quality image in a reasonable amount of time. A summary of how the parameters need to be changed to achieve maximum signal, minimum noise, maximum spatial resolution and minimum total acquisition time, T , is given in Table 2.1.

Metallomic imaging mass spectrometry using the LA-ICP-MS system has been used

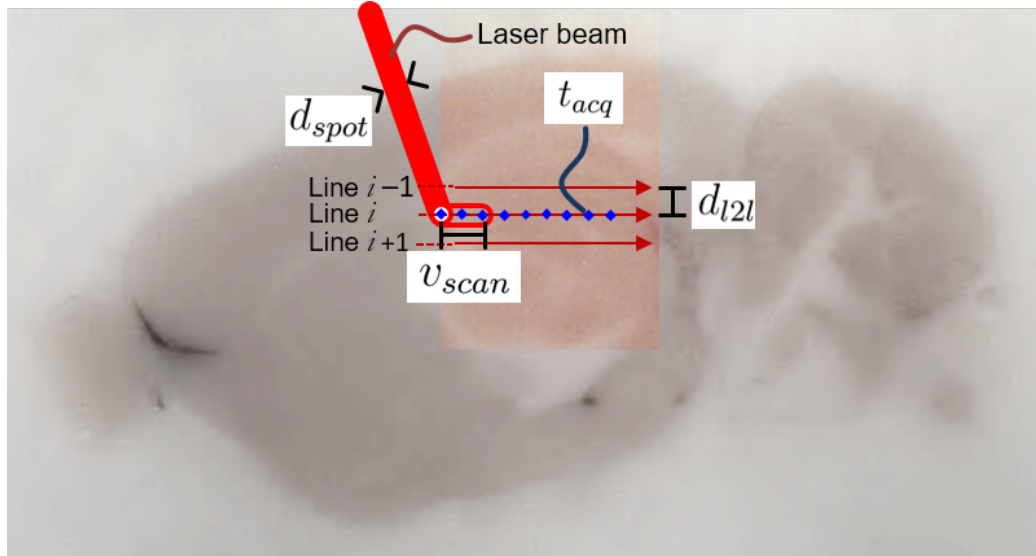


Figure 2·7: Diagram of spatial parameters affecting final image resolution.

for a variety of applications with a detailed summary of its use for biological samples provided by Becker et al. (2014). LA-ICP-MS has been used for coarse localization of biometals in a variety of animal models for neurological conditions including Alzheimer’s disease (Hutchinson et al., 2005; Matusch and Becker, 2012; Hare et al., 2016), stroke (Becker et al., 2010), and tumors (Becker and Salber, 2010). Other studies have sought to identify the amount of exogenous metals injected into the brain, such as gadolinium-based MRI-contrast agents in the brains of rats and pigs using LA-ICP-MS (Pugh et al., 2012). Development of LA-ICP-MS has recently undergone significant advancements aimed toward improving spatial resolution (Becker et al., 2014) and analysis of neuropsychiatric disorders (Uerlings et al., 2016b). While very recent work has been done to show elevated levels of iron using MIMS in the brains of mice receiving a controlled cortical impact injury (Portbury et al., 2017), this injury model is not representative of microvasculopathy and closed-head injuries we strive to study. The use of MIMS for assessing diffuse BBB compromise in animal models of TBI is still an unstudied application.

A related technology called matrix-assisted laser desorption/ionization (MALDI)-imaging mass spectroscopy (IMS) may be used for analysis of large proteins and other biomolecules (Caprioli et al., 1997). The quality of the data produced through this technique is similar to MIMS in that each spatial location produces a spectrum of m/z -values; however, in the case of MALDI, the m/z -values are larger and typically many more data points in the spectrum are acquired. MALDI-IMS has been used as a more robust method to replace traditional pathological assessment techniques, such as IHC or in-situ hybridization, for evaluating a variety of processes including drug metabolism and pathological assessment (Cornett et al., 2007). Many of the algorithms developed for MIMS may also be used for MALDI processing.

2.4 Current Biomedical Image Registration Methods

Investigation of disease mechanisms in translational medicine often involves acquisition and analysis of multiple image modalities to inform the underlying pathogenesis. Indeed, multiple image modalities may be required in clinical medicine as well depending on the suspected contributor of symptoms. Part of the role of imaging in translational medicine is to determine the microscopic and mechanistic contributors to a disease using high-resolution imaging and highly-specific markers. The ultimate goal is to use these findings to identify specific biological processes to target for the design of clinically-relevant biomarkers and measurements. The ability to determine the spatial relationships between independent modalities facilitates the characterization of disease processes. These comparisons are enabled by casting disparate modalities into a common coordinate system using image registration such that there is a correspondence between anatomical features and pathologies.

A variety of modalities are used extensively in translational research including: IHC,

IHF, and in-situ hybridization. Also frequently used are conventional clinical imaging modalities such as magnetic resonance imaging (MRI), positron emission tomography (PET), ultrasound (US), etc. The objective of this thesis is to develop methods for recently emerging imaging modalities which result in vector-pixel/voxel images such as MIMS, MALDI, and diffusion tensor imaging. While all techniques have been developed specifically for MIMS, the multi-channel, multi-modal image registration (MMMCIR) method, detailed in Section 4.5, could be directly applied to pairwise registration of any 2-D vector-pixel images.

A large number of publications have been written on medical image registration, including many on multi-modal methods. Most multi-modal image registration publications have addressed the problem of determining the correspondence between MRI, PET, US, and other relevant clinical modalities. While these works have achieved robust results for these image modalities, two distinct features of MIMS limit the ability to directly apply most methods: (1) each spatial location is defined by a vector of values rather than a scalar value, and (2) the intensity characteristics of the MIMS modality are unique in a variety of ways making extensions of many modality reduction techniques and filtering methods difficult. The existing literature details algorithms for pairwise image registration either between multi-channel images with each channel representing the same modality, or for multi-modal scalar-valued images. No methods directly dealing with multi-modal, multi-channel image registration are available.

The problem of pairwise image registration (IR) is broadly defined by three aspects: (1) the transformation model, (2) the cost function, and (3) the optimization method. While each aspect may have several suitable methods which vary in their complexity and appropriateness for a given problem, the most widely tuned aspect of the IR

problem for correspondence between multiple modalities is the cost function. Mutual information (MI) was proposed for use as a cost function for multi-modal medical image registration by Maes et al. (1997) and Viola and Wells III (1997). As a probabilistic measure requiring the computation of the joint density function (JDF), the MI metric does not depend on a direct functional relationship between the intensities of the two images, but rather relates the amount of shared information there is in the intensity characteristics. Due to the computational burden typically associated with computing a JDF, many approaches to multi-modal IR have sought to cast the problem as a uni-modal one by determining a suitable alternative representation of the input images, or by using approximations to the computation of the JDF such that its construction and the subsequent optimization of MI are facilitated.

To address the challenges presented by multi-modal images, most approaches target improving the computation of the cost function in some way. Heinrich et al. (2012) developed a modality-independent neighborhood descriptor (MIND) based on the principle of neighborhood self-similarity. The MIND value is calculated for each pixel in the image and is shown to produce similar visual patch properties for anatomically corresponding features represented in different modalities (uniform areas, corners and lines in different modalities result in similar MIND patch appearance). Optimal transformation parameters are determined by minimizing the sum of squared differences between the MIND representation of both images via Gauss-Newton optimization method. Another approach computes an entropy image, essentially capturing relevant structural features in the original images, to enable the optimization of an L1 or L2 cost function (Wachinger and Navab, 2012). By casting the multi-modal IR problem as a uni-modal one, the computation of the cost function and the methods available for optimization are greatly simplified. These methods only work, however, if certain assumptions, such as consistency of local intensity characteristics, are

present in both modalities being used for registration. Since the structural information and intensity properties within MIMS are often complementary across channels, these assumptions cannot be directly applied to the intensity characteristics specific to MIMS.

Many compelling simplifications for determining optimal transformations between two images using maximization of mutual information have been developed. Kern and Pattichis (2007) assumed Gaussian characteristics to relate the frequency-domain properties of images to the surface of the MI cost function in the transformation space. The authors showed robust registration of two hyperspectral images with empirical convergence guarantees so long as the neighborhood around the MI surface was sufficiently small (such that linearity assumptions hold). Other approaches use standardized basis functions, such as B-splines (Thévenaz and Unser, 2000) or the Gauss transform (Špiclin et al., 2011), to calculate the JDF. This allows for the use of gradient type optimization functions by simplifying the expressions for the gradient of the cost function with respect to the parameters being optimized. Several publications have proposed surrogates to direct computation of the JDF via ensemble estimates (Sricharan and Hero, 2012), Rényi entropy and minimum spanning entropic graphs (Neemuchwala and Hero, 2005; Sabuncu and Ramadge, 2008). While these methods may be extended for vector-pixel images, their description and validation are shown only for scalar valued images.

Several free software platforms have been developed for use in a variety of medical image processing tasks. One of the oldest platforms, FreeSurfer, first released circa 1999, has a variety of functions, including image registration and segmentation, but was developed for human brain MRI images (Fischl, 2012). Another software package used for image registration and segmentation is the Insight Segmentation and Regis-

tration Toolkit (ITK) (Yoo et al., 2002) and its extensions, elastix (Klein et al., 2010) and Advanced Normalization Tools (ANTs) (Avants et al., 2011). These packages include a variety of options for registration, including various cost functions, transformation models, and optimization methods. Still, due to the ubiquity of scalar, volumetric images such as MRI, registration tools for handling multi-modal vector pixel images have yet to be developed.

There have been some efforts to improve the processing and interpretation of IMS data, both for MIMS and MALDI. Software tools for visualizing data and correcting instrument artifacts have been developed for MATLAB (Robichaud et al., 2013) and Excel (Uerlings et al., 2016a). Since the IMS modality is still in its early stages of development, standardized methods beyond visualization and data conditioning are not widely used. In a recent work, structural and intensity information supplied by IHC photomicroscopy images was used to model the relationship between MALDI channel characteristics and IHC properties (Van de Plas et al., 2015). This work on image fusion did require registration of MALDI and optical images, but relied on manually selected control points with an affine transformation model.

Chapter 3

Assessment of TBI via Traditional Imaging Modalities

The primary focus for this portion of the thesis is to provide tools for measuring the correlation of injury severity parameters with subsequent behavioral and neuropathological outcomes. These tools are based on established methods in computer vision and machine learning to provide novel and quantitative insights into data with the objective of gaining a better understanding of TBI. This chapter presents the acquisition and processing of photographic and fluorescent images and high-speed videos. The high-speed videos recorded during the neurotraumatic episodes are used to better understand and compare the head kinematics occurring in both of the neurotrauma models under investigation. Methods developed for analyzing photographs and fluorescent images of brain tissue taken after administration of an albumin binding fluorescent dye known as Evans blue (EB) are also presented. Whole brain color images were acquired to assess the extent of visible surface pathology. To this aim, a pixel-wise classification algorithm is presented to enable grading the severity of surface pathology (Tagge et al., 2017). Finally, methods for processing and analyzing fluorescent images of the EB-injected brains to semi-quantitatively assess blood-brain barrier (BBB) dysfunction are described.

3.1 High-Speed Video for Tracking Head Movement

One important aspect of comparing impact neurotrauma (INT) and blast neurotrauma (BNT) is understanding the similarities between the head kinematics experienced during both injuries. Additionally, exploring the relationship between the severity of the neuropathological and behavioral deficits following TBI and motion of the head during the injury is a topic of great interest. The mouse models of INT and BNT are compared using high-speed videos acquired during the injury period. These videos are used to detect the position of the mouse's nose so that subsequent processing could be done to estimate higher order position derivatives. Under both TBI models, a brief impulse of force is delivered to the left-lateral side of the head resulting in a rapid head acceleration. The head motion typically lasts on the order of a few hundred milliseconds with the most severe head accelerations occurring during the first 30-50 *msec*. For this reason, high-speed video (HSV) footage with a 100 *KHz* frame rate is used for tracking and analyzing the motion of the head throughout the duration of the injury period. The specific technical contributions for this effort include development of an object segmentation and localization algorithm followed by application of Kalman filtering for estimation of velocity, acceleration and jerk (third derivative of position).

Before injury exposure, the mouse's nose is marked with white paint to provide a prominent feature for tracking in each HSV frame, shown in Fig. 3.1. The initial processing objective for the videos is detection of the position of the object of interest in each frame of the HSV, which we specify as the bright-painted spot on the mouse's nose. This task is subject to the following technical challenges:

- Variation in size, shape and pixel intensity of the object (mouse's nose)



(a) Raw image



(b) Contrast-adjusted image

Figure 3.1: Initial frame of a high-speed video from a mouse undergoing blast neurotrauma. The mouse's nose is the central-most bright point in the frame. A mounted accelerometer can also be seen as a bright spot in the bottom-left corner of the frame. (a) Raw grayscale image. (b) Contrast-adjusted image (to aid in visualization).

- Occlusion of the object for some parts of the video

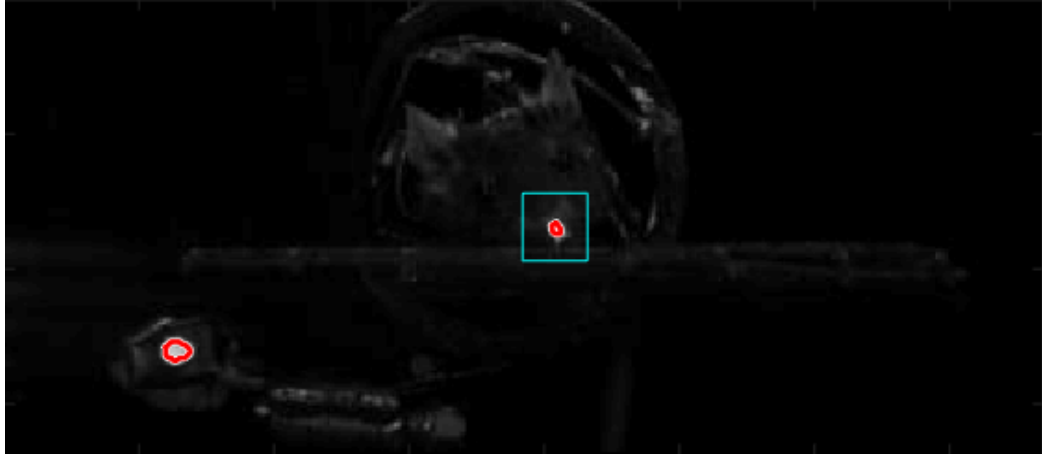
While real-time object detection is not a requirement, the goal was to develop a method for segmenting and localizing the object quickly, for as many frames as possible, and with minimal user interaction.

In order to accurately estimate the x - and y -image coordinates of the object, two segmentation algorithms were used depending on the frame's characteristics: either the Chan-Vese (CV) active contours method (Chan and Vese, 2001) or k-means clus-

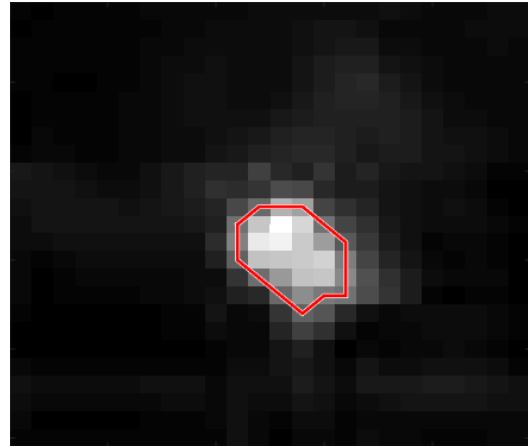
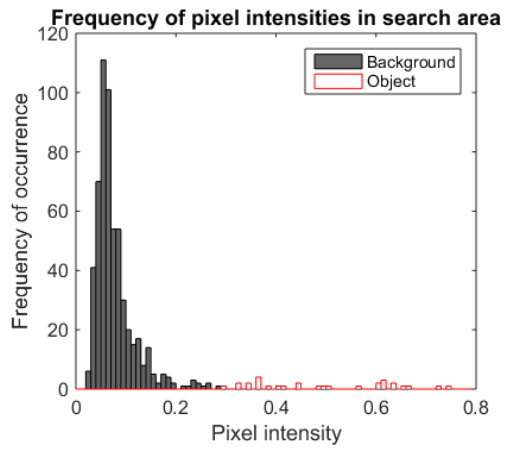
tering (Bishop, 2006). The CV and k-means algorithms are well suited to address the aforementioned technical challenges since both attempt to separate data into two distinct groups without explicitly enforcing specific group characteristics. Compared to CV, k-means is more sensitive to characteristics of the intensity distribution. However, since segmentation by k-means clustering is faster than by CV, segmentation by k-means is first attempted to identify object and background regions. If the segmentation result using k-means varies significantly from the previous frame's result, the CV algorithm is used for segmentation of the current frame instead.

All frames in the HSV are converted from RGB images into luminance images. Regions of interest in the first frame are localized by identifying the pixels whose values exceed a threshold γ_0 . The first frame of a representative HSV is shown in Fig. 3-2(a) with the two regions in the image exceeding γ_0 outlined in red. The component closest to the center of the frame is selected as the object of interest. This initial segmentation provides the seed position for the first frame. To segment the object of interest after this initial frame, the object position from the previous frame is used to designate a search area of p pixels in the image, shown as a cyan box in Fig. 3-2(a). The pixels in this designated patch in the image are the only ones considered for segmentation of the object from the background. As previously mentioned, k-means clustering, with $k = 2$ to differentiate the foreground (object) from the background in the patch, is attempted on the pixels within this search area (Fig. 3-2(b)). This produces a two class mask whose boundary is shown as a red curve in Fig. 3-2(c). Once the object boundary is defined, the weighted centroid of the object serves as the x - and y -position of the nose in the given frame.

After segmentation of the frame by k-means, the result is compared to the previous frame's mask. If the area of the current frame's mask is greater than twice the area



(a) Candidate objects (intensity $\geq \gamma_0$) in the first frame. Search area indicated by cyan box.



(b) Histogram of k-means ($k = 2$) result in (c) Contour indicating boundary between k-means classes in patch

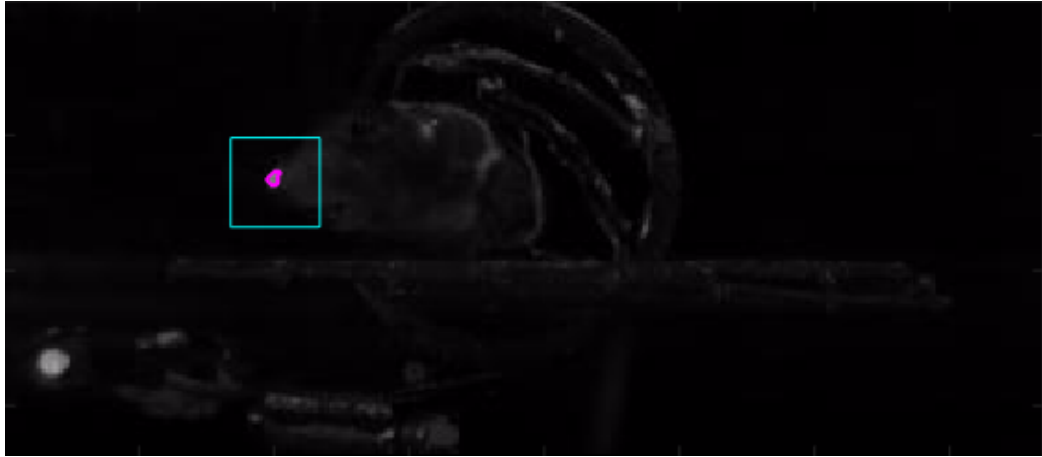
Figure 3·2: High-speed video segmentation procedure using k-means.

of the previous frame's mask, or if the minimum intensity of the current object is less than half the minimum intensity of the previous object, then the search area is reduced and the CV algorithm is used to segment the object instead of k-means. Figure 3-3 goes through the intermediate outputs depicting a frame for which k-means does not provide suitable segmentation so the CV algorithm is applied instead. As shown in Fig. 3-3(c), the total area of the mask using k-means was 301 pixels while the previous frame's mask area was 17. Using CV on a smaller patch, Fig. 3-3(d) shows that a 20 pixel foreground class is identified as the object resulting in a reasonable segmentation for that frame.

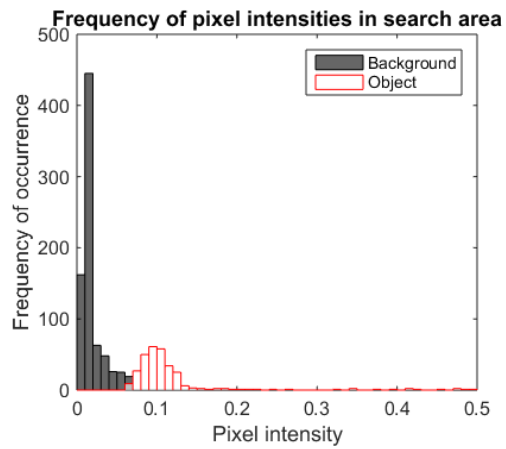
The CV method defines a contour by minimizing the energy of a level-set. The energy is defined as the sum of internal and external energies derived from image properties (see Eqn. (3.2)). The contour is defined as the zero-level curve of a Lipschitz level-set function, $\phi(t, x, y)$. Some examples of level-sets can be seen in Fig. 3-4 where the z -axis gives the value of the level-set and the zero-level set, C , is shown in red. The level-set evolves over time by minimizing the energy functional F subject to c_1 (mean intensity inside the contour), c_2 (mean intensity outside the contour), and C :

$$\inf_{c_1, c_2, C} F(c_1, c_2, C) \quad (3.1)$$

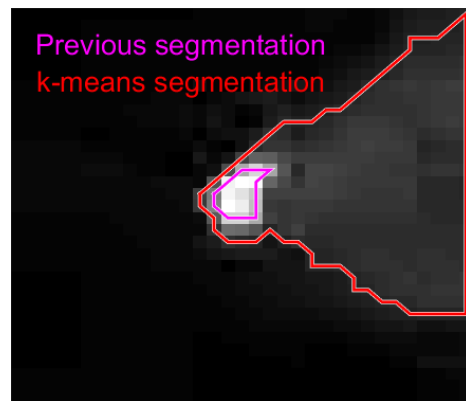
As previously mentioned, the energy function is defined over the space of the image patch, $x, y \in \Omega$, and quantifies both contour specific energies, as well as image intensity (u_0) energies to define $F(c_1, c_2, \phi)$. The user may also adjust the weighting parameters μ , ν , λ_1 , λ_2 to emphasize or lessen the importance of each of the



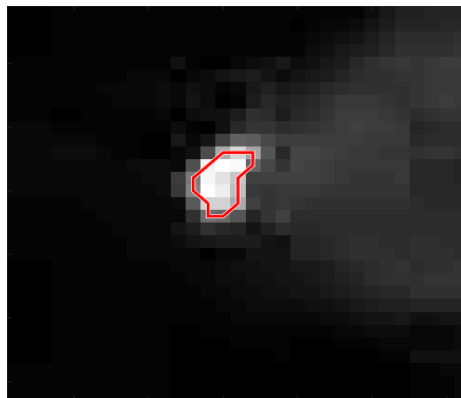
(a) k-means failure frame with previous frame's segmentation in red



(b) Histogram of k-means result in patch



(c) k-means mask boundary



(d) CV mask boundary

Figure 3.3: High-speed video segmentation using Chan-Vese after failure of k-means.

integrals. The CV energy functional is defined as follows:

$$\begin{aligned}
F(c_1, c_2, \phi) = & \underbrace{\mu \cdot \int_{\Omega} \delta(\phi(t, x, y)) |\nabla \phi(t, x, y)| dx dy}_{\text{length } C} + \underbrace{\nu \cdot \int_{\Omega} H(\phi(t, x, y)) dx dy}_{\text{area inside } C} \\
& + \underbrace{\lambda_1 \int_{\Omega} |u_0(x, y) - c_1|^2 H(\phi(t, x, y)) dx dy}_{\text{intensity variance inside curve}} \\
& + \underbrace{\lambda_2 \int_{\Omega} |u_0(x, y) - c_2|^2 (1 - H(\phi(t, x, y))) dx dy}_{\text{intensity variance outside curve}} \tag{3.2}
\end{aligned}$$

where weighting parameters for each of the integrals may take the values:

$$\mu \geq 0 \qquad \nu \geq 0 \qquad \lambda_1, \lambda_2 > 0$$

$$\text{Heaviside function:} \qquad H(z) = \begin{cases} 1 & \text{if } z \geq 0 \\ 0 & \text{if } z < 0 \end{cases}$$

$$\text{Dirac function:} \qquad \delta(z) = \frac{d}{dz} H(z)$$

The energy functional is minimized by explicit differentiation of F with respect to t by holding c_1 and c_2 constant (Chan and Vese, 2001). This then gives an expression for $d\phi/dt$ which can be approximated using finite differences. The level-set ϕ is iteratively adjusted until $\frac{d\phi}{dt} \approx 0$ or some other criterion is met (for example maximum number of iterations). A publicly-available implementation of the CV algorithm was used (Wu, 2009). Parameter values are given in Table 3.1.

This object detection scheme is used to extract the x - and y -position of the mouse's nose in all HSV frames of interest. The resulting tracked position is shown in Fig. 3.5(b). Because the raw position points are too variable to give informative

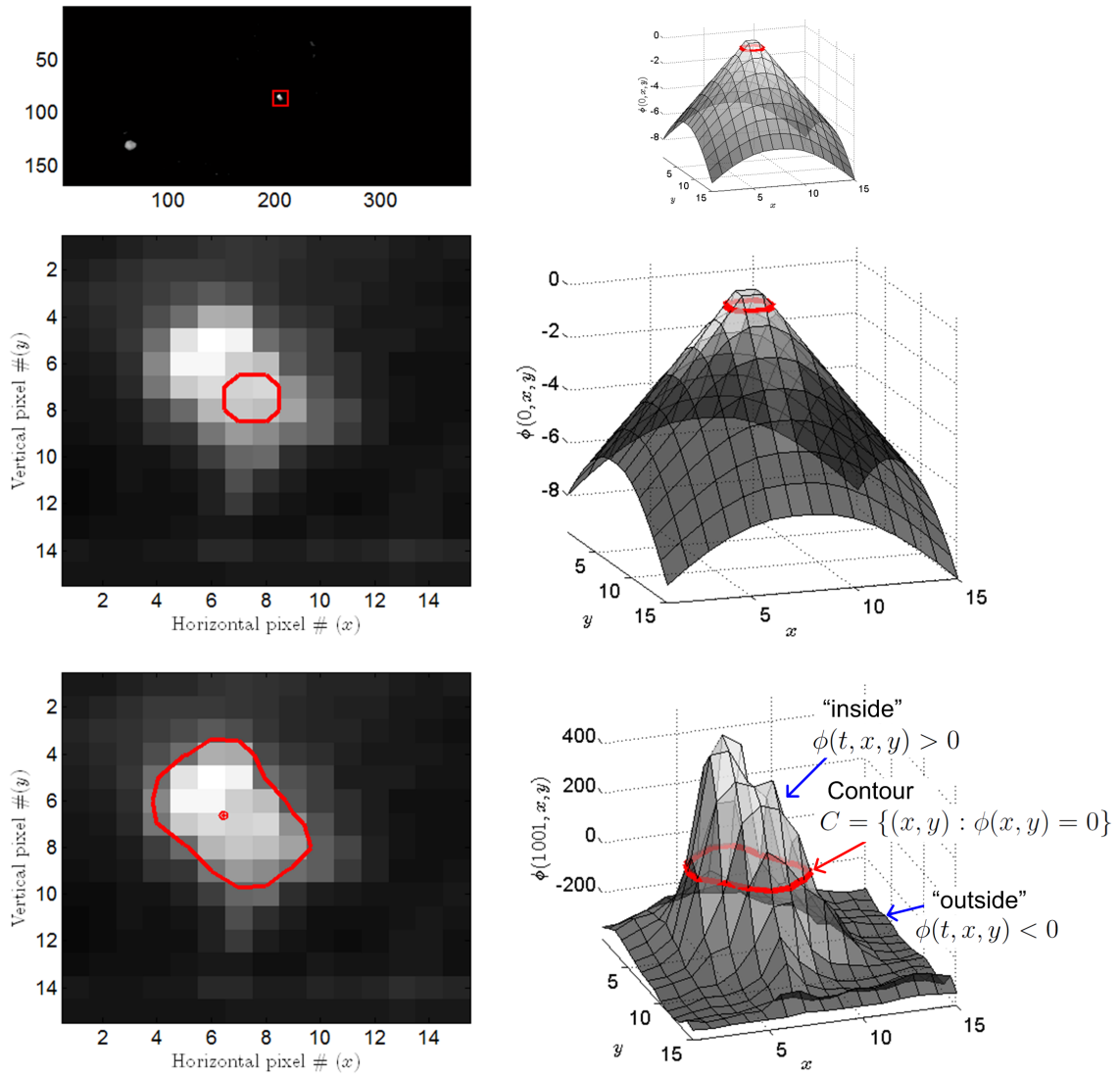


Figure 3.4: Evolution of Chan-Vese segmentation. The left column depicts the image of the search area around the object and the right column shows the level-set function, $\phi(t, x, y)$. The top left image shows the bounding box around the search area of the object. This region of interest is used to define Ω in the CV algorithm and initialized with a level-set (top and middle right images). The top right image shows ϕ colored in terms of the function's values and the middle right image shows is colored by the image pixel values. After 1000 iterations ($t = 1001$) the level-set is conformed to optimize F (Eqn (3.2)). The regions of the level-set are indicated in the bottom right image.

Table 3.1: Parameter values used for Chan-Vese algorithm

μ length weight	λ_1 inside intensity weight	λ_2 outside intensity weight	ν area weight	Max. Iter.
0.01×255^2	1	1	0	1000

second- and third-derivatives (see Fig. 3-5(a) and top row of Fig. 3-6), additional filtering is required to extract quantities of interest from the higher-order position derivative curves. To be used as a comparison to the Kalman Filter tracking method, forward-backward filtering of the raw position by a 2-nd order Butterworth filter (BF) with a cutoff frequency of 2 *KHz* is used to calculate first- and higher-order derivatives by taking corresponding-order finite differences of the position curve. Raw *x*-position data and higher-order derivatives can be seen in the first row of Fig. 3-6. The second row of Fig. 3-6 depicts results from the BF. Clearly, filtering reveals interesting features, such as high intensity spikes, in the higher-order derivative plots.

Kalman filtering is the approach most commonly used for object tracking since the mechanisms (whether physical or some known functional relationship) governing the object's motion may be incorporated through the state transition model. The Kalman filter (KF) system is described by two equations: the process model (Eq. 3.3) and the observation model (Eq. 3.4). Assuming a linear process model and Gaussian noise, the posterior probability, $p(S_k|z_{1:k})$, is also Gaussian and therefore is completely specified by the mean, $S_{k|k}$, and the covariance, $P_{k|k}$. Variable definitions and values used for the KF are given in Table 3.2.

$$\text{Process Model:} \quad S_k = AS_{k-1} + Bu_k + w_k \quad (3.3)$$

$$\text{Observation Model:} \quad z_k = CS_k + v_k \quad (3.4)$$

Table 3.2: Kalman filter variable definitions. Definitions with a “*” indicate that in this application, these values are constant and do not change, but in general may be defined as a function of k .

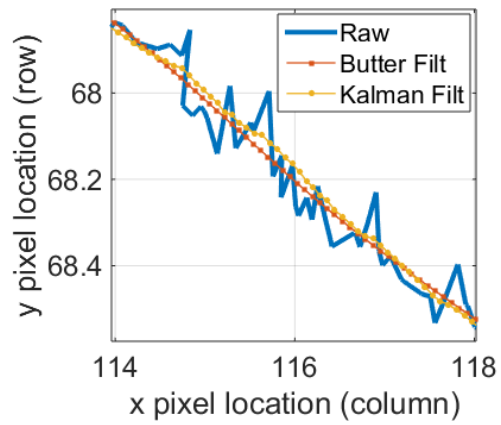
State vector	$S_k = \begin{bmatrix} x & \dot{x} & y & \dot{y} \end{bmatrix}^T$
State transition matrix	$A = \begin{bmatrix} 1 & \Delta t & 0 & 0 \\ 0 & 1 & 0 & 0 \\ 0 & 0 & 1 & \Delta t \\ 0 & 0 & 0 & 1 \end{bmatrix}$
Control matrix	$B = \begin{bmatrix} (\Delta t)^2/2 & \Delta t & (\Delta t)^2/2 & \Delta t \end{bmatrix}^T$
Control value*	$u_k = \text{constant}$
Process noise*	$w_k = \mathcal{N}(0, Q_k)$
Noise covariance*	$Q_k = \begin{bmatrix} ((\Delta t)^2/2)^2 & (\Delta t)^3/2 & 0 & 0 \\ (\Delta t)^3/2 & (\Delta t)^2 & 0 & 0 \\ 0 & 0 & ((\Delta t)^2/2)^2 & (\Delta t)^3/2 \\ 0 & 0 & (\Delta t)^3/2 & (\Delta t)^2 \end{bmatrix} \times \sigma_a^2$
Process variance	$\sigma_a^2 = 10^{-5}$
Observation vector	$z_k = \begin{bmatrix} x & y \end{bmatrix}^T$
Measurement matrix	$C = \begin{bmatrix} 1 & 0 & 0 & 0 \\ 0 & 0 & 1 & 0 \end{bmatrix}$
Measurement noise*	$v_k = \mathcal{N}(0, R_k)$
Measurement covariance*	$R_k = \mathbb{I} \times \sigma_m^2$
Measurement variance	$\sigma_m^2 = 1$
Sample time difference	$\Delta t = 1$
Frame number	k

Table 3.3: Kalman filter prediction and update steps

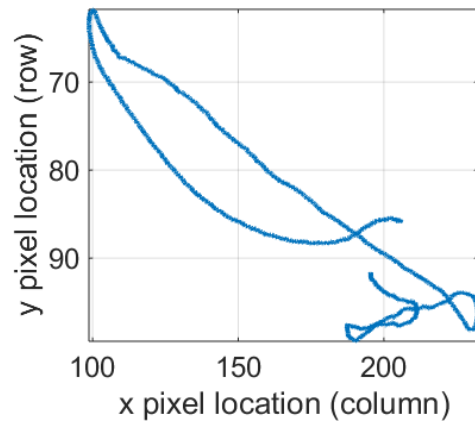
Prediction Step	Update Step
	U0. Compute Kalman gain $K_k = \hat{P}_k C^T (C \hat{P}_k C^T + R)^{-1}$
P1. Predict state $\hat{S}_k = AS_{k-1} + Bu_k$	U1. Update state estimate $S_k = \hat{S}_k + K_k (z_k - C \hat{S}_k)$
P2. Predict covariance $\hat{P}_k = AP_{k-1}A^T + Q$	U2. Update covariance estimate $P_k = (\mathbb{I} - K_k C) \hat{P}_k$

Through the KF, the current state, S_k , can be predicted as a function of the previous state S_{k-1} . Using the observations z_k , the state S_k can be updated to reflect the information added by the observable states. Specifically, the goal is to maximize the posterior probability $p(S_k|z_{1:k})$. Since the posterior is Markovian, the most probable state may be computed given only the current observation. The KF output is implemented in a two step process: a prediction step followed by an update step. The computations involved in each step are detailed in Table 3.3.

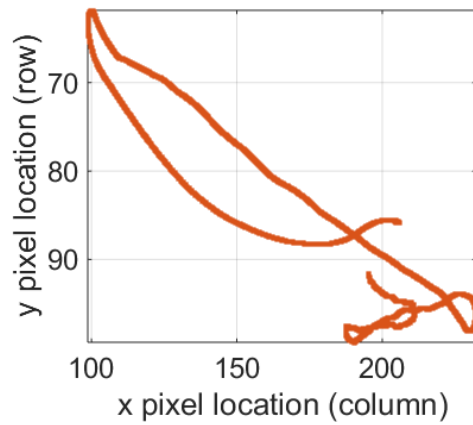
In order to implement a KF, the state transition matrix A , the control matrix B , the measurement matrix C and the covariance matrices Q and R , are assumed to be known. While A and B are given directly by knowledge of the process, in this case the kinematic equations from physics, and C is derived directly from the observable states, the noise characteristics of the system are typically determined empirically or by some knowledge of the system. For simplicity in this application, Δt was normalized to equal 1 rather than the true temporal sampling rate. The process and the measurement variance terms were then initially set based on data properties, then adjusted until results from the KF resembled those from the BF. Results from the KF using the parameters indicated in Table 3.2 are shown in Fig. 3.5(d) and the bottom row of Fig. 3.6. The nose position results from the two filtering methods are compared with the raw data in Fig. 3.5(a).



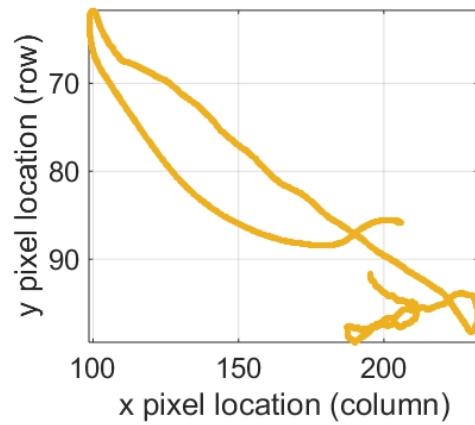
(a) Zoomed in portion of position curve



(b) Raw position curve



(c) Butterworth filtered position



(d) Kalman filtered position

Figure 3-5: Mouse nose position results from segmentation, Butterworth filtering, and Kalman filtering.

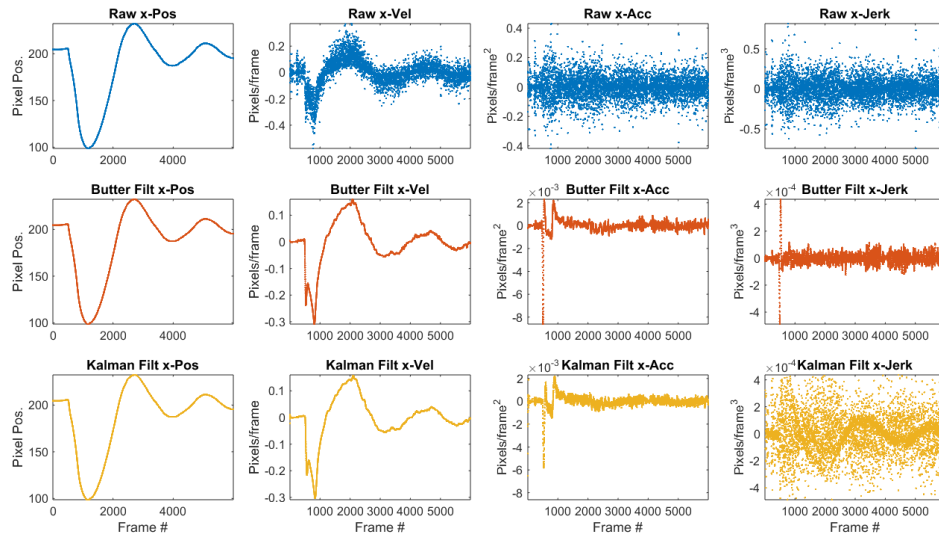


Figure 3-6: Comparison of Butterworth filtering and Kalman filtering for estimating higher-order position derivatives.

There are several advantages of using the KF rather than traditional low-pass filtering for estimation of higher-order position derivatives. First, the KF exploits the true underlying relationship between position and its higher-order derivatives. The KF also permits flexibility in the amount of smoothness enforced on each element of the state vector independently through the covariance matrix Q . Another advantage of KF over the BF is the lack of artifacts introduced by any finite impulse response filter, such as ringing artifacts. One of the major difficulties of using the KF is suitable parameter selection, particularly of the noise variance terms and the covariance matrices. Still, enabling direct, model driven estimations of unobserved states by leveraging information from noisy measurements makes the KF an incredibly powerful tool for motion tracking applications. While not examined in detail as part of this work, one of the KF's greatest strengths is also the ability to predict states using the process model even when measurements are missing.

The methods developed for processing the high-speed videos were utilized in part for

a recently submitted publication (Tagge et al., 2017). For this publication, additional scaling of the points was required to represent the values in terms of physically meaningful units (meters and seconds). The object detection function based on both k-means and CV segmentation adaptively detects a deforming object with non-uniform illumination and produces position estimates which are accurate enough to yield informative position derivatives after filtering. The Kalman filter implementation provides a flexible framework for model-based smoothing of the position derivatives of interest.

3.2 Semi-supervised Segmentation for Gross Pathological Assessment

In an attempt to compare not only the behavioral and physical mechanisms of mouse models of blast neurotrauma (BNT) and impact neurotrauma (INT), the characteristics and the extent of neuropathology in each injury model were also of interest. To better understand the relationship between surface pathology and other injury parameters, high-resolution (1995×1612) RGB images of brains from mice injected with a blue, albumin-binding fluorescent dye called Evans blue (EB), were taken with a Nikon D5200 digital camera under cross-polarized white light illumination.

For each brain, an image was taken of each of the following surfaces (Fig. 3·7): dorsal, left, ventral, and right. The objective was to identify distinct surface pathologies in the photographic images (PI) and quantify the extent and severity of the pathology. Four tissue classifications were used to describe the range of pathologies observed in the PIs: blood, Evans blue, complex contusions, and normal tissue. As shown in Fig. 3·8, each of these categories was found to occupy distinct regions in RGB space. Motivated by the separation of the classes in this color space, the goal was to create a scheme whereby each pixel in the image of the brain could be labeled as either

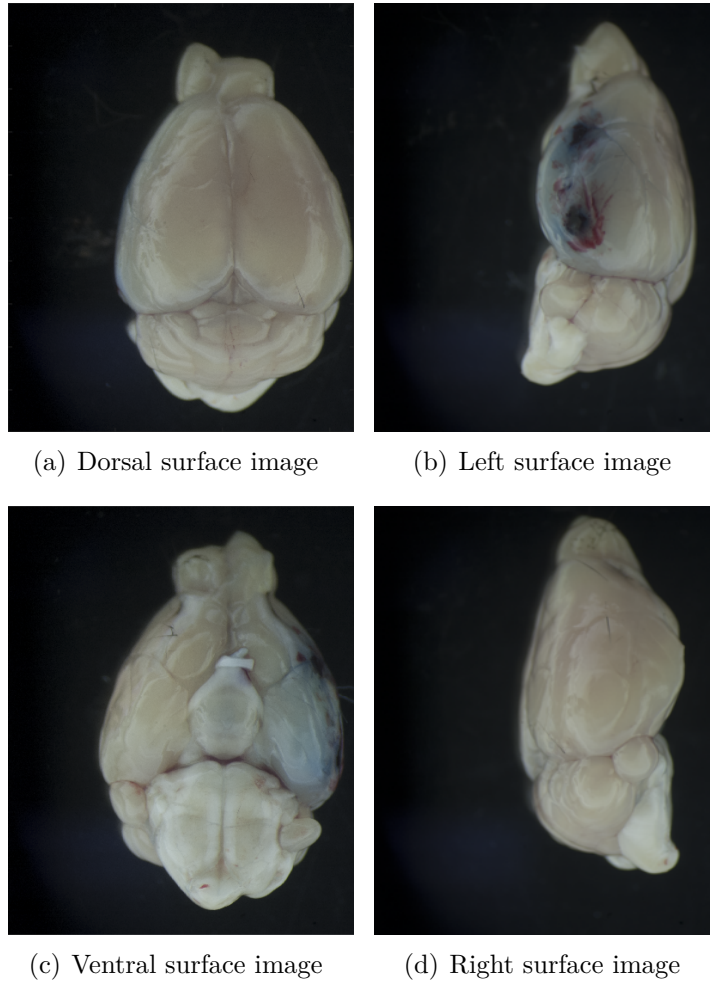
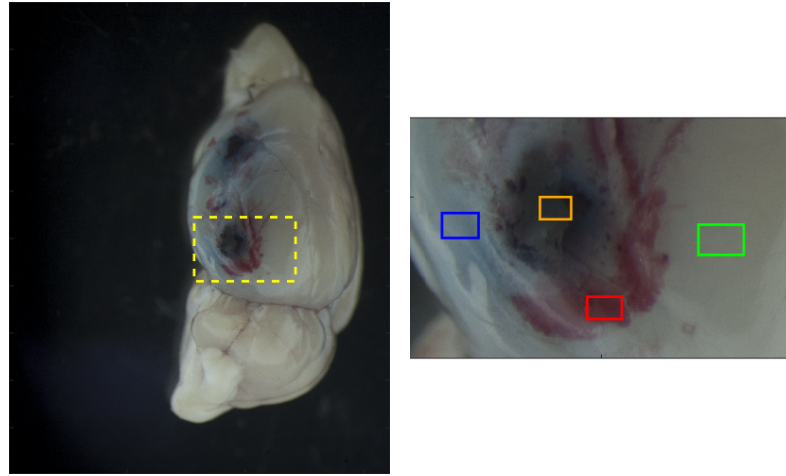


Figure 3-7: Exemplary images from brain surface pathology of Evans blue-injected mice.

(1) blood, (2) Evans blue, (3) contusion, or (4) normal tissue.

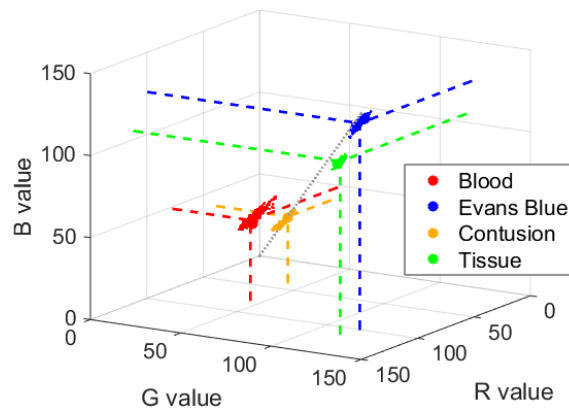
As a preliminary step, the foreground and background of the image need to be identified. In many images, this can be done via intensity thresholding followed by hole-filling morphological operations. Other images, such as the the ventral view of the brain in Fig. 3-7(c), require a more complex method to achieve a smooth segmentation which encompasses the tissue boundary, since dark areas at the edge of the tissue blend into the background. To circumvent the ambiguity between dark pathologies



(a) \vec{P} with surface pathology (b) Representative class patches



(c) \vec{P} patches from each class



(d) RGB scatter plot of class patches

Figure 3-8: Examples of characteristic pathologies in a left surface RGB photographic image.

and the background in an intensity-based RGB image \vec{P} , whose pixels \vec{p} take on a triplet value $\{R, G, B\}$, the gradient-magnitude image, G , was used to represent the photo image. This image is used to guide an edge contour around the boundary of the tissue using the geodesic active contours algorithm (GAC) (Caselles et al., 1997). Similar to the CV active contours method, this method minimizes an energy which depends on the image's characteristics, such as intensity consistency inside and outside of a level-set curve, as well as a term which considers edge properties of the image. The MATLAB function `activecontour.m` from the image processing toolbox was used to define a mask using GAC.

Figure 3.9 shows the outputs from the steps required to create a tissue/background mask from an image \vec{P} . The steps can be summarized as follows:

1. Convert the RGB-image, \vec{P} (Fig. 3.7(c)), into a maximum-intensity scalar image, L (Fig.3.9(a)), according to the following formula at each pixel location, p :

$$L(p) = \max_{\vec{p} \in \{R, G, B\}} \vec{P}(p)$$

2. Determine a scalar threshold, γ , from L using the `graythresh.m` MATLAB function. Create a mask $M_\gamma = L \geq \gamma$.
3. Calculate a gradient magnitude image, G , from L (Fig. 3.9(c)), which will be used as the input image for the MATLAB function `activecontour.m`
4. Isolate the largest connected component from M_γ and create a new closed and inflated mask, M_0 , using a structuring element sufficient to ensure that M_0 fully encompasses the tissue (yellow curve in Fig. 3.9(d))
5. Using a hierarchical approach, at each level s , for $s = 1, \dots, \mathbb{S}$, down-sample G by a factor of φ_s to give a down-sampled image, G^{φ_s} , where each dimension of G^{φ_s} is equal to $1/\varphi_s$ of the dimension in G . For the data and initial contour

inputs into MATLAB's `activecontour.m`, use G^{φ_s} and the appropriately resized $M_{s-1}^{\varphi_s}$, respectively. The output is the mask M_s . Figure 3.9(d) shows the results for $\varphi_1 = 8$ with $M_0^{\varphi_1}$ shown in yellow and M_s shown in white.

6. While $s \leq \mathbb{S}$, after a mask M_s is generated, the mask is dilated by a small amount to create a suitable initialization for the next level of GAC segmentation. The new mask M'_s must also be up-sampled to match the dimensions of $G^{\varphi_{s+1}}$. Figure 3.9(e) shows the results for $s = \mathbb{S} = 2$ where $\varphi_{\mathbb{S}} = 1$. The mask $M_1^{\varphi_{\mathbb{S}}}$ is depicted in yellow in the figure with $M_{\mathbb{S}}$ shown in red.

The final result of the segmentation procedure is a mask, $M = M_{\mathbb{S}}$, whose non-zero values indicate pixels corresponding to tissue regions in the image \vec{P} .

Once a mask differentiating tissue and background pixels is created, the objective is to assign a class ((1) blood, (2) Evans blue, (3) contusion, (4) normal tissue) to each of these pixels. The method developed maximizes the probability of a class label given the RGB-triplet value of the pixel being considered. Let the RGB value of a pixel be given by $\vec{p} = \{R, G, B\}$ and the class labels be given as integers $c = \{1, 2, 3, 4\}$ to mean blood, Evans blue, contusion and normal tissue, respectively. Given these definitions, the classification problem is simply the maximization of the class probability given a value for \vec{p} :

$$\hat{c}_{\vec{p}} = \arg \max_c p(c|\vec{p}) = \arg \max_c \frac{p(\vec{p}|c)p(c)}{\sum_c p(\vec{p}|c)p(c)} \quad (3.5)$$

While the distribution for $p(c|\vec{p})$ is not directly available, the distribution $p(\vec{p}|c)$ can be estimated with some labeled data, which by Bayes rule can be used to calculate $p(c|\vec{p})$.

The distribution $p(\vec{p}|c)$ for any \vec{p} can be approximated given sufficient examples of colors which occur in a given class. Assuming that the color characteristics of each

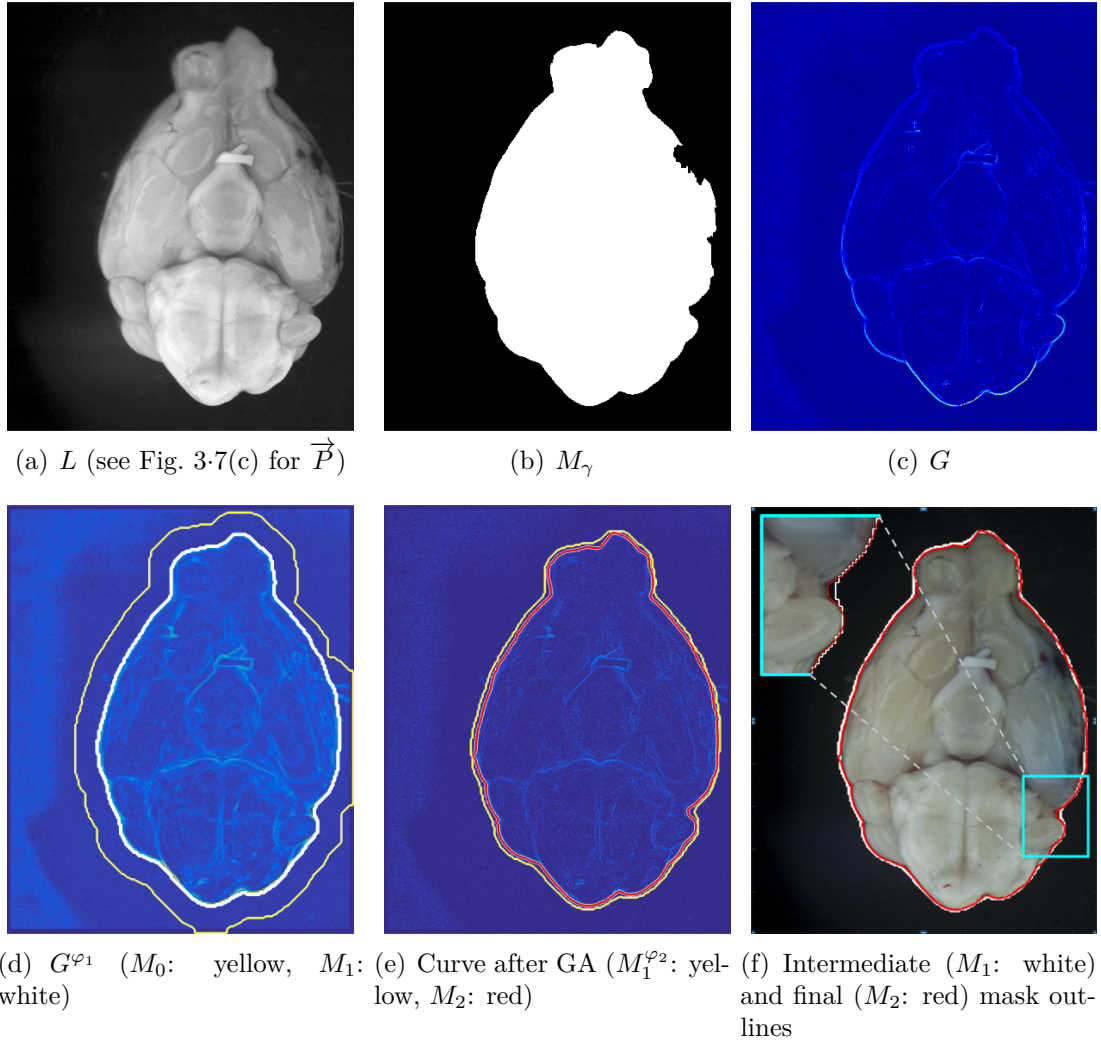


Figure 3-9: Steps to define the tissue segmentation mask for macroscopic photo images (a) Maximum intensity scalar image, L . (b) Intensity threshold mask, M_γ . (c) Gradient magnitude image, G . (d) Geodesic active contours on a downsampled gradient magnitude image G^{φ_1} with the initial mask M_0 outline shown in yellow and the final mask outline, M_1 , shown in white. (e) GAC result on G with initial mask $M_1^{\varphi_2}$ outline shown in yellow and M_2 outline shown in red. (f) Depiction of $M = M_2$ outline in red along with M_1 outline in white on the RGB image \vec{P} .

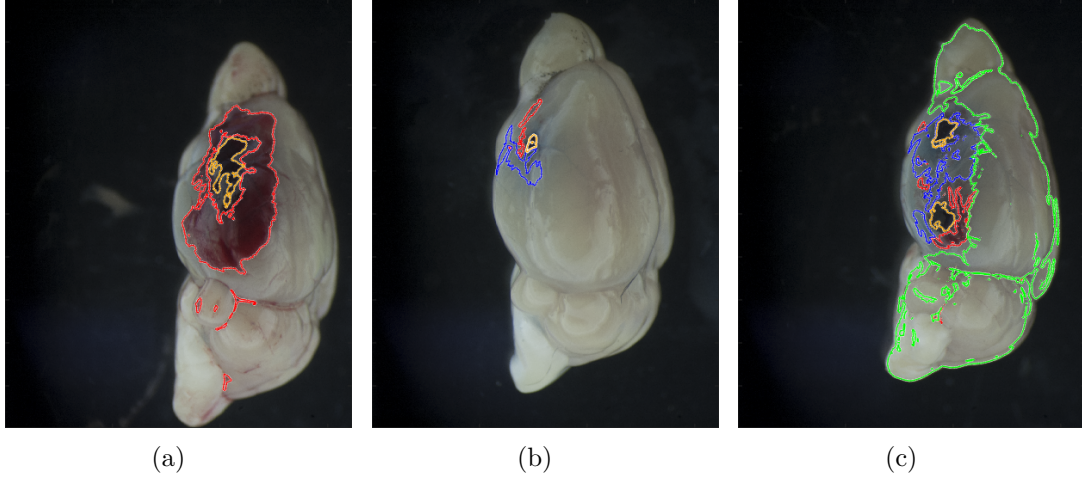


Figure 3-10: Example images showing areas used for building the probability of observing each color given a class. The outline colors are defined as follows: blue indicating Evans blue, red indicating blood, orange indicating contusions and green indicating tissue.

class are similar in all images, the idea is to learn $p(\vec{\rho}|c)$ from representative pixels belonging to each class in a set of images $\mathcal{P} = \{\vec{P}^{(n)}\}_{n=1}^N$. This is done by selecting regions of images in \mathcal{P} which clearly represent a given class label c . The pixels within these segmented regions, shown outlined for three images in Fig. 3-10, are used to build a histogram $h(\vec{\rho}|c)$ in RGB-space. For each class c , kernel density estimation (KDE), described in detail in Section 4.5.3, is used to approximate the density $p(\vec{\rho}|c)$ using the populated regions in the histogram $h(\vec{\rho}|c)$. This essentially spreads out and normalizes the non-zero values in $h(\vec{\rho}|c)$ such that unobserved $\vec{\rho}$ values have a non-zero probability. Once the distribution $p(\vec{\rho}|c)$ is constructed based on the partially segmented “training” images in \mathcal{P} , classification of each pixel in the tissue region of a query image can be evaluated according to Eqn. 3.5 where $p(c)$ is assumed to be uniform. A summary of the procedure for classifying pixels in an image $P^{(n)}$ is depicted in Fig. 3-11. The classification results for select left-view images are shown in Fig. 3-12.

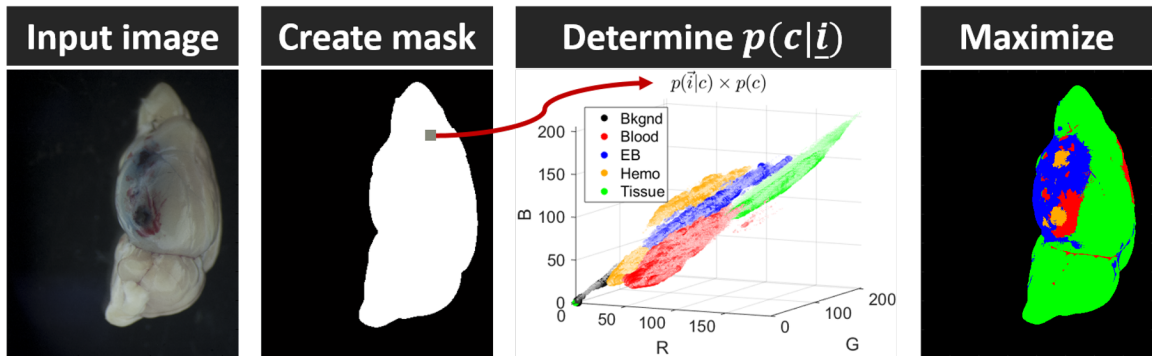


Figure 3-11: Procedure used to determine per pixel label of gross pathology surface images. For each pixel in the masked area, the RGB value $\vec{\rho}$ of the pixel is used to determine the probability of the pixel given each class c . The pixel is classified as the class which yields the maximizes product $p(\vec{\rho}|c) \times p(c)$. Since $p(c)$ is uniform in this application, this is equivalent to maximizing $p(\vec{\rho}|c)$.

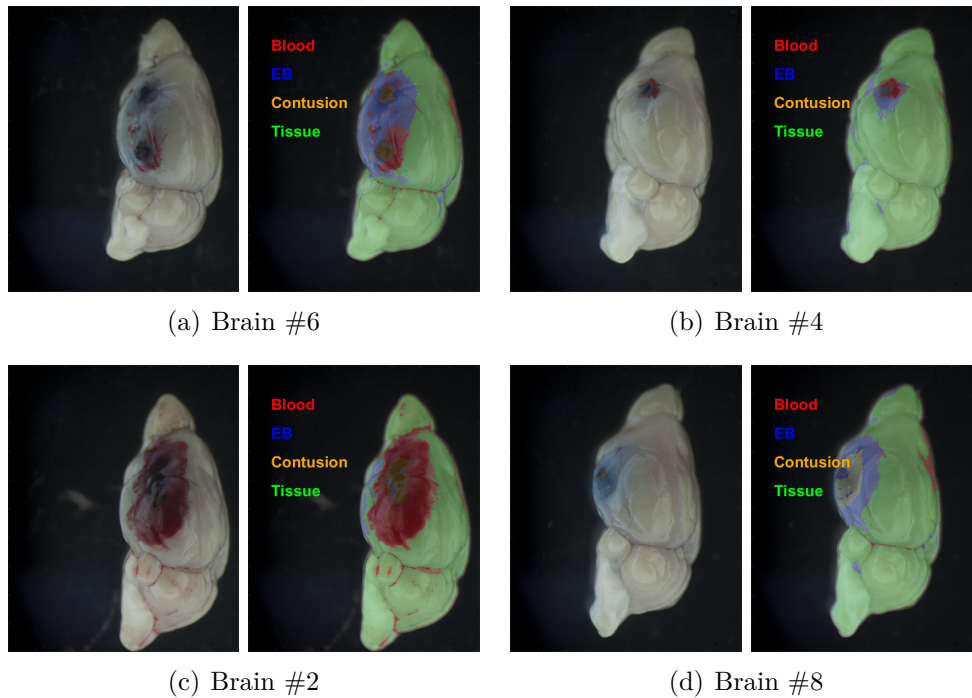


Figure 3-12: Example results obtained using the proposed pathology classification method

The method developed in this section for per-pixel labeling of pathology using a subset of supervised labeled pixels enables objective classification of tissue pathology in a query image whose color space characteristics are consistent with the model data. This method was used to support the grading of brain gross pathology in a recently submitted paper (Tagge et al., 2017) and has the potential to be used in future work by extracting pathology-based features beyond the RGB-pixel values.

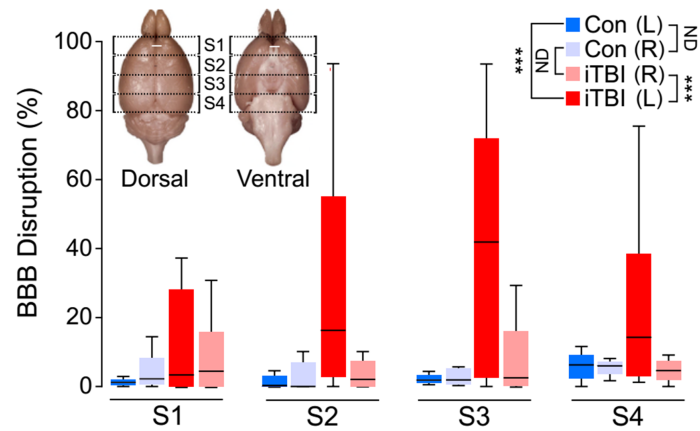
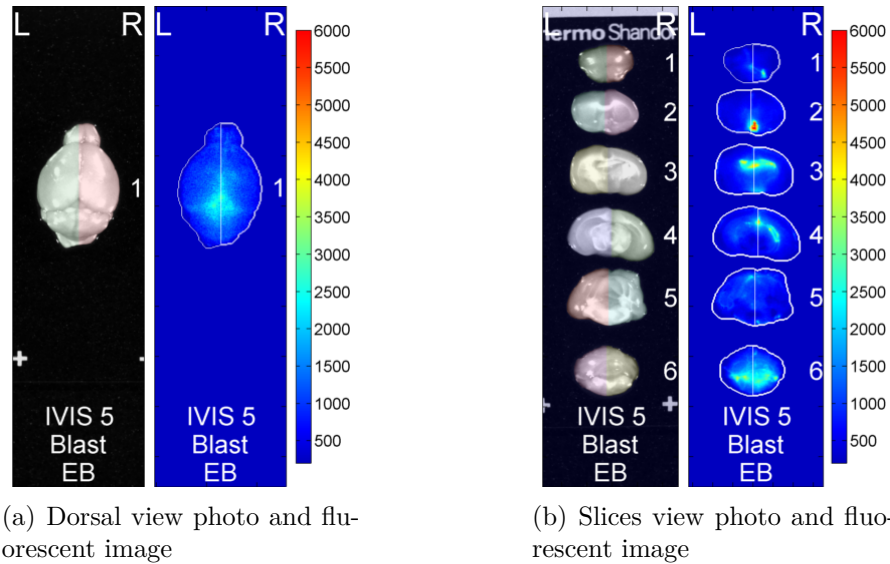
3.3 Evans Blue Fluorescent Imaging for Evaluating Blood-Brain Barrier Dysfunction

By injecting a blue fluorescent dye, Evans blue (EB), with excitation wavelength of 535 *nm* and emission wavelength of 680 *nm*, it was possible to analyze levels of the molecule in the brain tissue using fluorescent imaging. The dye molecule binds to albumin in the blood, and thus the presence of the dye in the brain tissue indicates a compromise of the blood-brain barrier (BBB) at least severe enough to extravasate albumin (approximately 15 *nm*). As such, fluorescent imaging via the IVIS Spectrum In Vivo Imaging System (PerkinElmer, Waltham, MA) provides a proxy for determining the degree of BBB dysfunction by directly observing the fluorescent signature of EB. Compared to the macroscopic pathological imaging discussed in Section 3.2, fluorescent images provide a complementary method for assessing levels of EB in the brain. While the instrument's Living Image software affords a variety of post processing options which were leveraged, large-scale, systematic processing is not straightforward using Living Image alone. A suite of large-scale post-processing functions were developed in MATLAB to aid in the analyses of these images.

A *sequence* in the IVIS spectrum imaging system is defined as a set of sequential fluorescent image acquisitions with different parameters, including changes in the

excitation/emission filter pairs, exposure times, etc. For each parameter set, the data are saved in a folder with six files: two `*.txt` files containing the acquisition parameters and four 16-bit images: a grayscale luminance image, a fluorescent image, a luminance calibration and a fluorescent calibration. Since all images in a *sequence* are acquired sequentially without the object being moved, all images are co-registered by default. For the IVIS imaging data acquired to understand BBB dysfunction in TBI, each sequence involved fluorescent imaging with an excitation filter of 535 *nm* and acquisition with 14 different emission filters ranging from 580 to 840 *nm* with a 20 *nm* spacing. This range of emission filters was used to enable spectral unmixing using the Living Image software. The large volume of files generated as well as the nested nature of the data make data exploration and comparison challenging. To address these issues, a method for extracting all the data from a sequence into a structure was developed. The information from the `*.txt` files is also extracted and organized into a table.

For each brain, three fluorescent *sequences* were acquired: a ventral view, a dorsal view (Fig. 3·13(a)), and a view of six slices of the brain (Fig. 3·13(b)). For each *sequence*, the luminance image was used to segment the tissue from the background. The left and right side of each component in the image were defined relative to the major- and minor-axes determined using the `regionprops.m` function in MATLAB. The ability to automatically define specific regions of interest in the images enabled the analysis of left-versus-right sides of the brain and facilitated the aggregation and processing of data. This functionality was used to support a finding that the levels of the fluorescent signal associated with EB were elevated in the left side of the brains of mice having suffered a left-lateral impact neurotrauma (Tagge et al., 2017)(Fig. 3·13(c)).



(c) Figure 5C from (Tagge et al., 2017)

Figure 3-13: Both (a) and (b) show the luminance image on the left used to identify tissue and background. The coloring indicates the left-versus-right side which was determined by the major- and minor-axes of each component in the image. The region boundaries are indicated in the EB fluorescent image, derived from spectral unmixing using the Living Image software. Results from the cohort imaged in this way are shown in (c)

3.4 Summary of Contributions

The methods described in this chapter were developed in an effort to enable objective, quantitative analysis of traditional biological imaging modalities. Application of well-known methods to better understand the head kinematics and pathological consequences of mouse models of TBI was accomplished. The techniques described in this chapter were used to support several biological findings in a recently submitted publication (Tagge et al., 2017). Contributions made towards this effort can be summarized as follows:

- Development of a mouse-nose tracking algorithm which uses k-means and Chan-Vese algorithms for segmentation and Kalman filtering for estimation of position and higher-order motion derivatives
- Development of a semi-supervised classification method for labeling four brain tissue classes of interest: blood, Evans blue, contusions, and normal tissue
- Development of functions to support automated and systematic analysis of fluorescent imaging data from the IVIS spectrum instrument

Chapter 4

Algorithms for Metallomic Imaging Mass Spectrometry (MIMS) Data Processing

Using a mass spectrometer as the primary sensor for creating spatial images was first attempted in the late 1990's (Caprioli et al., 1997; Pacholski and Winograd, 1999). Imaging mass spectrometry (IMS) is more widely used in a technique known as matrix-assisted laser desorption/ionization (MALDI) whereby the specimen being analyzed is sprayed with a matrix which absorbs the energy at the wavelength of the inciting laser. This causes ionized molecules to be dislodged from the surface of sample. These ionized molecules are then introduced into the mass spectrometer and analyzed across several orders of magnitude of mass to charge ratio. Unlike MALDI, metallomic imaging mass spectrometry (MIMS) is a technique which enables the analysis of the most basic element of materials: their atomic composition. Samples imaged via MIMS require limited processing and no application of a matrix. In conjunction with a standard operating procedure and highly accurate standard materials available from the National Institute of Standards and Technology (NIST), MIMS enables precise quantification of the elemental composition of a material. Because of the novelty of this method for biological specimen analysis, few methods exist for assisting in data extraction, conditioning and interpretation. One of the major contributions of this thesis is development of methods specifically to address the

challenges associated with MIMS data, including unique noise characteristics, large dynamic range, and unique anatomical representations in images.

4.1 MIMS Data Acquisition, Pre-Processing and Rendering

4.1.1 MIMS Acquisition Protocol

As described in Section 2.3.2, the MIMS system has two primary components: the laser ablation (LA) system on the front end and the spectrometer on the back end. For the applications in this work, the back end spectrometer was either an optical emission spectrometer (OES) or an inductively coupled plasma mass spectrometer (ICP-MS). Without loss of generality, the back end spectrometer instrument will be referred to as a mass spectrometer (MS) in this Chapter. To acquire a dataset, the first step is to provide the instructions in the form of an *.1zs file to the LA system. To produce these instructions, CETAC's DigiLaz III software is used in conjunction with a custom MATLAB graphical user interface (GUI), developed by Boston University undergraduate students Daniel Brewster and Casey Kurosawa. The GUI facilitates the construction of more complex data acquisition routines. Fundamentally, the DigiLaz III software provides a GUI through which the user can interact with live video footage to construct an imaging routine. Figure 4-1 shows a screen shot of the DigiLaz III software GUI. The information inputted using DigiLaz III populates an excel table which DigiLaz III uses to generate an *.1zs file. The parameters defined using the DigiLaz III software are indicated in Table 4.1.

Table 4.1: Per line parameters used by DigiLaz III software to generate *.lzs files for the CETAC LSX-213 laser ablation instrument.

Spatial Specifications (columns 1 - 11)

Scan Name	X1	X2	Y1	Y2	Z1	Z2	Method	Aperture Size	Space Between Spots	Space Between Lines
string	$[\mu m]$	$[\mu m]$	$[\mu m]$	$[\mu m]$	$[\mu m]$	$[\mu m]$	category	$[\mu m]$	$[\mu m]$	$[\mu m]$
Nominal parameter values	–	–	–	–	–	–	Single Line Scan	20	0	20

Laser Specifications (columns 12 - 17)

Energy	Pulse Rep Rate	Scan Rate	Number of Shots	Defocus	Defocus Amount
[%]	$[Hz]$	$[\mu m/s]$	integer	Y/N	[%]
5	20	60		N	0

Gas and Timing Specifications (columns 18 - 25)

He Flow Rate	Pause Between Samples	Shutter Delay	Gas Blank	Trigger Delay	Sample Run Time	Total Sample Time	Number of Runs
$[L/min]$	$[sec]$	$[sec]$		$[sec]$	$[sec]$	$[sec]$	integer
550	25	10	10	0	depends on line length		1

The optical system that is part of the CETAC LA instrument has limited field of view; therefore, to generate an LA routine, the DigiLaz III software first constructs an image of the ablation cell by stitching a 12×8 grid of smaller field of view images together (see Fig. 4-1, bottom right). This mosaic image is representative of the entire $39.6 \times 39.6 \text{ mm}^2$ ablation area within the cell. The image can be saved and used to identify arbitrary stage coordinates within the LA cell. Our group's custom MATLAB GUI takes this mosaic image as an input and allows the user to indicate multiple regions of interest within the ablation cell (see Fig. 4-2). Using this map between pixels in the mosaic image and stage positions, the MATLAB GUI allows the user to draw regions of interest on the mosaic image to generate an *.xls file with the appropriate parameters. The *.xls file can be uploaded into the DigiLaz III software to generate a correctly formatted LA protocol. The MATLAB GUI facilitates the synthesis of an LA routine in three respects: 1) it enables guided and automated naming of the lines, 2) it allows the user to quickly indicate imaging regions that may be spatially distant with respect to the field of view of the live video, thus eliminating the need to reposition the stage in order to get an appropriate field of view, and 3) it is easier to identify distinct samples within the cell since the full imaging region is the focus rather than the live video field of view being the focus. The MATLAB GUI also allows for specific imaging sequences, such as calibration or standard regions, to be repeated automatically.

In addition to parameterization of the LA instrument, operation parameters for the MS instrument must also be specified. Each instrument is accompanied by a manufacturer-provided software which enables the specification of acquisition parameters including isotope selection, instrument sensitivity, isotope sampling time parameters, among others. These parameters can be adjusted to fit experimental requirements and constraints. An example of the an MS GUI is depicted in Fig. 4-3.

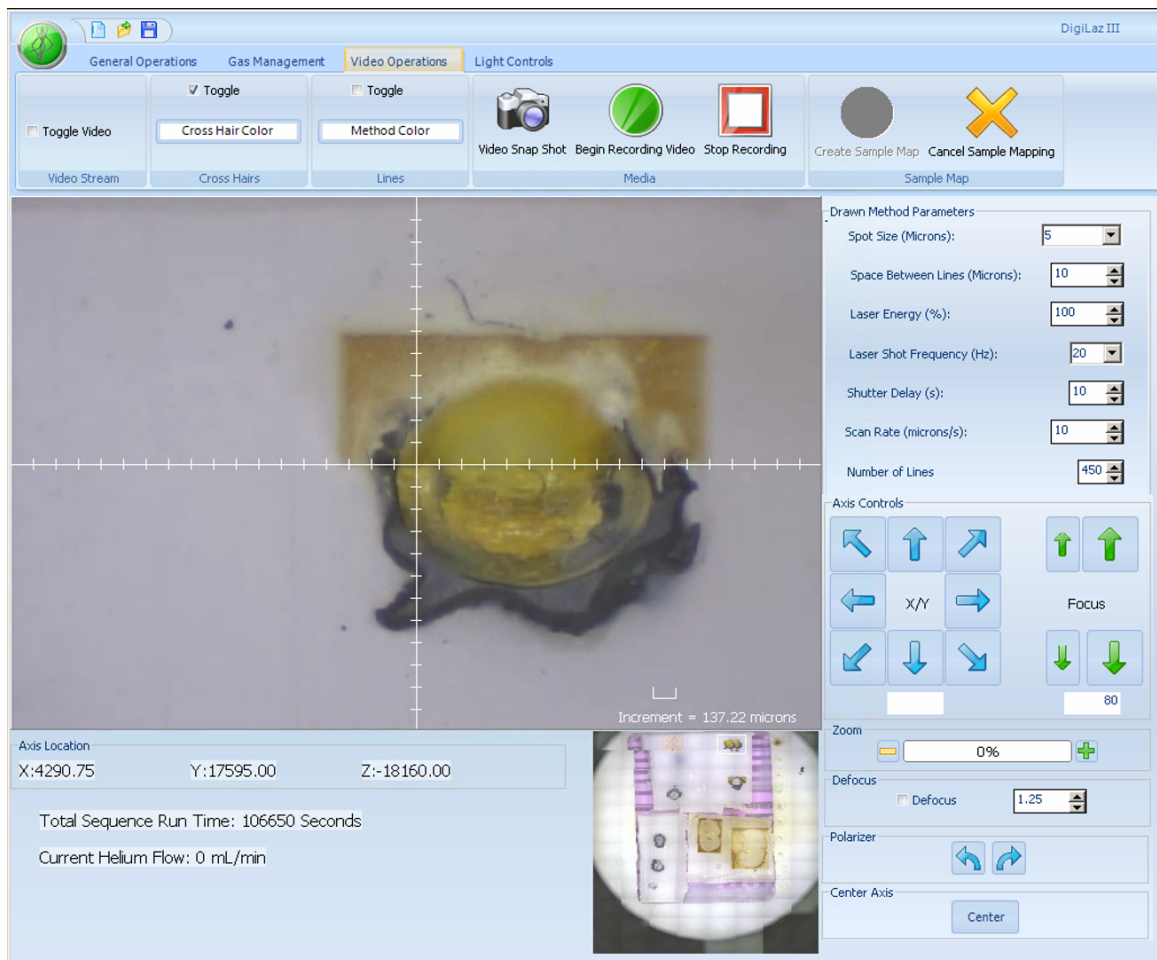


Figure 4-1: DigiLaz III graphical user interface.

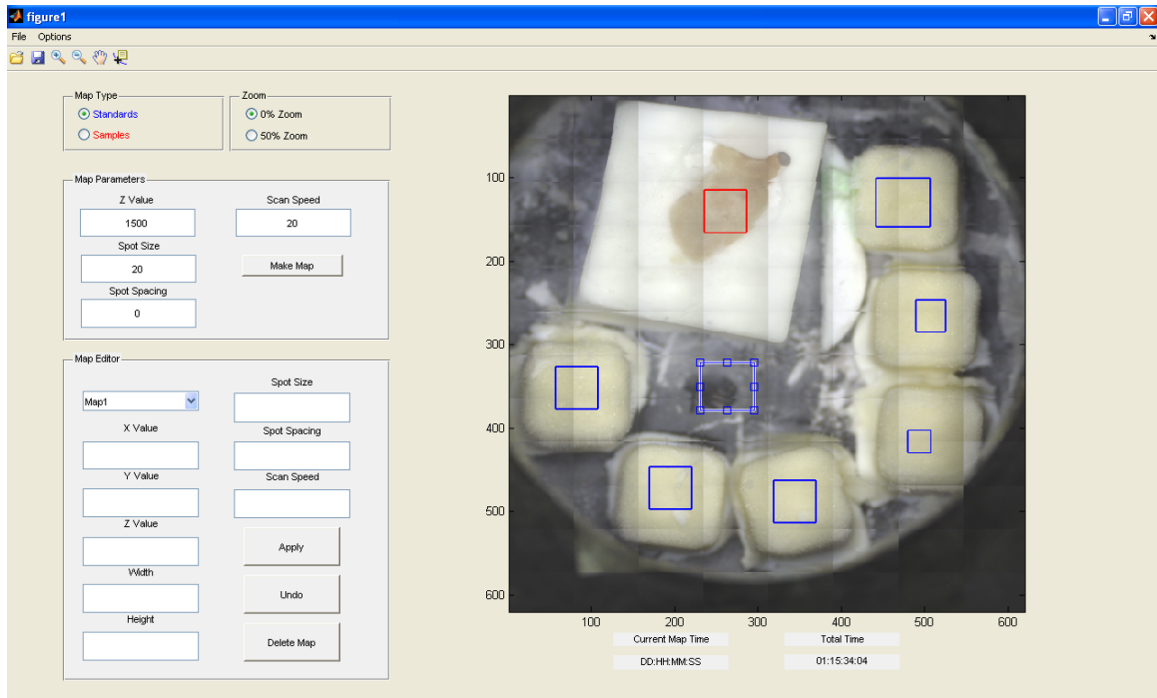


Figure 4-2: MATLAB graphical user interface for constructing laser ablation routines.

100pc8-10-12MR.met - Method Editor - Thermo ELEMENT

File Edit Setup View Resolution Interference Correction Plot Help

Resolution: Medium Runs: 1 Estimated Total Time: [h:min:s] 00:00:01
 Mode: 1 Passes: 1

Method Data		Interference Correction		Quality Control		Mass Window	Mass Range	Magnet Mass	Settling Time	Sample Time	Samples Per Peak	Segment Duration	Search Window	Integration Window	Scan Type	Detection Mode	Integration Type
Entry	Isotope	Calib	Accurate Thresh	Mass	Method Mass Offset												
1	C13	0	13.0028	0.0000	20	13.002 - 13.003	13.003	0.050	0.0010	20	0.004	0	100	EScan	Triple	Integral	
2	Ca44	0	43.9549	0.0000	20	43.954 - 43.956	43.955	0.065	0.0010	20	0.004	0	100	EScan	Triple	Integral	
3	Mn55	0	54.9375	0.0000	20	54.936 - 54.939	54.938	0.030	0.0010	20	0.004	0	100	EScan	Triple	Integral	
4	Fe56	0	55.9344	0.0000	20	55.933 - 55.936	54.938	0.001	0.0010	20	0.004	0	100	EScan	Triple	Integral	
5	Cu63	0	62.9291	0.0000	20	62.927 - 62.931	54.938	0.001	0.0010	20	0.004	0	100	EScan	Triple	Integral	
6	Zn64	0	63.9286	0.0000	20	63.927 - 63.930	63.929	0.028	0.0010	20	0.004	0	100	EScan	Triple	Integral	
7	Zn70	0	69.9248	0.0000	20	69.923 - 69.927	63.929	0.001	0.0010	20	0.004	0	100	EScan	Triple	Integral	
8	Gd157	0	156.9234	0.0000	20	156.920 - 156.927	156.923	0.072	0.0010	20	0.004	0	100	EScan	Triple	Integral	
*																	

Figure 4-3: Example of manufacturer's graphical user interface for the specification of parameters of the Element ICP-MS instrument.

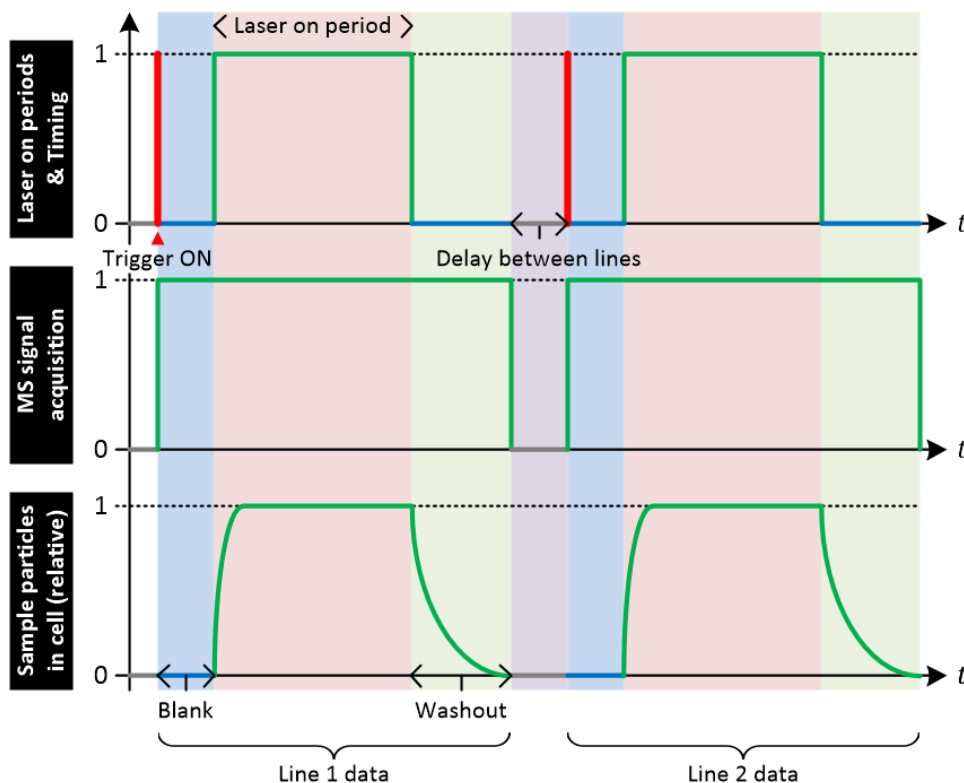


Figure 4-4: Timing diagram showing relative timing of the laser (top), the spectrometer (middle), and the amount of particles generated from the laser ablation cell (bottom) for two lines of data. [Blue area] MS begins sampling data once trigger signal is received from the LA instrument (blank period). [Red area] Laser fires on the sample and generates particles in the ablation cell. [Green area] Laser turns off, but the MS continues to sample data (washout period). [Purple area] Time delay between lines inserted to allow both the LA instrument and the MS to prepare for the acquisition of a new line of data (no data).

The LA and MS communicate via an electrical trigger signal. The trigger signal indicates the start of a line of data in the metallomic image and prompts the MS to begin acquiring data for the indicated isotopes. Each line begins with a *laser off* period where the shutter is maintained on the laser, but the MS begins sampling the detector. A *laser on* period starts during which particles are generated from the sample. Once the *laser on* period ends, the spectrometer continues sampling for the

total user defined period. A time delay between lines, where neither the laser nor the spectrometer are active, is incorporated to ensure proper synchronization of the instruments. The timing of the trigger and data acquisition events are depicted in Fig. 4-4. For the MS instruments, the data for all indicated isotopes are saved in a text file with an instrument-specific formatting. Data acquisition was primarily conducted by analytical chemists Noel Casey, Ph.D., and Bo Yan, Ph.D.

4.1.2 Raw Data Extraction

The raw data from the instrument are saved as formatted text files. While the format varies slightly depending on the spectrometer used in the experiment, the extraction procedure is generally the same for all file types. A custom MATLAB function automatically recognizes the instrument used and parses the raw data within the files accordingly. These data are stored as matrices within a data structure in MATLAB. Spectrometer-specific processing algorithms will be discussed later in this section.

The raw data from a given experiment will be referred to as a MIMS *sequence* and denoted as $\vec{\mathcal{I}}$. A MIMS sequence may contain an arbitrary number of unique images, where an “image” here is defined as a spatial MS representation of a unique underlying entity (ie NIST glass, tissue, calibration standard, etc). Figure 4-5 shows that through the procedure mentioned in Section 4.1.1, the user can select multiple regions in the ablation cell and sequentially image each area in a single acquisition experiment. Typically, for calibration purposes, a range of calibration standards with similar ablation characteristics as the sample of interest are imaged throughout the experiment between tissue samples. Additionally, standard reference materials may also be periodically imaged to assess instrument stability. Each raw data file associ-

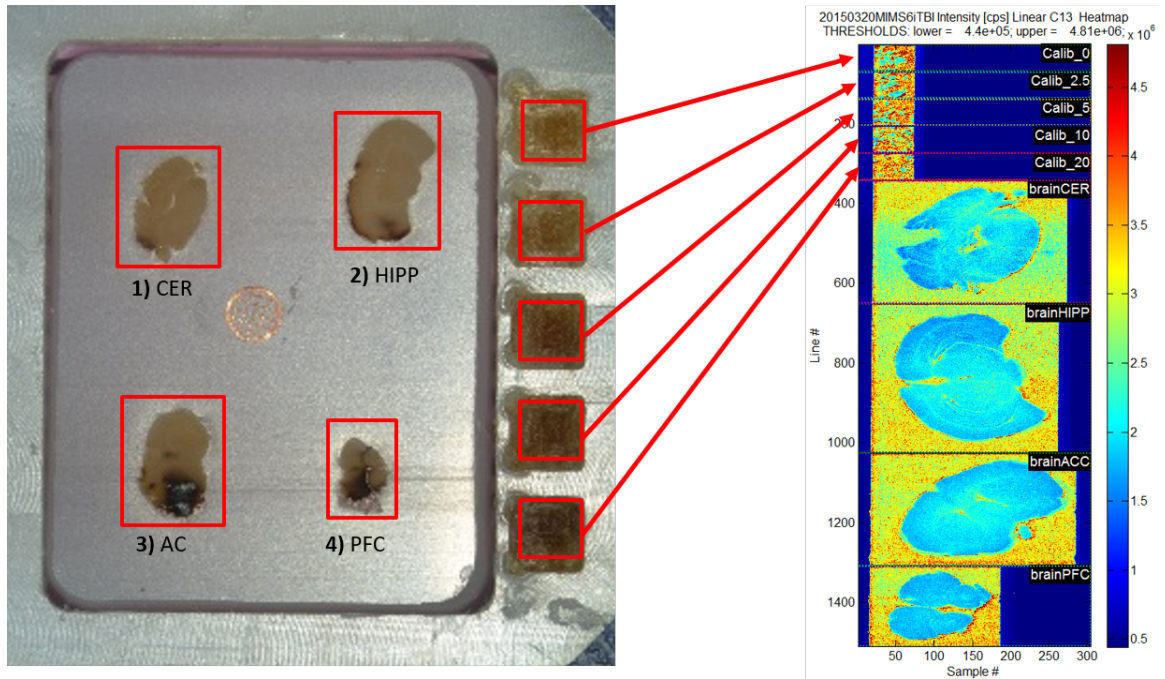


Figure 4-5: Depiction of a MIMS sequence, defined as the raw data from an LA-ICP-MS experiment.

ated with a given line is assigned a line label. These line labels are used to identify distinct sample “types” within the sequence.

4.1.3 Image Rendering Tools

In order to accurately visualize captured data, several image processing and rendering tools are developed (see Fig. 4-6 for an example of outcomes). As mentioned in Section 2.3.2, the data provided by the LA-ICP-MS and -OES systems are given in units of counts per second (*cps*) (Row 1, Fig. 4-6). For each isotope, data from a calibration experiment (Row 2, Fig. 4-6) is used to parametrize a calibration curve (Row 3, Fig. 4-6) which provides a functional relationship between *cps* and parts per million (*ppm*). This relationship can be used to represent MIMS in terms of *ppm* (Row 4, Fig. 4-6). The method for preparing matrix-matched calibration standards

to provide data for a calibration curve is sample-specific. Using the LA raster scanning parameters and the MS sampling time, the horizontal and vertical axes can be represented in terms of spatial distance (Row 4, Fig. 4-6) yielding a quantitative and spatially-accurate representation of the underlying object.

Additionally, a line unwrapping method was required for visualizing OES data. The raw data from the OES is shown in Fig. 4-7(a). The data are structured such that the raw data from the instrument form a $P \times Q$ matrix which contains data from an $U \times V$ image where $U \geq P$ and $V \leq Q$. This essentially means that a row of the raw data matrix contains multiple spatial lines. The example in Fig. 4-7(a) has $U = 5P$ and $V = Q/5$. The number of data points in each line varies by approximately ± 1 sample due to very slight discrepancies between the scan speed and acquisition time, preventing the ability to simply “stack” each row from the raw data matrix into U/P rows with V data points each. Because each of the spatial lines do not have the same number of data points, the rising (or falling) edges of each line are instead automatically aligned. On a line-by-line basis, the unwrapping algorithm first roughly aligns two spatially-neighboring lines (blue and red lines in Fig. 4-7(b)) by maximizing the cross-correlation, then shifting the current line by the cross-correlation accordingly (cyan line in Fig. 4-7(b)). Because each line is imaging a slightly different spatial feature, the cross-correlation aligns overall signal features, but not specifically the rising edges of the lines. Therefore, a secondary alignment step was performed by identifying the rising (or falling) edge of the signal and using this point to anchor the current line to the $U \times V$ image being constructed (Fig. 4-7(c)). The final output is an aligned, physically-representative image of the ablated object (Fig. 4-7(d)).

Tools for customized pseudo coloring, multi-channel visualization, image overlaying

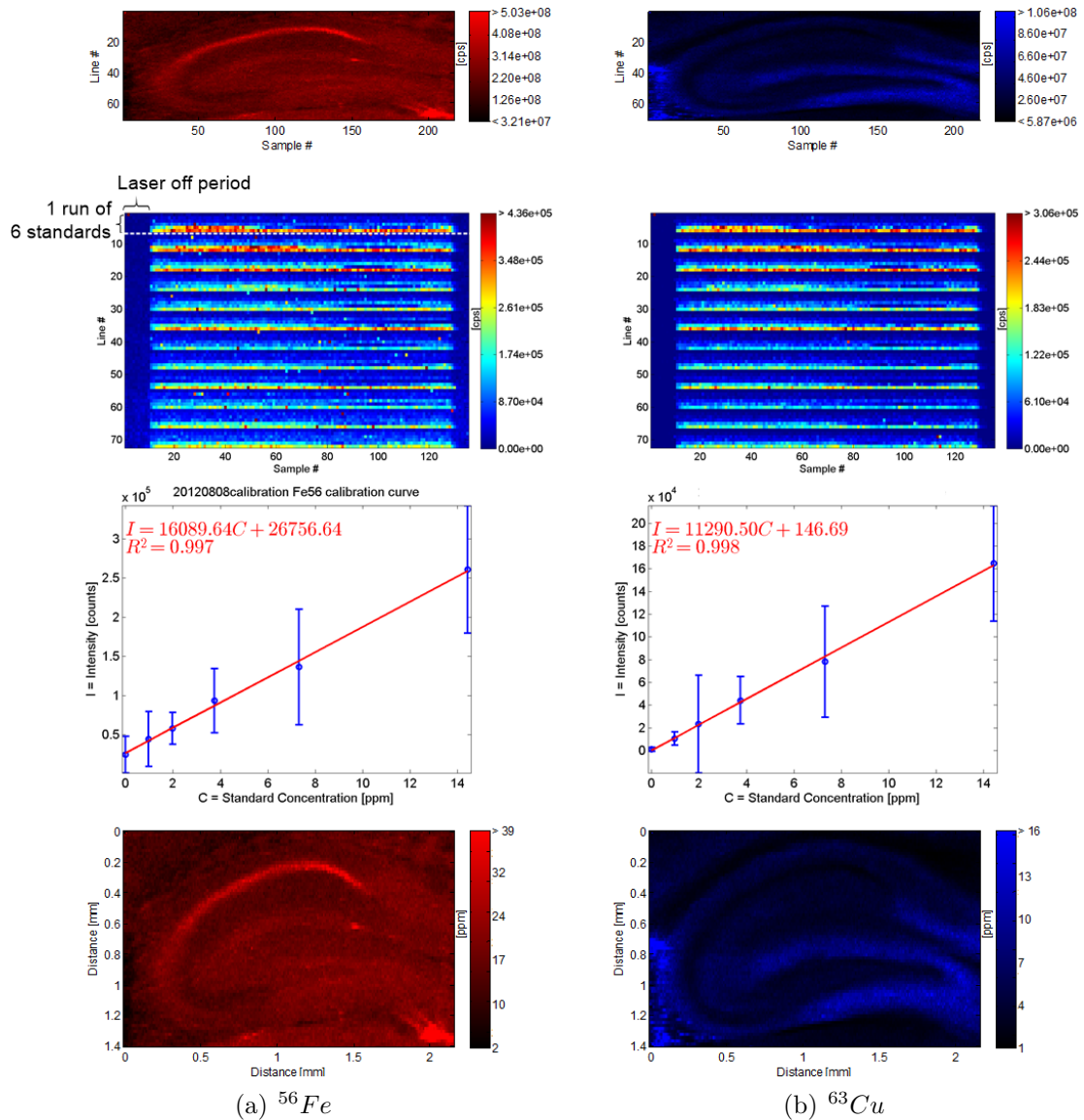


Figure 4-6: Each column shows data for (a) ^{56}Fe and (b) ^{63}Cu . **Row 1:** pseudo-coloring of the raw data in cps . **Row 2:** data from a calibration experiment where multiple samples were collected for six standards with a known concentration in ppm . **Row 3:** derived calibration curve. **Row 4:** data from Row 1 calibrated to ppm and with axes scaled to reflect physical dimensions

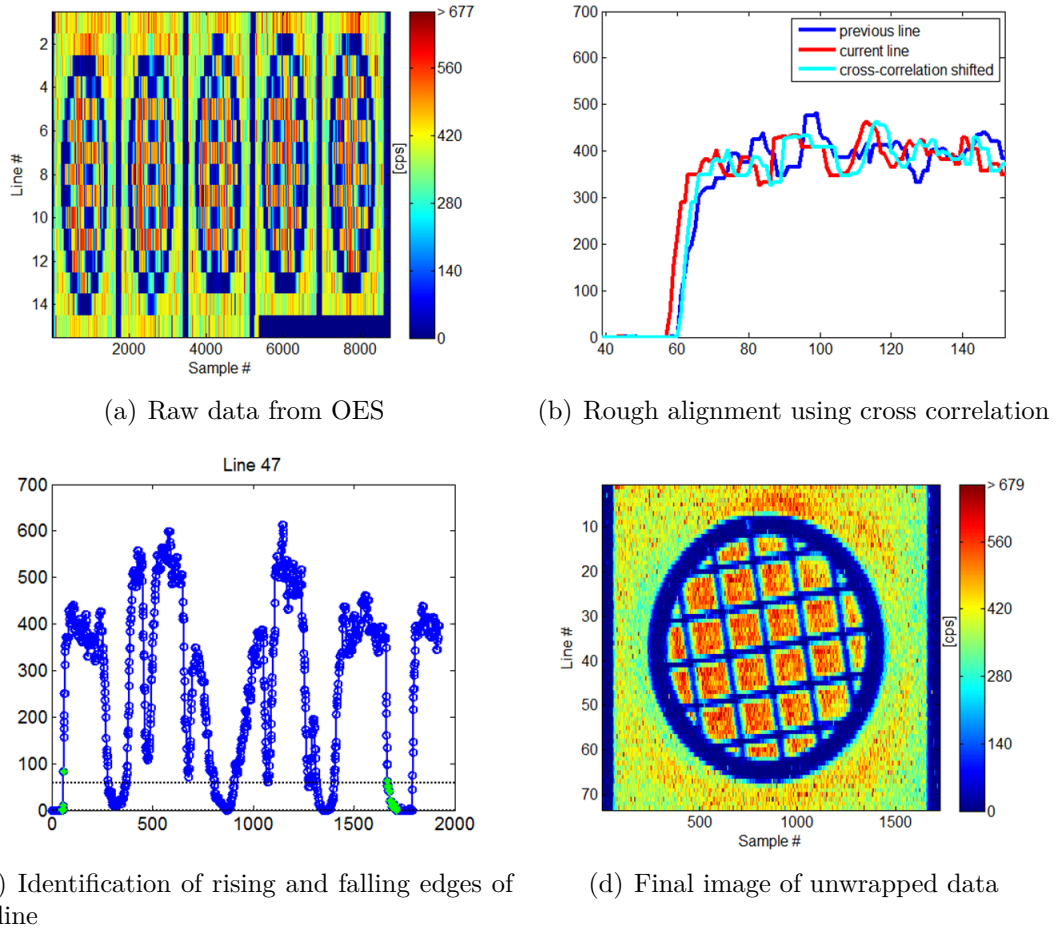


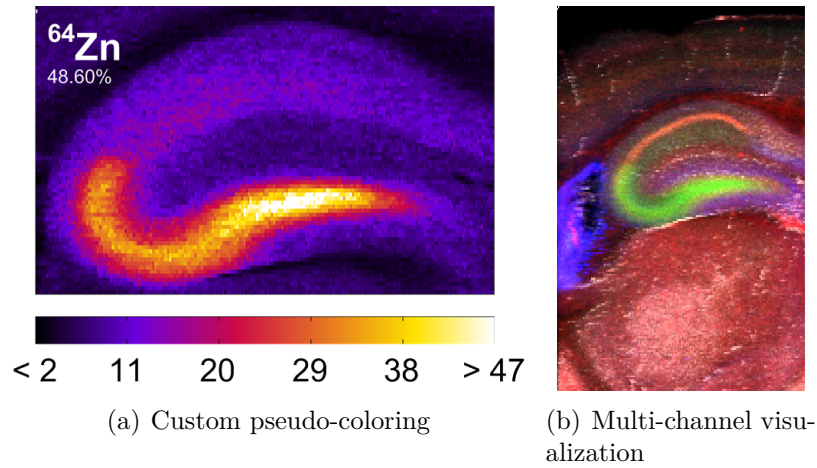
Figure 4-7: Steps required for unwrapping raw data from the optical emission spectrometer (OES). (a) Raw data with multiple spatial lines per line of acquired data. (b) Alignment of current line (red) with previous line (blue) via shifting by the cross-correlation lag value (cyan). (c) A line of data with the points of the detected rising and falling edges shown with green markers. (d) Final unwrapped image.

and a manual image registration GUI were also developed. Visual representations of these tools are shown in Fig. 4-8 and throughout this work. These functions are listed and described in Appendix B.2.

4.2 MIMS Region Segmentation

Identifying distinct regions in a MIMS image is an important preprocessing step both for subsequent visualization and data analysis. As shown in Fig. 4-4, each MIMS image includes three distinct periods: an initial laser off *blank* period (blue), a *laser on* period (red), and a laser off *washout* period (green). Additionally, when imaging a sample, the imaged area during the laser on period can be segmented into two regions: data associated with the *sample* and a *background* region. Segmenting these data is particularly challenging because the properties associated with each of these distinct regions vary depending on the isotope under consideration and the material being ablated. Generally, the signal during the *blank* and *washout* periods tends to be the lowest while the signal within the laser on portion is higher. A variety of factors including isotope sensitivity, sensor drift, polyatomic interferences, material properties, etc., result in images where this general pattern may not hold.

Before defining the segmentation procedure in detail, notation that will be used throughout this chapter is needed. Figure 4-9 provides a reference to the notation used. Consider a MIMS sequence, $\vec{\mathcal{I}}$, with T -types of samples and d -channels acquired. Each data type, $\tau = 1, \dots, T$, in the MIMS sequences can be thought of as a d -channel, vector-pixel image, \vec{I}_τ . The i -th channel of the image \vec{I}_τ will be indicated as $I_\tau^{(i)}$ where $i = 1, \dots, d$, and the pixel values in each channel indicate the intensity in counts per second (*cps*) detected by the MS for a distinct isotope. For example, $i = 1$ may represent the metallic intensity for ^{13}C , $i = 2$ the intensity for



I_F : Fe/Cu/Zn MSI, I_M : Atlas, MI = 0.6106, $T = [-6.9, 1.3, 0.0, 1.1, 1.0, -0.1]$
 Original MI: 0.6199, Original $\mu = [0.0, 0.0, 0.0, 1.0, 1.0, 0.0]$

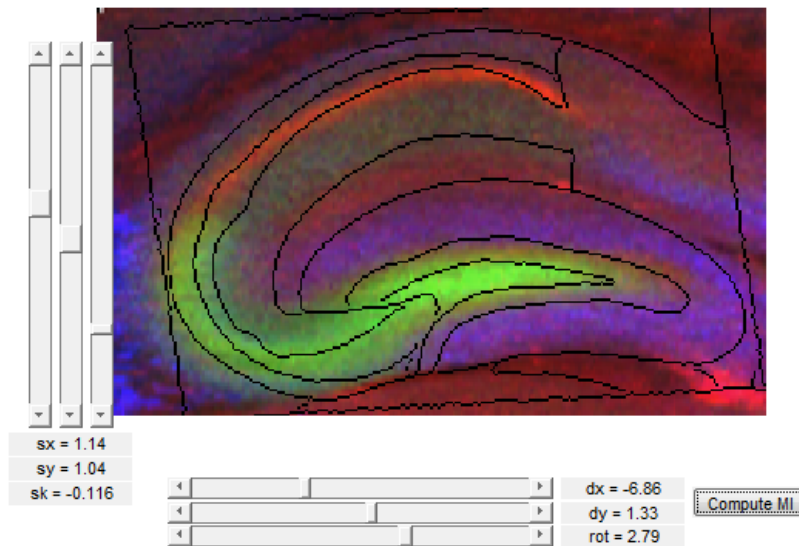


Figure 4-8: Examples of select image processing and rendering tools. (a) Depiction of a calibrated MIMS image with a fire colormap with *ppm* values indicated by the colorbar. (b) Multi-channel psuedo-colored image depicting four channels of data ^{56}Fe [red], ^{63}Cu [blue], ^{64}Zn [green], ^{56}Gd [white] (c) Manual affine image registration GUI where I_M (moving image) is displayed as edges overlaid on the I_F (fixed image). The mutual information value is given as well as the six values in the transformation matrix A , discussed in more detail in Section 4.5.2.

^{140}Ce , $i = 3$ the intensity for ^{65}Cu , and so on.

The objective of MIMS segmentation is to assign one of four labels to each pixel in the image \vec{I}_τ : (1) *blank*, (2) *washout*, (3) *background*, and (4) *sample*. Notice that for the MIMS sequence shown in Fig. 4-9, the ^{13}C and ^{66}Zn channels for the “brainHIPP” image, \vec{I}_τ , have vastly different intensity properties for each of the regions of interest. Because the sequence of events on each line follows the sequence of events detailed in Fig. 4-4, channels which have properties consistent with the labels of interest can be identified. The function leverages the intensity characteristics of each channel to ultimately create a mask $M_\tau \subseteq \{1, 2, 3, 4\}$ whose values correspond to the label of each pixel in the image.

In this thesis, the MIMS sample types can be categorized into three distinct groups: certified reference materials, calibration standards, and samples of interest. Samples of interest are primarily biological samples including sections of mouse brains (Chapter 5) and human lacrimal sacs (Chapter 6), but for optimization of the acquisition procedure and instrument settings, 3.05 *mm* copper grids (Electron Microscopy Sciences, 2016) were also imaged. The primary certified reference material used was the NIST glass 612 (National Institute of Standards and Technology, 2016) and the calibration standards were prepared in our laboratory. Both the NIST and Calibration images have masks $M_\tau \subseteq \{1, 2, 3\}$ since the *laser on* portion of the image does not have two distinct regions as MIMS of samples do.

Ideally, the intensity properties of the different regions of the image would have separable modes, making image segmentation by k-means clustering or identification of Gaussian components (by parameterization of a Gaussian mixture model (Bishop, 2006)) straightforward approaches. While it may be true that the intensity characteristics of some channels in a MIMS image exhibit a high degree of separability,

$$\vec{\mathcal{I}} = \{\mathcal{I}^{(i)}\}_{i=1}^d \quad \mathcal{I}^{(i)} = \{I_\tau^{(i)}\}_{\tau=1}^T$$

* NIST segments, $\tau = 1$

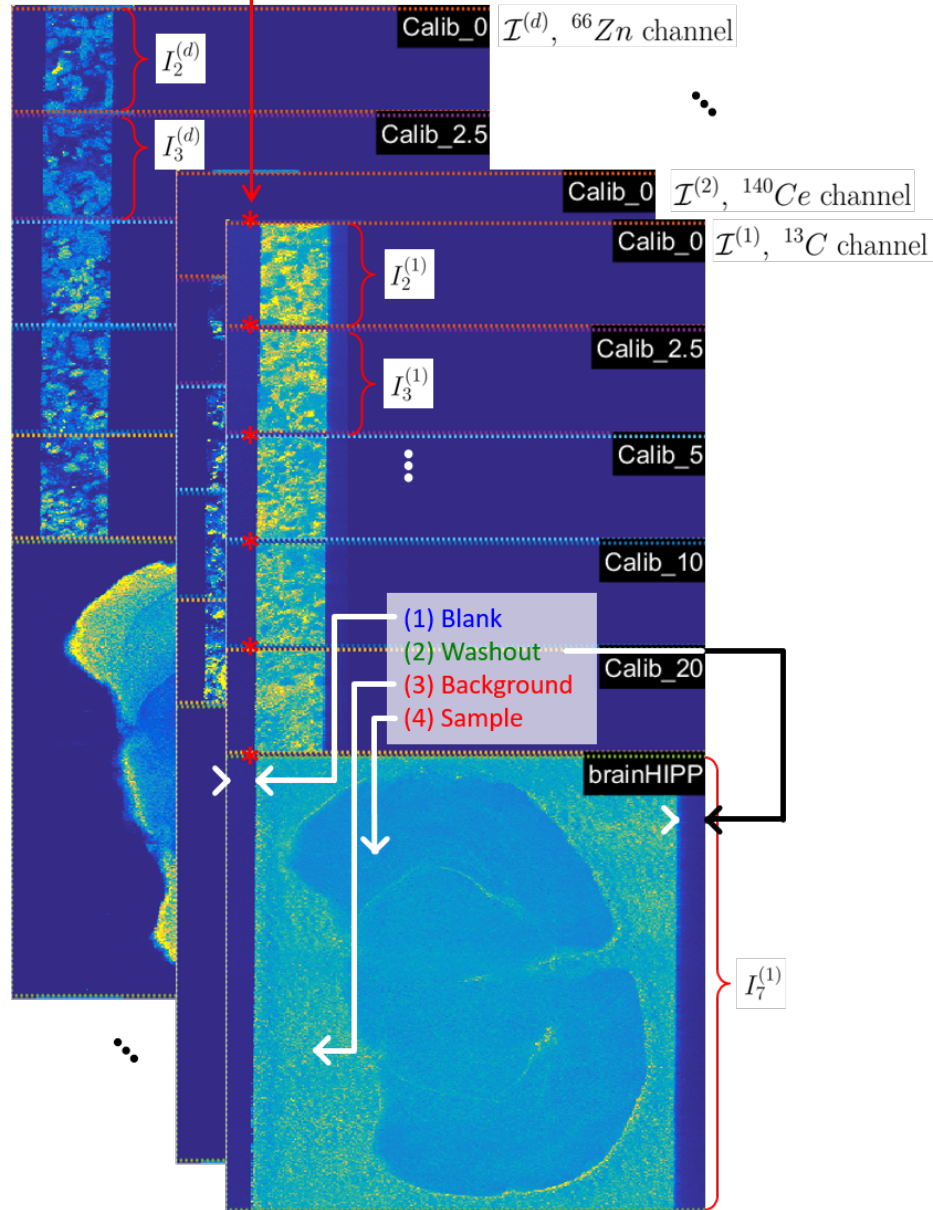


Figure 4-9: MIMS sequence overview with mathematical notation.

this is not always the case and automated identification of such channels would be required nonetheless.

The segmentation algorithm uses a rule-based approach to identify channels whose intensity characteristics clearly represent either the *laser on* region, the *sample* region, or neither. The algorithm is dependent upon the line characteristics detailed in Fig. 4-4. The ground-truth mask is expected to have the following properties:

1. A minimum *blank* period of 5 *sec*
2. A *sample* which takes up at least 25% of the total imaging area and is not represented in the blank region of the image

For each channel in the image, a bimodal segmentation algorithm identifies the two most prominent histogram peaks then uses the minimal intensity between these peaks as a threshold to produce an intensity mask $K_\tau^{(i)} \subseteq \{0, 1\}$. The properties of the mask $K_\tau^{(i)}$ are evaluated and the mask is categorized as either being representative of *laser on* area ($M_\tau > 2$), of *sample* area ($M_\tau = 4$), or of neither. Figure 4-10 shows an example of a channel image $I_\tau^{(i)}$ along with the mask $K_\tau^{(i)}$ for each of the possible categories. Once all d channels are evaluated, the channel masks in each category ($g = \{laser\ on, sample\}$) are used to create a segmentation image defined as:

$$S_\tau^g(p) = \sum_{i \in c} K_\tau^{(i)}(p) \subseteq \{0, 1, \dots, |i \in g|\}$$

Two cluster k-means is then applied to $S_\tau^{laser\ on}$ (Fig. 4-11(a)) to generate a k-means label image $K_\tau^{laser\ on} \in \{0, 1\}$ (Fig. 4-11(b)). The k-means result is checked to ensure the *laser on* part of the image is assigned a cluster label of one and is filled. The output is then used to create a preliminary mask of the MIMS type M'_τ (Fig. 4-11(c))

defined as follows:

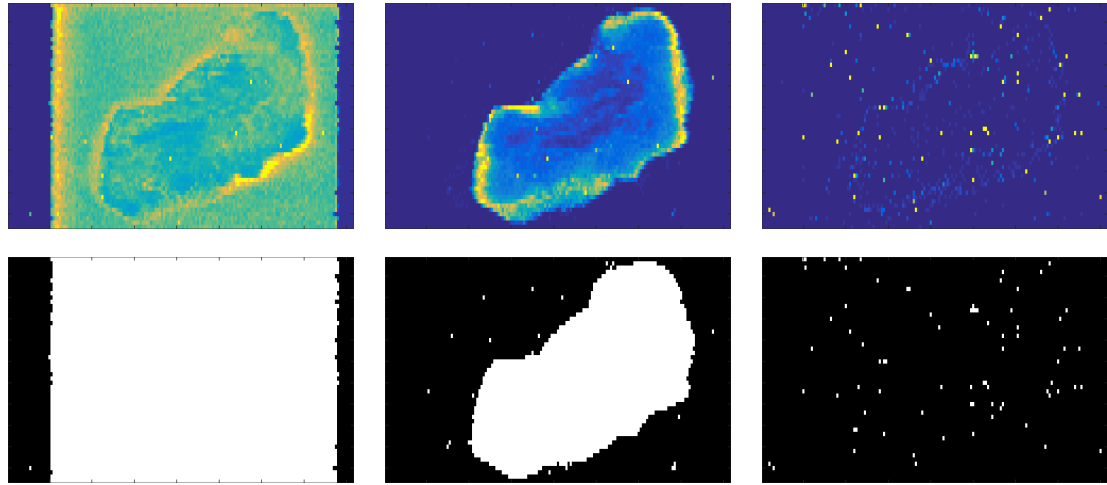
$$M'_\tau (p \in \text{first half of columns}) = \begin{cases} 1 & K_\tau^{\text{laser on}}(p) \neq 1 \\ 3 & \text{otherwise} \end{cases}$$

$$M'_\tau (p \in \text{second half of columns}) = \begin{cases} 2 & K_\tau^{\text{laser on}}(p) \neq 1 \\ 3 & \text{otherwise} \end{cases}$$

Note that $M'_\tau = M_\tau$ for the NIST and calibration standard MIMS types. For sample types, the part of $M'_\tau = 3$ will be further divided into *background* and *sample* using the channel masks categorized as *sample* masks. Again, using S_τ^{sample} (Fig. 4-12(a)), a two cluster k-means mask is generated (Fig. 4-12(b)), ensuring the background part of the image has a cluster label of zero. With $M_\tau = M'_\tau$ as a starting point, the sample pixels are then defined as follows:

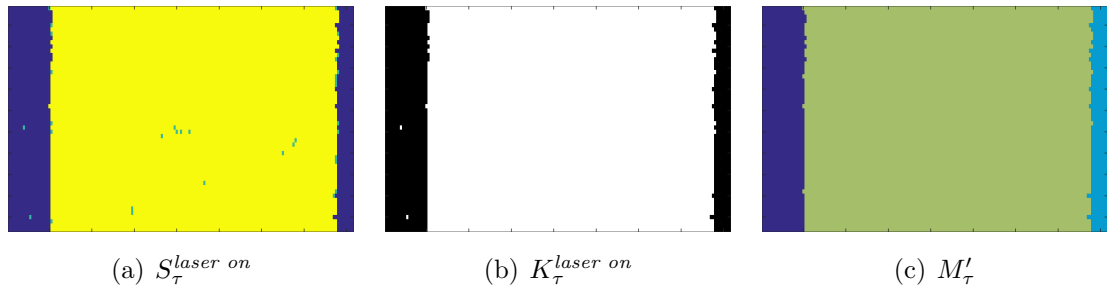
$$M_\tau(p) = \begin{cases} 4 & M'_\tau(p) = 3, K_\tau^{\text{sample}}(p) = 1 \\ M'_\tau(p) & \text{otherwise} \end{cases}$$

The final segmentation mask M_τ is shown in Fig. 4-12(c).



(a) Example of *laser on* channel image and mask (b) Example of *sample* channel image and mask (c) Example of neither channel image and mask

Figure 4-10: Examples of the channel categorization routine used by the segmentation algorithm. The top row depicts the intensity adjusted channel images $I_{\tau}^{(i)}$ and the bottom row depicts the associated mask $K_{\tau}^{(i)}$. Column (a) shows a representative *laser on* channel, column (b) shows a representative *sample* channel, and column (c) shows an example which does not get assigned a category.



(a) $S_{\tau}^{laser\ on}$

(b) $K_{\tau}^{laser\ on}$

(c) M'_{τ}

Figure 4-11: Intermediate images used to define a *laser on* mask

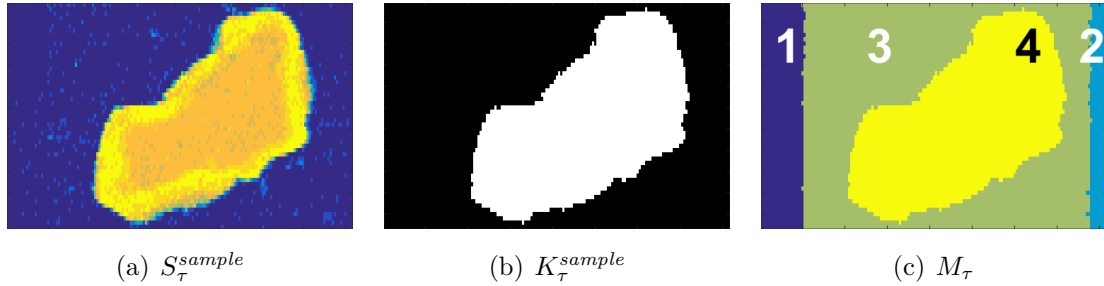


Figure 4.12: Intermediate images used to define the final MIMS segmentation mask

4.3 MIMS Calibration

Calibration of the MIMS images is the process of parameterizing a linear function to map counts per second (*cps*) from the instrument to absolute concentrations of isotopes in parts per million ($ppm = \mu g/g$). This is done by preparing laboratory standards with similar ablation characteristics as the sample of interest (called matrix-matched standards) at precisely known concentration values. These matrix-matched standards are ablated along with samples of interest and the data from these regions are used to calibrate the rest of the MIMS sequence. In this section, the focus will be on the post-processing procedure used to calibrate data rather than on the protocol for synthesizing matrix-matched standards. The assumption that raw data in *cps* are linearly related to their absolute concentrations in *ppm* within some range of concentrations is used widely throughout the literature (Becker et al., 2007; Niehaus et al., 2015). The matrix-matched calibrations are prepared at varying levels of known isotope concentrations to span the range of isotope concentrations thought to be in the sample.

To minimize total acquisition time, a series of calibration standards (typically five to eight) may be used to calibrate more than one sample of interest. The data acquired

during the laser on period of the calibration standards are isolated and then used to parametrize a line mapping *cps* to *ppm*. These parameters can then be applied to each channel of the MIMS sample image to represent data in terms of *ppm* rather than abundance as indicated by the MS.

To calibrate a MIMS dataset, the parameters $\alpha^{(i)}$ and $\beta^{(i)}$ from Eqn. 4.1 must be determined for all $i = 1, \dots, d$. This is done by fabricating a set of n_{stnd} calibration standards each with a known isotopes concentration in *ppm*. The known concentration represents the independent variable x_j for $j = 1, \dots, n_{stnd}$. Referring to Fig. 4-9, assume that the associated type numbers are $\tau = j = 1, \dots, n_{stnd}$ and the d -channel MIMS image associated with each calibration value is \vec{I}_τ , given as *cps* by the MS. For each set of calibration images and for each channel, a linear regression model (Eqn 4.1) is parametrized which in the least-squares sense optimally determines the relationship between the observed statistical values of the calibration data, $\vec{y}^{(i)}$, and the *ppm* values, \vec{x} . The values for $y_j^{(i)}$ are determined by segmenting the regions of the calibration image \vec{I}_j and using the data within the *laser on* portion of the image to define a summarizing statistic. For the applications in this work, $y_j^{(i)}$ represents the median of the data in the *laser on* portion of the calibration image $I_j^{(i)}$. While linear regression may also be performed using the mean, the median is chosen since it is more robust to outliers in the data.

$$\begin{aligned} \vec{y}_{cps}^{(i)} &= \alpha^{(i)} \vec{x}_{ppm} + \beta^{(i)} && \text{for } i = 1, \dots, d && (4.1) \\ \text{where } \vec{x} &= \begin{bmatrix} x_1 & x_2 & \dots & x_{n_{stnd}} \end{bmatrix}^T && \vec{y}^{(i)} &= \begin{bmatrix} y_1^{(i)} & y_2^{(i)} & \dots & y_{n_{stnd}}^{(i)} \end{bmatrix}^T \\ &&& y_j^{(i)} &= \text{median} \left[I_j^{(i)} \in \textit{laser on} \right] \end{aligned}$$

Using these linear mapping parameters, each channel of the MIMS sequence $\mathcal{I}^{(i)}$ can

be converted into *ppm* values by applying the following pixel-wise operation:

$$\mathcal{C}^{(i)} = \frac{\mathcal{I}^{(i)}}{\alpha^{(i)}} - \frac{\beta^{(i)}}{\alpha^{(i)}} \quad (4.2)$$

While in theory the mapping between *cps* and *ppm* is fairly straightforward, several considerations require more in-depth evaluation of the data before parameterization of the regression model. Figure 4-13 has four subfigures depicting the challenges associated with calibrating samples of interest. Figures 4-13(a) and 4-13(b) present plots in a x -vs- $y^{(i)}$ form where the errorbars above and below each of the calibration points correspond to the upper and lower quartile of the data within the *laser on* period of $I_j^{(i)}$. The dashed horizontal lines in these plots indicate the upper-intensity range for the associated MIMS images. This upper-intensity value is defined as 1.5-times the 0.995-th quantile of the data associated with the sample ($M_\tau = 4$, defined using the MIMS segmentation algorithm). Figures 4-13(c) and 4-13(d) show normalized histograms of the intensities within each of the MIMS types indicated in the legend at the right of the plot. The vertical dashed lines show the median values of the data (equivalently $y_j^{(i)}$). The issues associated with parameterizing the linear relationships between *cps* and *ppm* fall into two main categories:

1. Calibration data issues

- (a) Instrument saturation within range of calibration values (Fig. 4-13(a))

The two samples acquired in the MIMS sequence are indicated by their sample numbers *4324_2* and *1581_1* with the dashed-lines depicting the upper-intensity ranges as explained previously. If the calibration curve saturates within the range of intensities present in the sample, only intensities up to the last valid standard value x_v are used to parametrize the best-fit linear model. All intensities greater than the maximum are mapped to the

last valid standard value (i.e. $\mathcal{I}^{(i)} \geq y_v^{(i)} \Rightarrow \mathcal{C}^{(i)} = x_v$). A procedure was developed to detect regions of the calibration curve which are saturated. The two lines shown in Fig. 4.13(a) show the lines of best fit using the valid calibration values (labeled “valid” and shown with a purple line) and using all the calibration points available (labeled “ppmi” and shown with a green line).

- (b) The noise floor of the data for some (or all) of the calibration standards is above the levels in the sample (Fig. 4.13(b))

Again, the figure shows the upper-intensity ranges for the samples *3733_2* and *5257_1* along with the first three calibration standard values along with errorbars. Clearly, the levels in the samples are well below even the $x_1 = 0$ ppm value in the calibration standard. This likely occurs either because of higher levels of certain elements in the matrix used to make the standards or because of differences in the ablation properties of the standards and the samples.

2. Mismatch between calibration curve range and sample of interest concentration range

- (c) Parts of the calibration curve are irrelevant given the range of concentrations present in the samples of interest (Fig. 4.13(c))

As can be seen, the upper end of both the normalized sample distributions fall below the 5 ppm value. To preserve the maximum amount of local linearity and to parametrize the best fit line based on values most likely found in the sample, $x_j > 5$ ppm are not used to parametrize the calibration curve.

- (d) The abundance of the isotope signal in the sample is well above the maximum calibration value (Fig. 4.13(d))

These samples would require a different set of calibration standards to be calibrated.

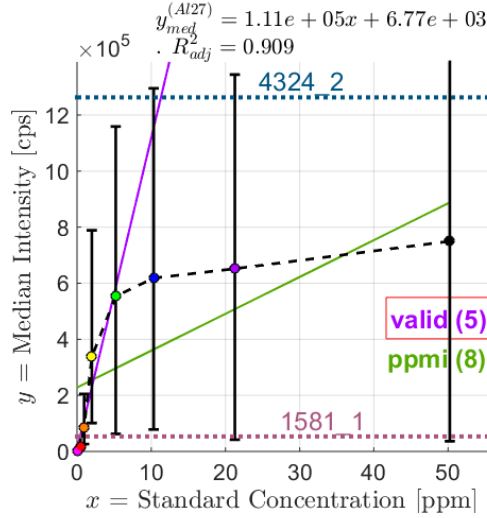
The steps of the calibration procedure can be summarized as follows:

1. Read MIMS sequence data into the workspace
2. For each image type in the sequence, create a mask M_τ
3. For calibration standard data, calculate the median of the data within the *laser on* period of the image ($M_\tau = 3$), these points will represent \vec{y}_j
4. Valid points in the calibration curve are identified by checking for regions of saturation and relevant *ppm* levels in the samples to be calibrated
5. For each isotope, parametrize the linear function mapping *ppm* to *cps*
6. MIMS images, $\mathcal{I}^{(i)}$, are converted to calibrated images represented in *ppm* using Eqn. 4.2

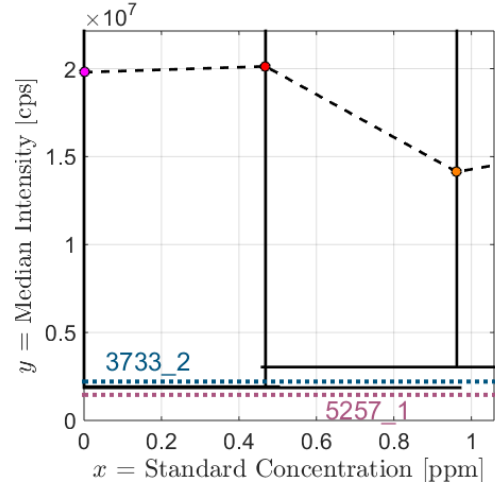
4.4 MIMS Channel Equalization

One of the major challenges associated with comparison and analysis of MIMS images is the variation in the intensity properties. To address this issue, the intensity distribution of each channel in a MIMS image can be equalized such that all distributions occupy a similar dynamic range. The technique provides a means to visualize MIMS channels and MIMS sequences in a normalized intensity domain for easier subjective comparison and subsequent analyses. Since the mapping is functionally deterministic, image intensity values in the normalized intensity domain can always be mapped back to the original raw intensity values.

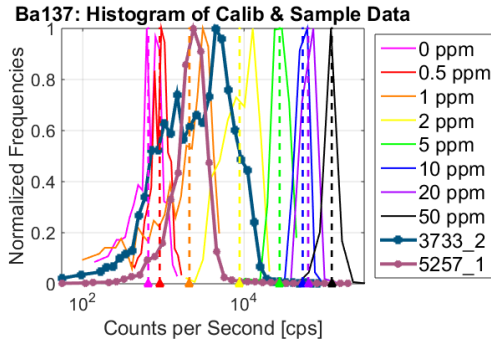
Channel equalization is performed on each channel and each type independently. Within a uniform region, the MIMS intensity values were experimentally observed to



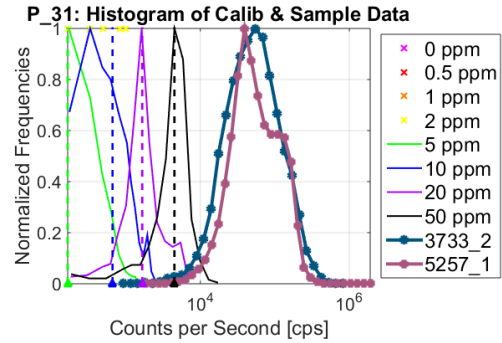
(a) Calibration curve saturation



(b) Data values below noise floor



(c) Unnecessarily high concentrations



(d) Sample levels exceed maximum calibration level

Figure 4-13: Calibration curve data screening and selection. The line plots shown in 4-13(a) and 4-13(b) show the median calibration standard values with error bars indicating the first and third quartile of data. The horizontal lines represent the upper-threshold values for the samples to be calibrated in the MIMS sequence. 4-13(a) includes two lines of the best fit for the “valid” region of the calibration curve (the first five data points) and for all *ppm* values. The distribution plots in 4-13(c) and 4-13(d) show a normalized histogram of the data within each off the calibration regions and the samples in the MIMS sequence. The vertical dotted lines indicate the median values for the color corresponding to the calibration standard distribution.

follow a log-normal distribution. Let the pixel intensity values from the i -th channel of the τ -th type MIMS image be represented by $\vec{x} = \text{vec}(I_\tau^{(i)})$, whose distribution and probability density function (pdf) are given in Eqn 4.3. Operating under the assumption that \vec{x} are log-normally distributed, by taking the natural log of the data, $\vec{y} = \ln \vec{x}$, the resulting data are normally distributed (Eqn 4.4) and classical mean variance equalization (MVE) can be performed.

$$X = \exp\{\mu + \sigma Z\} \quad \text{where } Z \sim \mathcal{N}(0, 1) \quad (4.3)$$

$$f_X(x; \mu, \sigma) = \frac{1}{x\sigma\sqrt{2\pi}} \exp\left\{-\frac{(\ln x - \mu)^2}{2\sigma^2}\right\}$$

$$Y = \ln X \sim \mathcal{N}(\mu, \sigma) \quad (4.4)$$

$$f_Y(y; \mu, \sigma) = \frac{1}{\sigma\sqrt{2\pi}} \exp\left\{-\frac{(y - \mu)^2}{2\sigma^2}\right\}$$

Due to high-intensity noise, the mean and variance calculated directly from the samples \vec{y} tend to be skewed towards higher values. To circumvent this bias, a Gaussian curve fitting strategy is used rather than direct statistics on the samples. A histogram of the sample values can be constructed, which serves as a scaled surrogate of the true pdf. The values of $I_\tau^{(i)}$ are quantized into B bins where the $m \times n$ pixel values are binned into the $\{q_b\}_{b=1}^B$ bins to give bin occupancy values $h(q)$. Given the underlying data are normally distributed with mean μ and variance σ^2 , then the histogram should take the form in Eqn 4.5. The Gaussian curve fitting problem can be converted into a quadratic fitting problem by taking the natural log of the function (Eqn 4.6). The problem becomes one of estimating the quadratic parameters $\{a, b, c\}$ which are

deterministically related to $\{C, \mu, \sigma\}$ by Eqn 4.7.

$$h(q) = C \exp \left\{ \frac{-(q - \mu)^2}{2\sigma^2} \right\} \quad (4.5)$$

$$\ln [h(q)] = \ln [C] - \frac{(q - \mu)^2}{2\sigma^2} \quad (4.6)$$

$$= \underbrace{\ln(C)}_a - \underbrace{\frac{\mu^2}{2\sigma^2}}_b + \underbrace{\frac{\mu}{\sigma^2}}_c q + \underbrace{\frac{-1}{2\sigma^2}}_c q^2$$

$$\mu = \frac{-b}{2c} \quad \sigma = \sqrt{\frac{-1}{2c}} \quad C = \exp \left\{ a - \frac{b^2}{4c} \right\} \quad (4.7)$$

The advantage of using this method over sample statistics is the ability to accommodate non-symmetric data and to algorithmically diminish the importance of outliers. Using iterative weighted least-squares estimation to determine the quadratic parameters, the effect of outlying points can be scaled down. The iterative method presented by (Guo, 2011) for solving for the parameters $\{a, b, c\}$ from Eqn 4.7 was implemented. The method iteratively estimates $\{a, b, c\}$ and uses these values to calculate $h_{(k)}$ by Eqn 4.6. The system of equations is given by Eqn 4.8 where \hat{h} represents the noisy histogram values and $h_{(k)}$ represents the estimated weighted histogram values at the k -th iteration. Parameter estimation can be considered complete after a maximum set of iterations, K , or after some convergence criterion is met.

$$\begin{bmatrix} \sum h_{(k-1)}^2 & \sum q h_{(k-1)}^2 & \sum q^2 h_{(k-1)}^2 \\ \sum q h_{(k-1)}^2 & \sum q^2 h_{(k-1)}^2 & \sum q^3 h_{(k-1)}^2 \\ \sum q^2 h_{(k-1)}^2 & \sum q^3 h_{(k-1)}^2 & \sum q^4 h_{(k-1)}^2 \end{bmatrix} \times \begin{bmatrix} a_{(k)} \\ b_{(k)} \\ c_{(k)} \end{bmatrix} = \begin{bmatrix} \sum h_{(k-1)}^2 \ln(\hat{h}) \\ \sum q h_{(k-1)}^2 \ln(\hat{h}) \\ \sum q^2 h_{(k-1)}^2 \ln(\hat{h}) \end{bmatrix} \quad (4.8)$$

$$\text{where } h_{(k)} = \begin{cases} \hat{h} & \text{for } k = 0 \\ \exp \{ a_{(k)} + b_{(k)}q + c_{(k)}q^2 \} & \text{for } k > 0 \end{cases}$$

Once reliable estimates are found for the quadratic parameters, Eqn 4.7 is used to calculate the estimated $\{C, \mu, \sigma\}$ which best parametrize $h(q)$. Of these, the values of interest are $\{\mu, \sigma\}$, which fully describe the Gaussian distribution from which \vec{y} are drawn. These points can then be transformed into a target Gaussian distribution $T \sim \mathcal{N}(\mu_{target}, \sigma_{target})$ using Eqn 4.9.

$$Z = \frac{Y - \mu}{\sigma} = \frac{T - \mu_{target}}{\sigma_{target}} \quad \Rightarrow \quad T = \underbrace{\frac{\sigma_{target}}{\sigma}}_{\alpha} Y + \underbrace{\mu_{target} - \frac{\sigma_{target}}{\sigma} \mu}_{\beta} \quad (4.9)$$

Samples from \vec{y} can then be transformed into a new domain $\vec{t} = \alpha \vec{y} + \beta$ in which the samples have a Gaussian distribution with target mean and variance $\{\mu_{target}, \sigma_{target}^2\}$. This transformation allows for systematic data visualization within a specific range (for instance between $[-3\sigma_{target}, 3\sigma_{target}]$) as well as mapping data with vastly different dynamic ranges into a similar intensity space. It should be noted that this transformation alone does not preserve the log-normality of the data since \vec{t} is a Gaussian distribution. Typical values used for Gaussian representation and visualization of the data are $\mu_{target} = 0$ and $\sigma_{target} = 1$.

The data can also be exponentiated to follow a log-normal distribution with defined properties. These properties are enforced by indicating intensity targets for specific points in the cumulative distribution function (CDF) of the log-normal distribution. The CDF of a log-normal distribution is given by Eqn 4.10 and the relationship between the underlying Gaussian distribution of the log-normal data and the log-normal distribution mean u and standard deviation v is given by Eqn 4.11. Letting $\vec{\ell}$ be the exponentiated samples from \vec{t} , the values for μ_{target} and σ_{target} necessary to achieve a specific log-normal behavior in the transformed domain can be calculated. Using the relationship between $\{\mu, \sigma\}$ and $\{u, v\}$, a pair of target intensity values with corresponding target CDF values are indicated: $(\ell_1, F_L(\ell_1)), (\ell_2, F_L(\ell_2))$. The

$\{\mu_{target}, \sigma_{target}\}$ values necessary to achieve these $(\ell_1, F_L(\ell_1)), (\ell_2, F_L(\ell_2))$ values can be solved for using Eqn 4.12. Transformed log-normal samples can be generated then by $\vec{\ell} = \exp\{\alpha \vec{y} + \beta\}$. In the function, target intensity and CDF pairs are (50, 0.5), (254.5, 0.9995) such that the resulting log normal distribution is spread mainly over the range of 8-bit intensity values (ie [0, 255]). The values needed to achieve these properties in $\vec{\ell}$ are $\mu_{target} = 3.912$ and $\sigma_{target} = 0.4945$.

$$F_X(x; \mu, \sigma) = \frac{1}{2} + \frac{1}{2} \operatorname{erf} \left[\frac{\ln x - \mu}{\sqrt{2}\sigma} \right] \quad (4.10)$$

$$\mu = \ln \left(\frac{u}{\sqrt{1 + v/u^2}} \right) \quad \sigma = \sqrt{\ln(1 + v/u^2)} \quad (4.11)$$

$$\sigma_{target} = \frac{\ln(\ell_1) - \ln(\ell_2)}{\sqrt{2} \left[\operatorname{erf}^{-1}(2F_L(\ell_1) - 1) - \operatorname{erf}^{-1}(2F_L(\ell_2) - 1) \right]} \quad (4.12)$$

$$\mu_{target} = \ln(\ell_1) - \sqrt{2}\sigma_{target} \operatorname{erf}^{-1}(2F_L(\ell_1) - 1)$$

The stepwise channel equalization procedure is explained below with results from intermediate steps shown in Fig. 4-14.

1. Given the i -th channel of data for the τ -th type, define a vector:

$$\vec{x} = \operatorname{vec} \left(I_\tau^{(i)} \cap \{M_\tau = \text{sample}\} \right) \quad \text{Fig. 4-14(a)}$$

- (a) Limit the dynamic range of the data and exclude data where $x = 0$

A histogram of these data is shown in Fig. 4-14(b).

2. Take the natural log to yield data which are assumed to be normally distributed:

$$\vec{y} = \ln(\vec{x}) \quad \text{Fig. 4-14(c)}$$

3. Create a B -binned histogram of $\vec{y} \Rightarrow \vec{h}$ (Fig. 4-14(d))

4. Estimate the parameters $\{a, b, c\}$ from the data \vec{h} using the iterative weighted

least squares estimation method (magenta curve in Fig. 4·14(d))

5. Use the estimated values to compute the parameters of the Gaussian curve $\{C, \mu, \sigma\}$
6. Define a target mean and standard deviation for the transformed distribution and compute the transformed data vector:

$$\vec{t} = \frac{\sigma_{target}}{\sigma} \vec{y} + \mu_{target} - \frac{\sigma_{target}}{\sigma} \mu$$

A histogram of these data is shown in Fig. 4·14(f).

7. To compute a transformed image which maintains a log-normal distribution, then exponentiate \vec{t}

$$\vec{\ell} = \exp \{ \vec{t} \}$$

A histogram of these data is shown in Fig. 4·14(e).

The advantage of using MIMS channel equalization is that raw data whose intensity ranges are dramatically different can be mapped into a normalized space where pixel values can be considered more equally. As shown in Fig. 4·15, different channels of a MIMS image may have very different intensity distributions and dynamic ranges. By conducting channel equalization, the ranges of the data can be fixed and compared more directly than in the raw data's original domain. Similarly, channel data which come from the same isotope but from different samples may have significant scale factor differences, as shown in Fig. 4·16. Once channel equalization is performed, the data ranges and intensity characteristics are transformed to have similar intensity distributions.

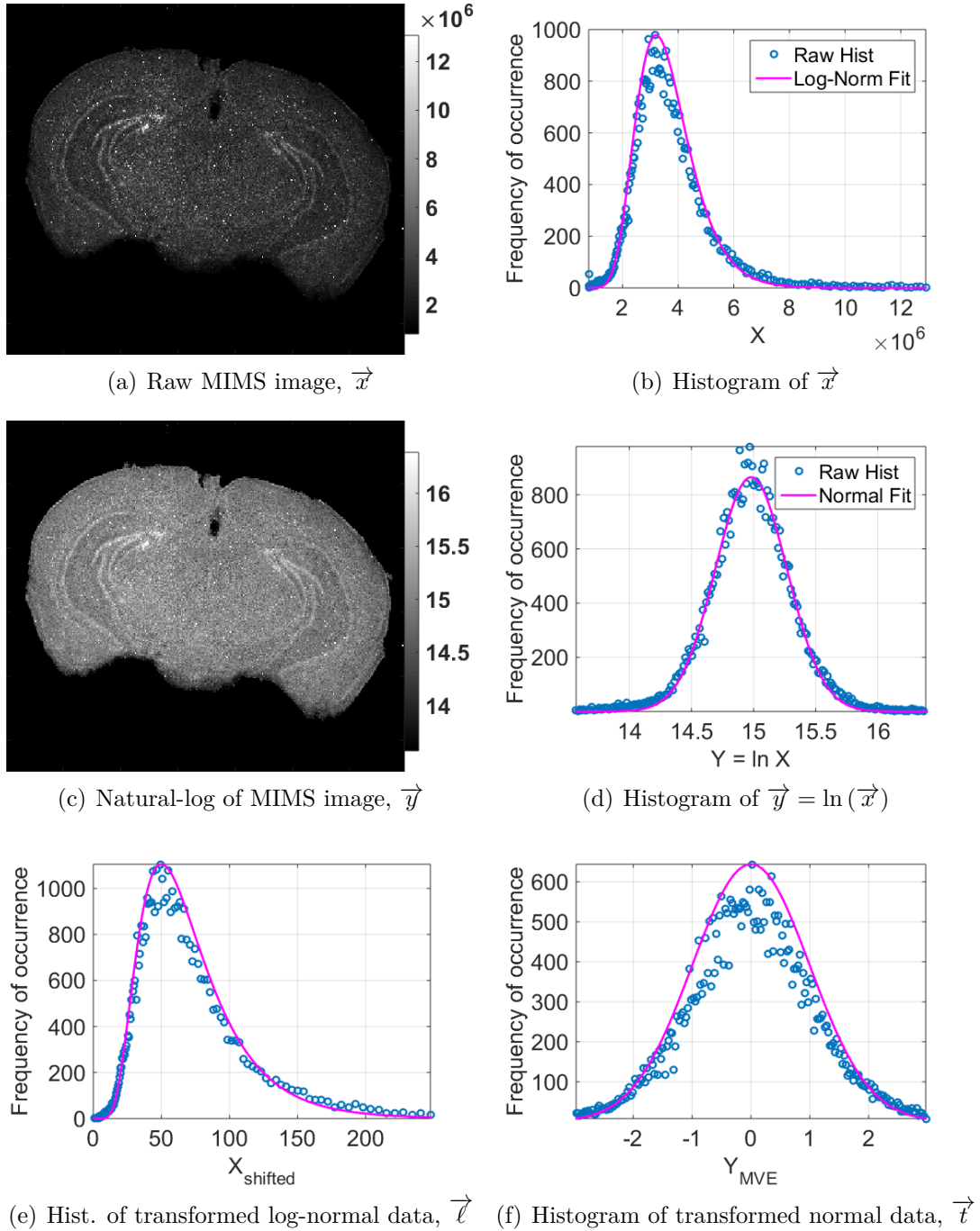


Figure 4-14: Images and histograms of raw log-normal MIMS data and their transformations

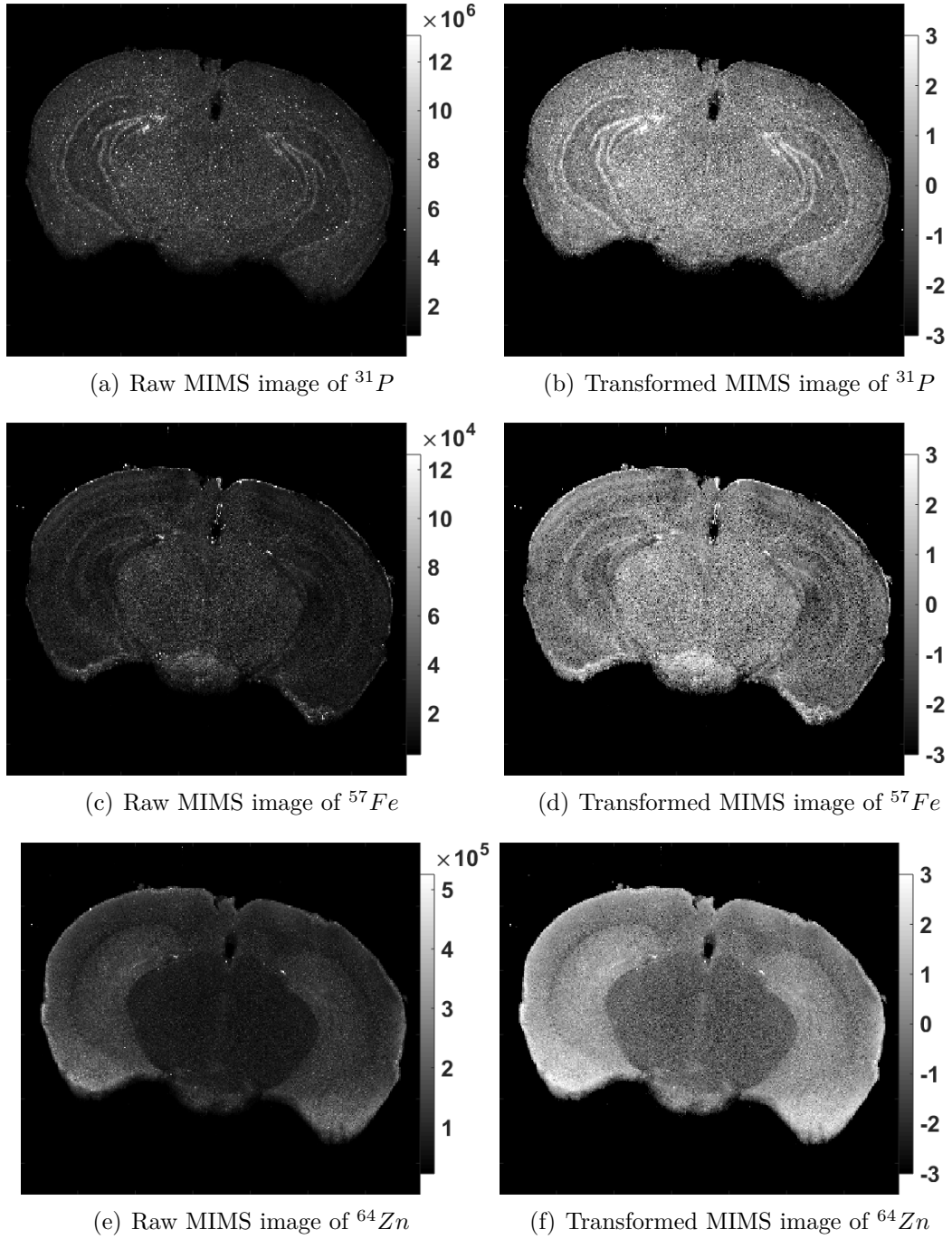


Figure 4.15: Channel equalization for comparing different channels within one MIMS image \bar{I}_τ in a normalized intensity domain.

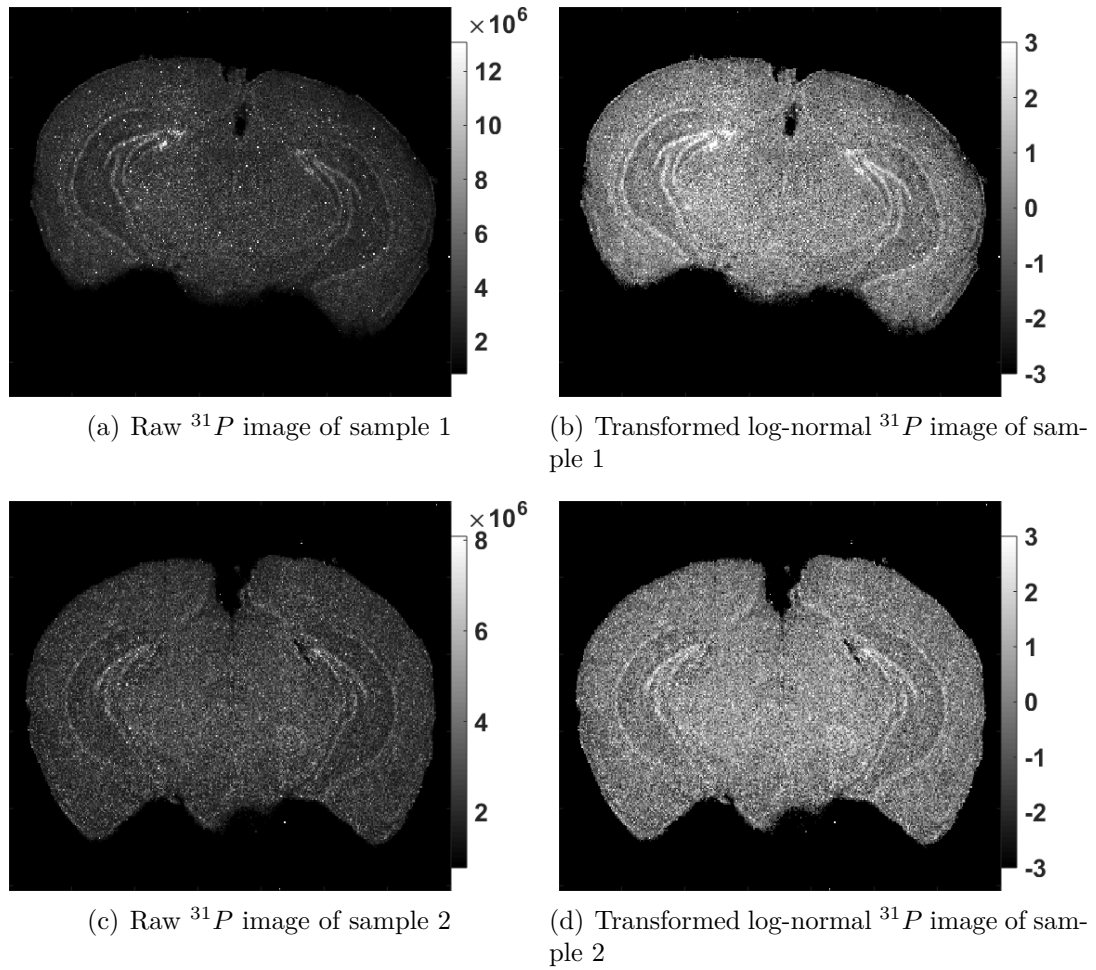


Figure 4.16: Channel equalization for comparing images between subjects.

4.5 Multi-modal Image Registration

Images of the brain provide essential information for the characterization of neuropathology. Various staining methods are used to probe distinct tissue features and provide unique insight for diagnosing brain abnormalities. In the context of this work, an imaging modality refers to a technique which captures a specific set of qualities associated with the object being imaged. In order to systematically analyze the same regions of the brain across distinct imaging modalities and across distinct individuals, image alignment is required. Image registration is a necessary first step to a deeper analysis of a database of brain images. The goals of image registration for using MIMS to inform TBI neuropathology are as follows:

1. *Multi-modal image comparison:* to enable objective, automated tissue segmentation by registering an already segmented template image to an unsegmented image. The segmentation of the template image can then be used to define regions in the unlabeled image. One such example would be the registration of an atlas image to a multi-channel MIMS as shown in Fig. 4-25(f).
2. *Multi-subject image comparison:* to directly enable between-sample comparisons by registering two similar images from two distinct samples to each other

Image registration between two images of the same modality is typically conducted by determining deformation parameters which minimize the difference between two images. Typically, a metric based on mean-squared error or correlation is used. While these measures work well for images whose feature properties are positively correlated, images with potentially uncorrelated but probabilistically related characteristics require a measure which incorporates these types of relationships. The idea of applying mutual information (MI) as the cost function for multi-modal image registration is

credited to Maes et al. (1997) and Wells et al. (1996). Both papers deal with rigid registration between magnetic resonance images and computed tomography scans. While these modalities are spatially three-dimensional, they are scalar valued. Other literature has examined deformable registration between two 2-D images using MI (Avants et al., 2008), but again this application was developed for 2-D, scalar-pixelated images. Utilization of MI for multi-modal, multi-channel 2-D images has not yet been developed, to the best of my knowledge.

One of the unique challenges posed by MIMS is the ability to simultaneously acquire data for multiple metallomic signals. Like an RGB photographic image (PI) with three channels, MIMS are d -channel images with each channel containing distinct information about the metallomic content of the brain. Most state-of-the-art registration algorithms consider single-channel images (similar to a luminance or grayscale image). Therefore, cost functions which accommodate multiple channels are not well documented.

4.5.1 Problem Formulation & Assumptions

Image registration is a method used to align two images by means of a spatial transformation. Typically, a parametric model defines this transformation and this model's parameters are estimated by minimizing a defined cost function. An image registration procedure requires definition of the following elements:

- a transformation model g parametrized by $\vec{\mu}$ which operates on the position coordinates $\vec{p} \Rightarrow g_{\vec{\mu}}(\vec{p})$
- a cost function or similarity metric which outputs a scalar value indicating the relationship between the two input arguments C and $D \Rightarrow S(C, D)$
- an optimization method for minimizing the cost function

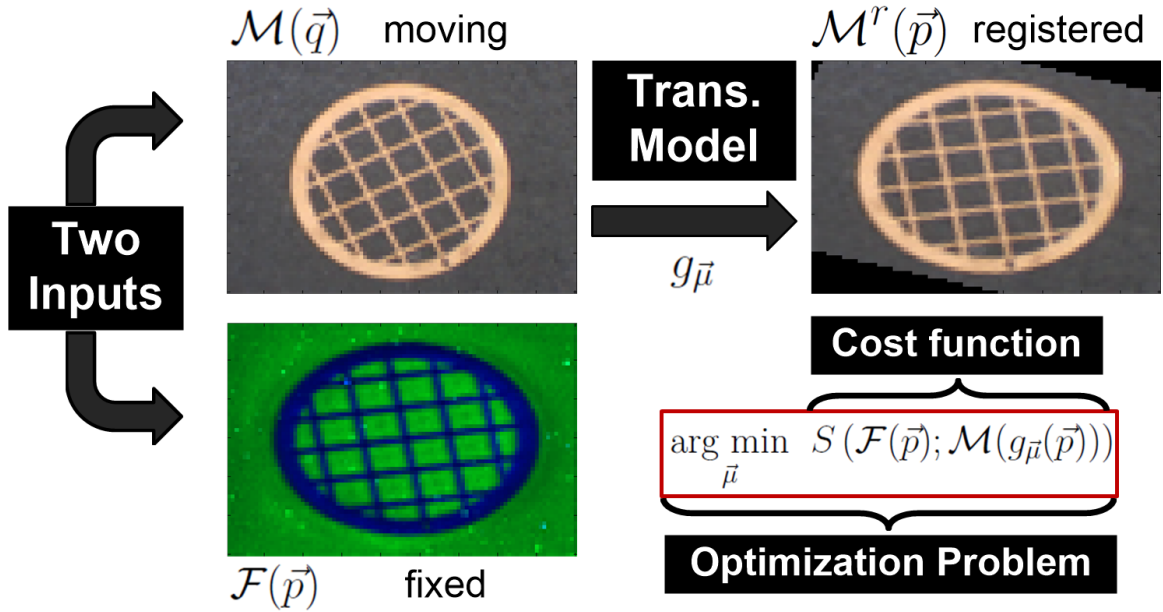


Figure 4-17: Overview of functions and parameters required to perform image registration

Using these definitions, the optimization problem for the registration of two images $\mathcal{F}(\vec{p})$ and $\mathcal{M}(\vec{q})$ can be written as follows:

$$\hat{\vec{\mu}} = \arg \min_{\vec{\mu}} S[\mathcal{F}(\vec{p}), \mathcal{M}(g_{\vec{\mu}}(\vec{p}))] \quad (4.13)$$

Figure 4-17 shows generally how the input images, transformation model, and cost function relate. Precise parameter and function definitions will be provided in subsequent sections.

In this work, the data are two images with corresponding but not necessarily identical features. These images may have scalar (grayscale, single-valued) or vector (such as red-green-blue, multiple isotope channels) values at each pixel location. Exemplary results for uni-modal (ground-truth PI) and multi-modal image pairs are presented in Section 4.5.5. The end goal of the described image registration function is to register label-free images to a segmented (or easily segmentable) template image, as

in Fig. 4.25(f). The image registration method uses a six-parameter affine transformation model with bicubic interpolation for transformations requiring off-grid image values. Optimal registration is determined by minimization of negative mutual information using simulated annealing as the optimization method.

4.5.2 Affine Transformation Model

Let the fixed (reference) image be denoted by $\mathcal{F}(\vec{p})$ defined on coordinates $\vec{p} = [i, j, 1]^T \in \mathbb{Z}^3$ and the moving (target) image be denoted by $\mathcal{M}(\vec{q})$ defined on coordinates $\vec{q} \in \mathbb{Z}^3$. At each pixel location, the image value could be a scalar or a vector. The moving image registered to the fixed image coordinate space will be denoted as $\mathcal{M}^r(\vec{p})$. Given that $\mathcal{F}(\vec{p})$ and $\mathcal{M}(\vec{q})$ are observed, we can define the relationship between $\mathcal{M}^r(\vec{p})$ and $\mathcal{M}(\vec{q})$ as follows:

$$\mathcal{M}^r(\vec{p}) = \phi \left\{ \mathcal{M} \left(g_{\vec{\mu}}(\vec{p}) \right) \right\} \quad \Leftrightarrow \quad \mathcal{M}(\vec{q}) = \phi \left\{ \mathcal{M}^r \left(g_{\vec{\mu}}^{-1}(\vec{q}) \right) \right\} \quad (4.14)$$

where $g_{\vec{\mu}}$ denotes the transformation function parametrized by $\vec{\mu}$. The transformation $g_{\vec{\mu}}(\vec{p}) = \vec{w} = [u, v, 1]^T \in \mathbb{R}^3$ generally specifies non-integer grid locations in \mathcal{M} . The values of $\mathcal{M}(\vec{w})$ are calculated using a bicubic interpolator $\phi\{\cdot\}$.

For the images being compared in this thesis, at least translation, rotation and scaling are required to adequately describe the image transformations needed to register image pairs. For completeness, the full six-parameter affine transformation model, represented as a 3×3 matrix $A_{\vec{\mu}}$, is used. It linearly operates on the position coordinates \vec{p} according to Eqn 4.15. The goal of registration is to determine the affine parameters $\vec{\mu}$ which minimize the differences between the two input images according to the defined cost function. The affine transformation matrix $A_{\vec{\mu}}$ is a combination of four geometric transformations: translation (in x and y), rotation, skew and scaling (in x

and y). The relationship between the geometric parameters $\vec{\mu} = \{t_x, t_y, \theta, s_x, s_y, s_k\}$ and the transformation parameters $\vec{a} = [a_1, a_2, a_3, a_4, a_5, a_6]^T$, as well as the individual geometric transform matrices are given in Eqn 4.16. Note that $A_{\vec{\mu}}$ is the result of a matrix product; therefore, the order of the geometric transformations is not commutative.

$$\vec{w} = A_{\vec{\mu}} \cdot \vec{p} \Rightarrow \begin{bmatrix} u \\ v \\ 1 \end{bmatrix} = \begin{bmatrix} a_1 & a_2 & a_3 \\ a_4 & a_5 & a_6 \\ 0 & 0 & 1 \end{bmatrix} \begin{bmatrix} i \\ j \\ 1 \end{bmatrix} \quad (4.15)$$

$$\begin{aligned} A_{\vec{\mu}} &= \left(\underbrace{\begin{bmatrix} 1 & 0 & t_x \\ 0 & 1 & t_y \\ 0 & 0 & 1 \end{bmatrix}}_{\text{translation}} \cdot \underbrace{\begin{bmatrix} \theta_c & -\theta_s & 0 \\ \theta_s & \theta_c & 0 \\ 0 & 0 & 1 \end{bmatrix}}_{\text{rotation}} \cdot \underbrace{\begin{bmatrix} 1 & s_k & 0 \\ 0 & 1 & 0 \\ 0 & 0 & 1 \end{bmatrix}}_{\text{skew}} \cdot \underbrace{\begin{bmatrix} s_x & 0 & 0 \\ 0 & s_y & 0 \\ 0 & 0 & 1 \end{bmatrix}}_{\text{scaling}} \right) \\ &= \begin{bmatrix} s_x \cos(\theta) & s_y(s_k \cos(\theta) - \sin(\theta)) & t_x \\ s_x \sin(\theta) & s_y(s_k \sin(\theta) + \cos(\theta)) & t_y \\ 0 & 0 & 1 \end{bmatrix} = \begin{bmatrix} a_1 & a_2 & a_3 \\ a_4 & a_5 & a_6 \\ 0 & 0 & 1 \end{bmatrix} \quad (4.16) \end{aligned}$$

where

t_x = positive value shifts image to the left

t_y = positive value shifts image up

θ = rotation angle, measured counter-clockwise from the x -axis

($\theta_c = \cos(\theta)$ and $\theta_s = \sin(\theta)$)

- s_x = change of scale in x direction
 s_y = change of scale in y direction
 s_k = shear factor along the x -axis = $\tan(\omega)$

(ω = the skew angle, measured clockwise from the y -axis)

4.5.3 Mutual Information Similarity Metric

Mutual information (MI) is well suited for multi-modal image registration since it enforces no functional relationship between the spatially corresponding intensity values in the two images. The definition for the MI between two discrete random variables X , taking values x_i for $i = 1, \dots, n$, and Y , taking values y_j for $j = 1, \dots, m$, is given in Eqn 4.17.

$$J(X; Y) = \sum_{i=1}^n \sum_{j=1}^m p_{X,Y}(x_i, y_j) \ln \left(\frac{p_{X,Y}(x_i, y_j)}{p_X(x_i)p_Y(y_j)} \right) \quad (4.17)$$

To compute the MI between \mathcal{F} and \mathcal{M}^r , a joint density function (JDF) of co-occurring intensity values in the two images must be approximated. Kernel density estimation (KDE) will be used to approximate the JDF.

Define the image \mathcal{F} as an $(M \times N \times d_{\mathcal{F}})$ matrix of values and the image \mathcal{M}^r as an $(M \times N \times d_{\mathcal{M}})$ matrix of values. Let the vectorized image \mathcal{F} be denoted as $\vec{X} = \{\vec{X}^{(1)}, \vec{X}^{(2)}, \dots, \vec{X}^{(d_{\mathcal{F}})}\} \in \mathbb{R}^{M \cdot N \times d_{\mathcal{F}}}$, and the vectorized image \mathcal{M}^r be denoted as $\vec{Y} = \{\vec{Y}^{(1)}, \vec{Y}^{(2)}, \dots, \vec{Y}^{(d_{\mathcal{M}})}\} \in \mathbb{R}^{M \cdot N \times d_{\mathcal{M}}}$, where in both cases each $(M \cdot N \times 1)$ column-vector corresponds to data from a single channel in the image and each row corresponds to the vector associated with a given spatial location. In order to simplify the notation for approximating the JDF $p(\vec{X}, \vec{Y})$, the matrices from the two images are concatenated a single matrix $\vec{Z} = [\vec{X}, \vec{Y}] \in \mathbb{R}^{M \cdot N \times (d_{\mathcal{F}} + d_{\mathcal{M}})}$. A schematic of the formation of \vec{Z} is provided in Fig. 4-18, where $i \in [1, d_{\mathcal{F}} + d_{\mathcal{M}}]$ indicates the column

of \vec{Z} and $c \in [1, M \cdot N]$ indicates the row, which corresponds to a pixel location in the original image space. Using this notation, KDE may be performed to approximate $p(\vec{Z})$ using each row of \vec{Z} as an $(d_{\mathcal{F}} + d_{\mathcal{M}})$ -dimensional data point.

For each column of \vec{Z} ($i \in [1, d_{\mathcal{F}} + d_{\mathcal{M}}]$), the following definitions are used (see Fig. 4-19):

- $\mathcal{R}^{(i)} = [b_{min}^{(i)}, b_{max}^{(i)}]$: the allowable range of pixel values in the i -th channel
- $K^{(i)}$: integer indicating the maximum number of bins used to quantize $\mathcal{R}^{(i)}$
- $k^{(i)} \in [1, K^{(i)}]$: integer which refers to the quantization bin number, called the *quantization index*
- $\Delta b_{\mathcal{R}}^{(i)} = \frac{b_{max}^{(i)} - b_{min}^{(i)}}{K^{(i)}}$: the distance between bin centers in the channel's pixel value space
- $z_{k^{(i)}}^{(i)} = b_{min}^{(i)} + \left(k^{(i)} - \frac{1}{2}\right) \Delta b_{\mathcal{R}}^{(i)}$: quantization index center in the channel's pixel value space. Typically called a *bin center*.
- $\mathcal{K}^{(i)}(u)$: kernel function. Any kernel function may be used as long as $\int_{-\infty}^{\infty} \mathcal{K}^{(i)}(u) du = 1$. Some examples of typical kernels are given in Table 4.3
- $h^{(i)} = \hat{\sigma} \cdot 2 \left(\frac{\pi^{1/2} (\nu!)^3 R(\mathcal{K})}{2\nu(2\nu)! \kappa_{\nu}^2(\mathcal{K})} \right)^{1/(2\nu+1)} (M \cdot N)^{-1/(2\nu+1)}$: kernel bandwidth. Computed using Silverman's rule of thumb given in (Hansen, 2009). ν is the kernel order and $\hat{\sigma}$ is the sample standard deviation. All parameters needed to compute h are given in Table 4.3.

For a d -channel image with $K^{(i)} = V \forall i$, there are V^d possible combinations of quantization indices. Let these combinations be indexed by n and let the kernel functions be separable such that $\mathcal{K}(u^{(1)}, u^{(2)}, \dots, u^{(d)}) = \prod_{i=1}^d \mathcal{K}(u^{(i)})$. The KDE of $p(\vec{z})$ is then given by:

$$p(n) = p\left(z_{k^{(1)}}^{(1)}, z_{k^{(2)}}^{(2)}, \dots, z_{k^{(d_{\mathcal{F}}+d_{\mathcal{M}})}}^{(d_{\mathcal{F}}+d_{\mathcal{M}})}\right) = \alpha \sum_{c=1}^{M \times N} \prod_{i=1}^{d_{\mathcal{F}}+d_{\mathcal{M}}} \mathcal{K}^{(i)}\left(\frac{Z_c^{(i)} - z_{k^{(i)}}^{(i)}}{h^{(i)}}\right) \quad (4.18)$$

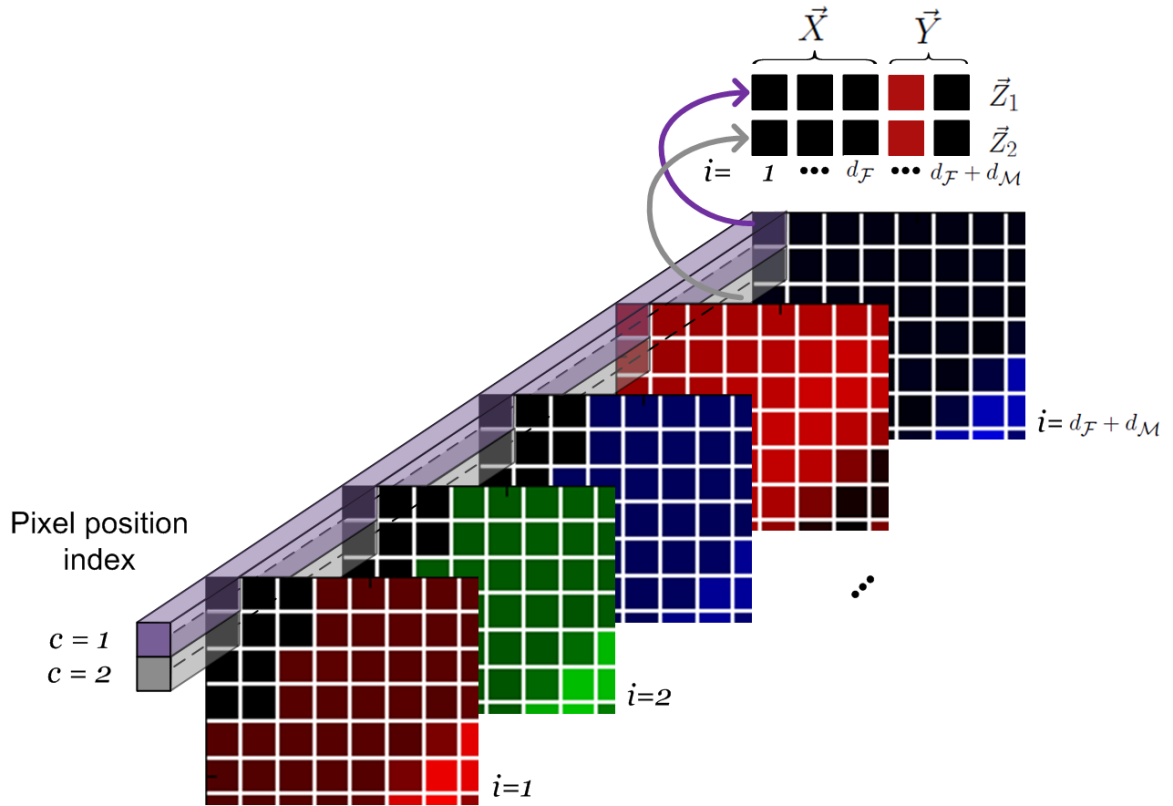


Figure 4-18: Construction of joint observations variable \vec{Z} for computing the probability function $p(\vec{Z})$

where α is a normalizing factor which ensures that the $\sum_{n=1}^{V^d} p(n) = 1$ and the value of n references the appropriate values of $k^{(i)}$ which can easily be mapped back to the pixel value space.

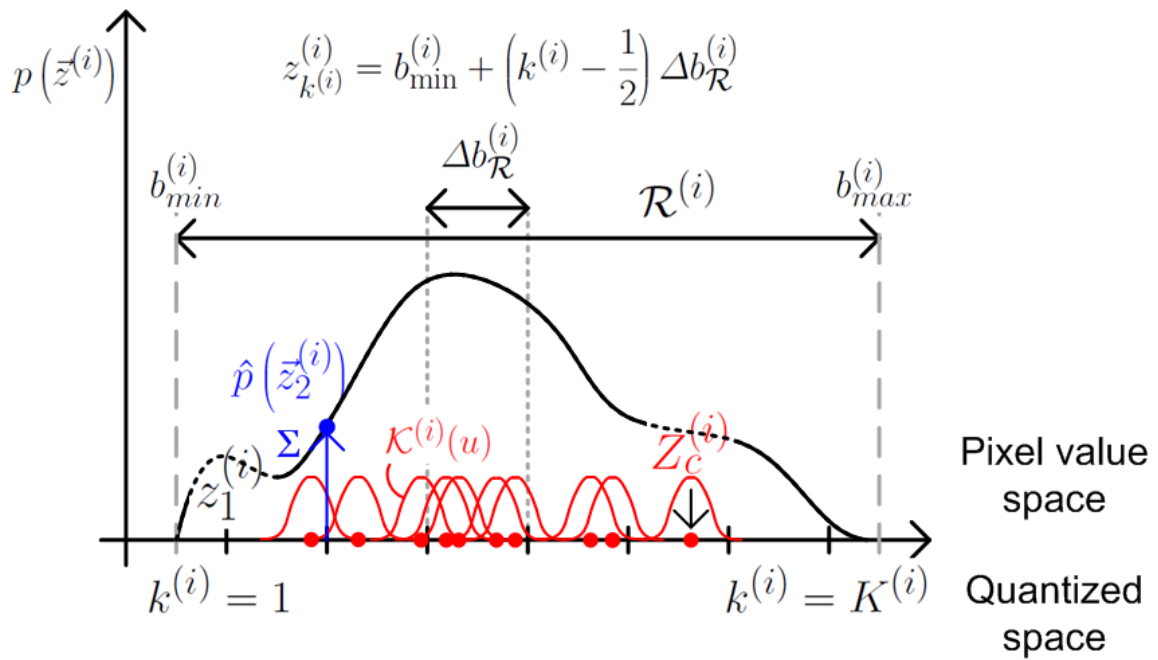


Figure 4-19: Visualization of KDE notation with floating point, pixel value space represented above the horizontal axis and quantized integer space represented below. KDE can be thought of as “dropping” a kernel (red curves) at each data point value (red points), then summing the normalized contribution of all the kernels dropped for all data points to determine the probability at a given point (blue arrow and text).

Table 4.3: Representative Kernels and their relevant parameters for KDE (Hansen, 2009). The last two columns give the values needed to compute the kernel bandwidth using the Silverman's rule of thumb method.

	$\mathcal{K}(u)$	$\kappa_2(\mathcal{K}) = \int u^2 \mathcal{K}(u) du$	$R(\mathcal{K}) = \int \mathcal{K}^2(u) du$
Rectangular	$\frac{1}{2} \mathbb{1}_{\{ u \leq 1\}}$	1/3	1/2
Triangular	$(1 - u) \mathbb{1}_{\{ u \leq 1\}}$	1/6	2/3
Epanechnikov	$\frac{3}{4} (1 - u^2) \mathbb{1}_{\{ u \leq 1\}}$	1/5	3/5
Quartic	$\frac{15}{16} (1 - u^2)^2 \mathbb{1}_{\{ u \leq 1\}}$	1/7	5/7
Triweight	$\frac{35}{32} (1 - u^2)^3 \mathbb{1}_{\{ u \leq 1\}}$	1/9	350/429
Tricube	$\frac{70}{81} (1 - u ^3)^3 \mathbb{1}_{\{ u \leq 1\}}$	35/243	175/247
Gaussian (ϕ)	$\frac{1}{\sqrt{2\pi}} \exp\left\{-\frac{1}{2}u^2\right\}$	1	$1/(2\sqrt{\pi})$
3 rd order B-spline	$\frac{1}{6} (4 - 6u^2 + 3 u ^3) \mathbb{1}_{\{ u < 1\}} + \frac{1}{6} (2 - u)^3 \mathbb{1}_{\{1 < u \leq 2\}}$	1/3	151/315

Once the joint density estimate is computed, the marginals can be computed by summing along the channels that depend on the other image:

$$p(\vec{x}) = \sum_{i=d_{\mathcal{F}}+1}^{d_{\mathcal{F}}+d_{\mathcal{M}}} \sum_{z^{(i)} \in \mathcal{R}^{(i)}} p(\vec{z}) \quad p(\vec{y}) = \sum_{i=1}^{d_{\mathcal{F}}} \sum_{z^{(i)} \in \mathcal{R}^{(i)}} p(\vec{z}) \quad (4.19)$$

Using these probability function estimations and the above definitions, Eqn 4.17 can be used to compute the MI between \mathcal{F} and \mathcal{M}^r giving:

$$J(\vec{X}; \vec{Y}) = \sum_{\vec{x} \in \mathcal{R}_X} \sum_{\vec{y} \in \mathcal{R}_Y} p(\vec{x}, \vec{y}) \ln \left(\frac{p(\vec{x}, \vec{y})}{p(\vec{x}) \cdot p(\vec{y})} \right) \quad (4.20)$$

4.5.4 Optimization

The optimal parameters of the transformation, $\hat{\vec{\mu}}$, are determined according to the maximization of mutual information as follows:

$$\hat{\vec{\mu}} = \arg \min_{\vec{\mu}} S(\vec{\mu}) = \arg \min_{\vec{\mu}} -J(\mathcal{F}(\vec{p}); \mathcal{M}(A_{\vec{\mu}} \cdot \vec{p})) \quad (4.21)$$

Simulated annealing (SA) is used to solve the optimization problem since this method is easy to implement, requires relatively few tuning parameters, and requires no a priori knowledge of the cost function (derivative is not required) (Ingber, 1993; Chen and Luk, 1999). SA is also attractive since it theoretically guarantees convergence to the global minimum (with infinite time). As the name suggests, SA algorithmically mimics the physical process of metal annealing and is used in condensed matter physics to analyze the properties of a large number of atoms (Kirkpatrick et al., 1983).

Broadly, SA works by attempting to find the state ($\vec{\mu}_{best}$) of lowest energy (minimum) according to a metric ψ . During each iteration, SA generates a new state $\vec{\mu}_t$ and

evaluates the state's energy $\psi_t = S(\vec{\mu}_t) = -J(\mathcal{F}(\vec{p}); \mathcal{M}(A_{\vec{\mu}_t} \cdot \vec{p}))$. The state is then considered for acceptance based on how the new energy compares to the previous energy ($\Delta E = \psi_t - \psi_{t-1}$). If the energy of the new state is less than the previous state's, then the new state is accepted. If the new state's energy is greater, then it is accepted with some probability. The algorithm is repeated until some user defined limit is reached (usually maximum number of iterations is reached or changes in the state or of the cost fall below some threshold). By occasionally accepting solutions that are "worse" according to $S(\vec{\mu}_t)$, this optimization strategy is less sensitive to local optima and is faster and more flexible than an exhaustive search method.

Figure 4.20 depicts a functional block representation of SA in the context of image registration. To perform optimization by SA, a state generating function (Eqn 4.23), a cost function (Eqn 4.20), an acceptance function (Eqns 4.24,4.25) and an annealing schedule (Eqn 4.22) must be defined. The user specifies an initial temperature (T_0), an initial state ($\vec{\mu}_0$), and a definition of the state space (bounds on the state space).

The SA procedure works to minimize the energy associated with the d -dimensional state vector $\vec{\mu}$ by semi-randomly exploring the state space according to the defined state generating function (Eqn 4.23). At the beginning of each iteration t , a new parameter vector $\vec{\mu}_t$ is generated by taking a temperature-sized step away from the previous state vector. The new state $\vec{\mu}_t$ is then applied to the moving image to create $\mathcal{M}^r(A_{\vec{\mu}_t} \cdot \vec{p})$. Next, the energy or cost function, ψ_t , is computed (Eqn 4.20) and sent to the acceptance function for evaluation (Eqns 4.24 and 4.25). If the energy decreases, the state will automatically be accepted (Eqn 4.24). If it increases, the new state will be accepted with some probability based on the acceptance function h_{SA} compared to the value of a uniform random variable u . The acceptance function h_{SA} is proportional to T_t and inversely proportional to ΔE (Eqn 4.25). The probability

of accepting the current state given that it increases the energy is proportional to the value of h_{SA} . Therefore, at higher temperatures, the algorithm is more likely to accept states that increase the energy. Also, the greater the increase in energy, the less likely that state is to be accepted. This promotes both exploration of the state space (particularly at the beginning of the optimization process when the temperature is higher) and eventual convergence to an acceptable solution. If the stopping criterion has not been met, the next step is to increase the iteration counter and update the temperature according to the annealing schedule (Eqn 4.22).

Annealing Schedule:	$T_t = T_0 \cdot \tau^t$	(4.22)
State Generating Fctn:	$\vec{y} \sim \mathcal{N}(\vec{0}, \mathbb{I}) \in \mathbb{R}^d$	
	$\bar{y} = \frac{\vec{y}}{\ \vec{y}\ } \sim \mathcal{N}(0, \ \vec{y}\ ^{-2})$	
	$\vec{\mu}_t = \vec{\mu}_{t-1} + T_{t-1}\bar{y} \sim \mathcal{N}(\vec{\mu}_{t-1}, T_{t-1}^2 \cdot \ \vec{y}\ ^{-2})$	(4.23)

Acceptance Fctn:	$\Delta E = \psi_t - \psi_{t-1}$	
------------------	----------------------------------	--

IF	$\Delta E < 0 \Rightarrow$ ACCEPT: $\vec{\mu}_t$	(4.24)
----	---	--------

ELSE	$h_{SA} = \left\{1 + \exp\left(\frac{\Delta E}{T_t}\right)\right\}^{-1}$	(4.25)
------	--	--------

$$u \sim \mathbb{U}(0, 1)$$

IF	$h_{SA} > u \Rightarrow$ ACCEPT: $\vec{\mu}_t$	
----	---	--

ELSE	$h_{SA} < u \Rightarrow$ REJECT: $\vec{\mu}_t = \vec{\mu}_{t-1}$	
------	---	--

In order to perform a thorough search of the state space, reannealing is used. Reannealing will reinitialize the temperature and the state to T_0 and $\vec{\mu}_0$ respectively and essentially re-run the described simulated annealing algorithm. Various criteria my

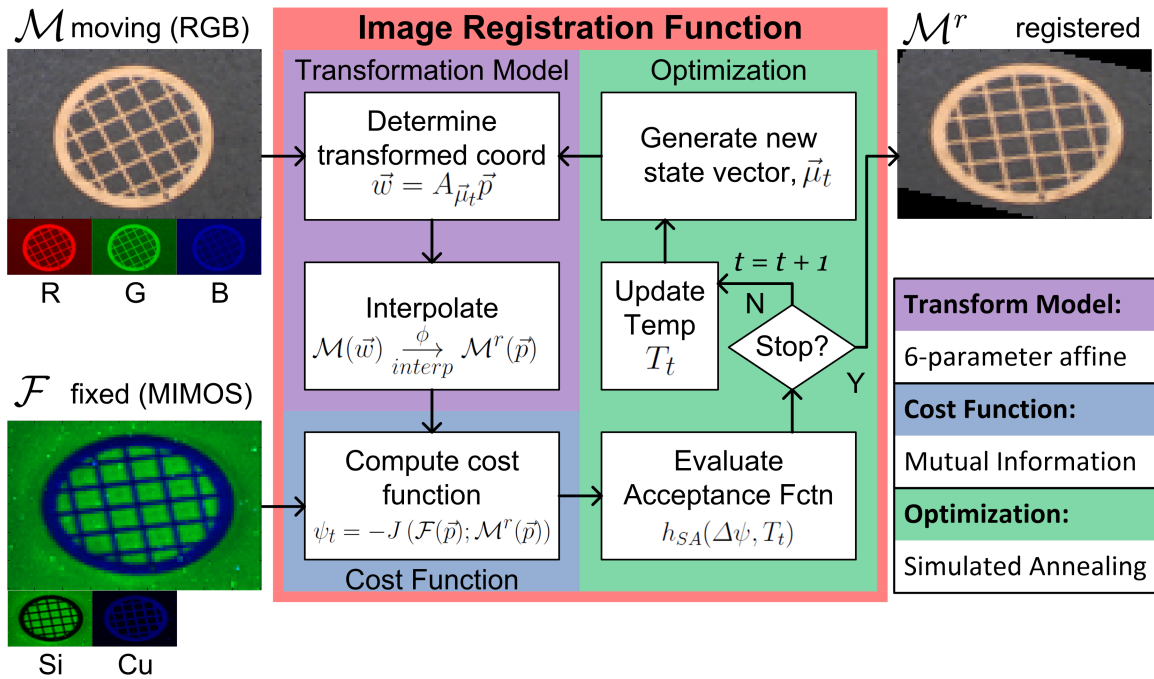


Figure 4-20: Functional block diagram of the image registration function. Each of the functional parts (transformation model, cost function, optimization function) require additional parameterization, but the function can be run with default parameters given two multi-channel images as inputs (one the fixed image and one the moving image). The final output is an optimal set of transformation parameters, $\vec{\mu}_{best}$, which can be used to generate \mathcal{M}^r .

be used to prompt reannealing. In this work, reannealing is triggered once a specified number of states which increase the energy have been accepted. The final output from the SA algorithm is the state vector, $\vec{\mu}_{best}$, which resulted in the minimum ψ over all iterations performed. Figure 4-21 shows a visualization of the various aspects of SA. As a final note, since the transformation parameters are on vastly different scales (translations tend to be much larger than the other parameters, the rotation in radians tends to be much smaller), a scale factor of the state space is introduced so that the state-generating function promotes approximately equal exploration of the range for each state.

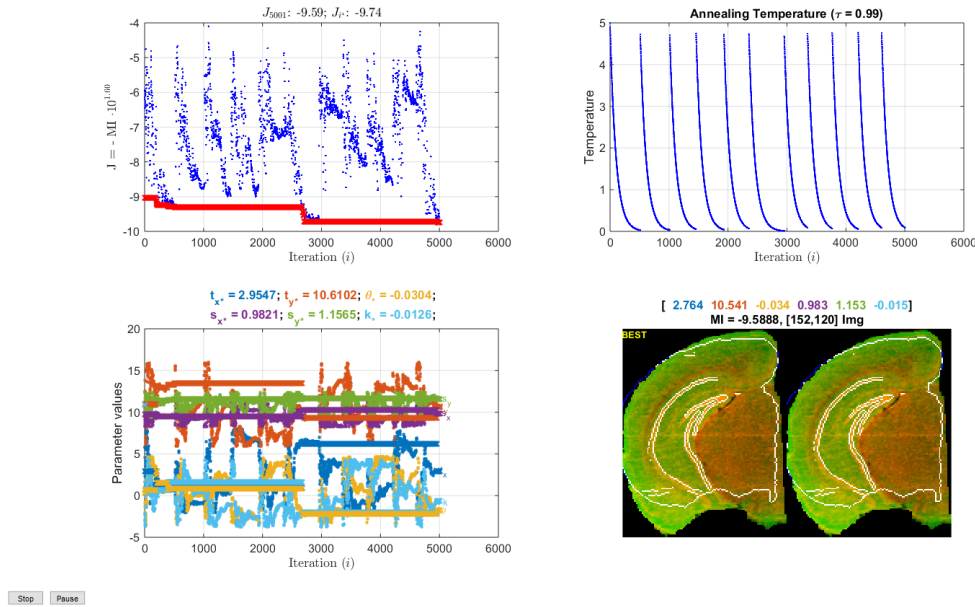


Figure 4-21: Visualization of image registration using simulated annealing. [Top Left] Cost function, $\psi_t = -MI$. [Top Right] Temperature, T_t . [Bottom Left] Plot of the scaled state vector with unscaled values of $\vec{\mu}_{best}$ in the text above the plot. [Bottom Right] Fixed image with $\mathcal{M}(A\vec{\mu}_t \cdot \vec{p})$ edges superimposed with the unscaled $\vec{\mu}$ used to generate \mathcal{M}^r shown above.

4.5.5 Results

For testing the multi-modal, multi-channel image registration (MMMCIR) method, the results from three different image sets whose properties are summarized in Table 4.4 are presented. Due to prohibitive computation time for larger images, all images were first resized such that $\max(M, N) < 100$. For a given experiment, both images were resized to the dimensions shown in the last column of Table 4.4. The images used as inputs for the experiments described are shown in Table 4.6. The results presented were generated using the parameters indicated in Table 4.5. All experimental results were generated using a Dell XPS 8700 computer with a 4th Generation Intel Core i7-4770 processor with 12GB Dual Channel RAM.

These three image pairs enable the testing of registration accuracy (Exp. 1 images), multi-modal capability (Exp. 2 and 3 images), and performance on arbitrary multi-subject registration (Exp. 3 images). The registration results between images of the copper grid in Exp. 1 and 2 can easily be visually evaluated because of the object's rigid and clear structural components. Interpretation of the registration results between images of the mouse hippocampal formation (HPF), while more in line with the objective of the image registration function, requires a degree of domain knowledge. Since the anatomical morphology and cellular structure of this area of the mouse brain is fairly stereotyped, having a pronounced laminar structure, knowledge of organization of these layers in the HPF was used to evaluate the registration results.

Table 4.4: Summary of image pairs used for image registration

Exp. #	Description	\mathcal{F} modality	Original $M_{\mathcal{F}} \times N_{\mathcal{F}}$	\mathcal{M} modality	Original $M_{\mathcal{M}} \times N_{\mathcal{M}}$	Resized $M \times N$
1	Copper grid	Photo	480×718	Photo	480×718	60×90
2	Copper grid	MIMS	73×1597	Photo	480×718	60×90
3	Hippocampus	MIMS	71×216	Atlas	649×1066	41×67

Table 4.5: Experimental parameters used

Symbol	Definition	Function where used	Value
ϕ	interpolator	Transformation model	bicubic
K	# of bins (equal in all dim.)	Cost Function	30
T_0	initial temperature	SA Optimization	5
τ	temperature decay rate	SA Optimization	0.997
c	parameter scale factors	SA Optimization	$[1, 1, 180/\pi, 10, 10, 50]$

Table 4.6: Depiction of images used in the image registration experiments described in Table 4.4. Note that all images are in reality matrices of scalar values which have been pseudo colored in order to enable simultaneous visualization

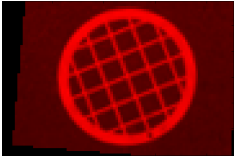
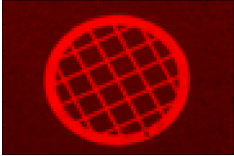

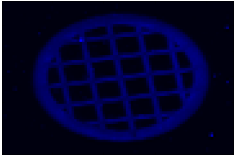
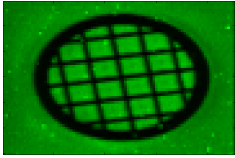
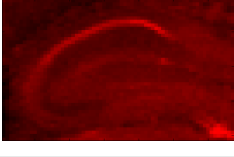
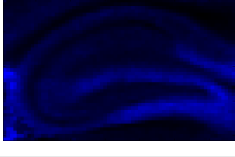
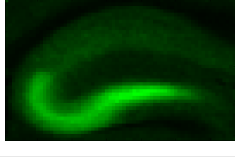

Exp. #	Image type	Channel 1	Channel 2	Channel 3
1	\mathcal{F} Photo	R-channel 		
1, 2	\mathcal{M} Photo	R-channel 	G-channel 	
2	\mathcal{F} MIMS (OES)	$Cu_{\lambda} - 224.7 \text{ nm}$ 	$Si_{\lambda} - 251.6 \text{ nm}$ 	
3	\mathcal{F} MIMS (MS)	^{56}Fe 	^{63}Cu 	^{64}Zn 
3	\mathcal{M} Graphic	Gray-scaled image 		

Table 4.7: Parameters and results for registration between a photograph of a copper grid with itself

$d_{\mathcal{F}}\text{-ch}$	$d_{\mathcal{M}}\text{-ch}$	# iter	hours	\mathcal{K}	ψ_{best}	t_x	t_y	$\vec{\mu}_{best}$				RMSE
								θ (rad)	s_x	s_y	s_k	
Ground Truth Parameters						-4	2	-0.0698	1.05	0.95	0.03	
1 (R)	1 (R)	1.8e4	1.53	norm	-0.8941	-3.9999	2.0026	-0.0705	1.0498	0.9499	0.0305	3.0380
1 (R)	1 (R)	1.8e4	1.21	epan	-0.9013	-3.9966	1.9974	-0.0695	1.0499	0.9498	0.0334	8.3663
1 (R)	2 (R,G)	8065	24.88	norm	-0.9421	-4.0199	1.9939	-0.0673	1.0488	0.9487	0.0380	20.9988

Table 4.8: Parameters and results for registration between a photograph of a copper grid with a MIMS of a copper grid

$d_{\mathcal{F}}\text{-ch}$	$d_{\mathcal{M}}\text{-ch}$	# iter	hours	\mathcal{K}	ψ_{best}	t_x	t_y	$\vec{\mu}_{best}$			
								θ (rad)	s_x	s_y	s_k
1 (Cu)	1 (R)	1.8e4	1.55	norm	-0.6943	-1.0766	1.3665	-0.2702	0.8287	1.0318	0.0597
2 (Cu, Si)	1 (R)	1e4	8.40	epan	-0.8137	-1.0660	1.3692	-0.2680	0.8249	1.0296	0.0552

Table 4.9: Parameters and results for registration between MIMS of the mouse brain with an atlas image

$d_{\mathcal{F}}\text{-ch}$	$d_{\mathcal{M}}\text{-ch}$	# iter	hours	\mathcal{K}	ψ_{best}	t_x	t_y	$\vec{\mu}_{best}$			
								θ (rad)	s_x	s_y	s_k
1 (^{56}Fe)	1 (gray)	1.8e4	0.85	epan	-0.2328	-2.7565	-0.4162	0.0566	1.0728	1.1904	-0.0340
1 (^{63}Cu)	1 (gray)	1.8e4	1.08	epan	-0.2142	-1.2191	0.1650	0.0499	0.9985	1.0394	-0.0109
1 (^{64}Zn)	1 (gray)	1.8e4	—	epan	-0.2028	1.1966	-0.3550	0.0995	1.0815	1.0553	-0.0408
$\sum_{i=1}^3 I^{(i)}$	1 (gray)	1.8e4	1.36	epan	-0.1926	-1.4443	-0.0137	0.0473	1.0060	1.0498	-0.0432
2	1 (gray)	1e4	2.45	epan	-0.4441	-1.5991	-1.1554	0.0552	0.9846	1.1689	-0.0439
3	1 (gray)	1562	16	epan	-0.6451	-1.5121	-0.0832	0.0536	0.9991	1.0465	-0.0169

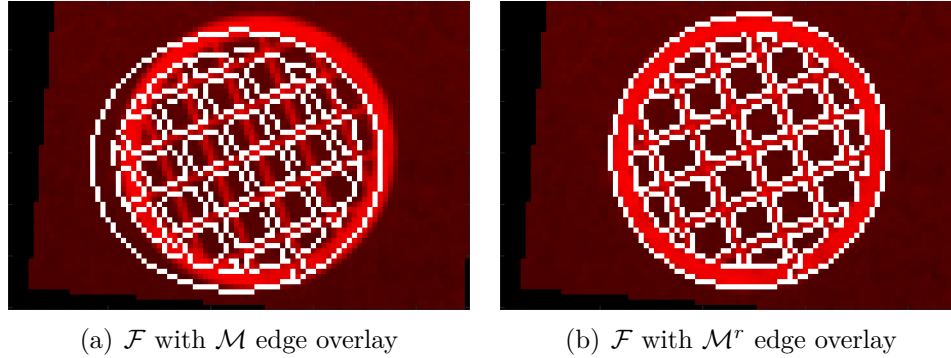


Figure 4.22: Exp. 1 registration result: Cu grid photo registered to Cu grid photo

Ground Truth Copper Grid Experiments (Exp. 1)

This experiment was conducted as a ground truth, proof of concept procedure to evaluate the accuracy of the registration function. The baseline image used in this experiment was the red channel from the RGB copper grid image, $I^{(R)}$. The fixed image was generated by applying a known transformation, $\vec{\mu}_{exp}$, to $I^{(R)}$ ($\mathcal{F} = I^{(R)}(A_{\vec{\mu}_{exp}} \cdot \vec{p})$). The original image served as the moving image input for the image registration function ($\mathcal{M} = I^{(R)}$). For this set of inputs, the expected output was the transformation applied to $I^{(R)}$ to create \mathcal{F} , $\vec{\mu}_{exp} = [-4, 2, -0.0698, 1.05, 0.95, 0.03]$. Numerical data and other relevant parameters are given in Table 4.7 and a visualization of the final result is shown in Fig. 4.22.

For all parameters and image inputs explored, the best affine parameters discovered through the image registration function were very close to the true value, $\vec{\mu}_{exp}$. Because of the differences in scale between the affine parameters, metrics such as Euclidean distance are not particularly informative for comparing error between parameters. Values of root mean-squared error between \mathcal{F} and \mathcal{M}^r are likely affected by differences in SA convergence and image interpolation for different affine parameters.

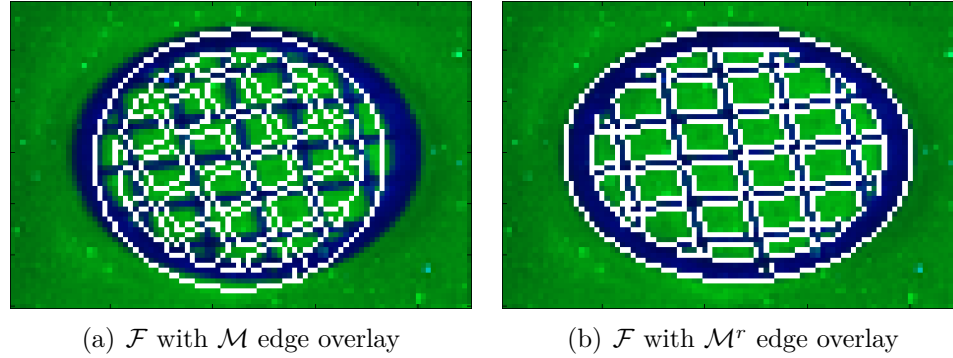


Figure 4-23: Exp. 2 registration result: Cu grid photo registered to multi-channel Cu grid MIMS

Overall, these experiments served to validate the functionality of image registration function, showing that given two input images \mathcal{F} and \mathcal{M} that are related through a known affine transformation, the function can recover the affine transformation parameters for both a scalar-pixel \mathcal{M} and a vector-pixel \mathcal{M} .

Multi-Modal Copper Grid Experiments (Exp. 2)

This experiment was conducted to ensure satisfactory functionality of the registration function on multi-modal data. Because the copper grid has well-defined features in both images, these data are ideal for visual assessment of registration accuracy. In this experiment, the MIMS image was input as \mathcal{F} since the data tend to be less uniform and thus are more susceptible to interpolation errors. The differences in morphology between the PI and the MIMS are because of the non-isotropic spatial dimensions of the MIMS image. Numerical data and other relevant parameters are given in Table 4.8 and a visualization of the final result is shown in Fig. 4-23. Ground truth is not available for this experiment since the two modalities are the result of entirely distinct acquisition techniques.

When compared to the ground truth experiment (Exp. 1), the variability of the

resulting $\vec{\mu}_{best}$ between different image input pairs in this experiment is similar. This suggests that even though \mathcal{F} and \mathcal{M} are different modalities, the image registration function successfully finds $\vec{\mu}$ which optimally aligns the two. The results from this experiment not only result in visually appropriate correspondence, but these results are consistent for both scalar- and vector-pixel images.

Multi-Modal, Multi-Subject Hippocampal Image Experiments (Exp. 3)

The multi-modal, multi-channel image registration function was tested on a representative biological dataset depicting a well-defined region of the mouse brain: the hippocampal formation. Data for a total of seven unique isotopes were collected for an approximately $2.5 \text{ mm} \times 4 \text{ mm}$ window of cortex, hippocampus and hypothalamus in the mouse brain. For this experiment, a schematic atlas of approximately the same sagittal region in the mouse brain was downloaded from Allen Brain Atlas (Atlas, 2013) (Fig. 4-24). This figure was cropped and recolored in Photoshop to create the image seen in Table 4.6 used for this experiment. Numerical data and other relevant parameters are given in Table 4.9 and a visualization of the final result is shown in Fig. 4-25.

Because of the small dimensions required for registration, some of the features of the original schematic atlas were diminished when downsampling by a factor of 16. This resulted in a severe lack of clean edges when displaying the edges as previously done for Exp. 1 and 2 (see Fig. 4-26(a)). For this reason, while the data presented are the result of the images as described in Table 4.6, the images shown in this section are the result of mapping $\vec{\mu}_{best}$ back onto the original, high resolution \mathcal{M} schematic image and then rescaling this image to match the original image dimensions of \mathcal{F} . Therefore, all results are shown on the 71×216 MIMS image (see Fig. 4-26(b) as an example).

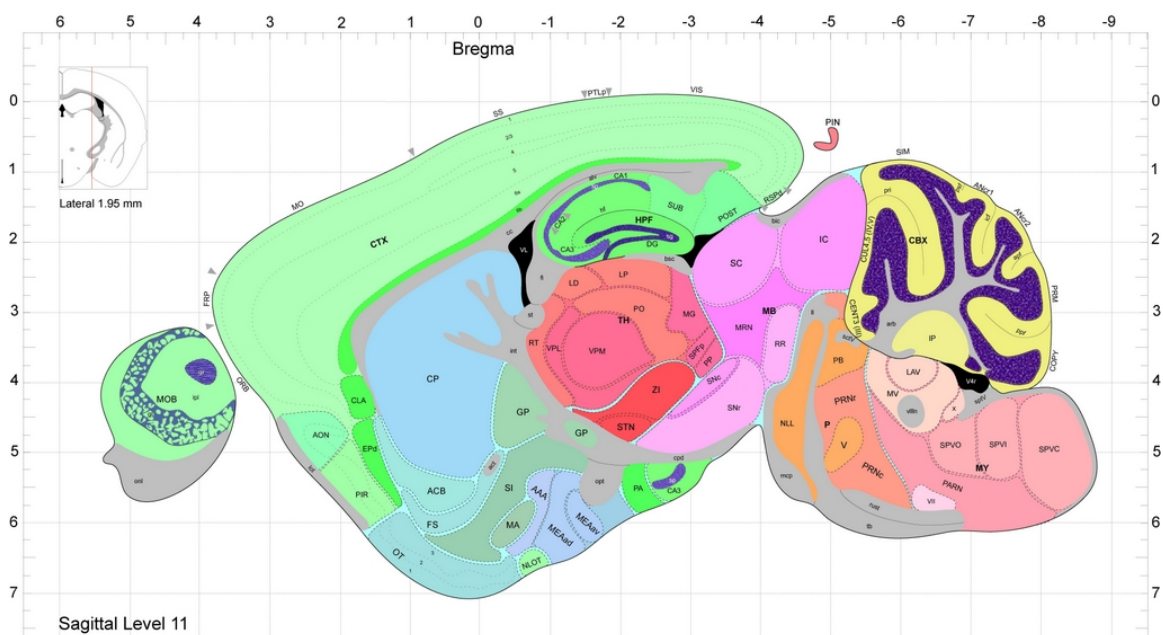


Figure 4-24: RGB colored schematic atlas of the approximate sagittal section corresponding to the MIMS data (from Atlas (2013))

Additionally, while the input fixed image may have been scalar valued (single channel), the results are displayed on a 3-channelled image so as to gain perspective of the image registration result relative to the other isotopes.

Overall, it is somewhat difficult to qualitatively assess the performance of the registration for the different cases considered. However, there were a few observations that are fairly evident. One is the incorrect feature registration when using only the ^{56}Fe channel (Fig. 4-25(b)). Here, the stratum oriens of CA1 (the darkest “C” shaped feature on the image in Table 4.6) is clearly aligned to the prominent line feature in the ^{56}Fe image. In context, however, this feature in the ^{56}Fe image is likely the CA1 pyramidal layer. Additionally, the estimated affine parameters vary significantly depending on which channel is used for registration. When registration is conducted using information from more than one channel, such as in the case of maximizing the sum of the 1-channelled MI values (Fig. 4-25(e)) and in the 3-channelled MIMS

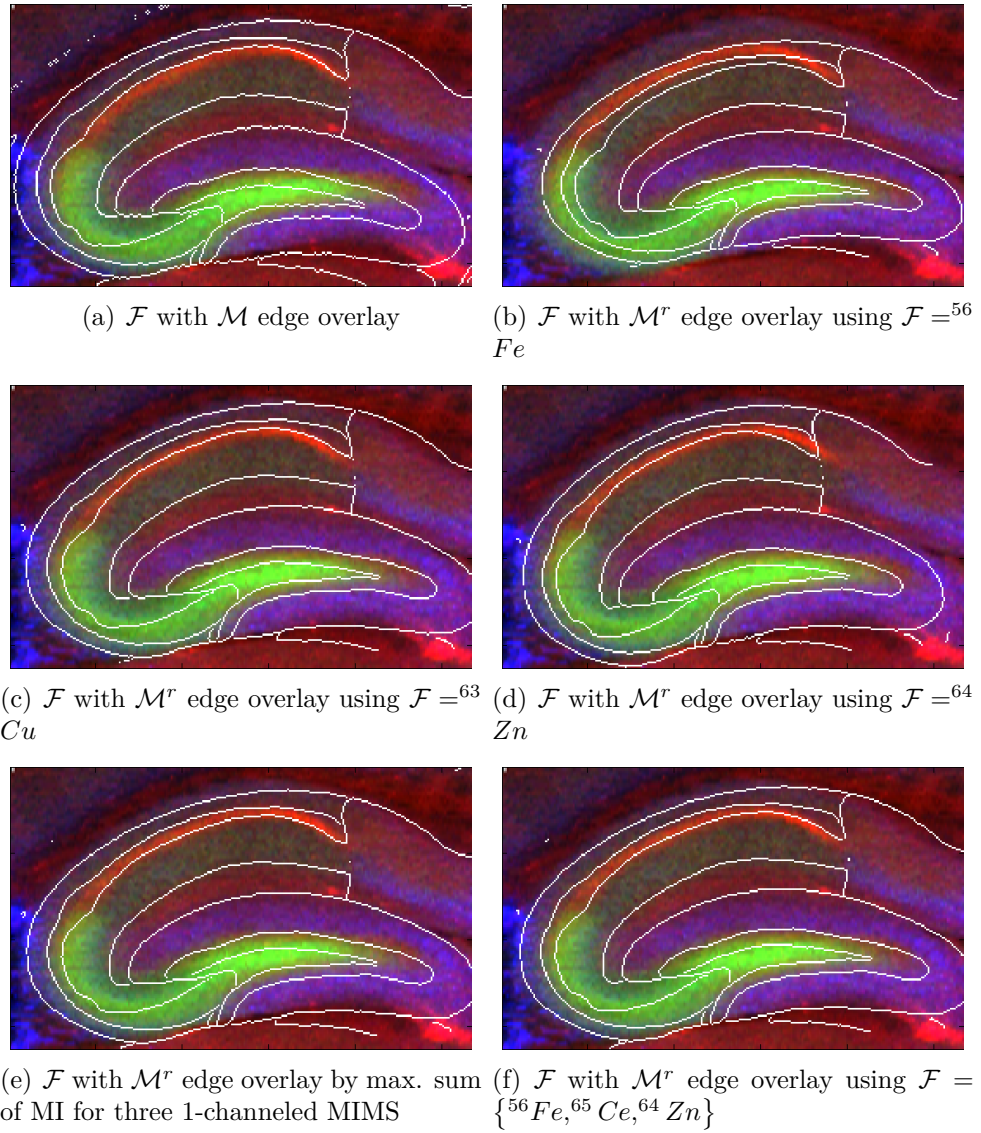
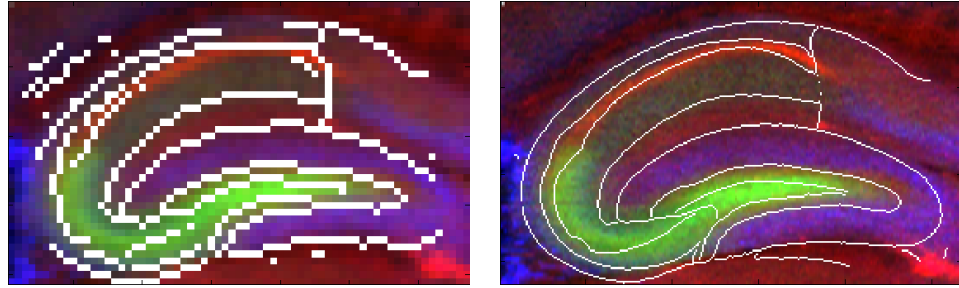


Figure 4-25: Exp 3 registration results: hippocampus segmentation image registered to MIMS

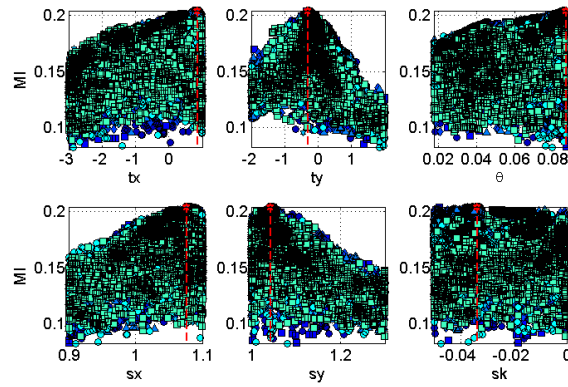
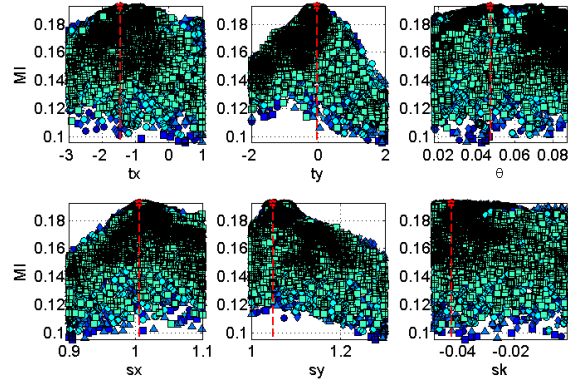


(a) Exp. 3 results using original image pair (b) Exp. 3 results mapped onto original MIMS

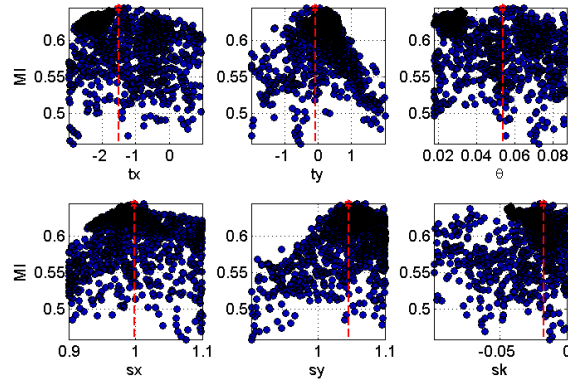
Figure 4-26: Display of mapping experimental results onto original image dimensions.

(Fig. 4-25(f)), the very prominent pyramidal cell layer of the CA1 region seems to correctly align. These results support the importance of taking multiple channels into consideration when determining a correspondence with a MIMS image.

Estimation of the best affine parameters for this experiment are generally not as clear as for the experiments conducted with the copper grid images. Figure 4-27 shows the projections of the MI onto the parameter axes for the MIMS ^{64}Zn channel (Fig. 4-27(a)), the summed MI on three 1-channel MIMS (Fig. 4-27(b)), and the 3-channel MIMS (Fig. 4-27(c)). These plots indicate that while some of the affine parameters have a prominent maximum within the range explored, others do not appear to have an optimal value (most notably θ and s_k). These ambiguities are likely a result of the limited state-space bounds and run-time. Despite these technical challenges, image registration results using multiple channels produced results which more closely agree with expected anatomical boundaries.

(a) Exp. 3 registration using ^{64}Zn channel

(b) Exp. 3 registration using sum of MI for three 1-channelled MIMS



(c) Exp. 3 registration using 3-channels

Figure 4-27: MI projection onto transformation parameter axis for various Exp. 3 inputs.

4.5.6 Discussion

Through these experiments, the functionality of the proposed multi-channel, multi-modal image registration function was established. A number of factors influencing registration accuracy and general properties of the image registration function were observed. One such observation was the effect of cost function smoothness on registration performance. The plots in Fig. 4-28 show the projection of the MI at each iteration of SA onto each of the transformation parameter axes. It is apparent that compared to Fig. 4-28(c), the distribution of the data in Figs. 4-28(a) and 4-28(b) have peaks that are more clearly defined for nearly all of the parameters. These sharp peaks are typically a reliable indicator of a “good” image registration result.

A second interesting and motivating reason for estimating multi-dimensional MI rather than other perhaps more simple schemes (such as maximization of the sum of MIs) reveals itself in Fig. 4-29. Figures 4-29(a) and 4-29(b) show MI values resulting from registration between two different fixed scalar images. Figure 4-29(c) shows data from an optimization function which maximized the sum of MI between two scalar images for each of the channels. In Fig. 4-29(c), the scaling peaks from both the ^{56}Fe image and the ^{63}Cu image are present, resulting in an ambiguous or non-specific value of s_y which maximizes MI. However, when computing MI for vector-valued images, it results in a singular peak in the parameter space, as seen in Fig. 4-29(d). While the MI in Figs. 4-29(a) and 4-29(b) is peaked in the s_y parameter space, this figure shows that final values reached using different channels are vastly different (exemplary final registration results can be seen in Figs. 4-25(b) and 4-25(c)).

Additional take-away points were the improvements in computational time without a significant effect on registration accuracy when using the Epanechnikov kernel rather than the Gaussian (Normal) kernel to compute the joint probability function. While

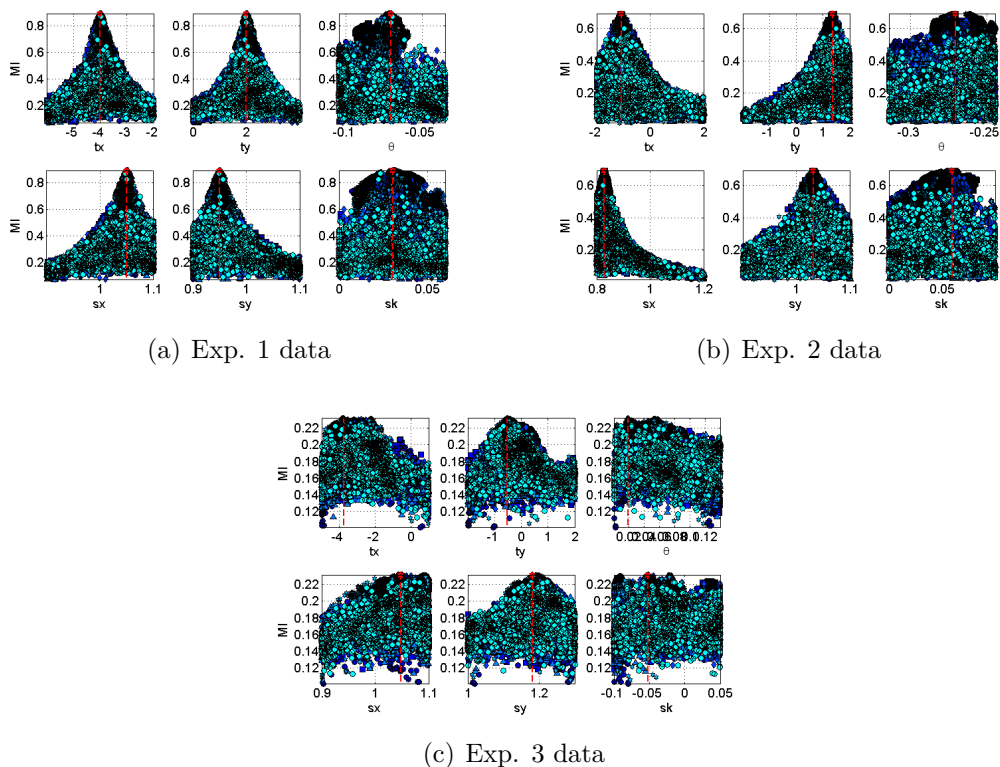


Figure 4-28: Examples of cost function projections onto transformation parameter axes for each of the MMMCIR experiments.

the results shown in this work are largely qualitative, the algorithmic infrastructure needed to perform multi-modal, multi-channel image registration has been developed and validated.

4.6 Summary of Contributions

The focus of this chapter has been on the algorithmic methods developed to address the technical challenges associated with visualization, analysis, and interpretation of MIMS data. Because the field of metallomic imaging mass spectrometry is still in its early stages, standard methods have yet to be defined. Contributions made towards addressing the challenges associated with MIMS data can be summarized as follows:

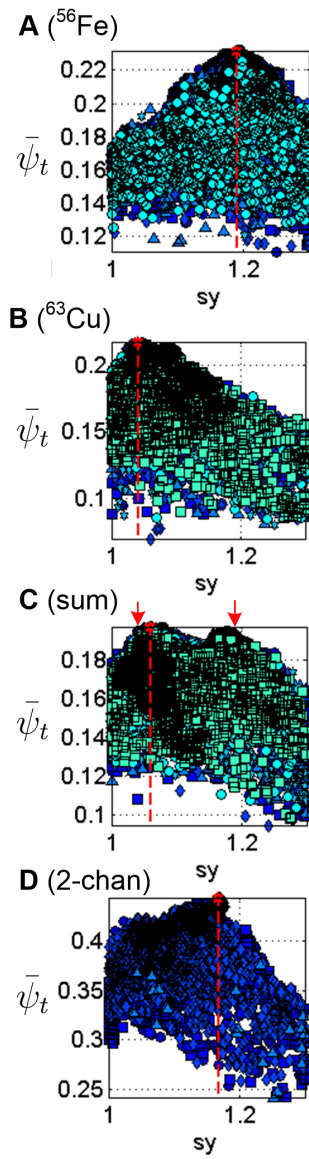


Figure 4-29: The data are from Exp. 3 image pairs. The images show various results for MI projected onto the s_y parameter axis for estimates of $\vec{\mu}_t$ during the image registration procedure.

- Development of functions for MIMS raw data extraction, segmentation, and visualization (Sections 4.1 and 4.2)
- Development of methods for representations of MIMS in a standard domain using calibration standards or image intensity properties (Sections 4.3 and 4.4)
- Development and validation of a novel method for multi-modal *and* multi-channel image registration using mutual information (Section 4.5)

These efforts have been used to provide evidence to support hypothesis of the underlying physiological events occurring in mouse models of traumatic brain injury (Tagge et al., 2017). Additionally, MIMS data extraction and visualization have been fundamental in the advancement of the data acquisition process, facilitating the establishment of this imaging method for precise analytical analysis of biological samples.

Chapter 5

Analysis of Metallomic Brain Images of Nanoparticle-Injected Mice

5.1 Experimental Objective

Metallomic imaging mass spectrometry (MIMS) is a method uniquely posed to provide quantitative information about the elemental-isotopic composition and spatial localization of a biological sample. As described in Section 1.3, elements which do not naturally occur in the brain may be intravenously injected to probe the degree of blood-brain barrier (BBB) dysfunction. The cocktail may be injected at various stages of the experiment depending on the goal of the assessment. In addition to injection of exogenous compounds, evaluation of physiologically-relevant elements and isotopes may also provide useful insight into the mechanisms of injury and the effects on the various brain regions.

Results from a case study of mice injected with a gadolinium-based MRI contrast agent suggest that mice exposed to an impact neurotrauma (INT) on the left-side of the head sustain left-sided disruption of the blood-brain barrier (BBB). As described in a recently submitted publication based on these results, and shown in Fig. 5-1 (Tagge et al., 2017):

“Focal BBB disruption and colocalizing serum albumin extravasation detected in the brains of living mice by dynamic contrast-enhanced MRI (DCE-MRI) neuroimaging with gadofosveset trisodium, an FDA-approved gadolinium-based contrast agent that binds serum albumin. High-field (11.7T) T1-weighted MRI (T1W-MRI, A and B) and DCE-MRI (C, D) with systemically administered gadofosveset trisodium. T1W-MRI and DCE-MRI were conducted 3 hours (A, T1W-MRI; C, DCE-MRI) and 3 days (B, T1W-MRI; D, DCE-MRI) after impact (IMP) or control (CON) exposure. T1W hyperintensity (A, B) colocalized with BBB permeability defect detected by DCE-MRI (C, D) in the left perirhinal cortex (arrows) 3 hours and 3 days after IMP but not CON exposure. Nonspecific signal was observed in the ventricles and sagittal sinus.”

The ^{157}Gd MIMS brain image for the impact exposed mouse (Fig. 5.1F) also exhibits a clear hyperintensity of the gadolinium signal colocalized with the in-vivo detected areas of BBB dysfunction.

Using the tools described in Chapter 4, MIMS brain images were registered with images from the Allen Mouse Brain Atlas (AMBA) (Atlas, 2013; Lein et al., 2007) to automate evaluation of signal levels in different subregions of the brain. Regions on the left and right side of the brain are used to explore whether individual mice in the INT cohort exhibited differences in elemental gadolinium distribution indicative of BBB disruption.

The goals of this Chapter are two-fold:

1. To demonstrate the use of the multi-modal, multi-channel image registration (MMMCIR) function to impart anatomical boundaries on MIMS brain image, and

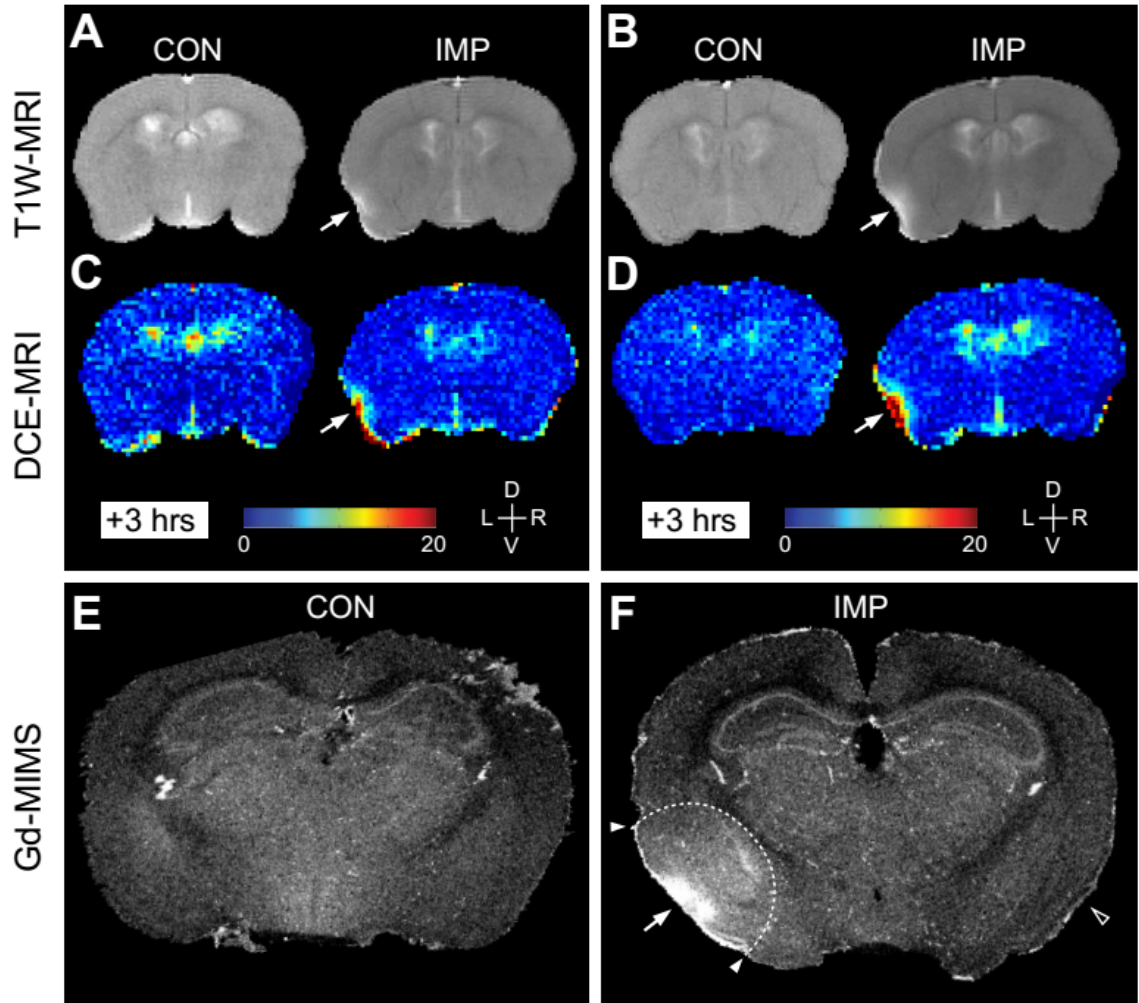


Figure 5.1: ^{157}Gd MIMS brain image for BBB compromise proof of concept. Full explanation for A–D is provided in the text. (A) T1W-MRI at 3 hours post injury. (B) T1W-MRI at 3 days post injury. (C) DCE-MRI at 3 hours post injury. (D) DCE-MRI at 3 days post injury. (E) ^{157}Gd MIMS brain image from a control mouse. (F) ^{157}Gd MIMS brain image from an impact (IMP) exposed mouse. Anatomical compass legend: D, V; dorsal, ventral. L, R; left, right. (copied from (Tagge et al., 2017, Fig.5))

2. To evaluate the signal levels in counts-per-second of left- versus right-sides of the brain in a cohort of MIMS brain image from approximately the same coronal location.

This chapter will first present the specifics of the tissue preparation and image selection in Section 5.2. Section 5.3 will detail the image preparation and the processing procedure done to extract the results shown in Section 5.4. A comparison of various experimental design choices will also be analyzed in Section 5.4.

5.2 Experimental Methods

Motivated by the naive and INT brains from the gadolinium-injected cohort (iGd), a distinct MIMS cohort was selected from an experiment involving 33 nanoparticle-injected animals (iNP) with corresponding MIMS brain image. While the experimental procedures and objectives for the iGd and iNP experiments were distinct, the tissue preparation were identical for both experiments.

5.2.1 Gadolinium-Injected Cohort (iGd)

The iGd experiment can be divided into two distinct procedures: (1) a TBI procedure and (2) an MRI procedure. A timing diagram of the experimental sequence for the iGd cohort is outlined in Fig. 5.2. The mice subjected to experimental left-sided closed-head impact injury (INT) were treated as follows: (1) Baseline-BUCS measured, (2) INT, (3) Post BUCS-1 measured, (4) INT, (5) Post BUCS-2 measured (3 *hrs* post-injury). Sled speeds for the impact neurotrauma were 5.1 ± 0.2 *m/s*. After injury, the mouse rested for approximately 15 *min* after measurement of the BUCS score before beginning the next step in the procedure. The naive mouse did not undergo any

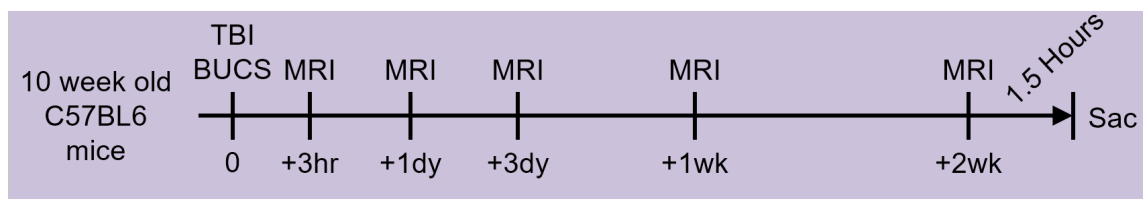


Figure 5.2: Timing diagram for gadolinium-based MRI contrast agent injected cohort (Figure courtesy of Andrew Fisher).

stage of the TBI procedure before being subjected to the MRI procedure. The MRI procedure involved imaging the mice with a Bruker 11.7T MRI instrument (High field MR Imaging Core, BU School of Medicine) using a sequence designed to enable to subsequent calculation of T1-weighted (signal and dynamic contrast-enhanced signal to assess BBB permeability defects. The mice underwent this imaging sequence five times over the course of a two week period at the following time points: [0 dy, 1 dy, 3 dy, 1 wk, 2 wk]. Prior to each MRI session, the mice were injected with a dose of a gadolinium-based MRI contrast agent ¹. Andrew Fisher, Chad Tagge, and Olga Minaeva, Ph.D., were primarily responsible for conducting the TBI procedure. Ning Hua, Ph.D., was responsible for the MRI procedure. An hour and a half after the fifth MRI sequence acquisition, the brains were harvested using the method detailed in Section 5.2.3.

5.2.2 Nanoparticle-Injected Cohort (iNP)

The mice in the iNP experiment were divided into two injury exposure groups: an impact neurotrauma group and a sham neurotrauma group. One naive control sample is analyzed as part of the experiment where there was no injury exposure and no injection. One hour before injury, mice were injected via the tail vein with 2 μg of

¹The dose was defined as 0.1 mL of a 0.25 mmol/mL gadofosveset trisodium, Lantheus Medical Imaging Inc., North Billerica, MA

a nanoparticle cocktail solution. The cocktail consisted of a gadolinium-based MRI contrast agent, 5 *nm* cerium oxide (CeO_2), 40 *nm* nanocrystals (NaY , Er , Ho), and 100 *nm* strontium titanate ($SrTiO_3$). The cocktail was made into a solution with 80 $\mu g/kg$ concentration using phosphate-buffered saline (PBS) as the diluent. As with the INT mouse from the iGd experiment, mice in the INT group were impacted on the left-side of the head. Brains were harvested using the method detailed in Section 5.2.3 24 hours after the injury exposure.

5.2.3 Tissue Fixation and Paraffin Embedding

Mice were euthanized by carbon dioxide asphyxiation and transcardially perfused with PBS until expelled fluids ran clear. Whole brains were then extracted, prefixed in 10% neutral-buffered formalin for two hours, then serial coronal section using a 1 *mm* brain-slicing matrix as indicated in Fig. 5-3(a). Brain sections were postfixed in 4% paraformaldehyde and stored at 4°C until paraffin embedding. The thick sections were then placed in a cassette with the rostral side facing the bottom and the left side facing the slanted side of the cassette. Paraffin-embedded sections are shown in Fig. 5-3(b). Each thick section is given a reference label corresponding to the predominate anatomical feature associated with that section. Listed rostral-to-caudal, the section labels were as follows: (1) prefrontal cortex (PFC), (2) anterior cingulate (AC), (3) hippocampal formation (HIP), (4) cerebellum (CER). Mark Wojnarowicz was primarily responsible for tissue preparation.

5.2.4 Input Image Information

Once paraffin blocks were available, MIMS brain images of the thick sections were acquired using the software tools described in Section 4.1. The entire paraffin block

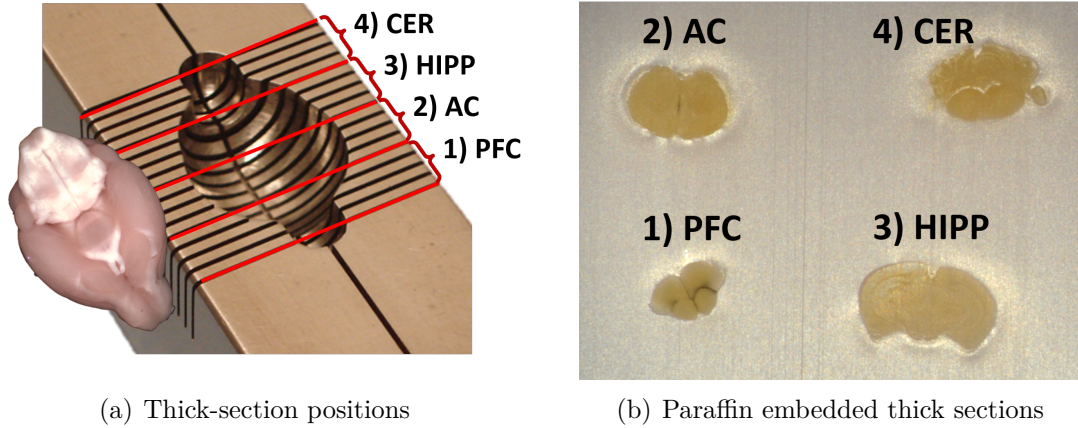


Figure 5-3: Thick section positions cut using the brain-slicing matrix.

was placed into the laser ablation sample chamber and the surface of the section being imaged was raster ablated. The acquisition parameters varied for each MIMS sequence and can be found in Table 5.1 for the iGd experiment and Table 5.2 for the iNP experiment.

Using the AMBA caudal-ventral-right (CVR) coordinate system (see Fig. 5-4), MIMS brain images from approximately the same coronal (x) position were selected. For the samples in the iGd experiment, the coronal plane was at $x = 7.3 \pm 0.2 \text{ mm}$ and those in the iNP experiment fell in the range of $x = 8.4 \pm 0.2 \text{ mm}$. MIMS acquisition and TBI exposure details are listed in Tables 5.1 and 5.2. For both experiments, the following five MIMS channels associated with physiologically- and pathologically-relevant elemental isotopes were selected for evaluation: ^{31}P , $^{57}\text{Fe}^{\text{II}}$, ^{63}Cu , ^{64}Zn , ^{157}Gd .

An atlas image derived from the AMBA atlas image available for download for Atlas (2013) (Fig. 5-6(c)) was used for registration to the MIMS brain image. Atlases from the more caudal region of the brain ($x = 8.4 \pm 0.2 \text{ mm}$ used for the iNP experiment)

^{II}for some samples, ^{56}Fe was acquired instead of ^{57}Fe . These specific cases are indicated in the results.

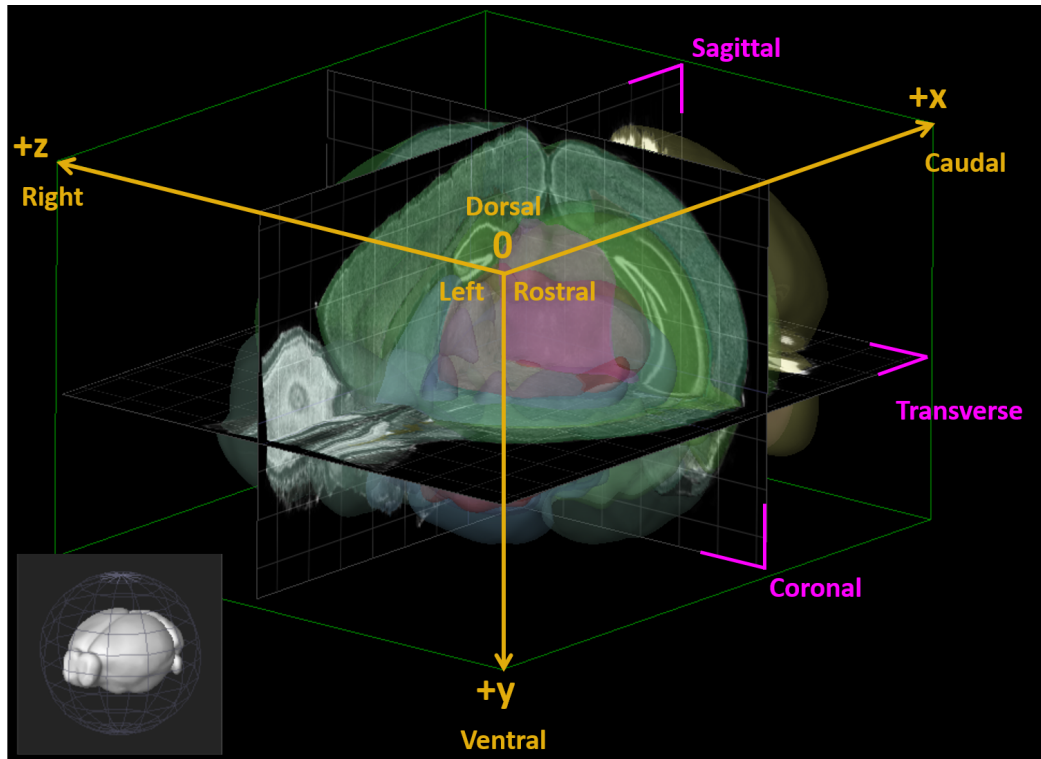


Figure 5.4: Mouse brain coordinate system used for AMBA where the x -axis goes in the rostral-to-caudal direction, the y -axis goes in the dorsal-to-ventral direction, and the z -axis goes in the left-to-right direction. The coordinate system is referred to as the CVR coordinate system for caudal-ventral-right being the direction of the positive x - y - z axes, respectively. Three planes are defined: the yz -plane is the coronal plane, the xz -plane is the transverse plane, and the xy -plane is the sagittal plane.

had a total of 13 labeled subregions defined by their 8-bit RGB values (Fig. 5.7(b)). The rostral sections from $x = 7.3 \pm 0.2 \text{ mm}$ used for the iGd experiment had 14 labeled subregions (Fig. 5.7(a)). The full names of the abbreviated regions are given in Table 5.3.

A common problem encountered when imaging tissue sections is out-of-plane sectioning. This issue can arise in any plane (coronal, transverse or sagittal) and is essentially defined as a plane whose corresponding x , y or z value is not constant. This stems

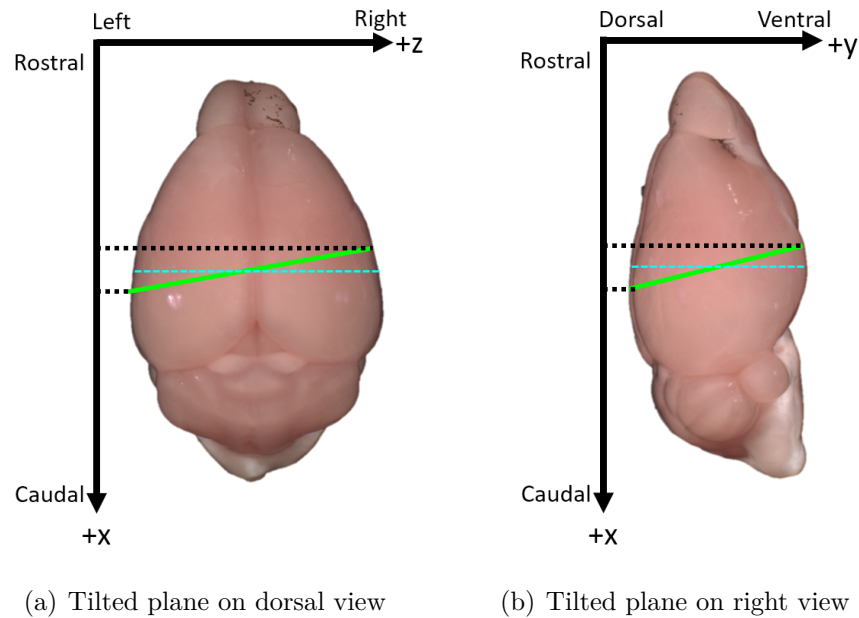


Figure 5-5: Out-of-plane coronal cuts on (a) dorsal and (b) right views. The green lines show an exaggerated example of a tilted coronal plane cut on each of the surfaces shown. The dashed cyan line shows what a constant coronal plane would look like. The dashed black lines show that the x -axis values on either extreme of the plane cut are not constant, which is the defining characteristic of a tilted plane.

from a variety of sources, including the cutting of the thick sections, the paraffin embedding, or angled mounting on the microtome (for thin sections). Characteristics of a tilted coronal plane are shown in Fig. 5-5. When the value of x is not constant across the cutting plane, the result may be that the left side is more caudal than the right side, as in Fig. 5-5(a), or that the dorsal part of the section is more caudal than the ventral part, as in Fig. 5-5(b). These out-of-plane cuts can be compounded and result in anatomical variance which is not easily corrected when referencing MIMS maps to specific brain atlas maps in a given anatomical plane.

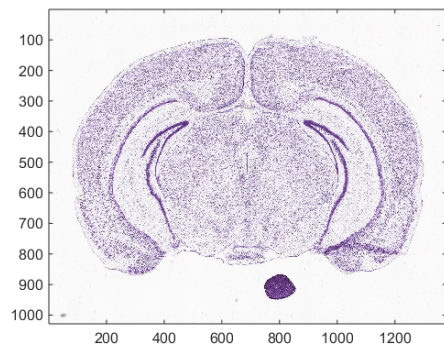
Coronal atlas section images from the AMBA are used to impart anatomical boundaries onto the MIMS. At $100\ \mu\text{m}$ intervals, the AMBA provides a Nissl stained^{III}

^{III}The Nissl stain is used to label extranuclear RNA granules for visualization of the cell body.

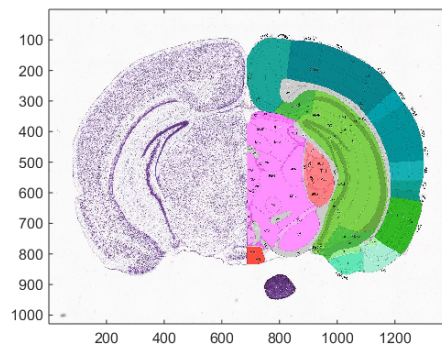
thin-tissue section ($25 \mu m$) with a corresponding image which labels anatomical structures from the medial line to the right side of the section. Since the AMBA sections are assumed to be nearly coronally-in-plane, the anatomy is symmetric about the midline so the anatomical structures on the left side of the section can be derived from the labeled structures on the right side. For use in the registration experiments, the selected Nissl-stained section (Fig. 5-6(a)) and the corresponding atlas image (Fig. 5-6(b)) were both downloaded from the AMBA website^{IV}. The atlas image is used to aggregate anatomical structures of interest and a new atlas-only image is derived from the original (Fig. 5-6(c)).

To address the issue of different left-side (L) versus right-side (R) anatomy caused by out-of-plane coronal sectioning, two AMBA coronal sections were selected to describe each coronal MIMS: one which best matched the anatomy on the right side of the section and one which best matched the anatomy on the left side of the section. Selection of the best corresponding section for a given MIMS brain image and side was done manually via examination of the hippocampal formation and the morphology of the hippocampal pyramidal cell layer. Out-of-plane sectioning which resulted in the dorsal part of the section being more caudal than the ventral part of the section (or visa-versa, as in Fig. 5-5(b)) was not accounted for.

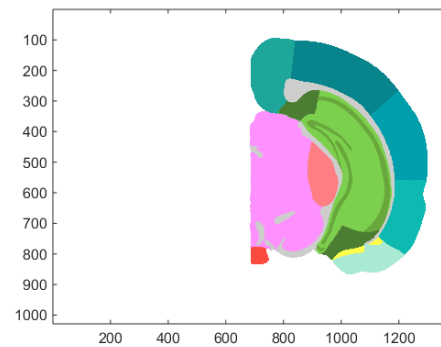
^{IV}May be downloaded using the API http://api.brain-map.org/api/v2/atlas_image_download/SectionDataSet?downsample=3&annotation=true for the appropriate SectionDataSet value and annotation from Tables 5.2 and 5.1



(a) Nissl image, \mathcal{N}



(b) Raw Atlas image



(c) Derived Atlas image, \mathcal{A}

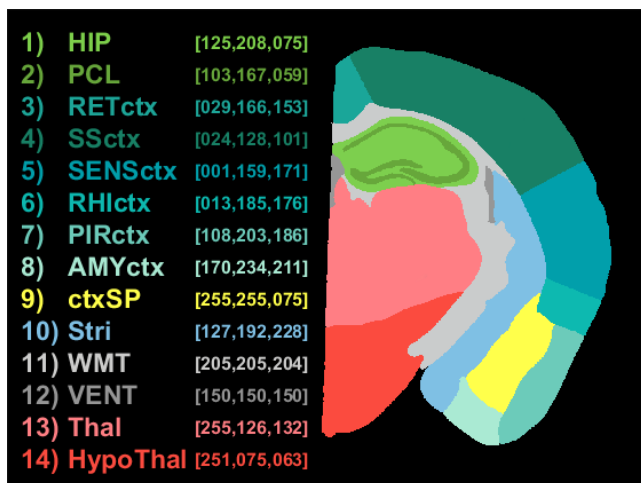
Figure 5-6: Allen Mouse Brain Atlas images used for MIMS registration procedure for major anatomical division of the brain.

Table 5.1: Gadolinium-injected (iGd) experiment information. Laser spot size, Line-to-line spacing, Laser scan speed, MS sampling time,

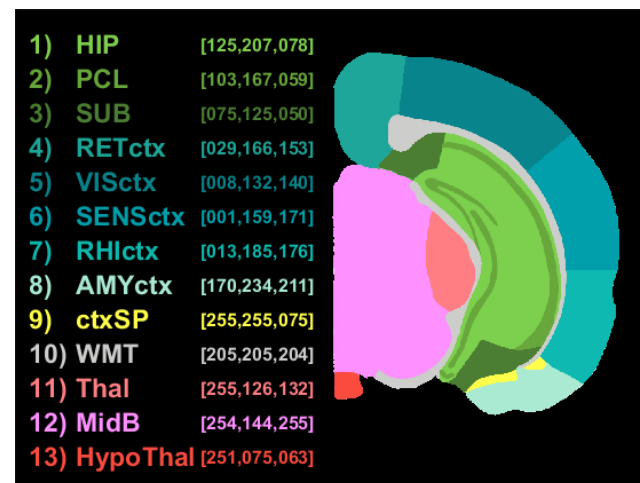
Sample ID	10	12
Exp. Group	impact	naive
Acquisition Date	20150714	20150713
d_{spot} [μm]	20	20
d_{l2l} [μm]	20	20
v_{scan} [$\mu m \cdot s^{-1}$]	40	40
t_{acq} [sec]	0.115	0.115
No. Isotopes	13	13
Bounding Box	285×1476	276×1478
Left-matched AMBA SectionDataSet Value (x in mm)	100960236 (7.2)	100960224 (7.5)
Right-matched AMBA SectionDataSet Value (x in mm)	100960236 (7.2)	100960228 (7.4)

Table 5.2: Nanoparticle injected (iNP) experiment cohort information

Sample ID	35	12	22	14	27	26	30
Exp. Group	control	sham	sham	impact	impact	impact	impact
Acquisition Date	20150413	20150324	20150818	20150818	20150415	20150819	20150923
d_{spot} [μm]	20	20	20	20	20	20	20
d_{l2l} [μm]	20	20	30	30	20	20	20
v_{scan} [$\mu m \cdot s^{-1}$]	40	40	60	60	40	60	60
t_{acq} [sec]	0.506	0.510	0.163	0.163	0.488	0.213	0.203
No. Isotopes	17	18	10	10	17	12	11
Bounding Box	219×340	206×324	163×702	149×675	193×329	228×520	196×554
Left-matched AMBA SectionDataSet Value (x in mm)	100960053 (8.6)	100960061 (8.4)	100960061 (8.4)	100960061 (8.4)	100960061 (8.4)	100960061 (8.4)	100960061 (8.4)
Right-matched AMBA SectionDataSet Value (x in mm)	100960061 (8.4)	100960065 (8.3)	100960065 (8.3)	100960069 (8.2)	100960061 (8.4)	100960061 (8.4)	100960065 (8.3)



(a) Atlas integer labels and colors for $x = 7.2 \text{ mm}$



(b) Atlas integer labels and colors for $x = 8.4 \text{ mm}$

Figure 5·7: Labeled atlas images used in MIMS brain image registration experiments. (a) Depiction of the rostral slices used for the iGd cohort which included 14 major brain structures. (b) Depiction of the caudal slices used for the iNP cohort which included 13 major brain structures. The full names for the anatomical regions abbreviations shown in the figures can be found in Table 5.3.

Table 5.3: Regional structure abbreviations and full names for atlas images used for registration

Abbreviation	Label # in $x = 7.2$	Label # in $x = 8.4$	Full Name
HIP	1	1	Hippocampus
PCL	2	2	Pyramidal cell layer in hippocampal region
SUB	—	3	Subiculum
RETctx	3	4	Retrosplenial area of cerebral cortex
VISctx	—	5	Visual areas of cerebral cortex
SSctx	4	—	Somatosensory and Somatomotor areas of the cerebral cortex
SENSctx	5	6	Sensory area of cerebral cortex (including posterior parietal association areas, auditory areas, and temporal association areas)
RHIctx	6	7	Perirhinal cortex (including entorhinal area, perirhinal area, and entorhinal area)
PIRctx	7	—	Piriform area of cerebral cortex
AMYctx	8	8	Amygdala (including postpiriform transition area and cortical amygdalar area)
ctxSP	9	9	Cortical subplate
Stri	10	—	Striatum
WMT	11	10	White matter tracts
VENT	12	—	Ventricles
Thal	13	11	Thalamus
MidB	—	12	Midbrain
HypoThal	14	13	Hypothalamus

5.3 Processing Pipeline

The registration procedure is divided into three sequential tasks: (1) image preparation, (2) registration initialization, and (3) image registration. For each MIMS brain image, two coronal sections from AMBA are selected: one to match left (L) anatomy and one to match right (R) anatomy. To determine the anatomical boundaries of a single MIMS brain image using the AMBA, the registration procedure is carried out twice, once for each side. The registration procedures are identical for both except that for L registration, the AMBA images is reflected across the midline of the dorsal-ventral axis of the brain.

5.3.1 Image Preparation

For a given MIMS brain image and a given side (either L or R), the Nissl image, $\mathcal{N}(x)$ (Fig. 5-6(a)) and the derived atlas image, $\mathcal{A}(x)$ (Fig. 5-6(c)) for the selected section at the location x (expressed in *mm* according to the CVR coordinate system) are loaded into the workspace. If the goal is to define left-side anatomy, then both images must then be reflected across the midline of the dorsal-ventral axis such that the AMBA images left and right side are switched. Images used for segmentation of a particular side of the brain are denoted as $\mathcal{N}^{(side)}$ or $\mathcal{A}^{(side)}$ where $side = \{L, R\}$. When the side does not influence the step, this notation is omitted. An intensity-based foreground/background masking is done on both \mathcal{N} and \mathcal{A} , yielding $M_{\mathcal{N}}$ (Fig. 5-8(d)) and $M_{\mathcal{A}}$ (Fig. 5-8(e)) respectively. The mask $M_{\mathcal{N}}$ provides a tissue boundary and defines a rectangular area which is used to crop out surrounding background pixels. The mask $M_{\mathcal{A}^{(side)}}$ identifies the side of the brain since all other pixels except those associated with labeled anatomical structures on the given side are background regions.

The corresponding MIMS brain image for a given sample is indicated as $\vec{I}(s)$ where s is the sample ID in Tables 5.1 and 5.2. Recall that \vec{I} is a d -channeled image where each channel has intensity characteristics and dynamic range specific to the elemental isotope corresponding to a given channel. To normalize the channel characteristics for image registration, a mean-variance equalized (MVE) image, \vec{I} , is produced as described in Section 4.4. The MIMS segmentation function, described in Section 4.2, is used to produce a foreground/background mask for the MIMS brain image, $M_{\vec{I}}$ (Fig. 5.8(f)). As with the AMBA images, this mask defines a rectangular area for cropping out the surrounding background (Bouding box values given in Tables 5.1 and 5.2).

5.3.2 Registration Initialization

Given the three masks ($M_{\mathcal{N}}$, $M_{\mathcal{A}}$, $M_{\vec{I}}$), the goal of this procedure is twofold: (1) to define the left and right side of the MIMS brain image, and (2) to provide suitable initial affine parameters, μ_0 , so as to limit the state space for registration between the selected AMBA image and the MIMS brain image. This is accomplished by registering the masks $M_{\mathcal{N}}$ and $M_{\vec{I}}$. The two masks, $M_{\mathcal{N}}$ and $M_{\vec{I}}$, are provided as inputs into the same image registration pipeline described in Section 4.5 and summarized in Fig. 4.20. Because the masks are binary images, rather than using the cost function $\psi_t = -J(\mathcal{F}(\vec{p}); \mathcal{M}^r(\vec{p}))$, the cost function is defined as the sum of absolute differences, $\psi_t = \sum_{\vec{p}} |\mathcal{F}(\vec{p}) - \mathcal{M}^r(\vec{p})|$, where $\mathcal{F} = M_{\vec{I}}$ and $\mathcal{M}^r = M_{\mathcal{N}}(A_{\vec{\mu}_t} \cdot \vec{p})$.

Assuming that overall the MIMS brain image has similar tissue shape and internal structures as the AMBA tissue, alignment of the Nissl mask $M_{\mathcal{N}}$ to the MIMS mask $M_{\vec{I}}$ via the affine parameters μ_0 results in a reasonable initial alignment of the two brain images. Additionally, by leveraging the fact that the AMBA images \mathcal{N} and \mathcal{A}

are spatially concordant, a suitable alignment between $M_{\vec{T}}$ and $M_{\mathcal{N}}$ allows for the definition of the right-side of the MIMS brain image as follows:

$$M_{\vec{T}}^{(R)} = M_{\vec{T}} \cap M_{\mathcal{A}^{(R)}} \left(A_{\vec{\mu}_0} \cdot \vec{p} \right)$$

where $M_{\mathcal{A}^{(R)}} \left(A_{\vec{\mu}_0} \cdot \vec{p} \right)$ is the right-side AMBA mask with the applied mask alignment transformation, $\vec{\mu}_0$. Note that an identical procedure can be carried out for the left side.

5.3.3 Image Registration Procedure

In order to objectively determine the correspondence between a MIMS brain image and a stereotyped anatomical atlas, the input image characteristics need to address specific assumptions and limitations associated with the MMMCIR function using mutual information. While the intensity features in the two input images need not be functionally related, the characteristics of their intensity distribution should be similar (that is if one image has a uniform intensity feature, the corresponding feature in the other image should also be uniform). MIMS channels used for MMMCIR are selected based on observably consistent structures in the brain which appear in both the MIMS brain image and the atlas image.

One of the most easily identifiable features in \vec{T} and \mathcal{N} is the pyramidal cell layer (PCL) in the hippocampal formation (HPF). Channels for which the PCL is clearly visible are identified for use in MMMCIR. The best channel depicting this anatomical feature is generally either an iron isotope (^{56}Fe or ^{57}Fe) or the ^{31}P isotope channel. An additional channel which broadly differentiates larger anatomical structures in the brain, such as the cortex, the white matter tract and the midbrain, is selected. Generally, the ^{64}Zn channel provided the clearest definition of additional large anatomical

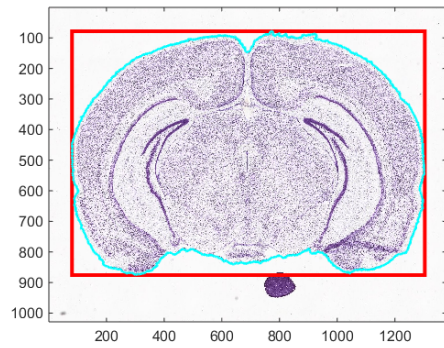
features. Specific details regarding the MIMS brain image input are presented in Section 5.4.

Because of the challenges associated with the raw form of the MIMS, most notably the long tail of the distribution with large-valued outliers, the MIMS channel data are mean variance equalized (MVE) to represent the intensity distribution as a standard normal as described in Section 4.4. The resulting MVE channel data are cutoff at ± 3 (all values less than or greater than this range were set to -3 or $+3$, respectively). This results in a normally-distributed probability density function (pdf) of the channel's intensity values. By limiting the intensity range to ± 3 , a more accurate quantized pdf can be obtained since highly-probable areas in the pdf can be represented by more bins rather than allocating bins to areas of very low probability. The atlas image, \mathcal{A} , was selected as the second input image for registration. Selection of \mathcal{A} over \mathcal{N} is discussed in Section 5.4.4.

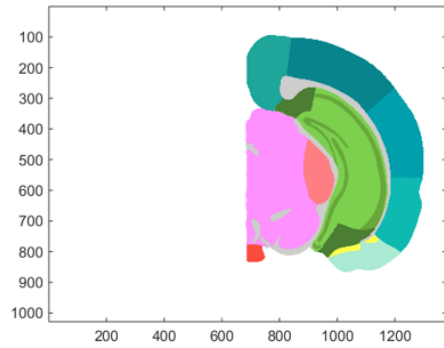
As shown in Fig. 5.10, the fixed image and moving image are set to be the side-masked, MVE channel(s) for the MIMS brain image and the AMBA atlas image, respectively. Unless stated otherwise in the results, all experiments are run with the default experimental parameters indicated in Table 5.4. One additional important implementation detail is the treatment of background pixels in both images. To prevent any influence of the image backgrounds on the image registration procedure, background pixels, as defined by $M_{\mathcal{A}}$ and $M_{\vec{\gamma}}$, are not used to calculate the mutual information. The optimal affine transformation parameters determined by the function, $\vec{\mu}_{opt}$, are the ultimate output of the image registration procedure. These parameters are used for conducting subsequent MIMS brain image analyses.

Table 5.4: Specification of MIMS brain image registration parameters

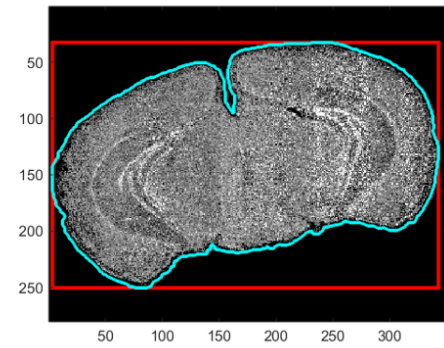
Symbol	Definition	Function where used	Value
\mathcal{F}	fixed image	input	$\vec{I}^{(side)}$: MVE 2-channel MIMS brain image with ^{31}P and ^{64}Zn
\mathcal{M}	moving image	input	$\mathcal{A}^{(side)}$ at position indicated in Tables 5.2 and 5.1
ϕ	interpolator	Transformation model	bicubic
—	background correspondences ignored	Cost Function	Any corresponding positions which overlap with background regions in either image are not used for computing J
$J(\bullet)$	cost function	Cost Function	J^{Σ} : summed-MI (see Section 5.4.4)
K	# of bins (equal in all dim.)	Cost Function	40
\mathcal{K}	kernel used	Cost Function	norm
T_0	initial temperature	SA Optimization	5
τ	temperature decay rate	SA Optimization	0.99
c	parameter scale factors	SA Optimization	$[1, 1, 180/\pi, 10, 10, 50]$
—	reannealing interval	SA Optimization	250
—	max. # iterations	SA Optimization	5000



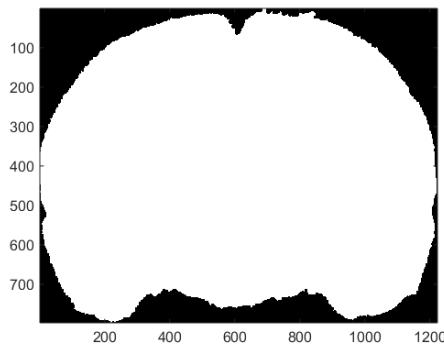
(a) Mask and Bounding Box for \mathcal{N}



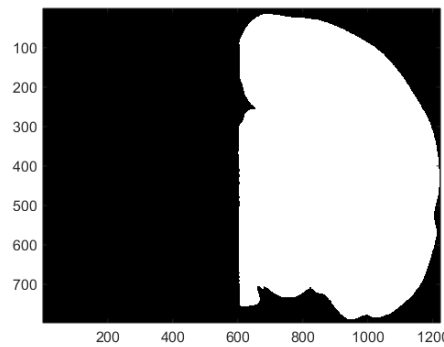
(b) Mask and Bounding Box for \mathcal{A}



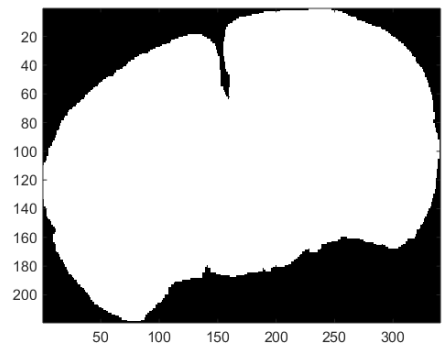
(c) Mask and Bounding Box for \vec{I}



(d) Nissl tissue mask, $M_{\mathcal{N}}$

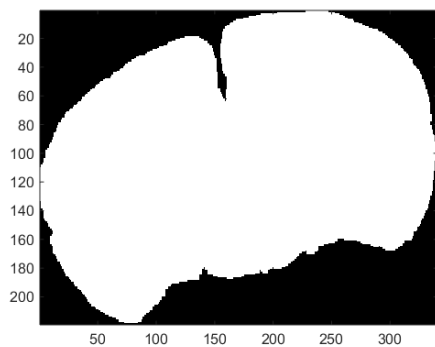


(e) Atlas tissue mask, $M_{\mathcal{A}}$

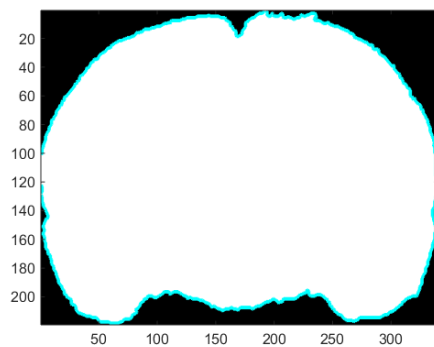


(f) MIMS tissue mask, $M_{\vec{I}}$

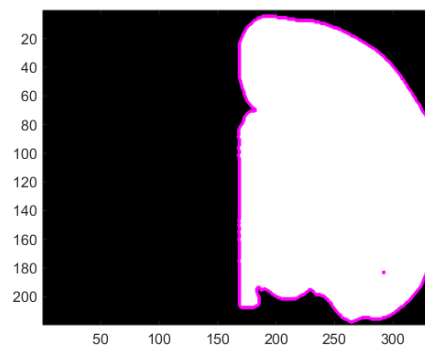
Figure 5.8: Foreground/background segmentation of original images with the tissue boundary shown in cyan and the bounding box shown in red (top row). The bottom row shows the cropped foreground (white) and background (black) masks. (d) Tissue mask $M_{\mathcal{N}}$ derived from the Nissl image \mathcal{N} . (e) Right-side tissue mask $M_{\mathcal{A}}$ derived from the atlas image, \mathcal{A} . (f) Brain MIMS tissue mask $M_{\vec{I}}$ derived from the MIMS brain image \vec{I} .



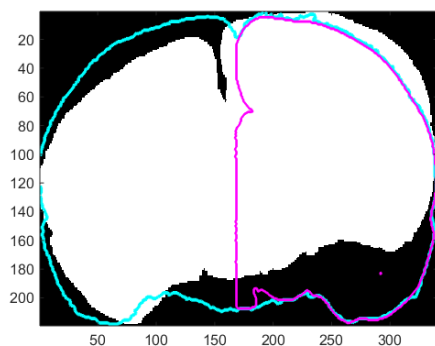
(a) MIMS tissue mask, $M_{\vec{T}}$



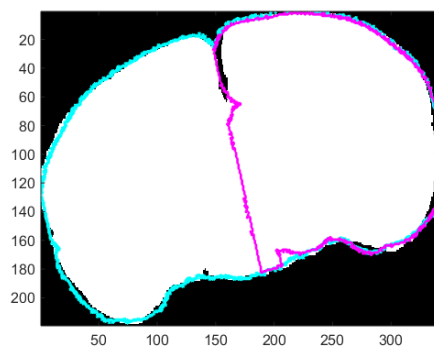
(b) Resized Nissl tissue mask, $M_{\mathcal{N}}$



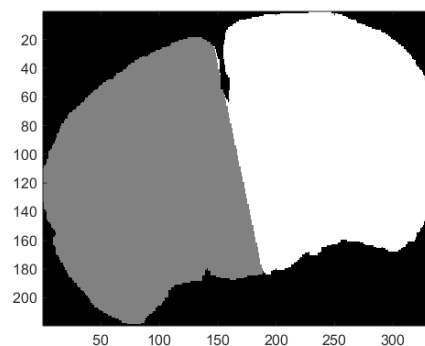
(c) Resized atlas tissue mask, $M_{\mathcal{A}}$



(d) Pre-mask-registration overlay



(e) Post-mask-registration overlay



(f) $M_{\vec{T}}$ shown with side-mask

Figure 5.9: The figure summarizes the registration initialization procedure where tissue masks are aligned. The inputs to the image registration function are the masks (a) $M_{\vec{T}}$ and (b) $M_{\mathcal{N}}$, as the fixed and the moving image, respectively. The initial alignment of the two masks is shown in (d). The optimal affine transformation parameters aligning $M_{\mathcal{N}}$ to $M_{\vec{T}}$ yield the results shown in (e). The mask $M_{\mathcal{A}}$ can be transformed by these parameters and used to define a right-side mask, $M_{\vec{T}}^{(R)}$ for the MIMS brain image (f).

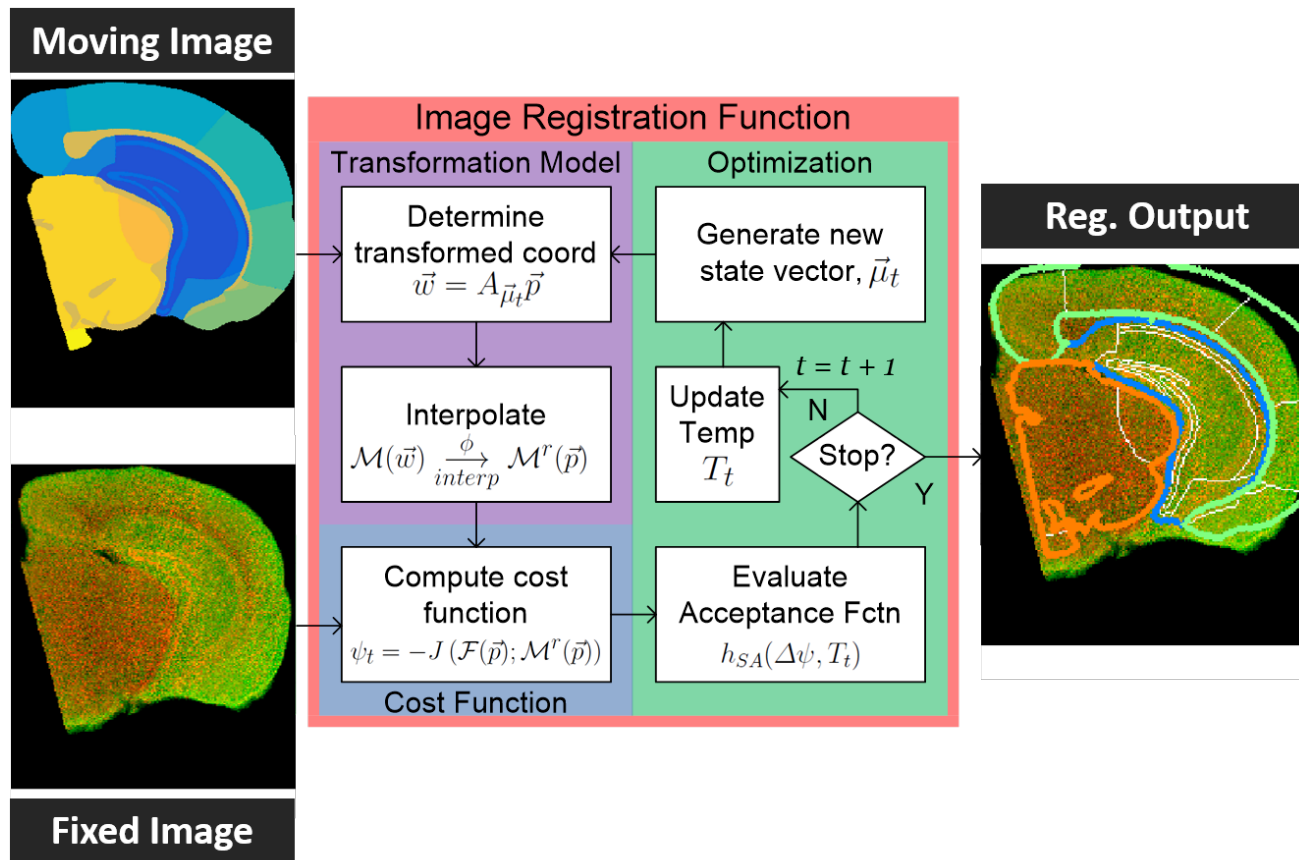


Figure 5-10: Multi-modal, multi-channel image registration procedure for automated anatomical segmentation of MIMS brain image.

5.4 Results and Discussion

As mentioned, analysis objectives were twofold: (1) to demonstrate the utility of the MMMCIR method for automated, objective segmentation of the MIMS brain images and (2) to use segments on the left and right sides of the MIMS brain images to evaluate signal levels. While the atlas image used for MMMCIR had 13 – 14 anatomical subregions (see Fig. 5·7), these subregions were combined to produce an anatomical subgroup image, \mathcal{G} , with the same dimensions as \mathcal{A} (see Fig. 5·11). Each pixel in \mathcal{G} takes on one of four distinct values, $\{0, 1, 2, 3\}$, which can be interpreted as an indicator for membership to one of the following subgroups: $\{(1) \text{ uninformative, (2) hippocampal formation (HPF), (3) cortical areas (CTX), (4) thalamus (TH)}\}$.

In the images presented throughout this section, MIMS brain image are shown as psuedo-colored images with various colored outlines drawn on top. This is simply a visualization strategy since, as previously discussed, registration with \mathcal{A} is done for the left and right side of the MIMS brain image separately. The transformations $\vec{\mu}_{opt}^{(L)}$ and $\vec{\mu}_{opt}^{(R)}$ can be applied to $\mathcal{A}^{(L)}$ and $\mathcal{A}^{(R)}$, respectively. Then the associated group images, $\mathcal{G}^{(L)}$ and $\mathcal{G}^{(R)}$, can be depicted together, as in Fig. 5·12(a). The color assigned to each anatomical subregion on each side in Fig. 5·12(a) is the same color that is used to show the outlines on the MIMS brain image image, as in Fig. 5·12(b). The white lines in the image correspond to the boundaries of the anatomical structures in $\mathcal{A}^{(L)}$ and $\mathcal{A}^{(R)}$.

In order to present numerical assessments of the signal levels on the left and right side of the brain for three anatomical subgroups and five intensity channels, a normalized

side difference metric, $\bar{\partial}^{(L-R)}(g)$, was developed:

$$\bar{\partial}^{(L-R)}(g, i) = \frac{\text{mean} \left[I^{(i)} \left(M_{\vec{T}} \cap \mathcal{G}^{(L)} = g \right) \right] - \text{mean} \left[I^{(i)} \left(M_{\vec{T}} \cap \mathcal{G}^{(R)} = g \right) \right]}{\text{quantile}_{75\%} \left[I^{(i)} \left(M_{\vec{T}} \right) \right] - \text{quantile}_{25\%} \left[I^{(i)} \left(M_{\vec{T}} \right) \right]} \quad (5.1)$$

where $I^{(i)}$ is the signal for the i -th MIMS channel and $g \in \{1, 2, 3\}$ is the subgroup value. This metric provides a normalized value which is suitable for varying dynamic ranges and data characteristics, so it can be used to compare the regional and focal elemental-isotopic tissue concentrations between different subjects and isotopes. The metric also combines statistics derived from the left and right sides of the MIMS brain image so that their relative values can be interpreted by a single number. We see that:

$$\bar{\partial}^{(L-R)}(g, i) > 0 \quad \dots\dots\dots \text{ indicates L} > \text{R}$$

$$\bar{\partial}^{(L-R)}(g, i) < 0 \quad \dots\dots\dots \text{ indicates L} < \text{R}$$

The magnitude of $\bar{\partial}^{(L-R)}(g, i)$ indicates the magnitude of the difference between the signal on the L and R side as a fraction of the “typical” data range (denominator of Eqn. 5.1). This metric is used to present results intended for cross-subject, cross-isotope evaluation. Without loss of generality, this metric may be computed using any intensity-adjusted version of the MIMS brain image (see Section 4.4 for details regarding applicable intensity-transformation methods).

Since MIMS characteristically have high-intensity spurious noise, a 3×5 median filter was applied to the raw MIMS channel \vec{T} then used to compute $\bar{\partial}^{(L-R)}(g, i)$. Due to the normalization factor which changes based on the magnitude of the image intensities, the final value of $\bar{\partial}^{(L-R)}(g, i)$ typically falls in the range of ± 2 regardless of what type of data is used to compute the metric.

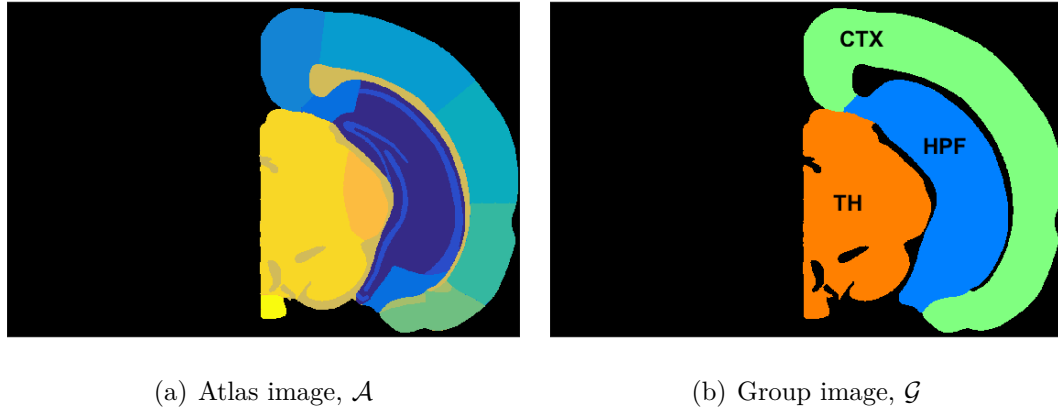


Figure 5-11: Anatomical subgroup image, $\mathcal{G}^{(R)}$, derived from the atlas image, $\mathcal{A}^{(R)}$. Each subgroup has an associated integer value: 0 = uninformative, 1 = hippocampal formation (HPF), 2 = cortical areas (CTX), and 3 = thalamus (TH).

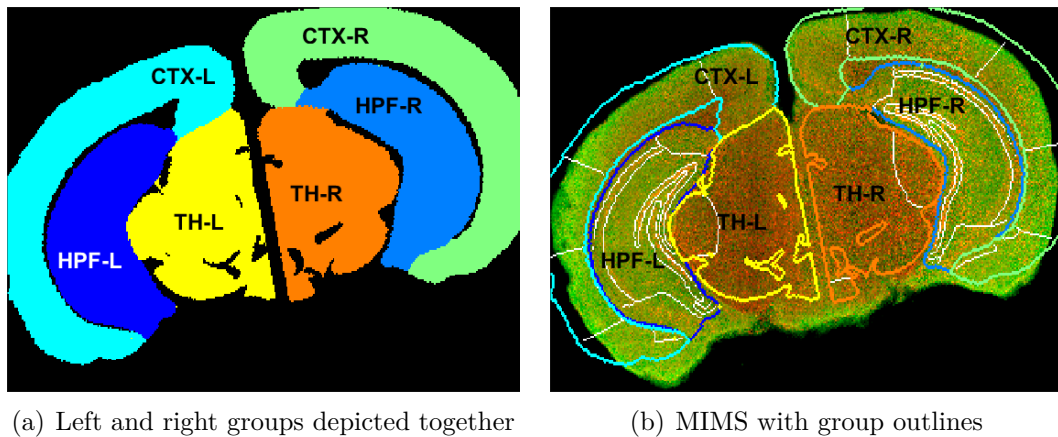


Figure 5-12: (a) Composite image showing the transformed $\mathcal{G}^{(L)}$ and $\mathcal{G}^{(R)}$ together. Each anatomical subregion on each side is assigned a unique RGB-value for visualization. (b) Multi-channel pseudo-color representation of the MIMS brain image with the R-channel corresponding to ^{31}P values and the G-channel to ^{64}Zn values. The white outlines show the anatomical structures from \mathcal{A} and the colored outlines show the groups on the left and right side.

5.4.1 Assessment of Gadolinium-Injected Cohort

Images of the five isotopes selected for detailed analysis c, ^{157}Gd) are provided in Fig. 5-13. To quantitatively verify the apparent elevated ^{157}Gd -signal on the inferior left perirhinal cortex of the iGd-10 MIMS brain image, the two MIMS brain images in this cohort were manually segmented into the three anatomical subgroups (HPF, CTX, TH) on the left and right side (Figs. 5-14(a) and 5-14(b)). The signal contained within each anatomical subgroup image, $\mathcal{G}^{(L)}$ and $\mathcal{G}^{(R)}$ (see Fig. 5-11(b)), was used to compute $\bar{\partial}^{(L-R)}(g, i) \forall g, i$. These results are plotted in Fig. 5-14(c).

Some data characteristics begin to present themselves in the plots of $\bar{\partial}^{(L-R)}$ for different isotopes. Most notably, the difference between the left and right side of the cortex in the ^{157}Gd -channel of iGd-10 is confirmed using the $\bar{\partial}^{(L-R)}$ metric (see Fig. 5-14(c)). The value of $\bar{\partial}^{(L-R)}(\text{CTX}, ^{157}\text{Gd}) \approx 2$ in the iGd-10 brain suggests that the difference between the mean value of the left and right side of the cortex is nearly twice as large as the interquartile range (IQR)^V. Additionally, the relatively large negative value of $\bar{\partial}^{(L-R)}(\text{CTX}, ^{57}\text{Fe})$ confirmed the visible high-intensity aberration on the right side of the dorsal part of the cortex in the ^{57}Fe -channel of iGd-12 (Fig. 5-14). While the four endogenous^{VI} isotopes (^{31}P , ^{57}Fe , ^{63}Cu , ^{64}Zn) would be expected to have approximately equal distributions on the left and right sides of the brain, particularly in the sham subject (iGd-12), there is not a strong confirmation of this hypothesis. The potential cause for some of these inequities are discussed in Section 7.2.

Anatomical boundaries were also produced using MMMCIR between \mathcal{A} and \vec{T} . Visualizations of the anatomical boundaries on the MIMS brain images are shown in Fig. 5-15(a) and 5-15(b) for iGd-12 and iGd-10 respectively. Both the spatial ex-

^VFor a standard normal distribution (zero mean, unit variance), 50% of the data lie within the IQR

^{VI}definition in biology: growing or originating from within an organism

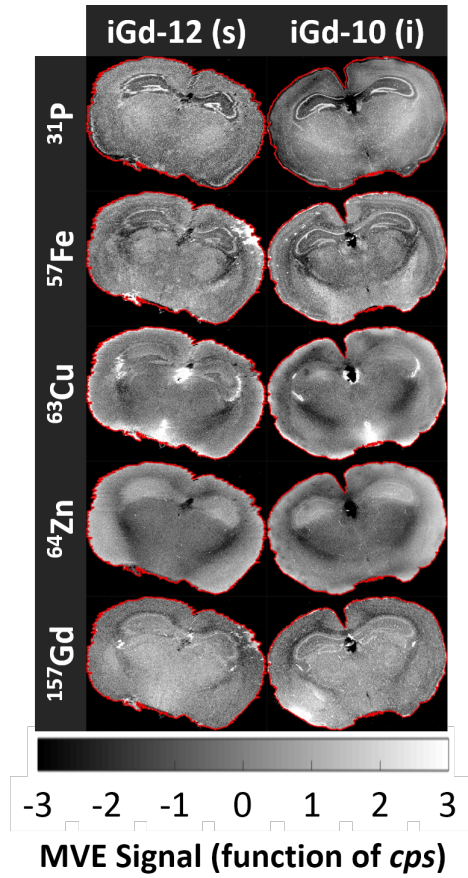
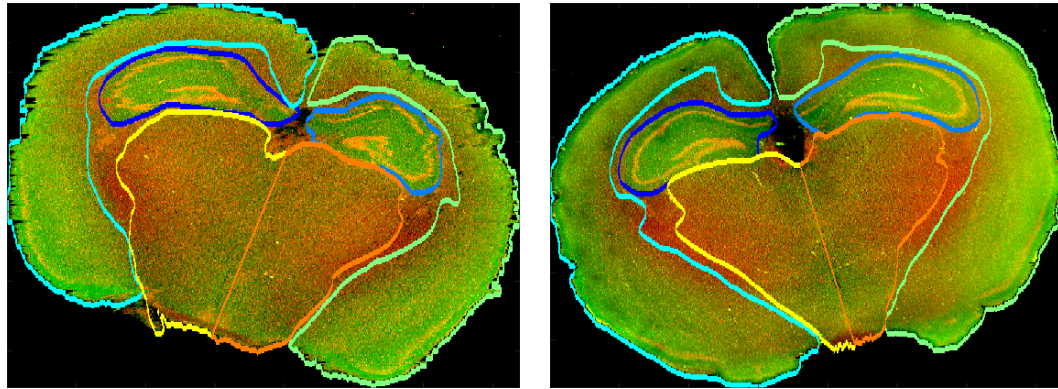
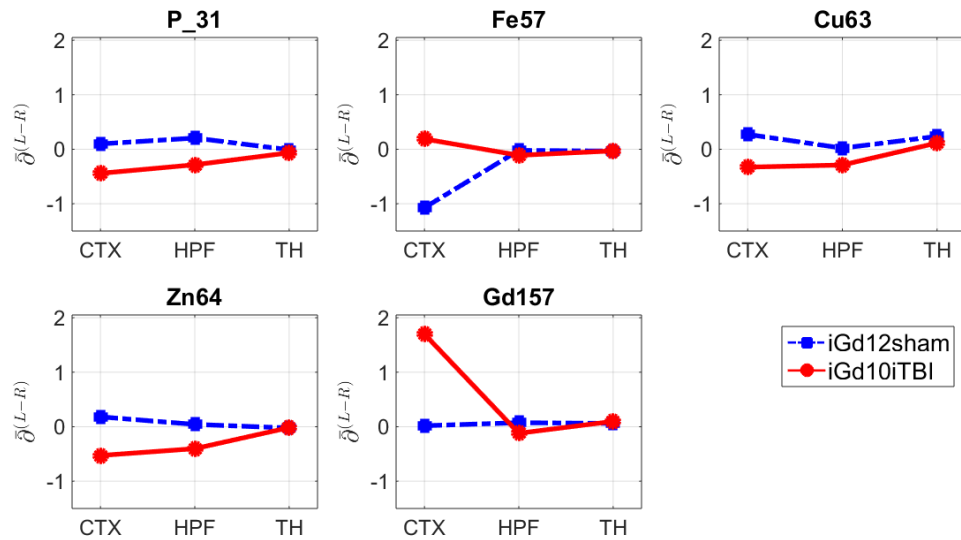


Figure 5-13: Gadolinium-injected MIMS brain images for relevant isotopes. All images are MVE to have standard normal intensity distributions of foreground pixels, and are visually limited to the range of the values between ± 3 . The (s) indicates the sham sample and the (i) indicates the impact neurotrauma sample.



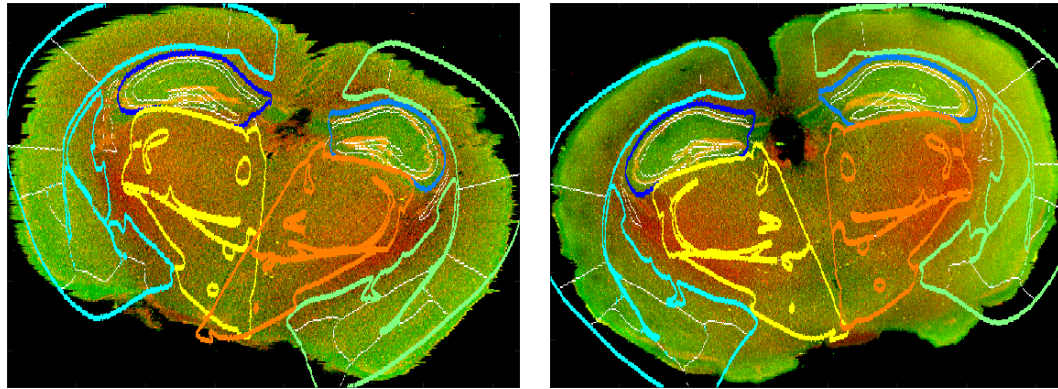
(a) iGd-12 manual segmentation

(b) iGd-10 manual segmentation



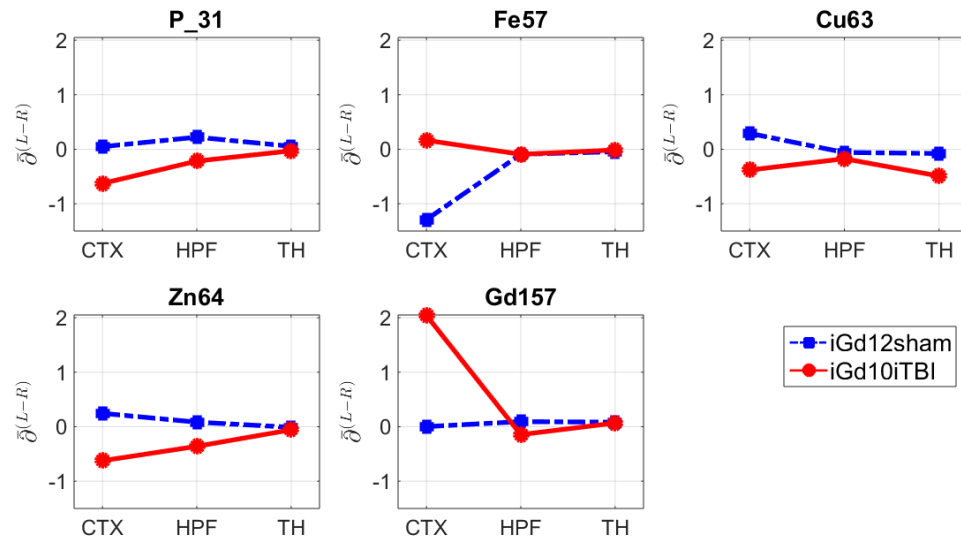
(c) Isotope levels in manually-segmented subgroups

Figure 5-14: All MIMS brain images are representations of the MVE signal for ^{31}P , represented as red, and ^{64}Zn , represented as green. The top row of images show the manual outlines for the three anatomical subgroups for (a) iGd-12 and (b) iGd-10. (c) Plots of the metric $\bar{\delta}^{(L-R)}$ for the selected isotopes.



(a) iGd-12 MIMCIR segmentation

(b) iGd-10 MIMCIR segmentation



(c) Isotope levels in MIMCIR segmented subgroups

Figure 5-15: All MIMS brain images are representations of the MVE signal for ^{31}P , represented as red, and ^{64}Zn , represented as green. The top row of images show atlas registration derived outlines for the three anatomical subgroups for (a) iGd-12 and (b) iGd-10. (c) Plots of the metric $\delta^{(L-R)}$ for the selected isotopes.

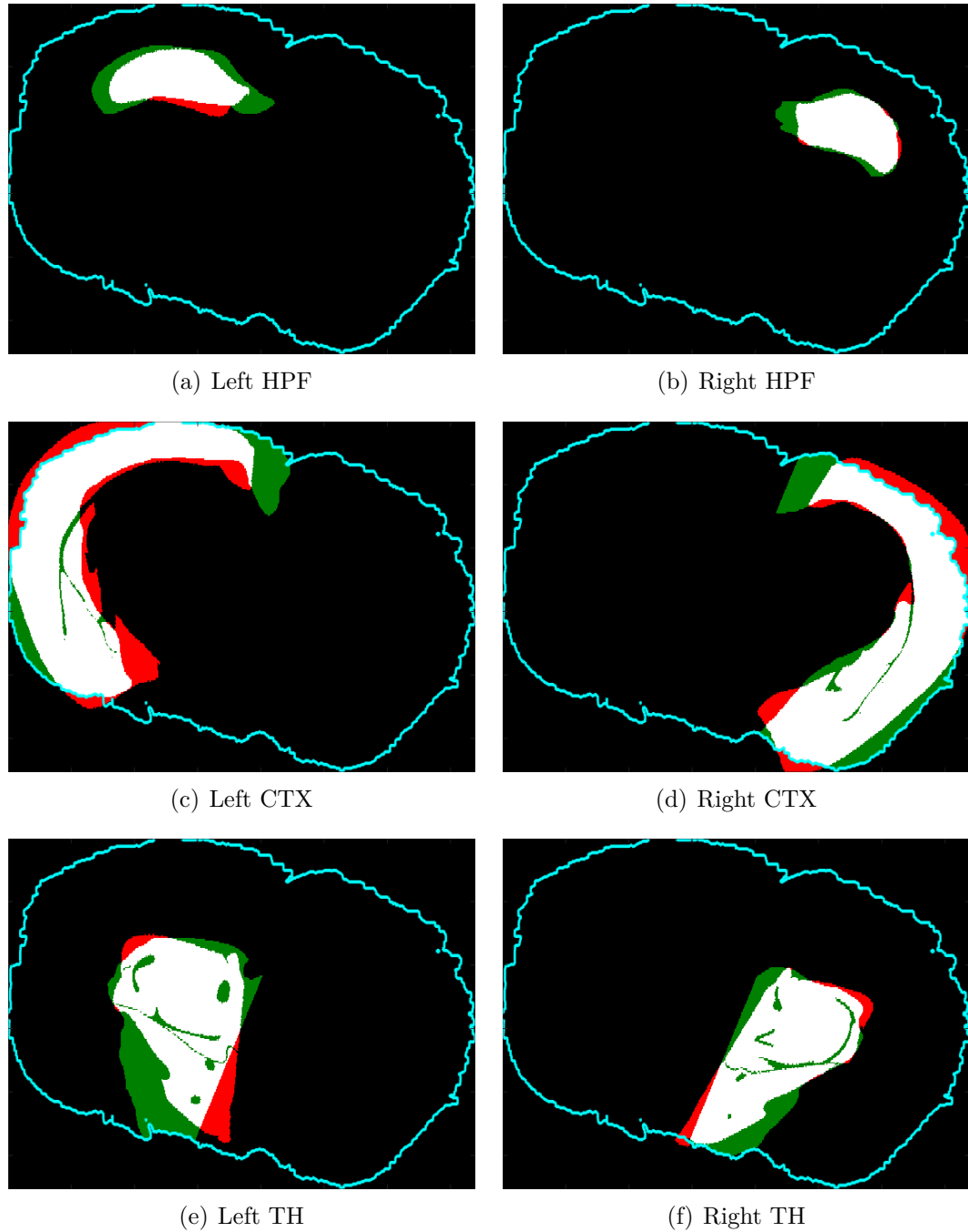


Figure 5-16: Visualization of anatomical subgroup segments for iGd-12. The colors in the image indicate the following: **White** – both manual and MMMCIR subgroups agree; **Green** – only manual segmentation (not MMMCIR) indicates the area as belonging to the corresponding subgroup; **Red** – only MMMCIR derived segmentation (not manual) indicates the area as belonging to the corresponding subgroup.

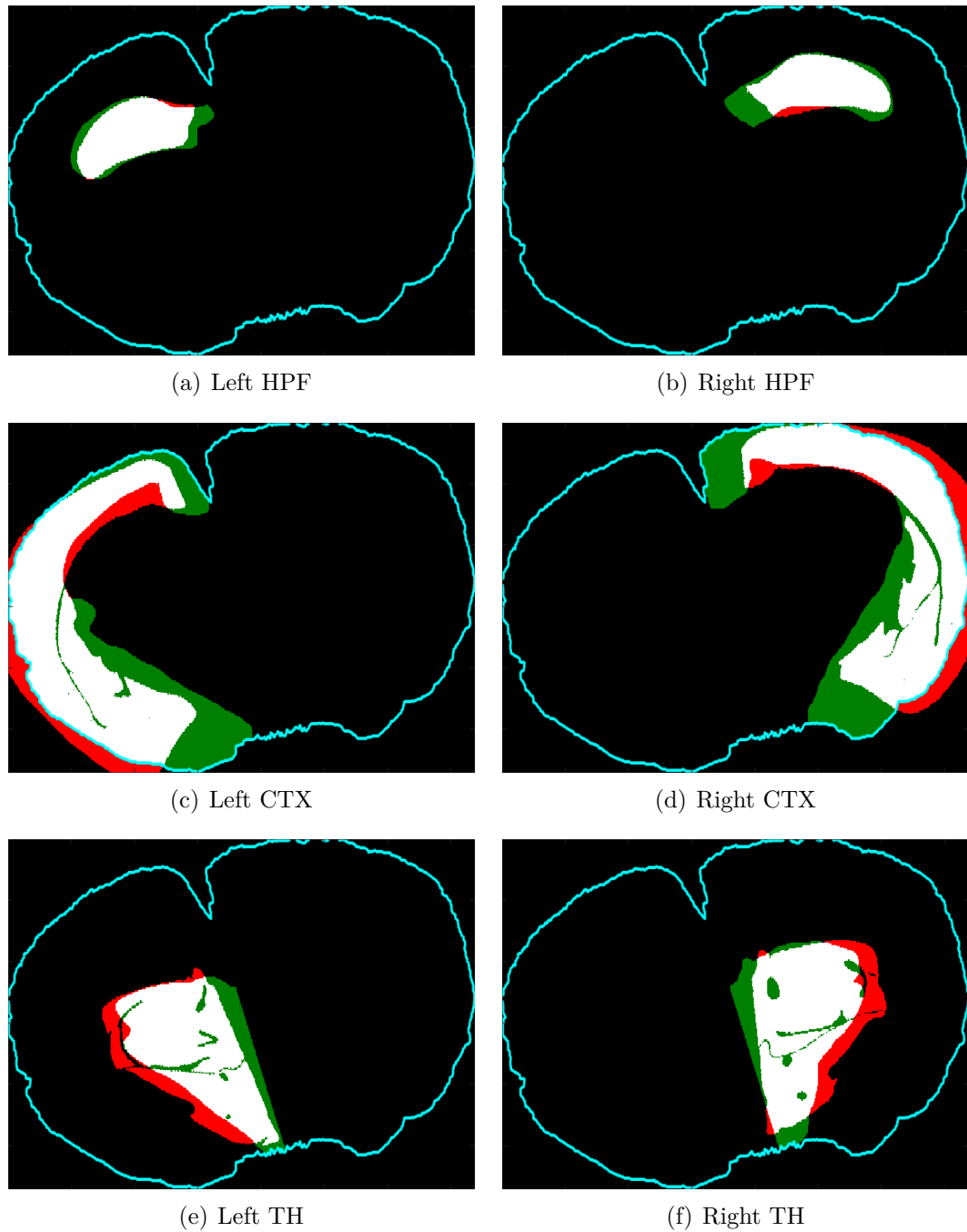


Figure 5-17: Visualization of anatomical subgroup segments for iGd-10. The colors in the image indicate the following: **White** – both manual and MMMCIR subgroups agree; **Green** – only manual segmentation (not MMMCIR) indicates the area as belonging to the corresponding subgroup; **Red** – only MMMCIR derived segmentation (not manual) indicates the area as belonging to the corresponding subgroup.

tent of the subgroups produced by manual segmentation and the MMMCIR with an AMBA image as well as the resulting values of $\bar{\partial}^{(L-R)}(g, i)$ were compared. A visualization comparing manually segmented subgroups, \mathcal{G}_{manual} , and MMMCIR derived subgroups, \mathcal{G}_{MMMCIR} , can be found in Figs. 5-16 and 5-17 for iGd-12 and iGd-10 respectively.

While the subgroups derived by manual segmentation and by MMMCIR do have a large degree of correspondence, one of the most notable deviations is that of the cortex. This is likely due to the fact that pixels from \mathcal{A} which corresponded to background pixels of \vec{I} in the registration procedure were not included in the computation of mutual information. Since these areas were not penalized (indeed if included they are actually favored, as discussed in Section 5.4.4), internal structures had a greater contribution to the final transformation. The deviation of the MMMCIR derived and the manually defined subgroup labels are likely a result of several contributing factors, including:

- anisotropic shrinkage of tissue introduced during the fixation process resulting in differing relationships between anatomical structures in the two input images
- suboptimal transformation parameters
- differences between \mathcal{A} section selected and true CVR-coordinate position of \vec{I}

Recommended extensions to address some of these challenges are discussed in Section 7.2.

Despite the difference between \mathcal{G}_{manual} and \mathcal{G}_{MMMCIR} , the values for $\bar{\partial}^{(L-R)}(g, i)$ did not vary significantly. The two most significant and explanatory values using the manual segmentations (the high intensity ^{157}Gd in the left cortex of iGd-10 and the high intensity ^{57}Fe in the right cortex of iGd-12) are very close in magnitude using

\mathcal{G}_{MMMCIR} . Some more drastic differences between $\bar{\partial}^{(L-R)}(g, i)$ values calculated using both segmentation methods are in the ^{63}Cu associated values. This is likely due to differential inclusion of the ventricles and, more specifically, the choroid plexus, which demonstrate expectedly high concentrations of copper. Since the ^{63}Cu -channel is not used for either manual or MMMCIR segmentation, its characteristics do not influence the results of \mathcal{G}_{manual} and \mathcal{G}_{MMMCIR} .

5.4.2 Assessment of Nanoparticle-Injected Cohort

Images of the five isotopes selected for detailed analysis (^{31}P , ^{57}Fe , ^{63}Cu , ^{64}Zn , ^{157}Gd) for all samples in the iNP cohort are provided in Fig. 5-18. The ^{31}P and ^{64}Zn channels were used as the 2-channel MIMS brain image input for MMMCIR. The \mathcal{A} image specified in Table 5.2 was registered to each sample for each side of the brain. The resulting outlines from registration with $\mathcal{A}^{(L)}$ and $\mathcal{A}^{(R)}$ can be seen in Fig. 5-19. While registration accuracy could not be numerically evaluated, the method subjectively succeeded at defining anatomical boundaries for the coronal MIMS brain image selected for evaluation in this cohort. Likely due to fewer tissue processing artifacts in the tissues from the iNP experiment, subgroup segments followed visual tissue boundaries more closely than the MMMCIR results from the iGd experiment. Anatomical subgroups were derived from \mathcal{A} and then used used to compute $\bar{\partial}^{(L-R)}(g, i) \forall g, i$. These results are plotted in Fig. 5-20.

While no large-scale population analyses measuring the normal spatial distribution of endogenous isotopes in the mouse brain have been conducted, it is reasonable to hypothesize that the levels of $\{^{31}\text{P}, ^{57}\text{Fe}, ^{63}\text{Cu}, ^{64}\text{Zn}\}$ on the left and right sides would be equal for a naive mouse. Considering the non-impacted samples in the iNP experiment, $\{35, 12, 22\}$, the $\bar{\partial}^{(L-R)}(g, i)$ values for these isotopes were in some cases

larger than the differences in the impact samples {14, 26, 27, 30}. One individual in particular, iNP-12, consistently had among the highest $\bar{\partial}^{(L-R)}(g, i)$ values for the endogenous isotopes, alerting a need for more in-depth analysis. Additionally, while the pathogenic biomarker ^{157}Gd is an isotope of particular interest, it can be seen from Fig. 5-18 that for the iNP-cohort, the isotope images had little to no signal. As such, the values for $\bar{\partial}^{(L-R)}(g, ^{157}\text{Gd})$ can be considered to be dominated by noise, and are therefore uninformative for drawing any conclusions.

Figure 5-21 plots the raw mean values^{VII} on the left and right side within the anatomical subgroups for two channels in particular, ^{31}P (Fig. 5-21(a)) and ^{64}Zn (Fig. 5-21(b)). Examination of these plots supports some of the underlying hypothesis for the unexpected $\bar{\partial}^{(L-R)}(g, i)$ values observed, particularly for iNP-12. While it is not unexpected that each elemental isotope may have its own characteristic signal variations and unique interferences, a consistent bias – whereby one side of the brain consistently has higher signal levels than the other side of the brain – appears to affect multiple samples; most clearly iNP-12 and iNP-26. Determining whether these biases between the mean signal values on the left and right side are of a biological origin would require a larger sample size and additional validation of the MIMS brain images. However, given the consistent magnitude of the difference, particularly in a non-INT sample, these results suggest that signal drift throughout the course of the MIMS acquisition must be corrected before drawing conclusions from these data.

^{VII}The raw images were median filtered with a 3×5 filter to diminish the effect of high-intensity outliers in the isotope image

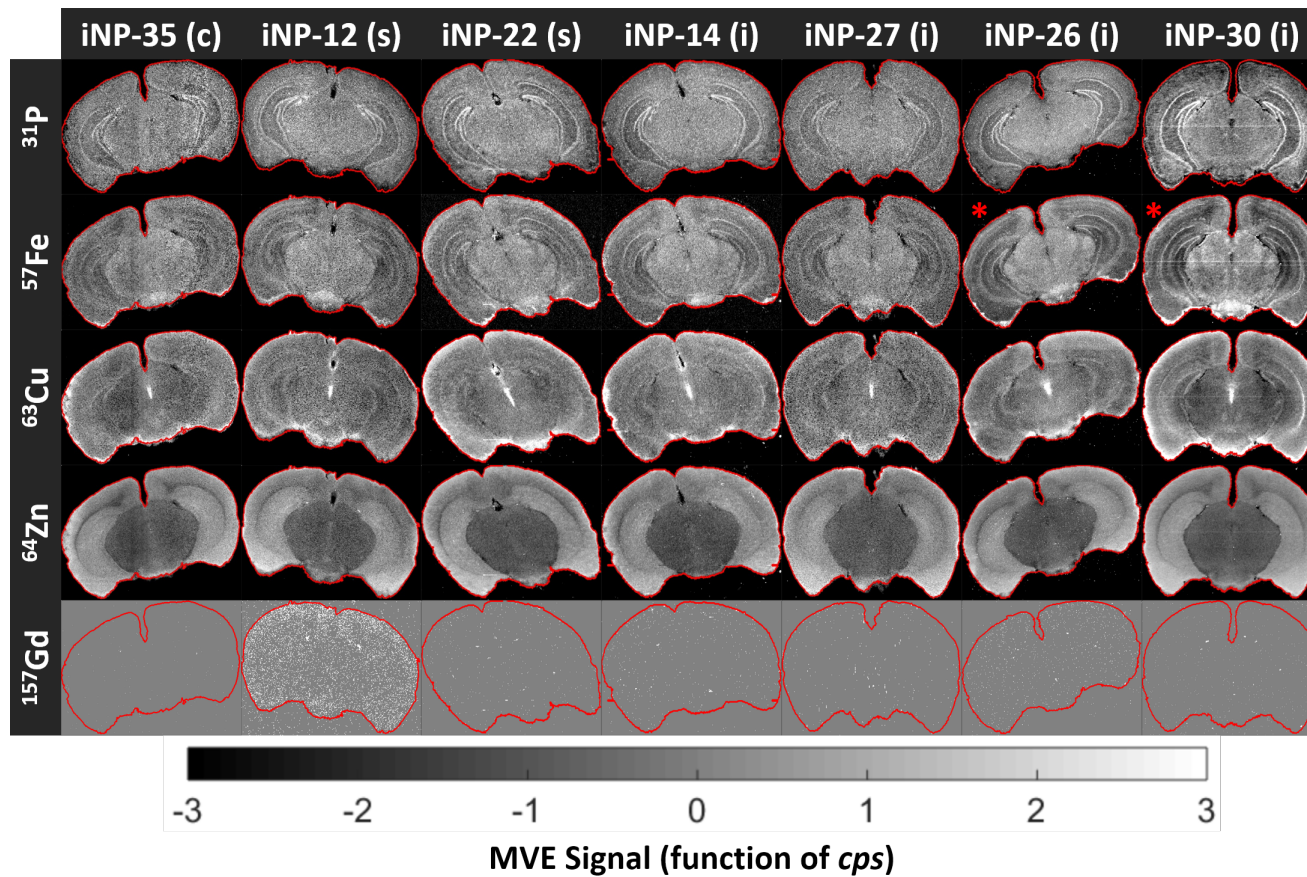


Figure 5-18: Nanoparticle-injected MIMS brain images for relevant isotopes. All images are MVE to have standard normal intensity distributions of foreground pixels, and are visually limited in the range of ± 3 . The (c) indicates a control sample, (s) indicates a sham sample and the (i) indicates a impact neurotrauma sample. The * symbol in the upper left corner of iNP-26 and iNP-30 indicate that an ^{57}Fe isotope was not acquired for these samples. Shown instead is the ^{56}Fe image.

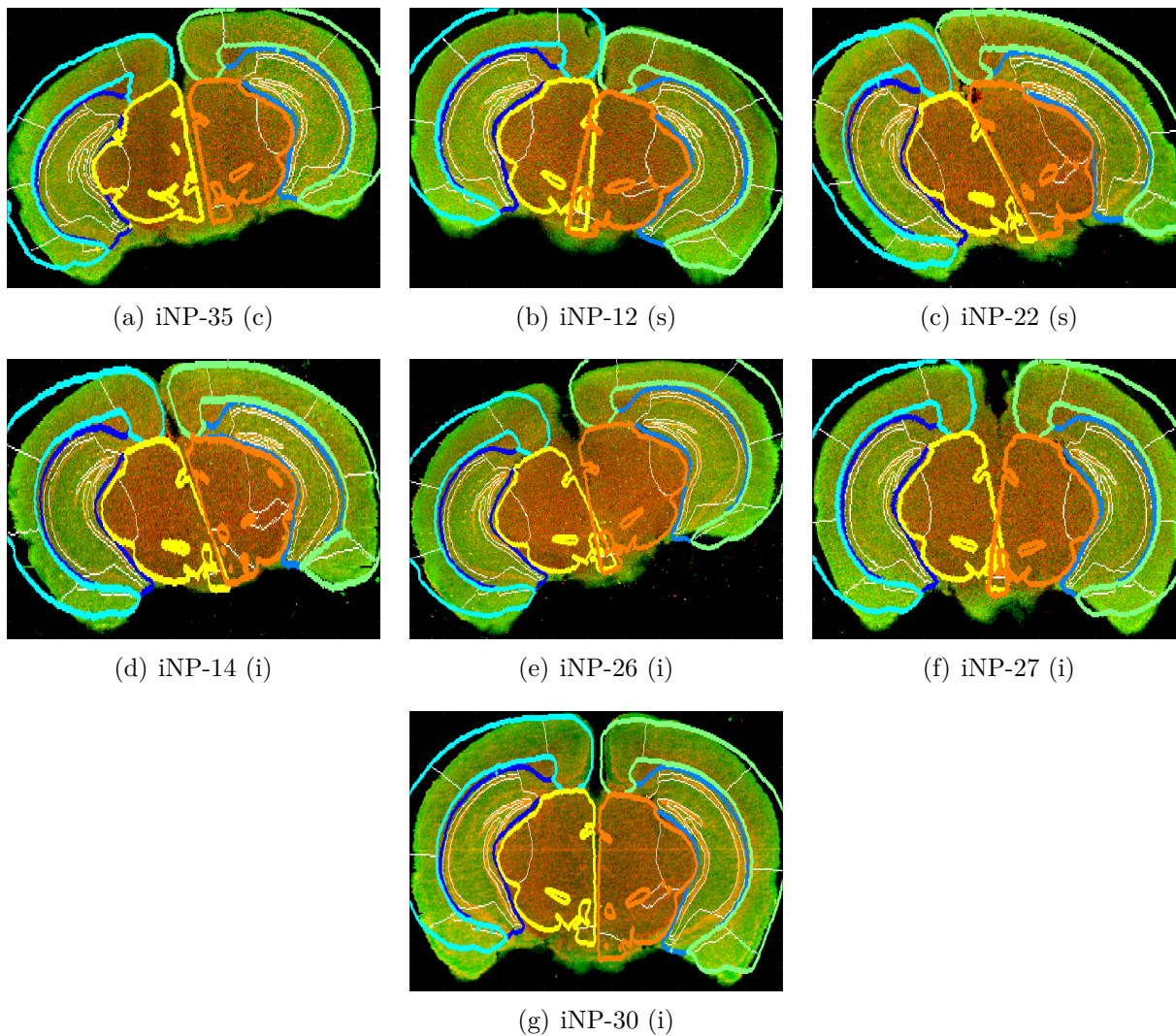


Figure 5-19: All MIMS brain images are representations of the MVE signal for ^{31}P , represented as red, and ^{64}Zn , represented as green. Images show outlines derived from atlas registrations for the three anatomical subgroups with white outlines showing the anatomical regions in the original AMBA images.

5.4.3 Mask Registration for MIMS Spatial Corrections

As mentioned in Section 5.3.2, the Nissl image tissue mask, $M_{\mathcal{N}}$, is registered to the MIMS tissue mask, $M_{\vec{T}}$. This procedure produces a set of transformation parameters, $\vec{\mu}_0$, which parametrize the affine transformation aligning $M_{\mathcal{N}}$ to $M_{\vec{T}}$. While this transformation was of interest for MMMCIR state-space specification, the inverse operation is also of interest. Since one of the goals of the AMBA is to provide a database of coronal section exemplars, the image aspect ratios and orientations can be treated as a gold-standard for tissue representation. Therefore, for representation purposes, aligning \vec{T} to \mathcal{N} is also beneficial for standardized visualization of MIMS.

One of the benefits to using the affine transformation model is that it is invertible by simply computing the inverse matrix $A_{\vec{\mu}_0}^{-1}$ (derived in Appendix C). Therefore, given a transformation which aligns $M_{\mathcal{N}}$ to $M_{\vec{T}}$ reasonably well, the transformation which aligns $M_{\vec{T}}$ to $M_{\mathcal{N}}$ is an automatic biproduct. In some cases, timing irregularities in the acquisition process lead to inappropriately scaled MIMS, as in Fig. 5-22(a). Using the mask registration parameters to determine $A_{\vec{\mu}_0}^{-1}$ and applying the inverse transformation to the MIMS, these spatial irregularities can be corrected (Fig. 5-22(b)). Other corrections shown in Fig. 5-22 mainly reorient the MIMS sections and slightly adjust the horizontal-to-vertical scaling ratio.

5.4.4 Factors Affecting Image Registration Outcome

The MMMCIR method developed offers a variety of design choices as well as tuning parameters. Before generating results for all subjects, a several experiments were conducted to support the procedure and parameters ultimately used for all images in the iGd and iNP cohorts (given in Table 5.4). To summarize, experiments were run

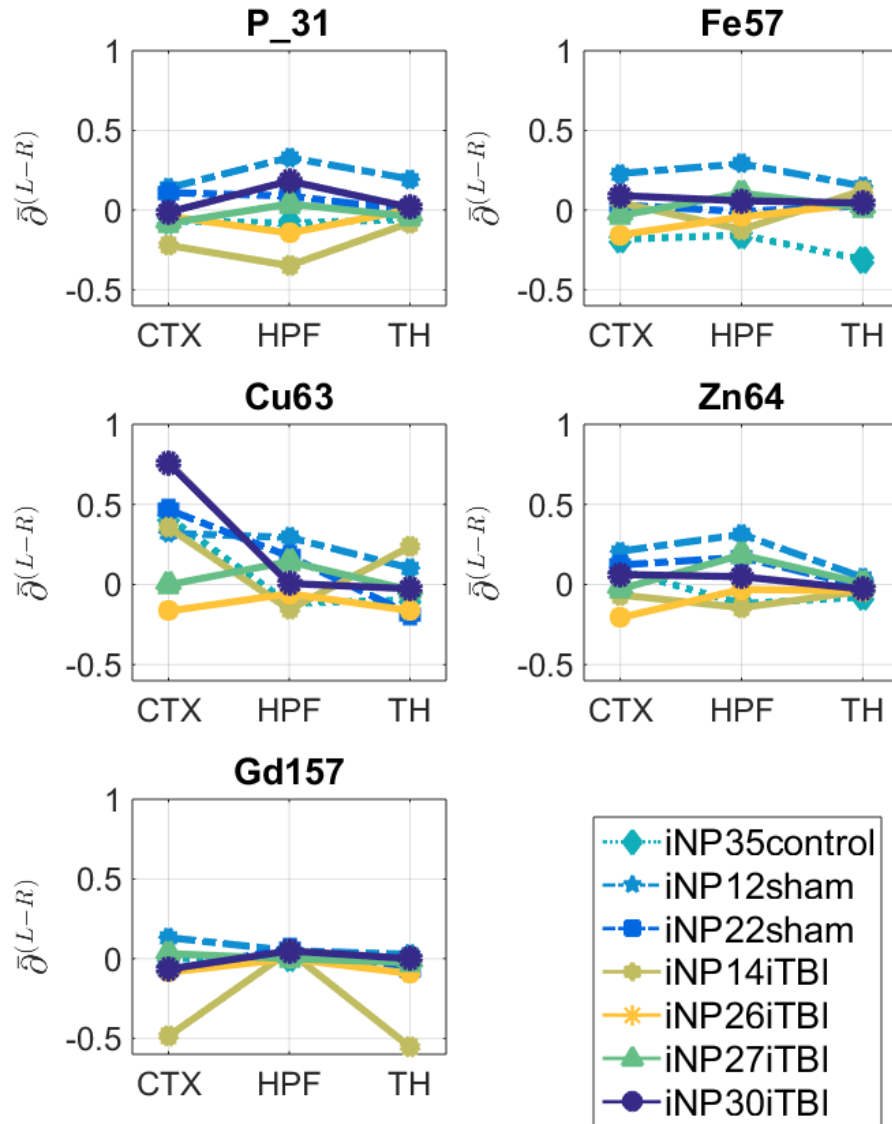


Figure 5-20: Values of the normalized side difference metric for the five isotopes considered for analysis. Each sample in the iNP cohort has a unique line color and marker. The lines are connected only to aid in the tracking of $\bar{\delta}^{(L-R)}(g, i)$ for the different anatomical subgroups. Samples not exposed to an INT have dashed lines and samples exposed to INT have solid lines.

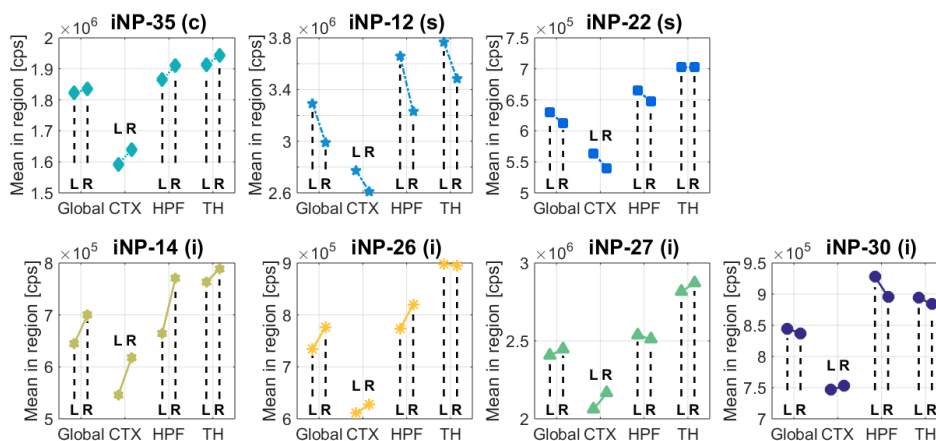
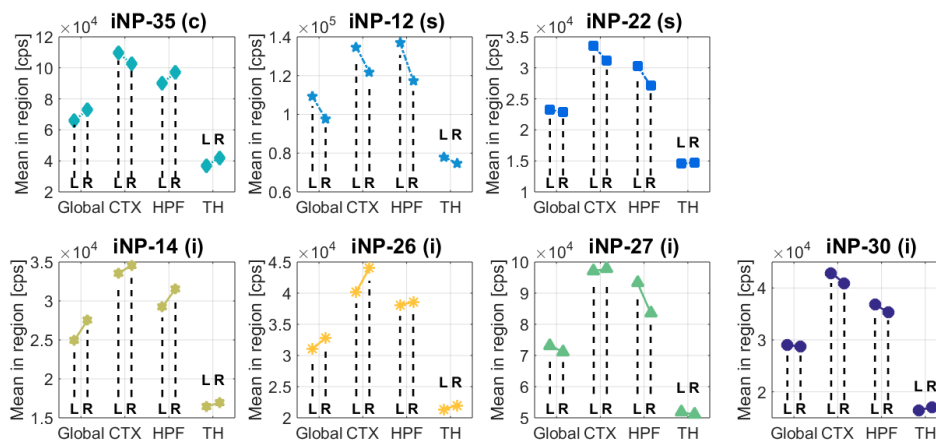
(a) ^{31}P (b) ^{64}Zn

Figure 5-21: Each data point represents the mean value of the median filtered isotope image for (a) ^{31}P and (b) ^{64}Zn within the indicated anatomical subgroup (shown on the horizontal axis). The “Global” group indicates pixels in the tissue area (thus “Global-L” is the mean of the pixels in the tissue area on the left-side).

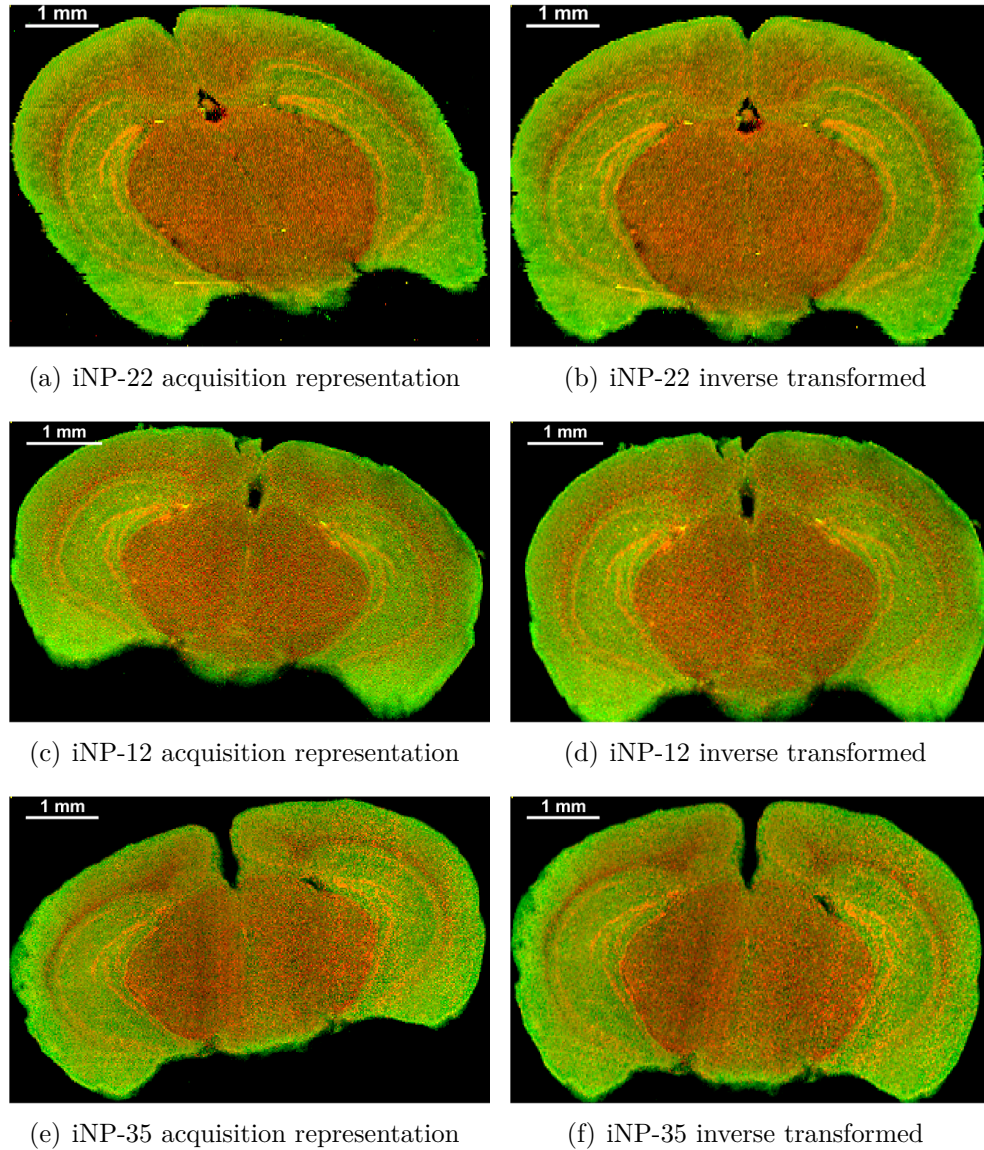


Figure 5-22: All MIMS brain images are representations of the MVE signal for ^{31}P , represented as red, and ^{64}Zn , represented as green. The left-column of images are MIMS brain images shown in the acquired orientation with spatial scaling determined from the acquisition parameters applied. The right-column shows the MIMS brain images with the applied inverse transformation, $\phi \left\{ \vec{I} \left(A_{\vec{\mu}_0}^{-1} \cdot \vec{q} \right) \right\}$ where $\phi\{\cdot\}$ is the bicubic interpolator.

using a two-channel (^{31}P and ^{64}Zn) MIMS, \vec{I} , as the fixed image and the $\mathcal{A}^{(side)}$ as the moving image. The cost function was a summed-MI metric:

$$J^\Sigma(\vec{I}, \mathcal{A}^{(side)}) = J(I^{(31P)}, \mathcal{A}^{(side)}) + J(I^{(64Zn)}, \mathcal{A}^{(side)})$$

The distributions needed to calculate $J(\bullet, \bullet)$ were quantized using a 40-bins per dimension and a Gaussian kernel. Any correspondences with background areas in either image were ignored in the calculation of $J^\Sigma(\vec{I}, \mathcal{A}^{(side)})$. Rather than using the Nissl image for registration, that atlas image was used. For each design choice discussed below, the other default design choices were used unless otherwise stated. The optimal parameters obtained using each discussed design variation are applied to $\mathcal{A}^{(L)}$ and the anatomical segmentations are shown on the iNP-30 image in Fig. 5-23.

Registration with Nissl Image versus with Atlas Image

The performance of the MMMCIR function depends on how closely the underlying data follow the assumption that the two input images depict corresponding objects with corresponding numerical properties. Because the Nissl image shows the location of the cell nuclei, a clear division between different anatomical segments is not always present. In addition, the Nissl image's intensities more closely resemble a binary image's (cell nuclei or no cell nuclei) than an image with variable intensities. As seen in Fig. 5-6(a), different cellular densities clearly delineate the hippocampal formation from the cortex and thalamus anatomical subgroups, but visually it is unclear whether the statistical properties of the cortex vary significantly from those of the thalamus, for instance. The anatomical segmentation result achieved when registering \vec{I} with \mathcal{N} are shown in Fig. 5-23(b).

Since the most clear structure visible in \mathcal{N} is the pyramidal cell layer (PCL), this is

very likely the feature which drives the alignment between \vec{I} and \mathcal{N} . To test this hypothesis, \mathcal{N} was registered to the ^{64}Zn -channel only, which does not have a clear intensity signal for the PCL. As expected, in a channel without the prominent PCL feature, the registration result was clearly uninformative.

Including Background Pixels in MI Calculation

The anatomical segmentation achieved when including the background in the calculation for MI is shown in Fig. 5.23(c). These are particularly poor results likely due to the fact that \mathcal{A} has anatomical segments that are perfectly uniform. Therefore, since the background is also nearly uniform, this promotes the maximal allowable alignment (meaning allowed by the state-space constraints) between peripheral anatomical regions and the background. While this can be prevented by excluding any correspondence between any pixel corresponding to a background area (Fig. 5.23(a)), this strategy also has the adverse effect of not enforcing a strict adherence to tissue boundaries and instead enforcing only meaningful (as measured by MI) correspondence between internal tissue features. If desired, tissue boundary adherence may be incorporated into the cost function by applying a penalty to background pixel correspondences thereby increasing the cost of background-aligned pixels.

True MI Using Joint Density Function versus Sum of Marginal MI

The calculation of MI (Eqn. 4.20) between two images requires the a representation of the joint distribution $p(\vec{x}, \vec{y})$ where \vec{x} represent the values in the fixed image and \vec{y} represent the values in the moving image. Consider the images used to generate the results where \mathcal{F} is a two-channel image taking values $x^{(1)}$ and $x^{(2)}$ and \mathcal{M} is a

one-channel image taking values y . The joint mutual information can be written as:

$$J(\mathcal{F}, \mathcal{M}) = \sum_{\underbrace{x^{(1)} x^{(2)} y}_{\sum_{x^{(1)}, x^{(2)}, y}}} p(x^{(1)}, x^{(2)}, y) \ln \left(\frac{p(x^{(1)}, x^{(2)}, y)}{p(x^{(1)}, x^{(2)})p(y)} \right)$$

If $x^{(1)}, x^{(2)}$ are independent then $p(x^{(1)}, x^{(2)}) = p(x^{(1)})p(x^{(2)})$ giving

$$\begin{aligned} J(\mathcal{F}, \mathcal{M}) &= \sum_{x^{(1)}, x^{(2)}, y} p(x^{(1)}, x^{(2)}, y) \ln \left(\frac{p(x^{(1)}, x^{(2)}, y)}{p(x^{(1)})p(x^{(2)})p(y)} \right) \\ &= \sum_{x^{(1)}, x^{(2)}, y} p(x^{(1)}, x^{(2)}, y) [\ln p(x^{(1)}, x^{(2)}, y) - \ln p(x^{(1)}) - \ln p(x^{(2)}) - \ln p(y)] \end{aligned}$$

The summed mutual information, J^Σ , is essentially the sum of the MI values between the moving image and each channel of the fixed image:

$$\begin{aligned} J^\Sigma(\mathcal{F}, \mathcal{M}) &= \sum_{x^{(1)}, y} p(x^{(1)}, y) \ln \left(\frac{p(x^{(1)}, y)}{p(x^{(1)})p(y)} \right) + \sum_{x^{(2)}, y} p(x^{(2)}, y) \ln \left(\frac{p(x^{(2)}, y)}{p(x^{(2)})p(y)} \right) \\ &= \sum_{x^{(1)}, y} p(x^{(1)}, y) [\ln(p(x^{(1)}, y)) - \ln p(x^{(1)}) - \ln p(y)] \\ &\quad + \sum_{x^{(2)}, y} p(x^{(2)}, y) [\ln(p(x^{(2)}, y)) - \ln p(x^{(2)}) - \ln p(y)] \end{aligned}$$

To separate the joint distribution, the most liberal assumption one can venture is that $x^{(1)}$ and $x^{(2)}$ are conditionally independent on y . Therefore, using Bayes rule, the following expression can be used for the joint distribution:

$$p(x^{(1)}, x^{(2)}, y) = p(x^{(1)}, x^{(2)}|y) p(y) = p(x^{(1)}|y) p(x^{(2)}|y) p(y)$$

Substituting this into the expression for $J(\mathcal{F}, \mathcal{M})$, we have:

$$\begin{aligned} J(\mathcal{F}, \mathcal{M}) &= \sum_{x^{(1)}, x^{(2)}, y} p(x^{(1)}|y) p(x^{(2)}|y) p(y) \\ &\quad \times [\ln p(x^{(1)}|y) + \ln p(x^{(2)}|y) + \ln p(y) - \ln p(x^{(1)}) - \ln p(x^{(2)}) - \ln p(y)] \end{aligned}$$

Separating terms and comparing $J(\mathcal{F}, \mathcal{M})$ to $J^\Sigma(\mathcal{F}, \mathcal{M})$ and using Bayes rule on J^Σ we have:

$$J(\mathcal{F}, \mathcal{M}) = \sum_{x^{(1)}, x^{(2)}, y} p(x^{(1)}|y) p(x^{(2)}|y) p(y) \left[\ln \frac{p(x^{(1)}|y)}{p(x^{(1)})} + \ln \frac{p(x^{(2)}|y)}{p(x^{(2)})} \right]$$

$$J^\Sigma(\mathcal{F}, \mathcal{M}) = \sum_{x^{(1)}, y} p(x^{(1)}|y) p(y) \ln \frac{p(x^{(1)}|y)}{p(x^{(1)})} + \sum_{x^{(2)}, y} p(x^{(2)}|y) p(y) \ln \frac{p(x^{(2)}|y)}{p(x^{(2)})}$$

Through these calculations, we see that under the assumption that $x^{(1)}, x^{(2)}$ are independent and conditionally independent on y ($p(x^{(1)}, x^{(2)}|y) = p(x^{(1)}|y) p(x^{(2)}|y)$), the expressions for J and J^Σ are equivalent. In this sense and under these assumptions, it provides reasonable support for J^Σ acting as a reasonable surrogate to J .

Figure 5-24 depicts the anatomical segmentation results obtained using J (Fig. 5-23(d)) and J^Σ (Fig. 5-23(a)) for cost functions. In both experiments, the Epanechnikov kernel was used with 30 bins per variable. Qualitatively, the outcomes using each result are indistinguishable. The optimal physical transformation parameters and the run times using each method are given in Table 5.5. Generally, as discussed in Section 4.5.6, using more bins and using the Gaussian kernel for estimating the joint distribution $p(\vec{x}, y)$ seems to give the most stable results for the cost function. To determine whether using the Epanechnikov results in a different shape of the cost function, the values for J and J^Σ were calculated for small perturbations about the $\vec{\mu}_{opt}$ parameters acquired using J . The plots in Fig. 5-24(f) show the results using J and J^Σ with Gaussian and Epanechnikov kernels. From this analysis, we see that the general shape provided by J -versus- J^Σ using either kernel are very similar. For a given kernel, values for J^Σ are greater than J and for a given MI computation method, values using the Epanechnikov kernel are greater than those using the Gaussian kernel.

Table 5.5: Experimental outcomes for registration using true-MI versus summed-MI on iNP-30 with 30 bins per dimension and an Epanechnikov kernel.

Parameter	Result via J	Result via J^Σ
$\vec{\mu}_{opt}$ $\begin{bmatrix} t_x \\ t_y \\ \theta \\ s_x \\ s_y \\ s_k \end{bmatrix}$	$\begin{bmatrix} 10.8 \\ 14.0 \\ -0.0011 \\ 0.99 \\ 1.12 \\ 0.0317 \end{bmatrix}$	$\begin{bmatrix} 8.5 \\ 12.7 \\ -0.0036 \\ 0.99 \\ 1.11 \\ 0.0169 \end{bmatrix}$
Run Time [<i>min</i>]	364	53

Motivated by the negligible differences between the cost function computation method and the type of kernel used, the computation time dictated the final design choices made to perform registration on the entire cohort. The implementation used to compute the joint distribution requires polynomial time whereas summing the MI of pairwise joint distributions requires only linear time making the method significantly faster in practice. Given the very small observable difference in anatomical segmentation performance and smoothness of the cost function, MMMCIR was run using the Gaussian kernel with 40 bins per dimension and J^Σ .

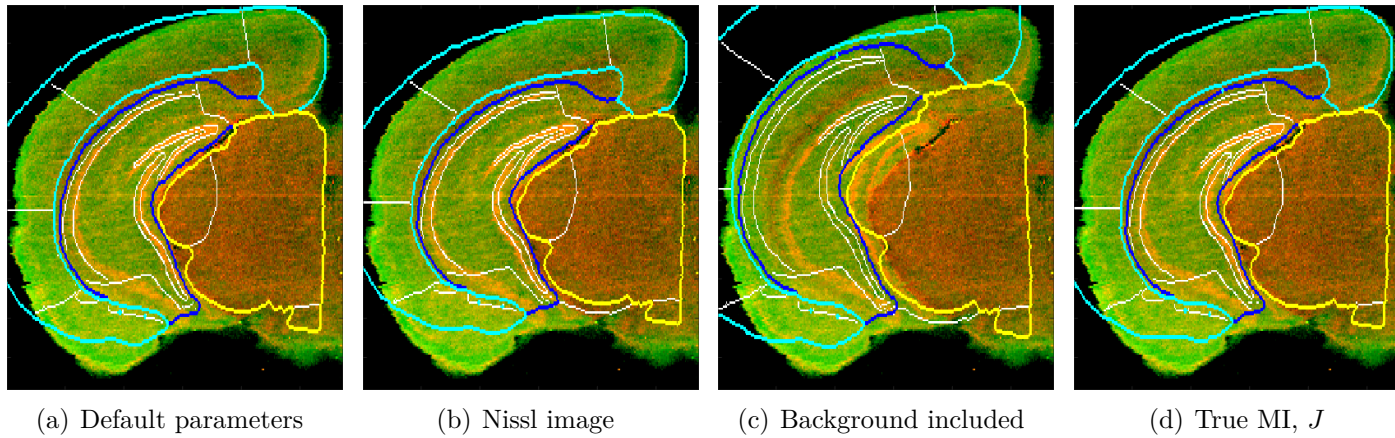


Figure 5.23: Comparison of registration results when including background pixel correspondences in the summed-MI calculation. MIMS are representations of the MVE signal for ^{31}P , represented as red, and ^{64}Zn , represented as green.

5.5 Summary of Contributions

This chapter has demonstrated the use of publicly available mouse brain atlases (Atlas, 2013) for automated anatomical segmentation of MIMS brain images. The method developed overcomes a variety of tissue processing artifacts by independently registering the left and the right sides of the brain. Using the developed multi-modal, multi-channel image registration, it was shown that given a MIMS brain image and a labeled atlas image from approximately the same coronal position, the MIMS brain images can be automatically segmented. These segments were subsequently used to identify differences between the corresponding anatomical regions on either side of the brain. These results numerically verified the observed increased ^{157}Gd -intensity in the left cortex of iGd-10 and provide convincing evidence for the need to correct for signal drift over the course of the MIMS acquisition process based on the results from the iNP cohort.

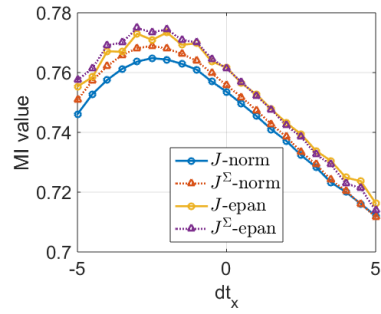
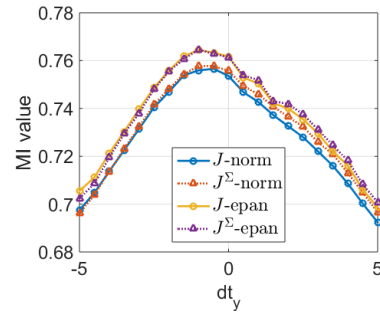
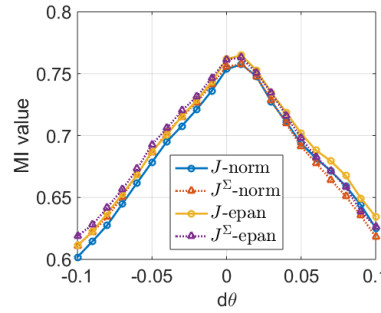
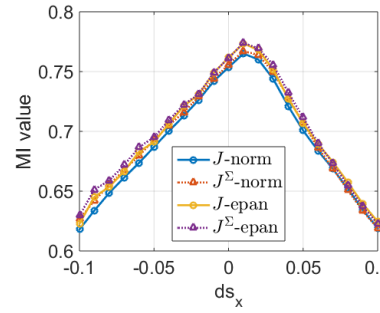
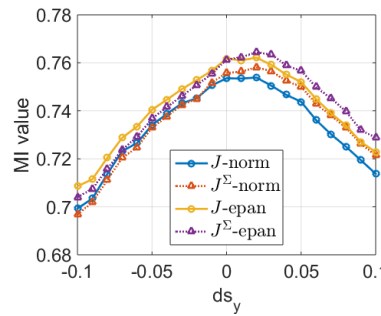
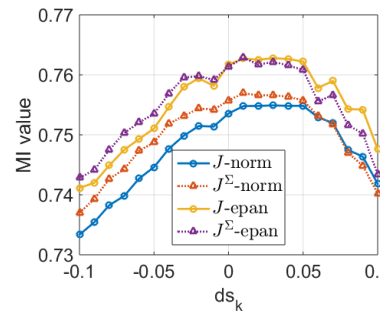
(a) MI values for $t_x = t_{x,opt} + dt_x$ (b) MI values for $t_y = t_{y,opt} + dt_y$ (c) MI values for $\theta = \theta_{opt} + d\theta$ (d) MI values for $s_x = s_{x,opt} + ds_x$ (e) MI values for $s_y = s_{y,opt} + ds_y$ (f) MI values for $s_k = s_{k,opt} + ds_k$

Figure 5·24: Comparison of registration results using true MI computation versus using summed-MI

Chapter 6

Analysis of Metallomic Images of Human Lacrimal Sac Biopsy Samples

6.1 Background

As one of the most exposed organs in the human body, the eye has a variety of accessory structures and physiological mechanisms to maintain normal function and ocular homeostasis. Two such structures that are affected by disease are the lacrimal sac and the nasolacrimal duct (Fig. 6-1). These structures are responsible for draining tears on the surface of the cornea, and can be obstructed by the formation of a concretion called a dacryolith. Dacryoliths have been found to be composed of a variety of materials including epithelial cells, lipids, amorphous debris with or without calcium and may contain bacteria or yeast (Hawes, 1988). The cause of pathogenesis is not well understood, but are in some cases thought to be initiated by bacterial load or a foreign body that serves as a nidus for further growth, such as an eyelash (Andreou and Rose, 2002; Jay and Lee, 1976).

Several retrospective studies have aggregated information regarding dacryocystorhinostomy (DCR) surgeries and the incidence of dacryoliths (Andreou and Rose, 2002; Anderson et al., 2003; Repp et al., 2009). A DCR is a surgical procedure performed in the event of a nasolacrimal duct (NLD) obstruction, often caused by the formation

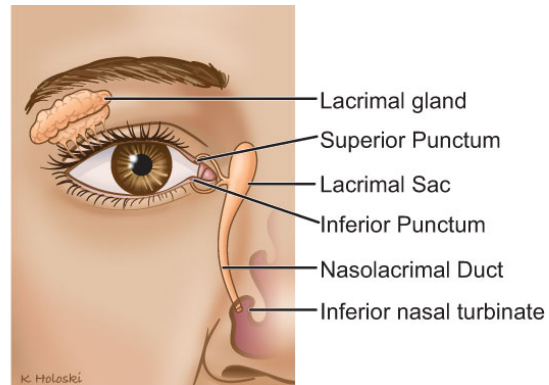


Figure 6-1: Anatomical diagram of lacrimal sac and nasolacrimal duct. Image from (Head and Neck Cancer Guide, 2017)

of a lacrimal sac dacryolith. The largest study to date by Anderson et al. (2003) aggregated ten years of clinical data from the Montgomery Ophthalmic Pathology Laboratory at Emory University and reported that of the 21,018 ophthalmic pathology specimens obtained between 1991 and 2001, 377 came from a DCR procedure. Prediction of the percentages of DCR cases required because of dacryoliths ranges from approximately 5.7% to 18% (Yazici et al., 2001; Repp et al., 2009).

A majority of dacryolith cases seem to occur in middle age and older women, though the statistic is often disputed likely due to the small numbers of individuals in the published studies (Repp et al., 2009). Nonetheless, given the unknown pathogenesis of dacryoliths and the apparent increased incidence in females, one hypothesis is that their formation is promoted by the introduction of toxic nanoparticles found in cosmetic and skin care products, as well as pollutants in the air. Imaging by metallic imaging mass spectrometry (MIMS) is uniquely suited to investigate this hypothesis.

6.2 Experimental Objective

Through a collaboration with surgeon Dr. Jeffery J. Hurwitz and pathologist Dr. David Howarth at Mount Sinai Hospital (MSH) in Toronto, Canada, we obtained eight lacrimal sac biopsy samples (LSBS) from five female individuals and one additional LSBS sample with no available clinical history. All tissue samples were procured under approved institutional review board (IRB) protocols at the Boston University School of Medicine (BUSM) and the equivalent approval was obtained from MSH. Tissue sharing was covered under a material transfer agreement between BUSM and MSH. All studies conformed with the principles of the Declaration of Helsinki. Relevant demographic and clinical information are provided in Table 6.1 and an image of the paraffin-embedded samples is provided in Fig. 6-2.

The ultimate goal of this project is to use these samples for a clinicopathological case study to investigate the presence of exogenous metals and the location of their occurrence within the samples with respect to clinically-relevant features such as epithelial cells, gram positive regions (of fungal origin), and lacrimal sac calcifications. As a preliminary assessment, the goal was to devise a MIMS acquisition method suitable for identification, localization, and quantification of metals in the samples. With the help of New England Eye Center's ophthalmic pathologist Dr. Nora Laver, hematoxylin and eosin (H&E) immunohistochemical (IHC) stained sections from the samples were used to identify various pathological features.

As will be explained in Section 6.3, a total of six MIMS sequences were acquired. Considering the LSBS for which more than one MIMS tissue image was available, a comparison of the signal quality and characteristics was conducted. Consistency of the resulting calibration curves acquired across different days and different instrument

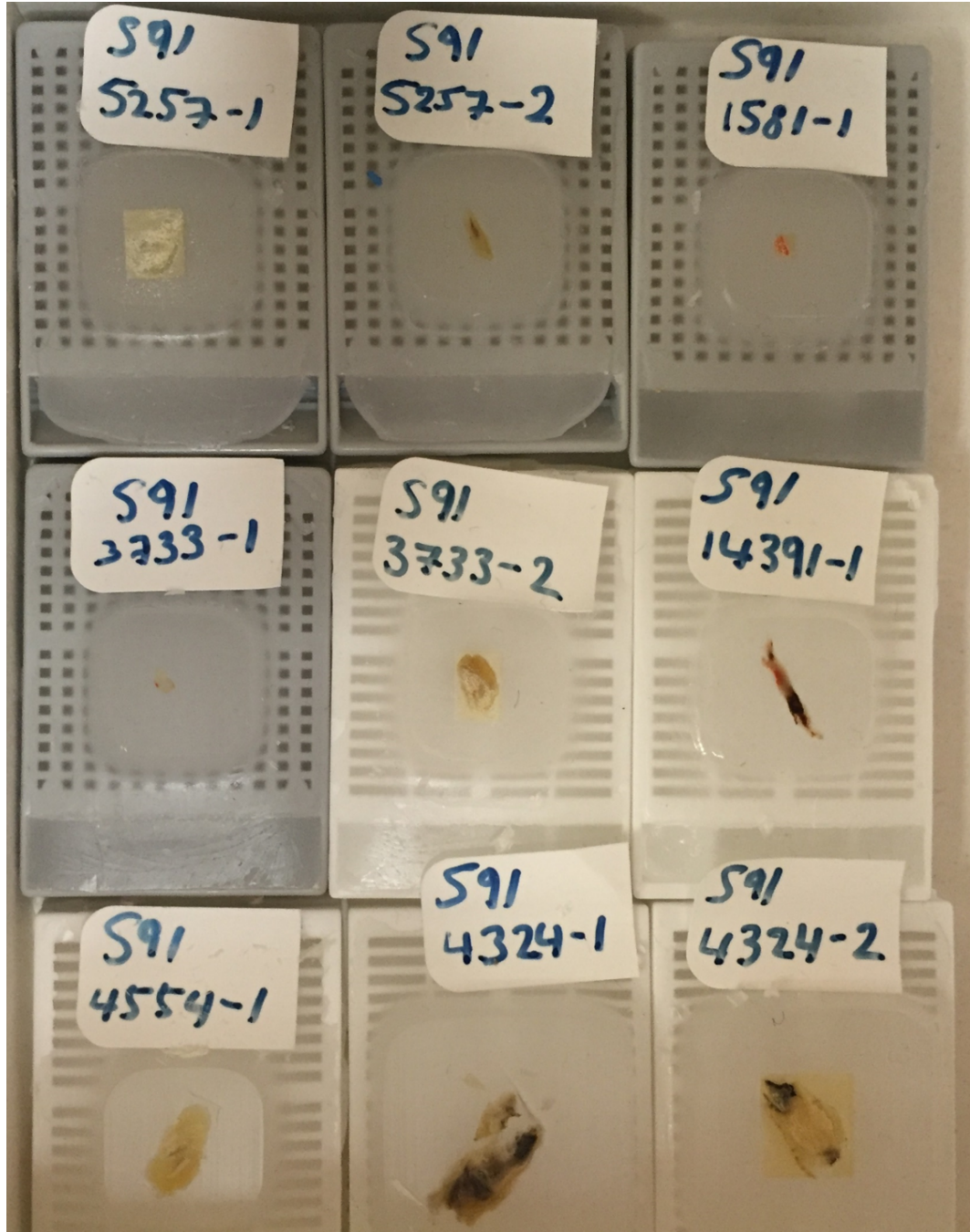


Figure 6·2: Paraffin-embedded lacrimal sac biopsy samples.

Table 6.1: Demographic information for lacrimal sac biopsy samples (LSBS). The “*” indicates that MIMS for these samples were acquired in three different MIMS acquisition sequences and calibration data is available for the last two MIMS (see Table 6.2).

LSBS #	Age	Gender	Clinical Presentation
3733	39	F	Right blocked tear duct
-1			Biopsy of right tear sac – Chronic inflammation
-2*			Stone from tear duct – Dacryolith
5257	49	F	Left blocked tear duct
-1*			Stone from tear duct containing yeasts
-2			Stone from tear duct containing yeasts
4324	28	F	Bilateral blocked tear duct
-1			Stone from right tear duct – Dacryolith
-2*			Stone from left tear duct – Dacryolith
4554-1	42	F	Blocked tear duct – Lacrimal duct stone
14391	62	F	Stone from right tear duct
1581-1*	N/A	N/A	N/A

modes is also presented. Finally, brief clinicopathological case studies for LSBS 14391 and 3733-2 are provided.

6.3 Experimental Methods

All nine samples (Table 6.1) underwent a series of MIMS acquisition analyses detailed in Table 6.2. All MIMS data were acquired with the CETAC LSX-213 laser ablation system parameters set to default values in Table 4.1 with spot size and line-to-line spacing of 50 μm and a scan speed of 50 $\mu m/s$ and a quadrupole ICP-MS (iCAP Q, Thermo Scientific). The first set of LSBS MIMS data, collected by Dr. Noel Casey (indicated by a 1.x in Table 6.2), could not be directly represented in terms of absolute concentration (in parts per million, *ppm*). Four samples were selected for a later series of experiments (indicated by a 2.x in Table 6.2) where a matrix-matched

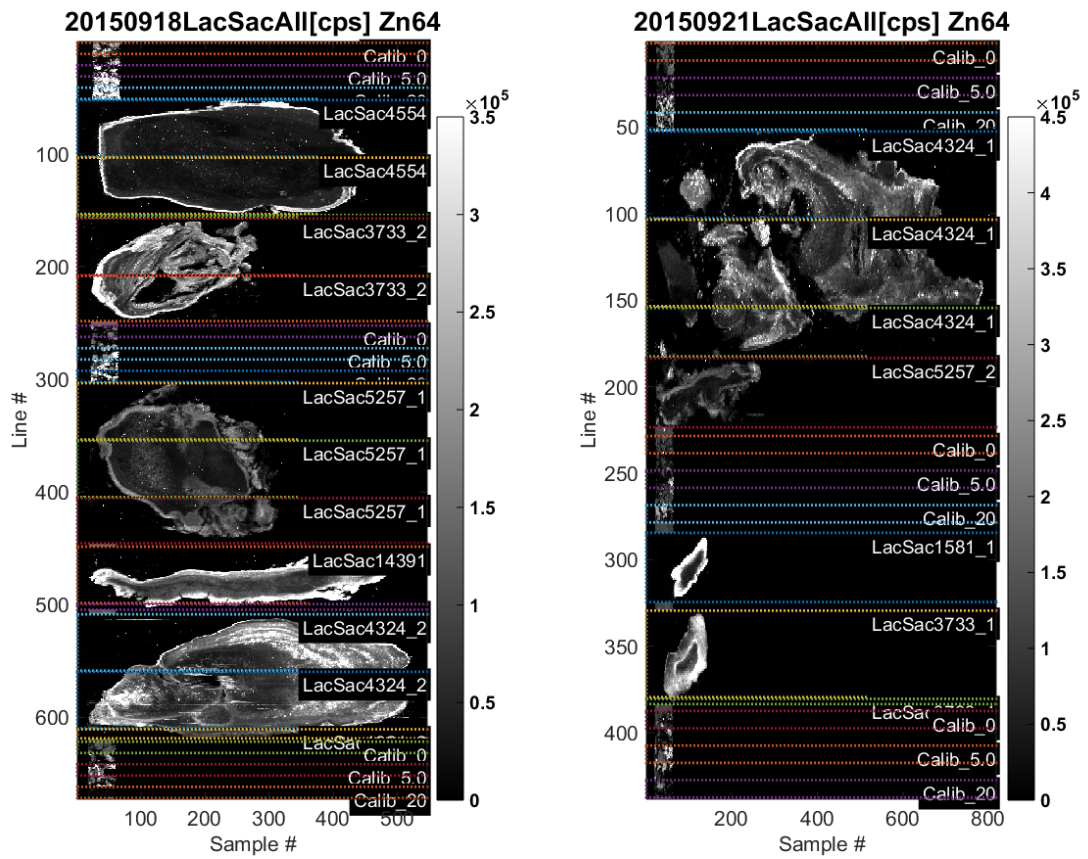
calibration material was included as part of the sequence. The procedure for creating the matrix-matched gelatin calibration standard material is detailed in Appendix A.3. These analyses were conducted by Dr. Bo Yan.

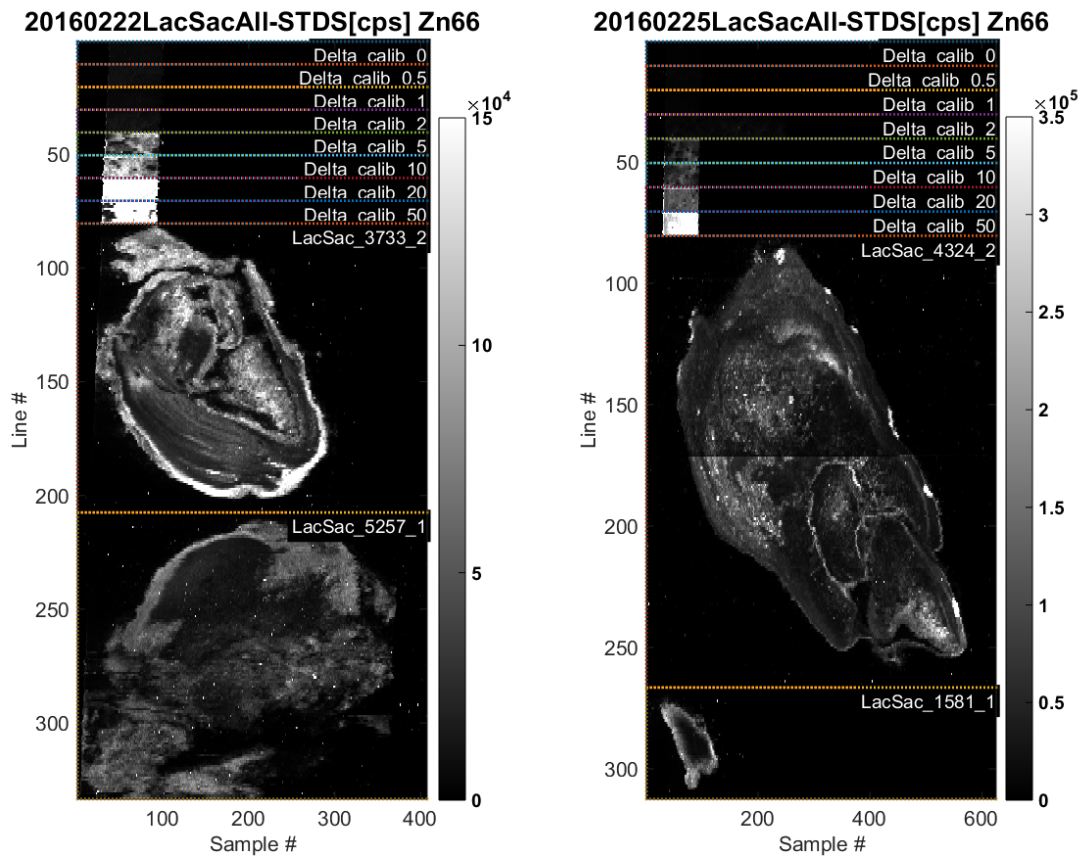
In the later set of experiments, each MIMS sequence was acquired twice with identical acquisition parameters except that the ICP-MS measurement modes were varied between acquisitions. These measurement modes provide a means of reducing analyte interferences during data acquisition. Each sequence was first acquired using the kinetic energy discrimination (KED) mode where the instrument is able to effectively filter out polyatomic and low-mass interferences. Using the same parameters, the sequence was acquired again while operating the instrument in its standard (STD) mode. Raw images of the zinc-isotope MIMS sequences for each experiment are provided in Figs. 6-3, 6-4, and 6-5. Since some of the isotopes selected for acquisition were different between the first and second set of experiments, the selected isotopes indicated in the figure vary.

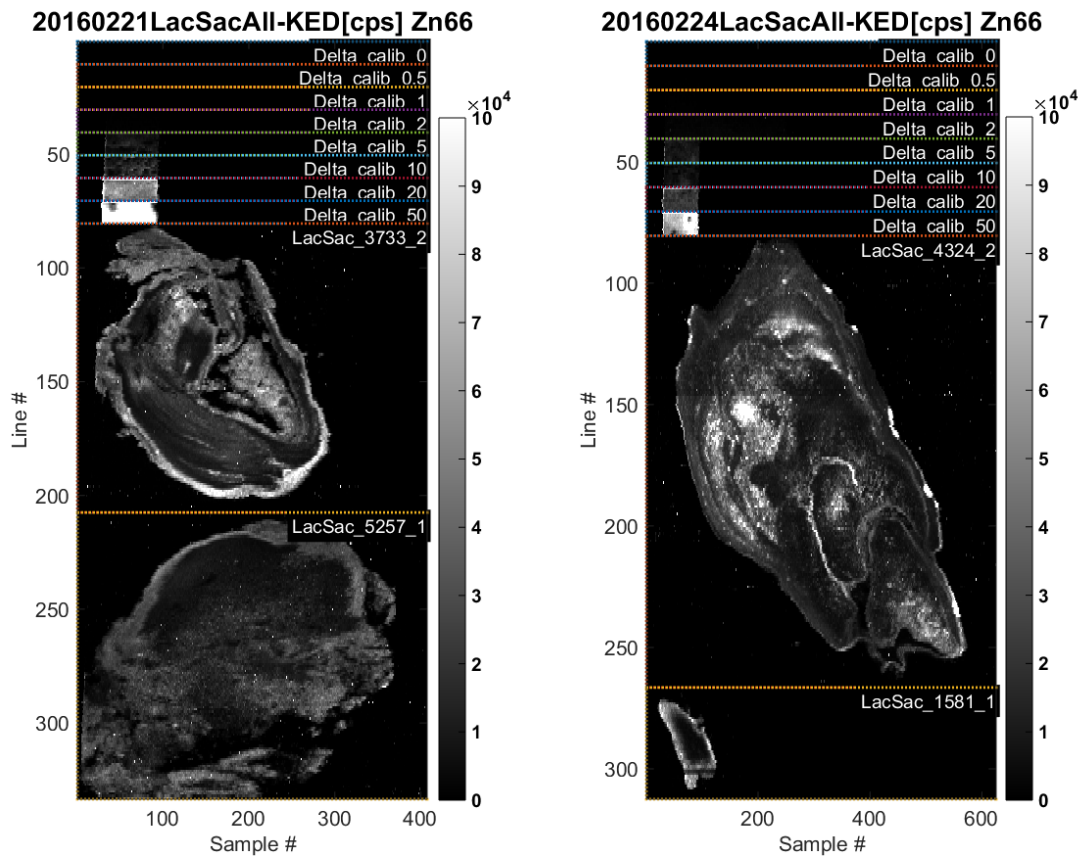
After MIMS images of the tissues specimens were acquired, H&E slides for each sample were prepared and imaged by Dr. Nora Laver. An example of the tissue images from optical imaging, H&E, and MIMS are presented in Fig. 6-6 for LSBS 3733-2. Since the MIMS data were acquired by ablating the surface of the paraffin-embedded LSBS block, each LSBS MIMS image represents a deeper tissue plane than previous images by tens of microns. This difference is not pathologically significant, but did result in differences between the morphology of tissue features from one MIMS tissue image to another. These differences in morphology prevented the use of multi-modal, multi-channel image registration for determining correspondence between MIMS tissue images from different acquisition dates and between MIMS tissue images and H&E section images.

Table 6.2: LSBS MIMS analysis summary.

Date	Mode	Cal?	Exp. Tag	3733-1	3733-2	5257-1	5257-2	4324-1	4324-2	4554-1	143191	1581-1
20150918	STD	✗	STD1.1		✓	✓			✓	✓	✓	
20150921	STD	✗	STD1.2	✓			✓	✓				✓
20160221	KED	✓	KED2.1		✓	✓						
20160222	STD	✓	STD2.1		✓	✓						
20160224	KED	✓	KED2.2						✓			✓
20160225	STD	✓	STD2.2						✓			✓

(a) STD1.1 ^{64}Zn MIMS sequence(b) STD1.2 ^{64}Zn MIMS sequence**Figure 6-3:** ^{64}Zn raw sequences from STD1 experiments

(a) STD2.1 ^{66}Zn MIMS sequence(b) STD2.2 ^{66}Zn MIMS sequence**Figure 6-4:** ^{66}Zn raw sequences from STD2 experiments

(a) KED2.1 ^{66}Zn MIMS sequence(b) KED2.2 ^{66}Zn MIMS sequence**Figure 6-5:** ^{66}Zn raw sequences from KED2 experiments

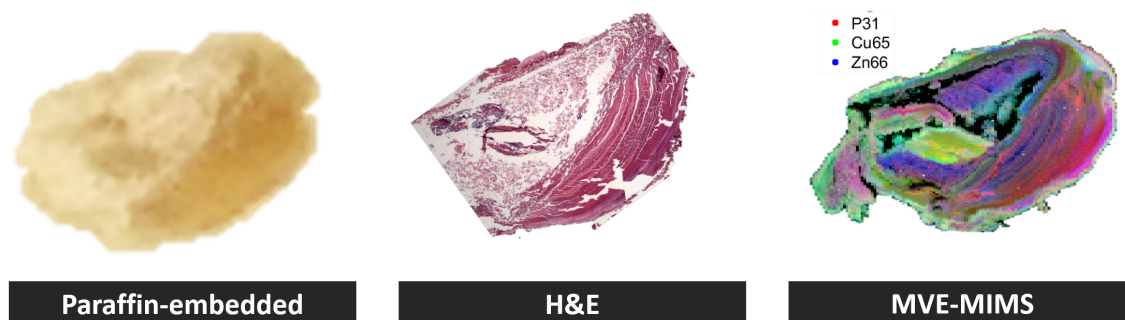


Figure 6-6: Various image modalities of LSBS 3733-2. The MVE-MIMS image is a false-colored representation of data from three simultaneously acquired isotope channels.

6.4 Processing Pipeline

To compare MIMS data acquired for a given LSBS sample across different dates, the mean-variance equalized elemental-isotope maps were generated as described in Section 4.4. Calibrated MIMS tissue images, when possible, were generated using the MIMS region labeling algorithm described in Section 4.2 and the method described in Section 4.3 for parameterizing a line of best fit to map from raw intensity (in cps) to absolute concentration (in *ppm*). Regions of interest for analysis in the clinico-pathological case studies were defined by first using k-means clustering ($k = 10$) to cluster regions in the H&E image. Distinct visible regions consistent with pathological features of interest were then used to manually merged these clusters so that the result roughly follows the visible distinct regions in the H&E image.

6.5 Results and Discussion

6.5.1 Comparison of MIMS Using Different Instrument Modes

Select MIMS channels from all nine samples acquired as part of STD1.1 and STD 1.2 experiments are shown in a grid in Figs. 6·7 and 6·8. All tissue maps of the same isotopes (columns in the grid) are displayed using the same color-scale, indicated on the first row of images from LSBS 1581-1. Each row represents a different channel from the same sample. The outlines around the tissue show the automatically-detected tissue boundaries as determined by the MIMS region segmentation algorithm, and the color of the boundary indicates whether the data was acquired in the **STD1.1** sequence or the **STD1.2** sequence. All images have a 1 *mm* cyan scale bar in the lower right corner. LSBS specimens from the same subject are grouped together by a yellow box around the rows on the image grid.

While not as clearly evident in the endogenous biometal MIMS tissue images in Fig. 6·7, by visualizing the toxic metals of all LSBS MIMS together in Fig. 6·8, subject-specific characteristics become more evident. For example, the ^{137}Ba channel in LSBS 3733-1 and 3733-2 samples reveal relatively high levels of ^{137}Ba with a pattern of distribution concentrated within the specimen. Quite differently, samples from LSBS 4324 demonstrate low ^{137}Ba levels. In addition to the general intensity level being similar, the pattern of where certain metals are found in the tissue (i.e. primarily in periphery, internal and uniform, striated following relevant H&E features) also seem to bare more similarity between two samples from the same patient versus between samples from different patients.

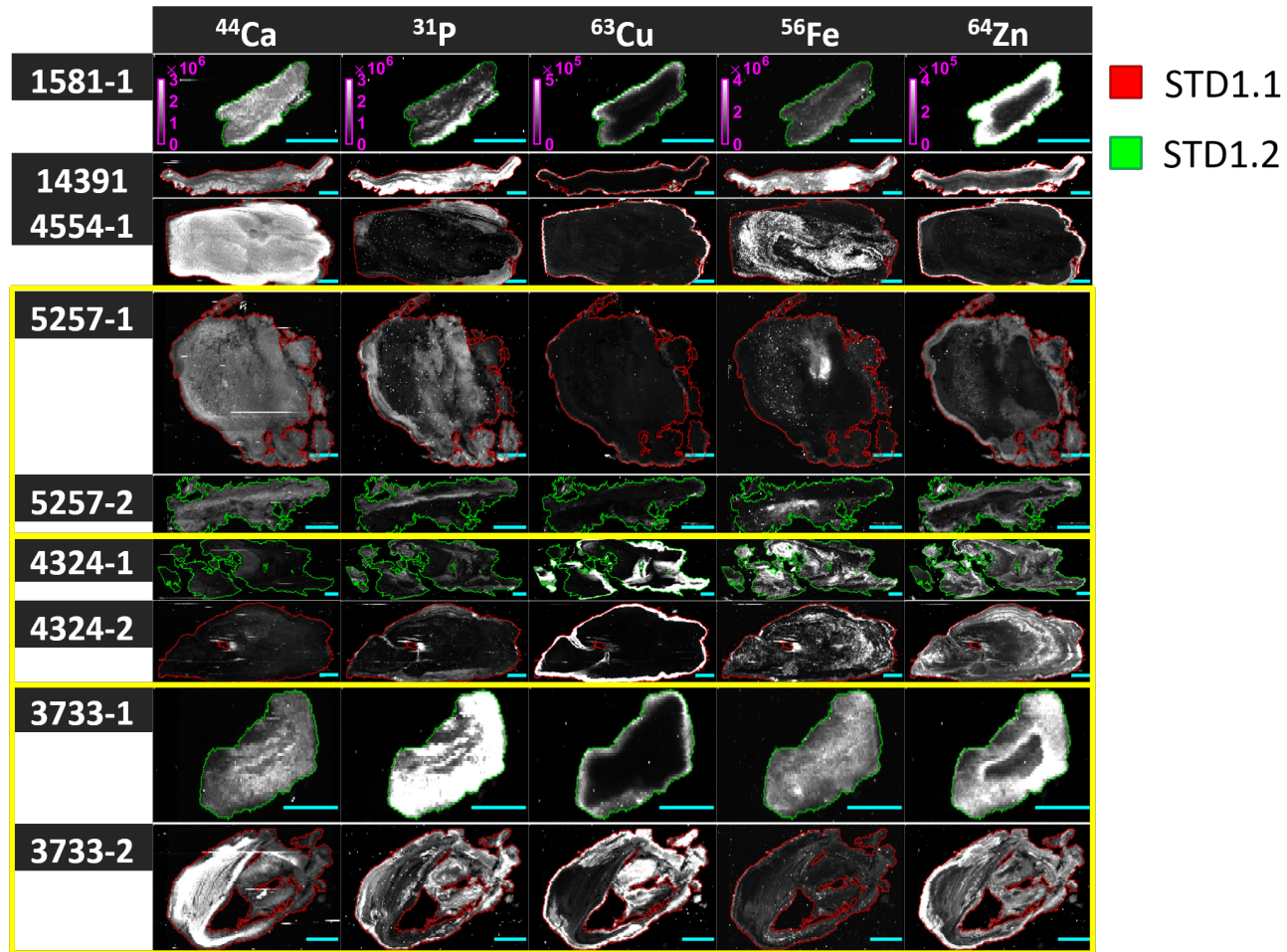


Figure 6-7: Raw LSBS MIMS tissue images from select endogenous biometals. All tissue maps in a given column follow the same color scale indicated in the LSBS 1581-1 image. The colored outlines delineate tissue boundaries and specify the experiment. The yellow boxes indicate that the LSBS specimens come from the same subject. The cyan bar indicates 1 *mm*.

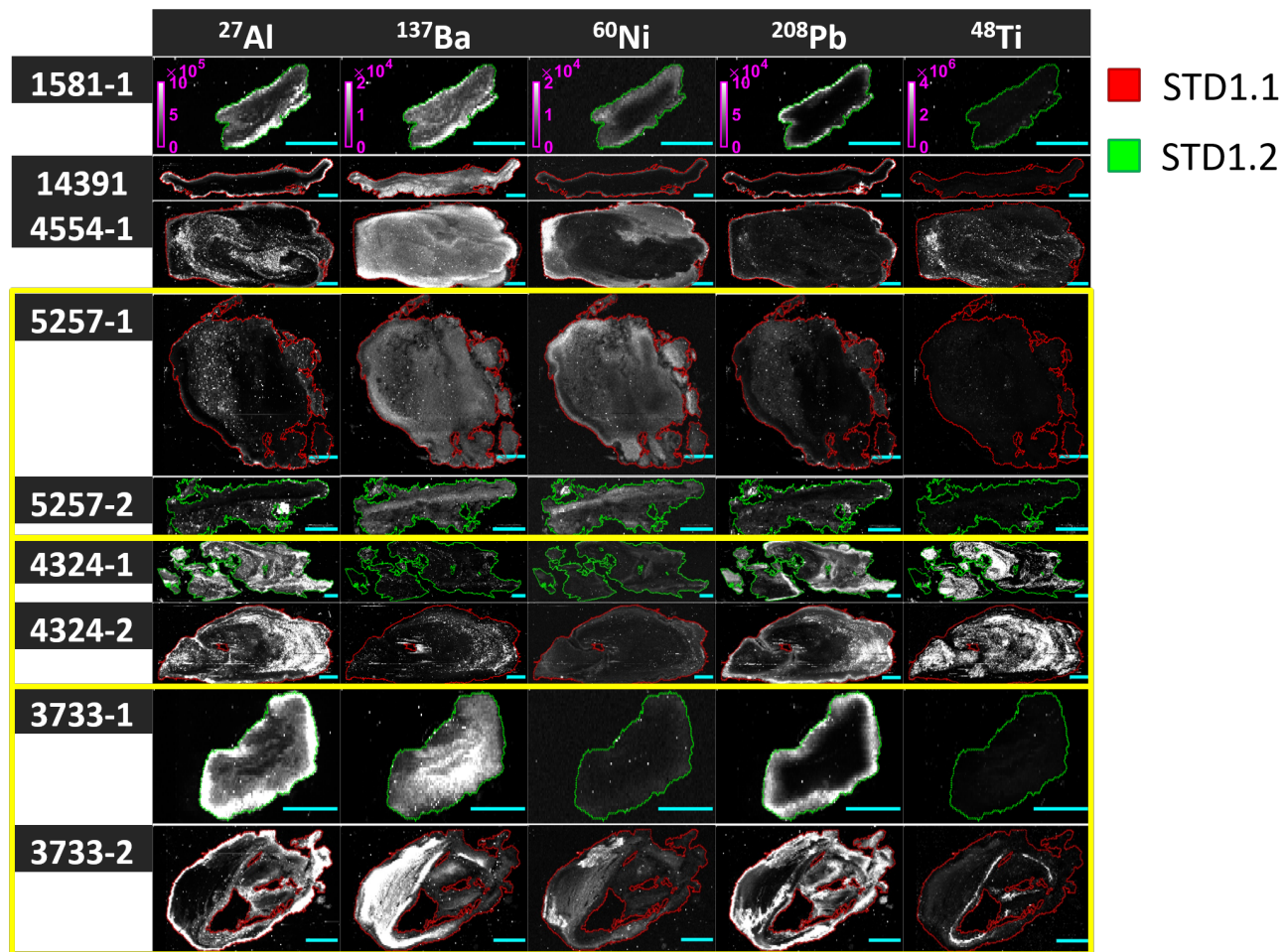


Figure 6-8: Raw MIMS from select toxic metal isotopes for all lacrimal sac biopsy samples. All MIMS in a given column follow the same color scale indicated in the LSBS 1581-1 image. The colored outlines delineate tissue boundaries and specify the experiment. The yellow boxes indicate that the LSBS specimens come from the same subject. The cyan bar indicates 1 *mm*.

To explore signal consistency within the tissue region across different experiment dates and instrument operating modes, the normalized frequency of raw signal intensities for all LSBS samples are plotted together for Zn -isotopes and ^{137}Ba in Figs. 6-9 and 6-10. While difficult to derive any conclusions directly from these plots, particularly since the data are confounded by the fact that the tissue plane in question was not identical across MIMS acquisition experiments, one can make the following observations:

1. tissue intensity characteristics give rise to a unique intensity distribution shape which appears to be roughly consistent across different experiment days,
2. the absolute and quantitative signal levels are not identical and depend on the instrument sensitivity that day as well as the instrument operating mode.

The last observation is unsurprising, as instrument “drift” and variation is a known characteristic of MIMS, motivating the need for instrument calibration before conducting an experiment. Additionally, since KED mode effectively is a method for removing polyatomic interferences, the lower recorded signal levels in the KED2.1 and KED2.2 experiments are also expected.

The first observation is most apparent through examination of the LSBS 1581-1 distributions in Fig. 6-9. In the three lower panels containing data from LSBS 1581-1 (blue curve), the distinctive bimodal pattern in the Zn isotope becomes apparent, appearing consistently in the three different MIMS acquisition experiments for this sample even despite changing the isotope considered and instrument operating modes. This provides evidence that MIMS truly captures underlying elemental characteristics regardless of experimental condition, though certain acquisition parameters lead to improved signal-to-noise ratio, signal stability and specificity. A discussion on the implications of instrument operation mode on calibration curve quality will follow.

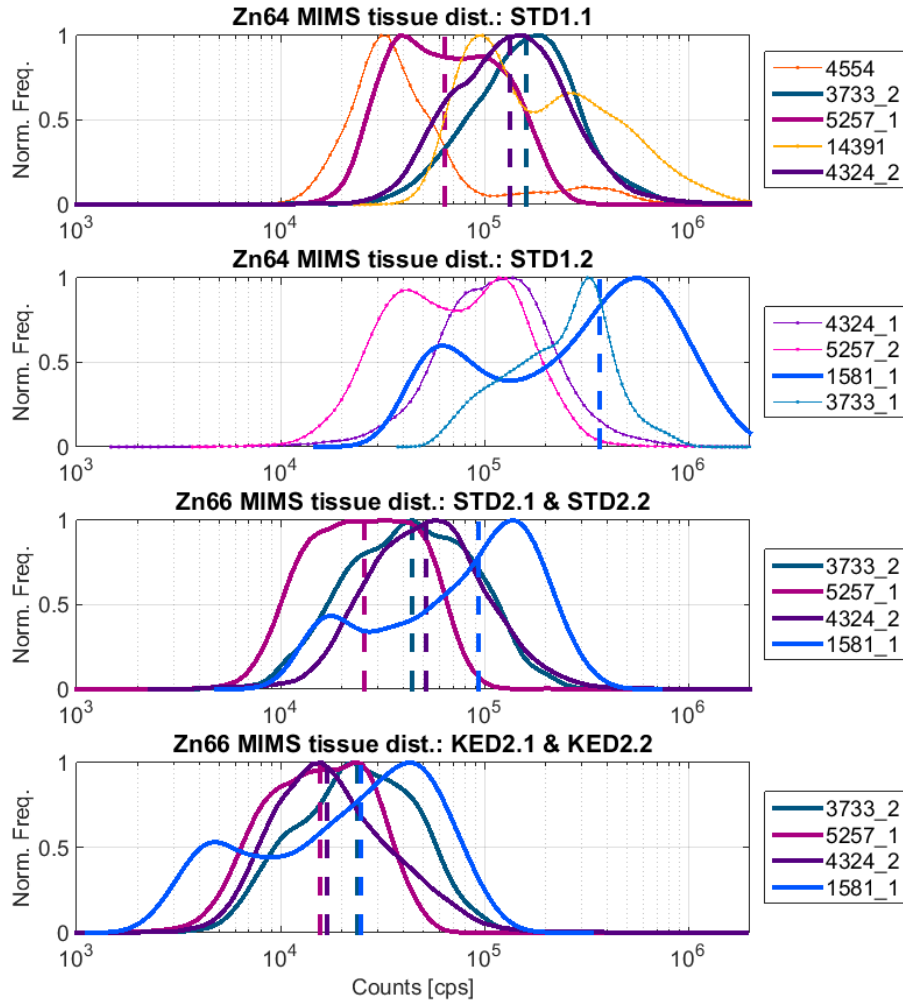


Figure 6-9: Comparison of Zn isotope signal distributions in tissue regions from all LSBS MIMS experiments. The vertical lines in each of the panels indicate the median intensity value within the tissue. The first two panels correspond to the ^{64}Zn isotope (natural abundance 48.63%) and the last two panels depict data from the ^{66}Zn isotope (natural abundance 27.90%). The range of intensities (x -axis) is the same for all panels.

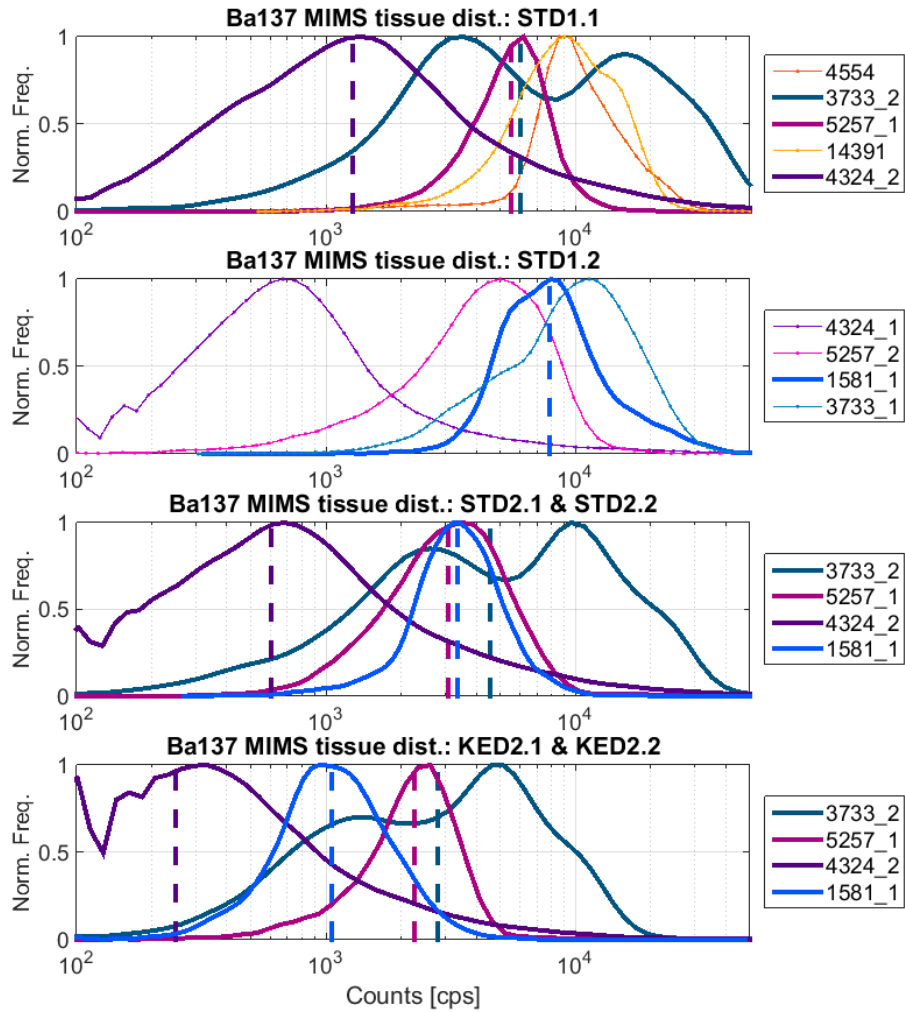


Figure 6-10: Comparison of ^{137}Ba signal distributions in tissue regions from all LSBS MIMS experiments. The vertical lines in each of the panels indicate the median intensity value within the tissue. The range of intensities (x -axis) is the same for all panels.

The second observation regarding differences in the absolute and quantitative signal levels between experiments is supported by inspection of the plots in Figs. 6·9 and 6·10. Through comparison of both the raw intensity range within the LSBS as well as the median signal levels (indicated by the vertical lines in the plots), it is evident that these values may vary significantly.

Through the three separate acquisitions for four of the LSBS, the qualitative differences between the resulting MIMS could be evaluated. Side-by-side comparisons of MIMS from the experiments are presented for LSBS 3733-2 in Fig. 6·11 and Fig. 6·12 for endogenous biometals and toxic metals, respectively. Because the raw intensity levels from each experiments tend to vary greatly as previously discussed, the images in Figs. 6·11 and 6·12 are mean-variance equalized (MVE) per the method in Section 4.4. Immediately apparent is the fact that the MIMS from the three experiments represent different tissue planes. While the MIMS from STD2.1 and KED2.1 have nearly identical tissue features, the tissue plane captured in STD1.1 is clearly distinct from the plane depicted in the 2.1 experiments. Still, a variety of distinct features such as the laminar banding in ^{31}P and the high-intensity internal band of ^{48}Ti are clearly present in all MIMS acquisitions of LSBS 3733-2.

A pairwise comparison of the signal characteristics from different experiments is conducted by computing the cross-correlation (CC) between the MVE-images. To define the CC metric, let the MIMS from the i -th isotope from one experiment be represented as $I^{(i)}$ and from the other experiment as $J^{(i)}$ with tissue masks $M_{\vec{T}}$ and $M_{\vec{T}}$

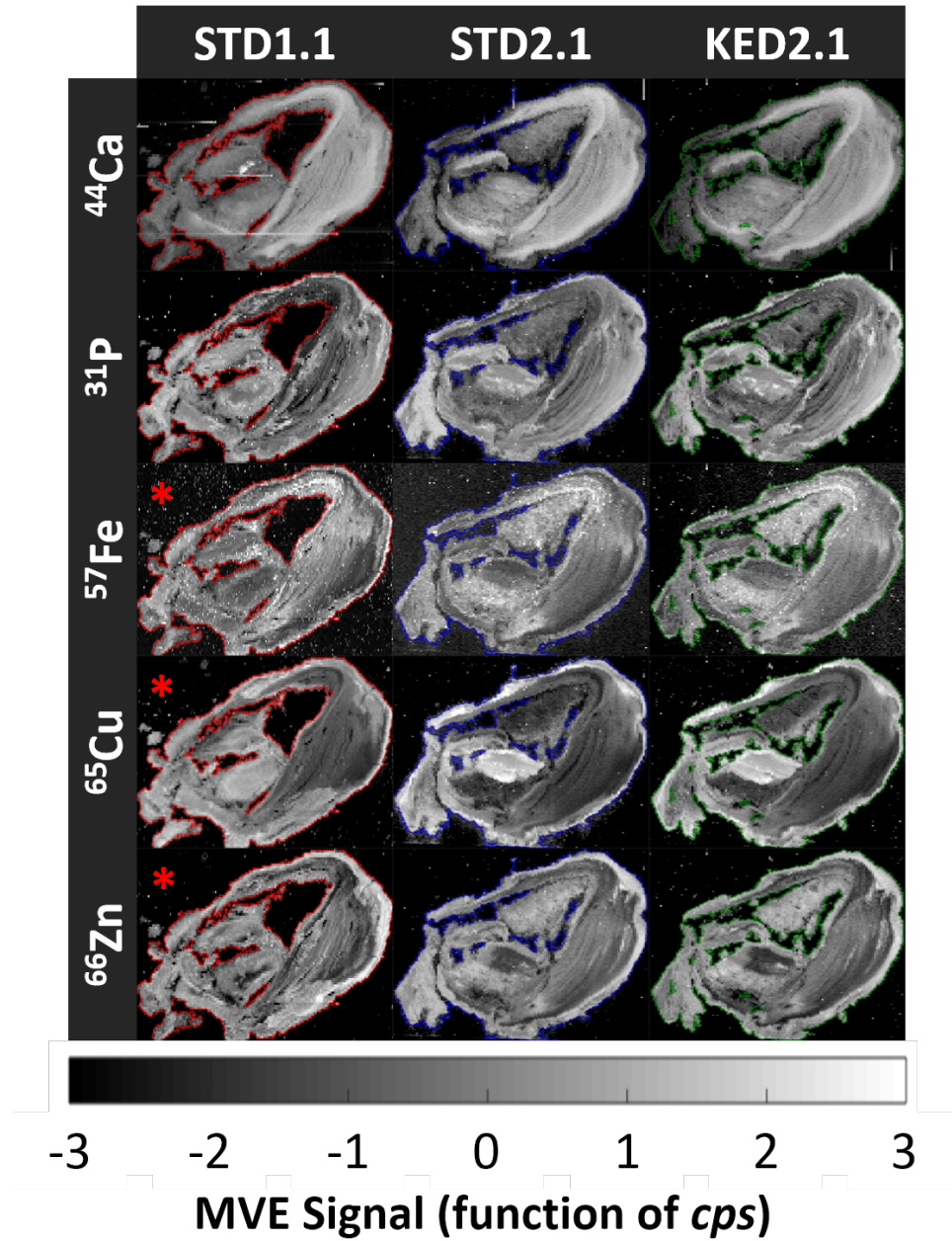


Figure 6-11: MVE-MIMS from select endogenous biometals for LSBS 3733-2. Tissue/background boundaries are depicted by the colored lines in the images. The * symbol in the upper left corner of STD1.1 images indicate that the $\{^{57}\text{Fe}, ^{65}\text{Cu}, ^{66}\text{Zn}\}$ isotopes were not acquired and shown instead are the $\{^{56}\text{Fe}, ^{63}\text{Cu}, ^{64}\text{Zn}\}$ images.

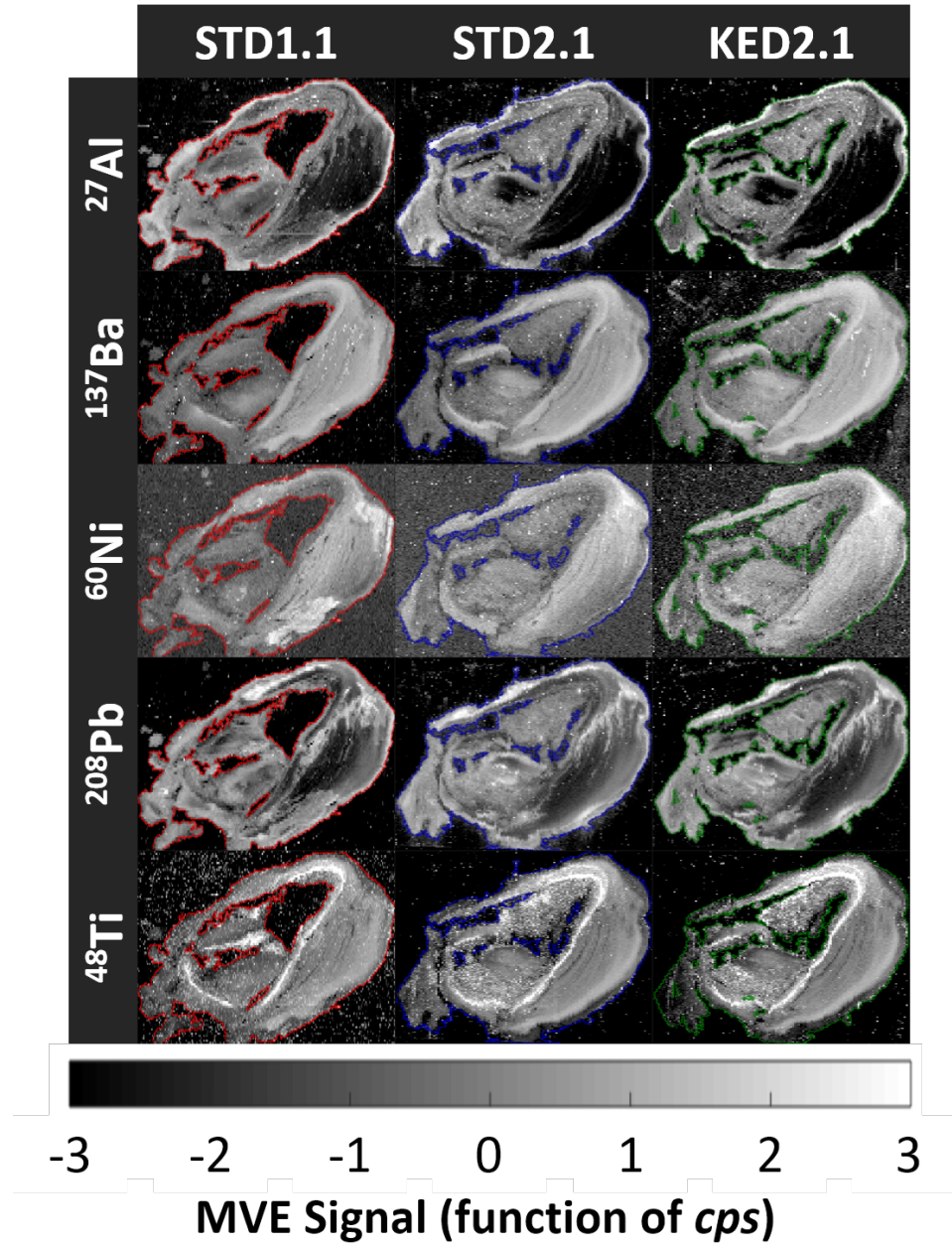


Figure 6.12: MVE-MIMS from select toxic metal isotopes for LSBS 3733-2. Tissue/background boundaries are depicted by the colored lines in the images.

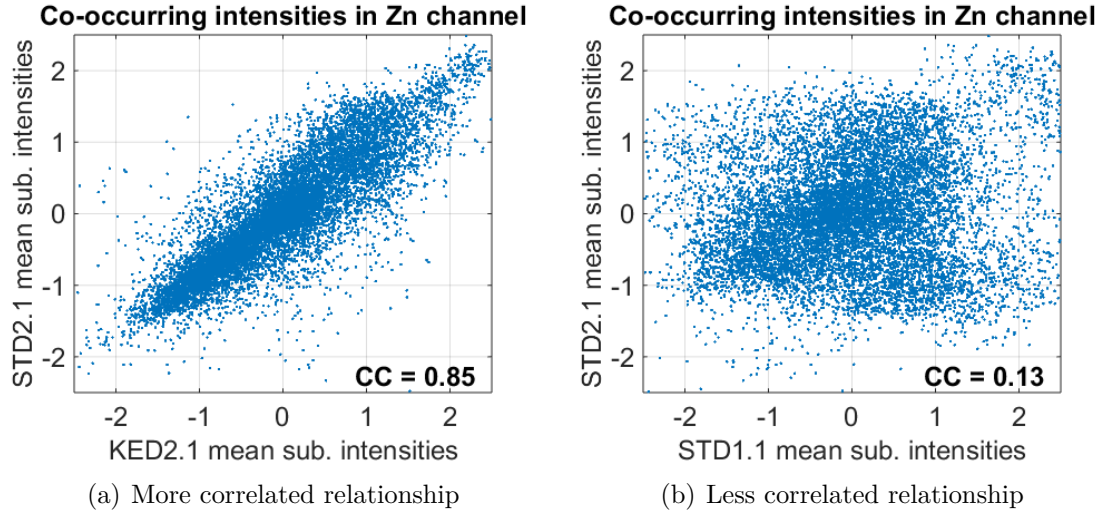


Figure 6-13: Intensity co-occurrence characteristics for (a) correlated and (b) uncorrelated MIMS of LSBS 3733-2.

respectively. The cross-correlation may be calculated as follows:

$$CC(\tilde{I}^{(i)}, \tilde{J}^{(i)}) = \frac{\langle \tilde{I}^{(i)}, \tilde{J}^{(i)} \rangle}{|p| \sigma_{\tilde{I}^{(i)}} \sigma_{\tilde{J}^{(i)}}} \in [-1, 1] \quad (6.1)$$

$$\text{where } p = \{M_{\vec{I}} \cap M_{\vec{J}} = 1\}$$

$$\tilde{I}^{(i)} = I^{(i)}(p) - \mathbb{E}[I^{(i)}(p)]$$

The CC metric is able to capture the degree to which two images follow a linear relationship. Absolute values of CC closer to 1 indicate a more linear (with slope being positive if $CC \approx +1$ and negative if $CC \approx -1$) relationship between co-occurring intensities in the images, as in Fig. 6-13(a), and absolute values of CC closer to 0 indicate a more noisy relationship, as in Fig. 6-13(b).

Since LSBS 3733-2 had the most prominent and distinguishable tissue features, it was selected to assess the relationship between the three experiments. As shown in Fig. 6-14, values for $CC(\text{KED2.1}, \text{STD2.1})$ are greater than $CC(\text{STD1.1}, \text{KED2.1})$ and $CC(\text{STD1.1}, \text{STD2.1})$, likely owing to the greater degree of direct correspon-

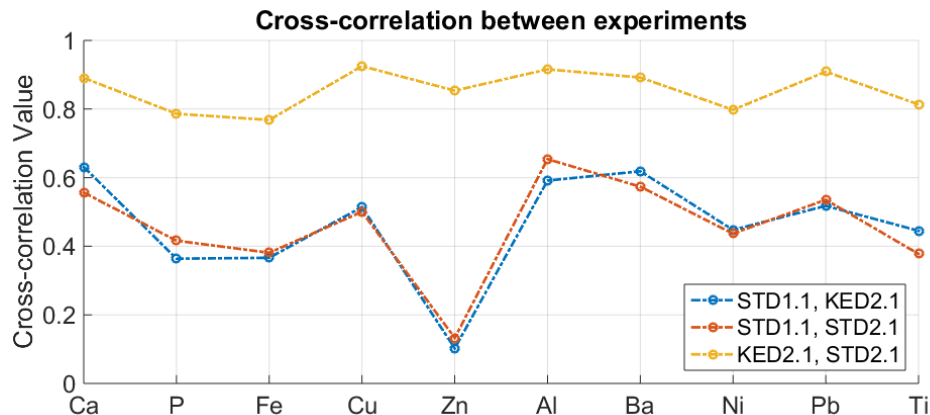


Figure 6.14: Cross-correlation between MIMS from different experiments for LSBS 3733-2.

dence between tissue features in the KED2.1 and STD2.1 experiments. The values of $CC(KED2.1, STD2.1)$ for this sample are all ≥ 0.768 with an average of 0.855. These high CC values indicate that the intensity characteristics of the sample in the two experiments are highly correlated and therefore it would be expected that the absolute concentrations derived from each experiment should also be similar.

6.5.2 Calibration Curve Characteristics

Calibration data from the four experiments for which suitable calibration material was acquired is compared. A total of eight standard concentration values were prepared: $\{0, 0.5, 1, 2, 5, 10, 20, 50\}$ ppm. The characteristics of the data used to parametrize the line of best fit mapping absolute concentration (C) to instrument intensity (I) varied based on isotope and instrument mode. In general, data acquired using KED mode yielded calibration curves with fewer artifacts (such as saturation and signal variability) and whose raw intensity values fell within the range of LSBS intensities. A summary of the curve characteristics for experiments with calibration data is provided in Table 6.3.

Table 6.3: Summary of calibration data characteristics from calibration experiments. Isotopes for which “ \Downarrow ” or “ \Uparrow ” is indicated in the “Curve spans range of data” column, the meaning is that the range of intensities in the tissue is greater than (\Downarrow , meaning calibration values are too low) or less than (\Uparrow , meaning calibration values are too high) the intensities spanned by the linear part of the curve. The “(s)” specification indicates that the calibration curve saturates at larger concentrations. The “(n)” specification indicates that the calibration curve appears to be dominated by noise. When “—” is indicated, the variance in the LSBS characteristics are too varied to specify a single property.

Isotopes	Linear in 0–5 <i>ppm</i>		Linear in 0–50 <i>ppm</i>		Curve spans tissue intensities		LSBS <i>ppm</i> apparent upper limit	
	KED	STD	KED	STD	KED	STD	KED	STD
^{27}Al	✓	✗	✗(s)	✗(n)	✓	\Uparrow	5	—
^{137}Ba	✓	✗	✗(s)	✗(n)	✓	\Uparrow	5	—
^{60}Ni	✓	✓	✓	✓	✓	✓	5	5
^{208}Pb	✓	✓	✗	✗	✓	✓	20	20
^{48}Ti	✓	✗	✓	✓	\Downarrow	—	> 50	—
^{44}Ca	✓	✗	✗(s)	✗(n)	\Downarrow	\Uparrow	> 10	—
^{31}P	✓	✗	✓	✓	\Downarrow	\Downarrow	> 50	> 50
^{57}Fe	✓	✗	✗(s)	✗(n)	\Downarrow	—	> 50	—
^{65}Cu	✓	✓	✓	✓	✓	✓	50	50
^{66}Zn	✓	✓	✓	✓	✓	✓	50	50

Three isotopes were selected to exhibit the variability in calibration curve characteristics. Each of the following figures (Figs. 6·15–6·17) depicts two lines of best fit using the calibration data: one for the full *ppm* range using all eight points (left and center plots) and one partial *ppm* range using only the lower five concentration values (right plot). The horizontal lines shown represent the values in the indicated LSBS which is $\geq 99.5\%$ of all intensity values in the LSBS MIMS.

The calibration curves for ^{66}Zn (Fig. 6·15) demonstrate the ideal scenario where intensity levels in the LSBS span the range of the intensity levels in the calibration data. For both KED and STD modes, the curves yield high R^2 values ($R_{KED2.1}^2 = 0.987$, $R_{KED2.2}^2 = 0.967$, $R_{STD2.1}^2 = 0.998$, $R_{STD2.2}^2 = 0.979$) which serve as a metric for fit quality. For other isotopes (e.g., ^{60}Ni , Fig. 6·16), the intensity levels in the tissue occupy a narrow band in the lower range of the standard concentration values (i.e., approximately 0 to 5 *ppm*). For these cases, only the relevant range of the calibration curve is utilized to parametrize the lines of best fit between *ppm* and *cps*. Finally, other isotopes, (e.g., ^{44}Ca) maintain high degrees of linearity for a small range of the curve before saturating, as in the center plot of Fig. 6·17(a). This characteristic saturation is observed most frequently in KED mode. In the STD mode, certain isotopes (those indicated by (n) in Table 6.3) were saturated at all calibration data values within the selected range prepared for calibration. The ^{44}Ca calibration data in STD mode (Fig. 6·17(b)), for instance, are saturated at all calibration concentration levels prepared. The more robust ability of the instrument to capture the full range of calibration standard concentrations prepared in KED mode is likely a result of the reduction in polyatomic interferences introduced in this mode.

The calibration data acquired in each experiment are used to parametrize one linear equation for each isotope. This equation (Eqn. 4.2) may then be applied to all

Zn66 comparison

- FIT: KED2.1
- MED: KED2.1
- FIT: KED2.2
- MED: KED2.2

Equations for 0 - 50 ppm Line

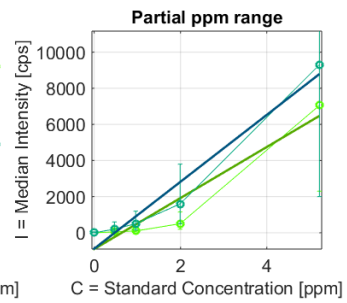
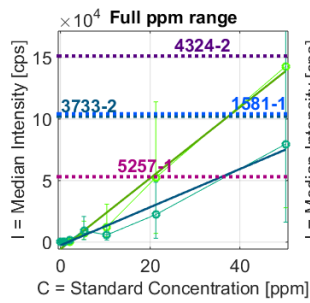
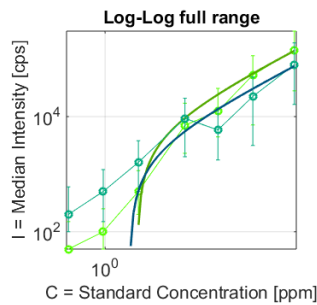
Equations for 0 - 5 ppm Line

$$I_{KED2.1}^{0-50} = 2.88 \times 10^3 C - 5.63 \times 10^3, R^2 = 0.987$$

$$I_{KED2.1}^{0-5} = 1.41 \times 10^3 C - 9.02 \times 10^3, R^2 = 0.912$$

$$I_{KED2.2}^{0-50} = 1.55 \times 10^3 C - 2.58 \times 10^3, R^2 = 0.967$$

$$I_{KED2.2}^{0-5} = 1.85 \times 10^3 C - 8.81 \times 10^3, R^2 = 0.957$$



(a) KED ⁶⁶Zn

Zn66 comparison

- FIT: STD2.1
- MED: STD2.1
- FIT: STD2.2
- MED: STD2.2

Equations for 0 - 50 ppm Line

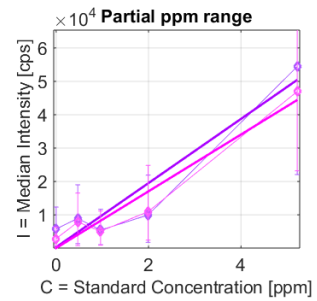
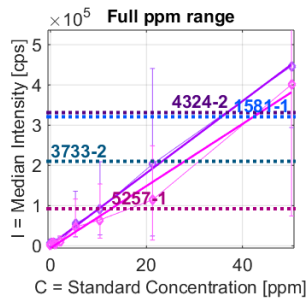
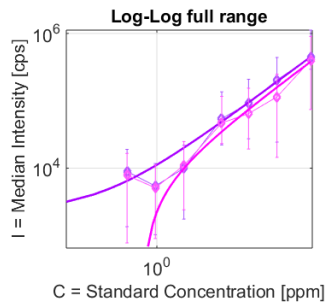
Equations for 0 - 5 ppm Line

$$I_{STD2.1}^{0-50} = 8.93 \times 10^3 C + 2.27 \times 10^3, R^2 = 0.998$$

$$I_{STD2.1}^{0-5} = 9.61 \times 10^3 C + 3.01 \times 10^2, R^2 = 0.904$$

$$I_{STD2.2}^{0-50} = 7.71 \times 10^3 C - 5.48 \times 10^3, R^2 = 0.979$$

$$I_{STD2.2}^{0-5} = 8.51 \times 10^3 C + 3.82 \times 10^1, R^2 = 0.944$$



(b) STD ⁶⁶Zn

Figure 6-15: ⁶⁶Zn calibration curve comparison

Ni60 comparison

- FIT: KED2.1
- MED: KED2.1
- FIT: KED2.2
- MED: KED2.2

Equations for 0 - 50 ppm Line

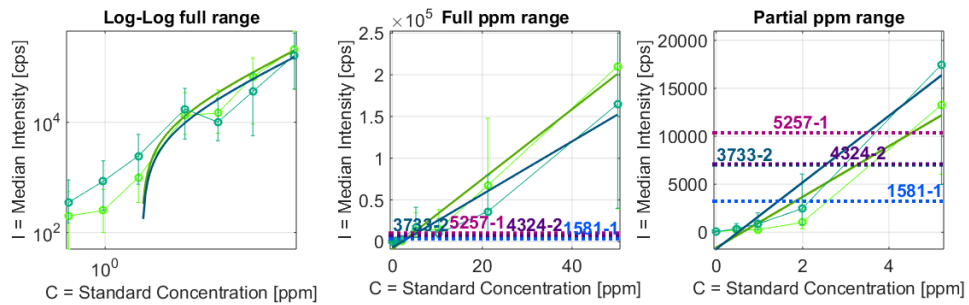
Equations for 0 - 5 ppm Line

$$I_{KED2.1}^{0-50} = 4.19 \times 10^3 C - 8.88 \times 10^4, R^2 = 0.979$$

$$I_{KED2.1}^{0-5} = 2.65 \times 10^3 C - 1.62 \times 10^3, R^2 = 0.912$$

$$I_{KED2.2}^{0-50} = 3.17 \times 10^3 C - 6.80 \times 10^4, R^2 = 0.947$$

$$I_{KED2.2}^{0-5} = 3.47 \times 10^3 C - 1.76 \times 10^3, R^2 = 0.943$$



(a) KED ⁶⁰Ni

Ni60 comparison

- FIT: STD2.1
- MED: STD2.1
- FIT: STD2.2
- MED: STD2.2

Equations for 0 - 50 ppm Line

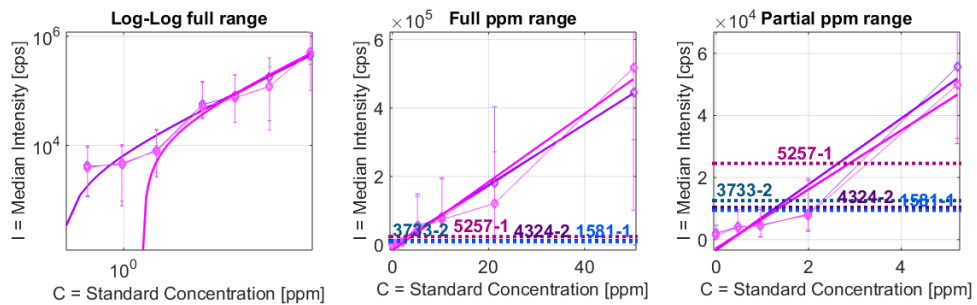
Equations for 0 - 5 ppm Line

$$I_{STD2.1}^{0-50} = 8.88 \times 10^3 C - 2.32 \times 10^3, R^2 = 0.998$$

$$I_{STD2.1}^{0-5} = 1.06 \times 10^4 C - 3.37 \times 10^3, R^2 = 0.930$$

$$I_{STD2.2}^{0-50} = 9.96 \times 10^3 C - 1.48 \times 10^4, R^2 = 0.964$$

$$I_{STD2.2}^{0-5} = 9.50 \times 10^3 C - 2.81 \times 10^3, R^2 = 0.938$$



(b) STD ⁶⁰Ni

Figure 6-16: ⁶⁰Ni calibration curve comparison

Ca44 comparison

Equations for 0 - 50 ppm Line

Equations for 0 - 5 ppm Line

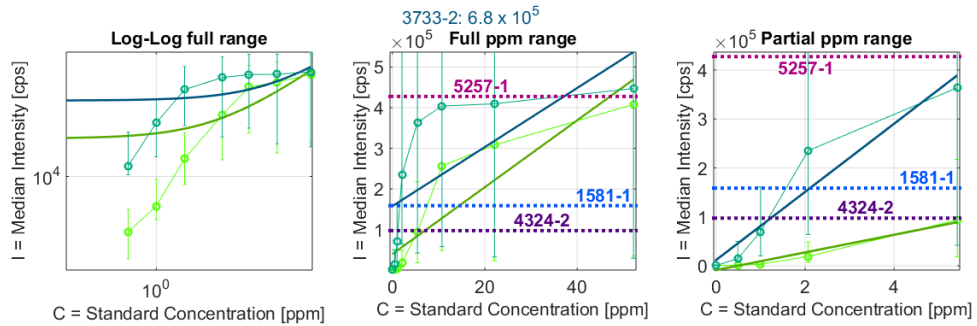
- FIT: KED2.1
- MED: KED2.1
- FIT: KED2.2
- MED: KED2.2

$$I_{KED2.1}^{0-50} = 8.23 \times 10^3 C + 3.97 \times 10^4, R^2 = 0.816$$

$$I_{KED2.1}^{0-5} = 1.80 \times 10^4 C - 8.64 \times 10^4, R^2 = 0.962$$

$$I_{KED2.2}^{0-50} = 7.27 \times 10^3 C + 1.58 \times 10^5, R^2 = 0.475$$

$$I_{KED2.2}^{0-5} = 6.96 \times 10^4 C + 1.19 \times 10^4, R^2 = 0.918$$



(a) KED ⁴⁴Ca

Ca44 comparison

Equations for 0 - 50 ppm Line

Equations for 0 - 5 ppm Line

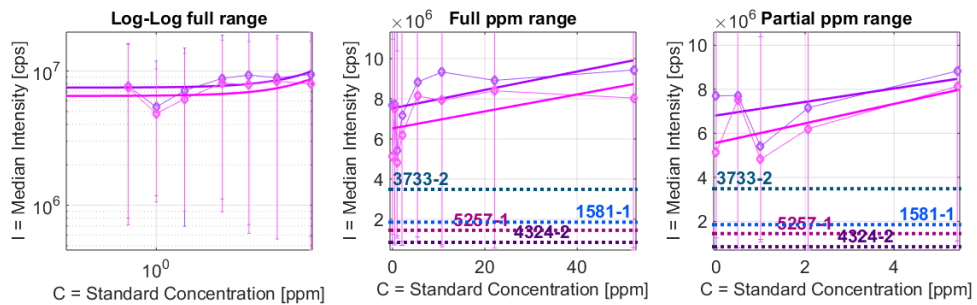
- FIT: STD2.1
- MED: STD2.1
- FIT: STD2.2
- MED: STD2.2

$$I_{STD2.1}^{0-50} = 4.58 \times 10^4 C + 7.52 \times 10^6, R^2 = 0.367$$

$$I_{STD2.1}^{0-5} = 3.06 \times 10^5 C + 6.81 \times 10^6, R^2 = 0.281$$

$$I_{STD2.2}^{0-50} = 4.23 \times 10^4 C + 6.52 \times 10^6, R^2 = 0.282$$

$$I_{STD2.2}^{0-5} = 4.42 \times 10^5 C + 5.57 \times 10^6, R^2 = 0.436$$



(b) STD ⁴⁴Ca

Figure 6-17: ⁴⁴Ca calibration curve comparison

LSBS acquired as part of the sequence so as to represent raw intensity values in terms of absolute concentration. Since four LSBS were acquired twice, once with the instrument in KED mode and once with the instrument in STD mode, the derived calibrated images from each experiment may be compared as a way of assessing the sample consistency in terms of absolute concentration. Having previously established the similarity between tissue features captured across all experiments, application of two different calibration curves enables assessment of the accuracy of the calibration procedure itself and offers additional insight into the instrument operating modes.

The calibrated LSBS images from the KED2.x and STD2.x experiments are shown for ^{66}Zn and ^{60}Ni in Fig. 6-18 and Fig. 6-19, respectively. Consistent with previous normalized MIMS comparisons from the various experiments presented in Figs. 6-11 and 6-12, the calibrated images show that while certain intensity characteristics in the LSBS are present in both KED and STD acquisition modes, the absolute concentration images still appear to differ by at least a scale factor.

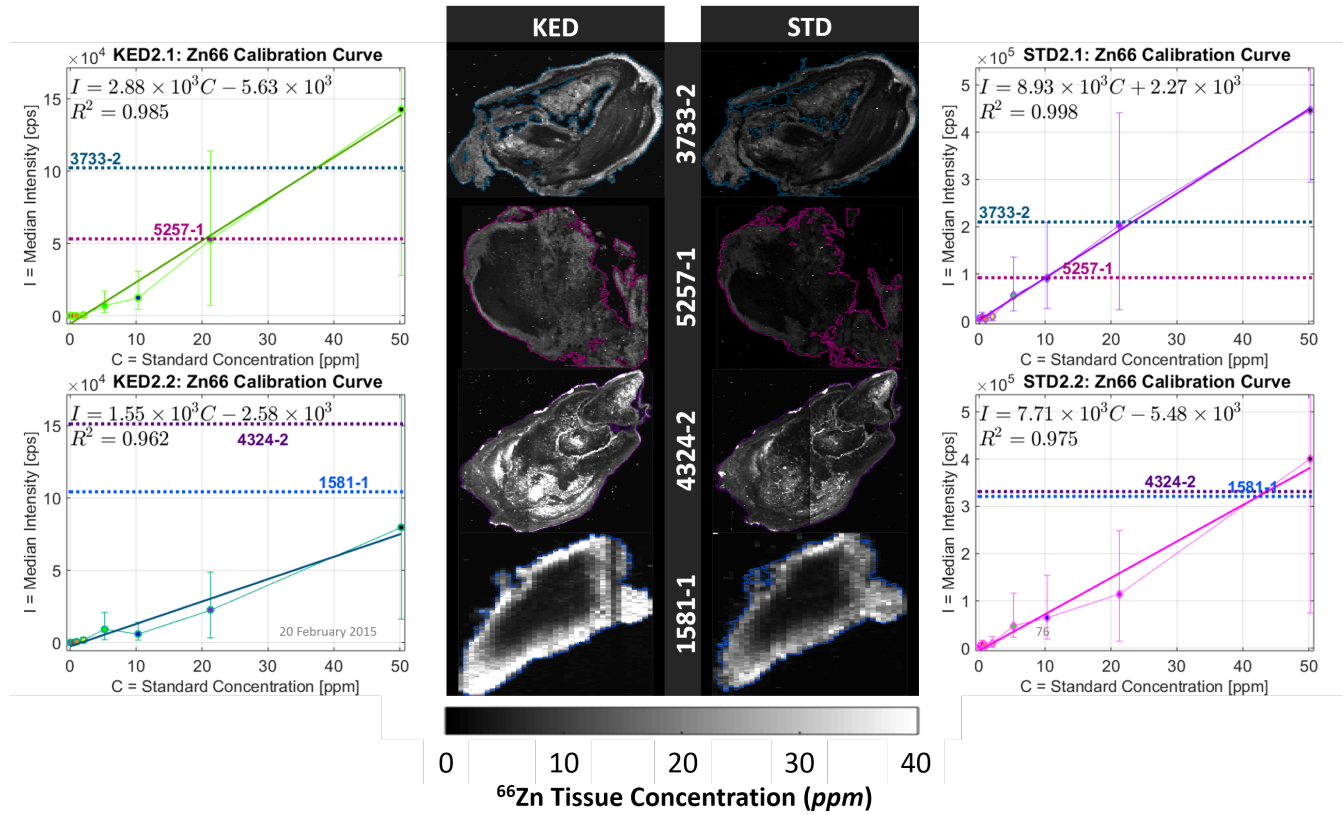


Figure 6-18: Comparison of ⁶⁶Zn LSBS represented in ppm.

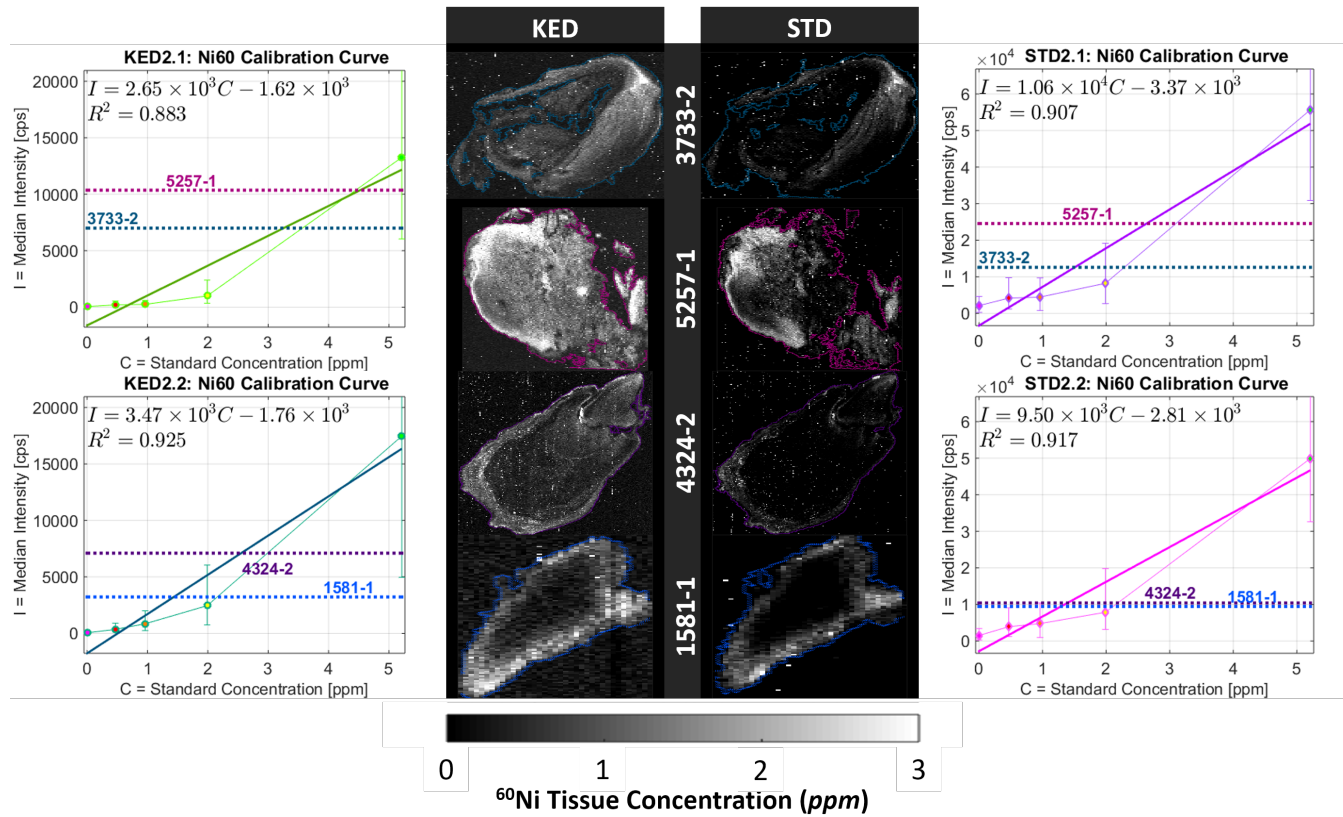


Figure 6-19: Comparison of ^{60}Ni LSBS represented in *ppm*.

6.5.3 Clinicopathological case studies

Two of the LSBS, samples 14391 and 3733-2, had clear pathological features in their H&E tissue sections, such as striated staining and areas that were distinctly dark red (indicating blood) and dark purple/blue (indicating cellular infiltrate, consistent with inflammation). Limited field of view and depth of the imaging plane in the H&E sections complicate determining the correspondence between the H&E and MIMS tissue images. As seen when comparing the MIMS tissue images and H&E images of LSBS 14391 in Fig. 6-21 and LSBS 3733-2 in Fig. 6-25, while there clearly are corresponding structures in both images, their direct relationship, particularly given non-affine deformations, is not directly obvious.

First, considering LSBS 14391, the MIMS data acquired as part of STD1.1 are presented in their mean-variance equalized (MVE) form in Fig. 6-20. Being that the most prominent features in the H&E image of LSBS 14391 are the deep red region on the right side of the image and the pink/purple striations on left and center part of the tissue (see Fig. 6-21(c)), two MIMS channels were selected which also shared these prominent features: ^{56}Fe pseudo-colored in red and ^{44}Ca psuedo-colored in green (see Fig. 6-21(a)). Using the `manualregGUI.m` described in Section 4.1.3, the affine parameters were adjusted until the approximate outlines and internal tissue features aligned. Figure 6-21(d) shows the two images checkered before adjusting the transformation and Fig. 6-21(e) shows the checkered result after manual manipulation of the x, y -translation, x, y -scale, rotation and skew. This approximate correspondence between the H&E image space and the MIMS image space was used to impart segments determined from the H&E image onto the MIMS images.

Relevant pathological features in the H&E image were identified by modifying k-means clustering results. Three clusters corresponding to the three most easily dis-

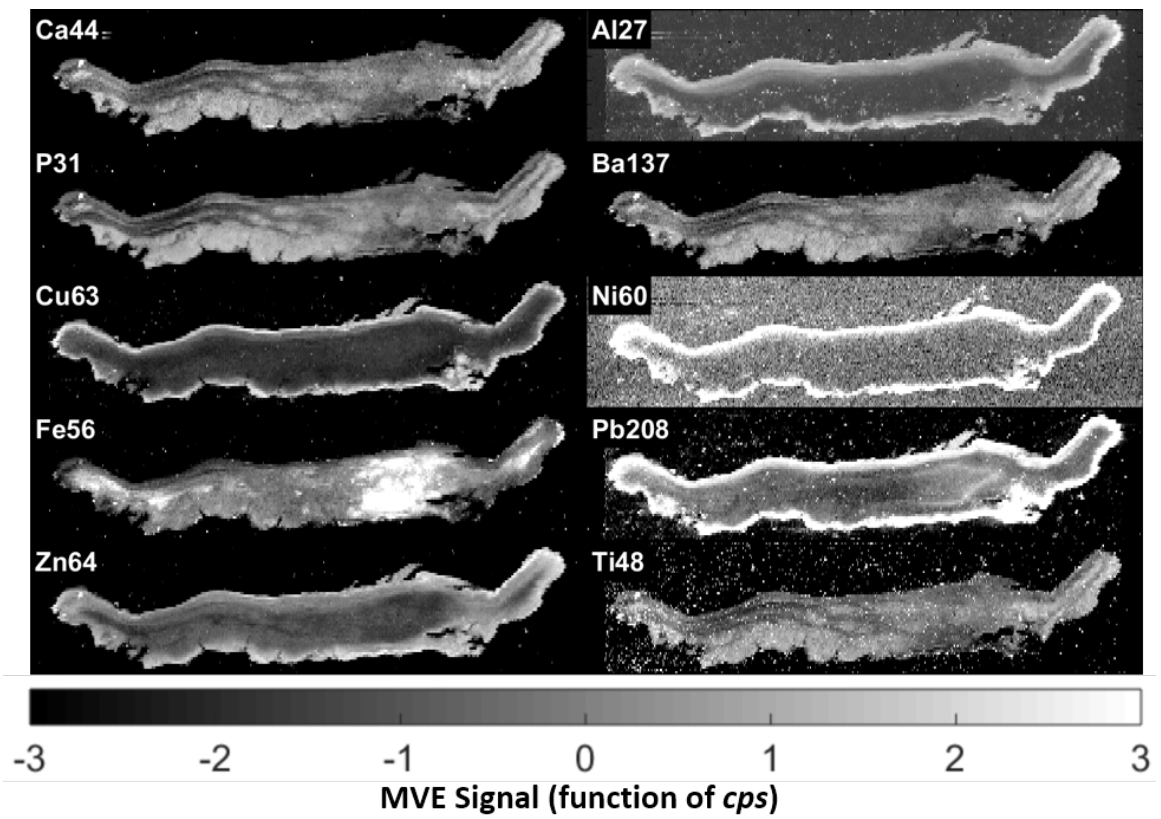
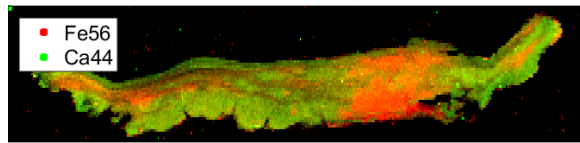
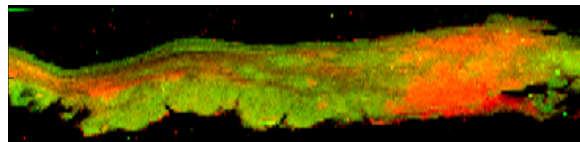


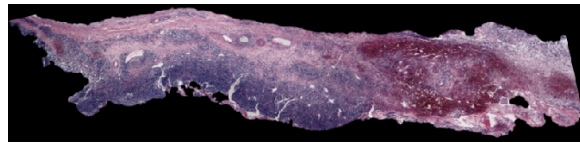
Figure 6-20: MVE-MIMS from select isotopes for LSBS 14391.



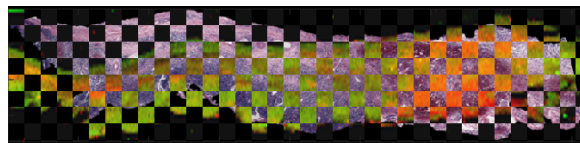
(a) Pseudo-colored raw MIMS image



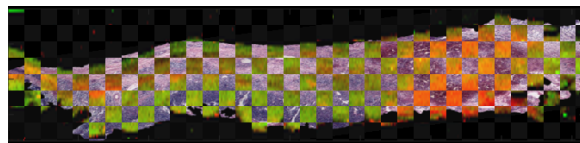
(b) Cropped MIMS image



(c) Raw H&E image

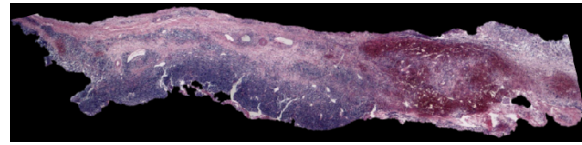


(d) Cropped MIMS image and raw H&E image checked



(e) Cropped MIMS image and transformed H&E image checked

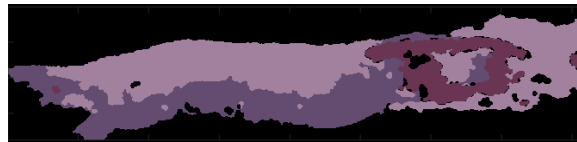
Figure 6·21: Images used for clinicopathological case study of LSBS 14391.



(a) Raw H&E image



(b) Raw 3 cluster H&E image

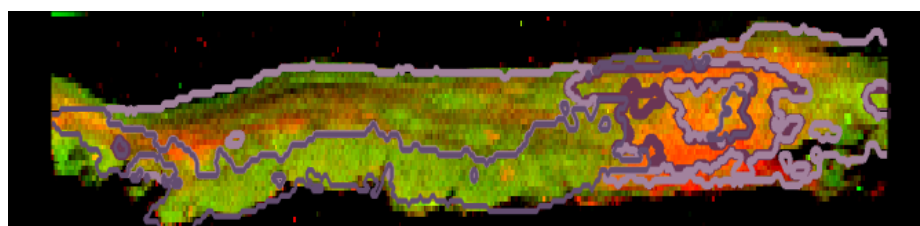


(c) Transformed and modified 3 cluster H&E image

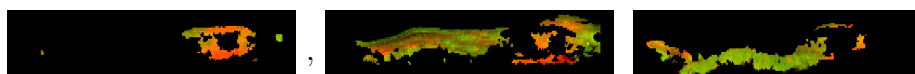
Figure 6·22: Segmentation of LSBS 14391 immunohistochemical image. Cluster colors are represented by the mean value of the pixels within each cluster.

tinguishable staining colors – deep red, light purple, and deep purple – in the H&E image were selected (see Fig. 6·22(b)). These raw clusters were then denoised and the clean cluster image was transformed into the MIMS image space using the transformation parameters determined using the `manualregGUI.m` function (Fig. 6·22(c)). The outlines of the H&E image segments are shown on the pseudo-colored MIMS image in Fig. 6·23(a) and the MIMS image pixels associated with each segment are shown in Figs. 6·23(b)–6·23(d). These segments derived from the H&E image were used to determine the median MVE-signal level for each isotope. These values are plotted in Fig. 6·23(e). Note that for these data, both the mean and median values yield similar results.

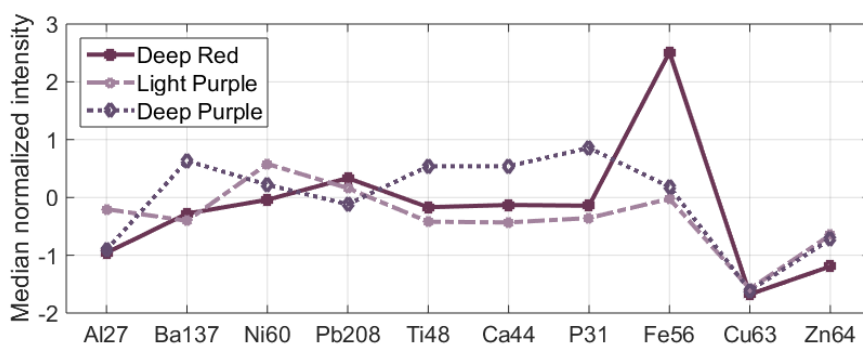
The two most apparent observations confirmed by the plot are the elevated ^{56}Fe MIMS signal within the segment corresponding to the deep red area in the H&E image and the co-occurring elevated levels of ^{31}P , ^{44}Ca , ^{48}Ti and ^{137}Ba within the



(a) MIMS with cluster segment outlines



(b) Deep red segment (c) Light purple segment (d) Deep purple segment



(e) Median signal per isotope per cluster segment

Figure 6-23: Visualization and analysis of immunohistochemical image derived segments for LSBS 14391 shown on MIMS image.

deep purple segment relative to other parts of the image. This striking observation may suggest that the inflammatory response, which is identified by the heavily hematoxylin-stained, deep purple area along the bottom edge of the LSBS in the H&E image, and confirmed by the high levels of ^{31}P and ^{44}Ca in the MIMS data, maybe related to the elevated ^{48}Ti and ^{137}Ba levels.

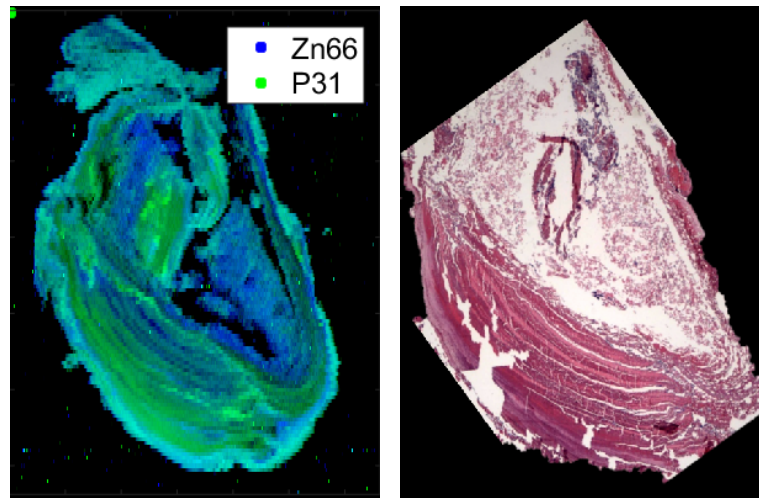
Analysis of LSBS 3733-2 from the KED2.1 experiment was attempted using the same method used for LSBS 14391 (manual registration of the H&E image with the MIMS followed by clustering of the H&E image), however, results were not successful likely owing to several characteristics of the H&E image including lower contrast, less clearly defined boundaries and less dense tissue structures (see Fig. 6-24(b)). Nevertheless,

examination of the various MIMS channels (see Figs. 6·11 and 6·12) reveals that certain tissue features appear clearly differentiated in the MIMS relative to the pathologies visible in the H&E image. A similar approach of k-means guided segmentation, where rather than performing k-means using the H&E image as before, the endogenous MIMS isotopes were used instead. The segments produced by k-means were grouped together such that five pathologies of interest were roughly defined by the clusters: 1) dense core, 2) squames, 3) inflammation, 4) striated interior, and 5) striated periphery. These MIMS-derived clusters are depicted in Fig. 6·24(c) and their approximate areas in the H&E image are indicated in Fig. 6·24(d).

The median MVE signal within each region of the MIMS tissue image for LSBS 3733-2 from the KED2.1 experiment was used to generate the plot in Fig. 6·25(a). Since these MIMS data were also acquired with a suitable set of calibration standards, a comparison of median absolute concentration within each segment is also possible and is shown in Fig. 6·25(b). While the interpretation of these results are still underway, the potential for deployment of MIMS for quantitative analysis of specific mechanisms was demonstrated through the analysis conducted on these two samples.

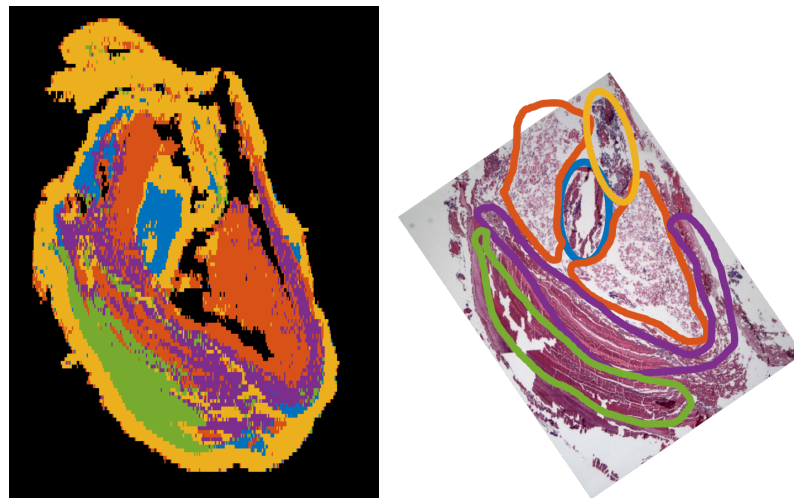
6.6 Summary of Contributions

In this chapter, the MIMS methods developed in Chapter 4 were demonstrated to provide unprecedented in-situ elemental-isotopic maps for identification, localization, and quantification of endogenous and exogenous metals in human lacrimal sac biopsy samples. The work described in this chapter demonstrates the unique ability of using MIMS to contextualize pathology with physiologically relevant information (i.e., such as context provided by ^{56}Fe for distribution of ^{208}Pb in Fig. 6·20). The analysis carried out in this chapter demonstrated that MIMS is a reproducible, analytical,



(a) Psuedo-colored MVE-MIMS

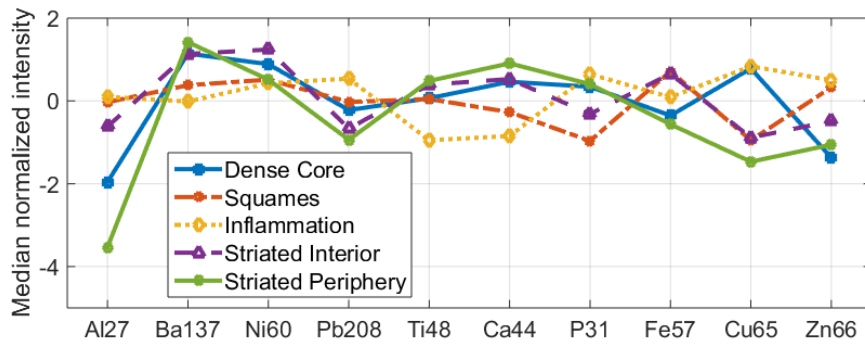
(b) Raw H&E image



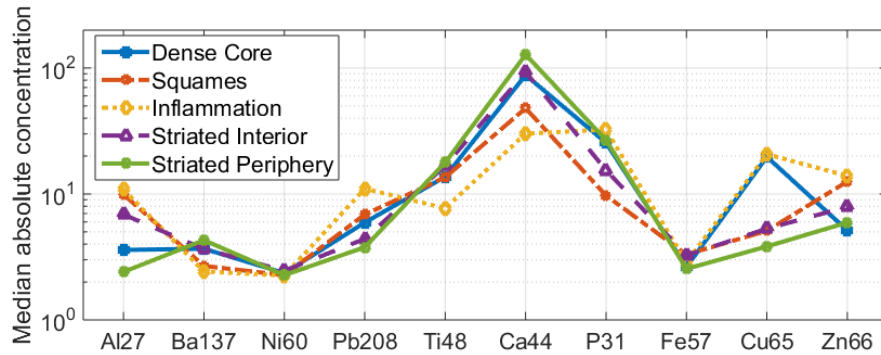
(c) Five clusters derived from MIMS tissue image

(d) Five clusters derived from MIMS tissue image

Figure 6-24: Images used for clinicopathological case study of LSBS 3733-2. Each color in (c) represents a cluster associated with the following tissue features: 1) dense core, 2) squames, 3) inflammation, 4) striated interior, and 5) striated periphery



(a) Median MVE signal per isotope per cluster segment



(b) Median absolute concentration per isotope per cluster segment

Figure 6-25: Median signal levels within MIMS-derived clusters for LSBS 3733-2 in experiment KED2.1.

quantitative method whose potential to enhance our understanding of a wide range of diseases has only just been explored.

An additional contribution made was the evaluation of the consistency of the MIMS acquisition procedure. Images produced using the kinetic energy discrimination (KED) and standard (STD) operating modes of the inductively-coupled plasma mass spectrometry (ICP-MS) instrument were evaluated both qualitatively in regards to the resulting elemental-isotopic tissue maps of LSBS specimens, and quantitatively in terms of the results derived from imaged calibration standards. Through these analyses, acquisition in KED mode is recommended. Upper bounds on the absolute concentration of the ten isotopes considered in the lacrimal sac biopsy samples are provided in Table 6.3.

Chapter 7

Conclusions

7.1 Summary of Contributions

The work described has aided in the development of a mouse model of traumatic brain injury by offering quantitative insights to standardize experimental parameters and subsequent neuropathological assessments. The algorithmic contributions could generally be summarized as combinations of classical and state-of-the-art techniques in image processing and computer vision. These techniques enable the robust and objective evaluation of the contributors to TBI severity and neuropathological sequelae. Aside from the analytic contributions, much of the work targeted novel assessments of animal models for TBI including large-scale grading of photomacroscopic images, kinematic analysis of head motion, and utilization of metallomic imaging mass spectrometry. While the described work fits into a much larger program aimed at understanding, diagnosing and improving outcomes for TBI, contributions made as part of this thesis addressed challenges encountered at various stages of the experimental process.

The first method discussed in Section 3.1 was the development of a tracking algorithm for the evaluation of a mouse's head motion during the blast and impact neurotrauma injury procedures using high-speed videography. In each frame, the algorithm deter-

mines the position of a painted point on the mouse's nose using a hybrid k-means and Chen-Vese segmentation algorithm. Application of this level-set method for segmentation was shown to work well despite frame-to-frame intensity variations and gave better results than k-means clustering alone. Since the head motion metrics of interest included peak acceleration (second derivative of position), a Kalman Filter was used to estimate nose velocity and acceleration in addition to a smooth position curve.

A variety of image processing methods were developed to aid in the objective evaluation of blood-brain barrier dysfunction using Evans blue extravasation as an indicator. These methods were developed to evaluate traditional biological imaging modalities including optical and fluorescent imaging. One method used partially labeled images to construct color models for four tissues classifications of interest (Section 3.2). These models were then used to perform per pixel classification in images of whole-brain photomacroscopy. These classifications enabled the evaluation of severity of surface pathology following impact neurotrauma. Methods for normalization and segmentation of fluorescent images were also developed (Section 3.3). These methods were subsequently used to develop a TBI severity grading system and to quantitate pathological signatures in the images.

A significant part of this thesis was focused on developing image processing tools for evaluating the metallic imaging mass spectrometry (MIMS) method. A suite of functions enabled the extraction, visualization and assessment of MIMS maps. Methods for MIMS-specific standardization, including mean-variance equalization (Section 4.4) and calibration to absolute concentration (Section 4.3), were developed as tools for inter-channel and inter-subject comparison of resulting elemental-isotope tissue maps.

Finally, the most novel and substantial contribution of this thesis was the development of a multi-modal, multi-channel image registration (MMMCIR) methodology to recover alignment parameters between two images having dramatically different characteristics (Section 4.5). Optimal affine transformation parameters were determined by maximizing the mutual information (MI) between the fixed image and the transformed moving image via simulated annealing. The algorithm required estimation of a probability density function, which was achieved using kernel density estimation.

The MMCIR method was used to register MIMS tissue maps from two distinct experimental cohorts with corresponding atlas images downloaded from the Allen Mouse Brain Atlas (Atlas, 2013) (Chapter 5). After correspondence between the MIMS tissue map and atlas image was determined, the anatomical structures defined in the atlas image was used to impart anatomical boundaries onto the MIMS tissue map. In essence, an automatic method for anatomical segmentation of MIMS tissue maps has been developed. This segmentation was subsequently used to compare signal levels on the left and the right sides of a coronal section of the MIMS tissue map. This comparison has confirmed signal differences in a pilot cohort of gadolinium-injected mice. However, the measurements made on an earlier cohort of nanoparticle cocktail injected mice motivated a need for drift correction of MIMS channels.

The final chapter presented work carried out to investigate nine human lacrimal sac biopsy samples obtained from collaborators at Mount Sinai Hospital, Toronto, Canada. This work included evaluation of the quality of calibration curves using the standard and kinetic energy discrimination modes on the mass spectrometer. Since four of the samples were acquired multiple times, these data confirmed the consistency of the obtained MIMS tissue maps, but also demonstrated the challenges associated with deriving an absolute concentration image from raw instrument intensities and

a set of imaged calibration standards. Preliminary clinicopathological analyses were carried out on two lacrimal sac biopsy samples where context provided by corresponding immunohistochemical images was used to evaluate pathological features of interest in the MIMS. These contributions have the potential to offer valuable insights into the progression and severity of dacryolith formation.

7.2 Future Work

Metallomic imaging mass spectrometry (MIMS) is a relatively new modality in the field of biological imaging and, as such, few methods exist to support MIMS data acquisition and analysis. Despite having demonstrated the unique capabilities of MIMS analysis for applications in BBB assessment and localization of toxic metals in tissue, more MIMS data are required to establish physiological baselines. The ultimate goal of the types of analyses described herein is the automatic identification of disease-specific features presented in MIMS maps. These elemental-isotopic signatures may subsequently be correlated to relevant physiological phenomenon (i.e., correlating localized elevated levels of iron with blood-containing areas in biological tissue) to inform our understanding of disease pathogenesis. Notwithstanding, future developments to improve aspects of the image registration procedure and the MIMS acquisition procedure would help streamline and support the analysis of these data for quantitative assessment of elemental-isotopic content in biological tissue.

The quality of image registration between MIMS brain maps and a traditional modality, such as a Nissl image, could be improved by designing a protocol where an adjacent tissue section is collected, stained, and imaged for use in registration with the neighboring MIMS brain map. This procedure would minimize the influence of out-of-plane cutting artifacts discussed in Section 5.2.4 since any artifact would be consistent for a

neighboring section. A method similar to that described in (Abdelmoula et al., 2014) could be implemented for automatic selection of the appropriate Allen Mouse Brain Atlas section best suited to impart anatomical boundaries on the tissue section.

Extensions made to the image registration (IR) speed and accuracy would also help to improve the utility of the MMMCIR function. One widely used method for improving IR accuracy is by using a multi-resolution approach where image correspondence is determined at a coarse resolution first and then used to initialize a higher-resolution IR experiment. Improvements to how image similarity is calculated and to the flexibility of the transformation model would also be natural extensions. The method used to calculate mutual information (MI) suffers from being computationally expensive and is intractable as the dimensionality of the joint density function increases. A recommended extension would be to implement a more efficient scheme for determining the similarity between multi-modal, multi-channel images, such as through entropic graphs (Hero et al., 2002). Non-rigid transformation models may also improve results, such as the symmetric normalization method for diffeomorphic mappings (Avants et al., 2007).

Beyond improvements to the existing MMMCIR architecture, the possibility of clean representation and detailed characterization of MIMS remains an open problem. The Allen Mouse Brain resources (Lein et al., 2007) have served as a gold standard for evaluating mouse anatomy and neurophysiology. Hare et al. (2012) constructed the first 3D atlas of iron, zinc and copper in a C57BL/6 mouse brain; however, the atlas represents data from a single mouse with fairly low spatial resolution ($80 \mu m$ isotropic in 2D and spaced every $150 \mu m$). This type of detailed characterization of metallomic brain composition in the mouse brain has yet to be achieved.

Further work towards reduction of instrument artifacts would also greatly improve

the reliability of the information provided by the MIMS method. In both cohorts considered in Chapter 5 there were a variety of cases where the levels of endogenous isotopes were expected to be approximately equal on the left and right side of the brain (indicated by a $\bar{\delta}^{(L-R)} \approx 0$), but the calculated values of $\bar{\delta}^{(L-R)}$ did not strongly support this hypothesis. While not visually apparent, these discrepancies are likely due to signal drift over time, a known issue in LA-ICP-MS. Newly-published works on MIMS operating procedures (Hare et al., 2017) and drift correction (Uerlings et al., 2016b) offer insights into data acquisition and post-processing best practices.

Appendices

Appendix A

Experimental Protocols

A.1 Tissue Preparation

The protocols are copied directly from Goldstein et al. (2012): “Mice were euthanized by CO_2 -asphyxiation and transcardially perfused with phosphate-buffered saline (PBS). Whole brains were prefixed in 10% neutral buffered formalin, block-sectioned into 2-mm coronal slabs, postfixed in 4% paraformaldehyde, paraffin-embedded, and serially sectioned at 10 μm .” Serial sectioning was not typically performed as part of metallomic imaging mass spectrometry preparation, where the face of the paraffin-embedded block was ablated.

A.2 Evans Blue Dye Injection and Imaging Method

The EBD image assessment algorithms developed for this work and presented in Chapter 3 were used to derive the results in a recent publication (Tagge et al., 2017, Fig. 5A-D). The EBD injection and imaging procedure are summarized as follows:

1. Mice received a 4 mL/kg intraperitoneal injection of 2% weight-by-volume EBD in saline one hour before the indicated experimental TBI condition
2. TBI experimental method is followed (including BUCS)

3. Mice were euthanized via CO_2 asphyxiation and transcardially perfused with phosphate-buffered saline (PBS) to allow blood and EBD to be washed from the circulatory system
4. Brains were harvested with care to remove the dura
5. Gross pathology was documented by photomacroscopy with a Nikon D5200 digital camera under cross-polarized white light illumination
6. The brains were sectioned (2 mm) coronally and imaged with an IVIS Spectrum In Vivo Imaging System (PerkinElmer, Waltham, MA)
7. Separate fluorescent images were acquired at 0.5 s exposure with 535 nm excitation filter and the following emission filters: $580, 600, 620, 640, 660, 680, 700, 720, 740, 760, 780, 800, 820, 840\text{ nm}$. Non-specific autofluorescence signal was removed by spectral unmixing algorithm (Living Image software, Perkin-Elmer)

A.3 Matrix-Match Calibration Standards for MIMS

Matrix-match calibration standards presented in Chapter 6 for calibrating STD2.x and KED2.x experiments were prepared as follows:

1. A stock solution was created such the concentration of each of the 14 elements in the stock solution was $\mathbb{X} = 100 \frac{\mu\text{g El}}{\text{g stock}}$
2. A 10% w/w gelatin solution was create with deionized water in a sterile beaker (that is for every 10 g water, 1 g of gelatin was added) . The solution was stirred for approximately an hour on a magnetic stirrer hot plate set to 50°C .
3. For each target calibration level $x \left[\frac{\mu\text{g El}}{\text{g Sol'n}} \right]$, a test tube was filled with the appropriate mass of gelatin solution ($v, [g]$) and stock solution ($w, [g]$) to achieve

the target *ppm* level x using the following equation:

$$x \left[\frac{\mu g \text{ El}}{g \text{ Sol'n}} \right] = \frac{w [g \text{ stock}] \mathbb{X} \left[\frac{\mu g \text{ El}}{g \text{ stock}} \right]}{v [g \text{ gelatin}] + w [g \text{ stock}]}$$

were v is the weight of the gelatin solution, w is the weight of the stock elemental solution, and \mathbb{X} is the average final *ppm* value of the stock elemental solution.

4. The test tubes of each of the final gelatin calibration standard solutions were thoroughly mixed by shaking the test tube and mixing the solution with a pipette.
5. The solutions were pipetted into a $1 \text{ cm} \times 1 \text{ cm}$ embedding block and stored at $4 - 8^{\circ}\text{C}$ until required for an experiment.
6. A $20 \mu\text{m}$ section of each block was placed on a glass slide for evaluation in a MIMS sequence acquisition.

To make all eight calibration standard values $x = [0, 0.5, 1, 2, 5, 10, 20, 50]$, a 10 mL elemental stock solution was made and a 60 mL gelatin solution. All masses and calculations may be recorded using a developed `GelatinStandardSolution.xlsx` spreadsheet.

Appendix B

Overview of MATLAB Tools Developed for MIMS

B.1 MIMS Raw Data Files and Resulting MATLAB Data Structures

The MATLAB function, `readfiles.m`, was developed to extract raw data from the spectrometer instruments in the Center for Biometals & Metallomics at the Boston University School of Medical. Since data from the optical emission spectrometer (OES), the magnetic sector field (MSF) mass spectrometer, and the quadropole (Quad) mass spectrometer are saved as three different file formats (`txt`, `fin2` and `csv`, respectively), `readfiles.m` identifies the file format and parses the data according to the instrument specific raw data structure. The OES instrument provides a single `txt` file per MIMS sequence with data laid out as in Fig. B-1. The file format for the MSF and the Quad instruments are both quite similar, each providing one file per line of data in a MIMS sequence with raw data structures shown in Figs. B-2 and B-3.

Regardless of the instrument used, calling `readfiles.m` outputs a data structure with a field for each isotope (or element when using OES) acquired. Each of these fields is an $M \times N$ matrix containing the raw intensity values recorded by the instrument

*.txt Files – OES, 1 file/sequence				
1,5nebcuGridvarSpe1,3/16/2012 23:51:38,admin				
100%,50um spot,12.5ums-1				
Element,Time(sec),LeftBkg,Center,RightBkg				
Ca3933, 0.0,	0,	0,	0	} $i = 1$
Ca3933, 0.2,	0,	314,	0	
Ca3933, 0.4,	0,	476,	0	
Ca3933, 0.6,	0,	625,	0	
⋮				
Ca3933,1749.8,	0,	1627098,	0	} $i = 2$
Ca3933,1750.0,	0,	1627306,	0	
Ca3933,1750.2,	0,	1627452,	0	
Cu2247, 0.0,	0,	0,	0	
Cu2247, 0.2,	99,	169,	184	
Cu2247, 0.4,	99,	171,	191	} $i = d$
Cu2247, 0.6,	99,	171,	196	
Cu2247, 0.8,	99,	175,	204	
⋮				
Zn2138,1749.6,	13827,	762316,	14466	} $i = d$
Zn2138,1749.8,	13827,	762316,	14470	
Zn2138,1750.0,	13832,	762316,	14470	
Zn2138,1750.2,	13832,	762335,	14470	
1,5nebcuGridvarSpe3,3/17/2012 0:51:29,admin				
100%,50um spot,12.5ums-1				
Element,Time(sec),LeftBkg,Center,RightBkg				
Ca3933, 0.0,	0,	0,	0	} $i = d$
Ca3933, 0.2,	0,	356,	0	
Ca3933, 0.4,	0,	538,	0	
Ca3933, 0.6,	0,	651,	0	

Figure B.1: Raw data structure in txt files from the optical emissions spectrometer.

*.fin2 Files – MSF, 1 file/line	
Finnigan MAT ELEMENT Raw Data	
Tuesday, July 10, 2012 21:59:49	
12709RightBrainC.FIN	
265	
0	
16,1 ⁱ	$i = 1$ $i = 2$ $i = d$
CPS	⋮
Time,Mg24>MR<,Mn55>MR<,Fe56>MR<,Cu63>MR<,Zn64>MR<,Cu65>MR<,Zn70	
1.016000,60512.000000,194440.000000,450426.000000,73408.000000,	
2.029000,43648.000000,184521.000000,409743.000000,51584.000000,	
3.043000,32736.000000,181539.000000,481189.000000,45632.000000,	
4.056000,23808.000000,168649.000000,460347.000000,48608.000000,	
5.070000,30752.000000,178563.000000,497057.000000,68449.000000,	
6.084000,23808.000000,155748.000000,540742.000000,55552.000000,	

Figure B.2: Raw data structure in fin2 files from the magnetic sector field MS.

*.csv Files – Quad, 1 file/line						
LacSac_5257_1_line16:02/22/2016 08:49:17 AM;						Header
Software:Name=Qtegra;Version=2.6.2205.66;File Version=1;						
Configuration:Machine=iCAP Q;						
Laser KEDS 16Feb:Additional Gas Flow 1=0;Additional Gas Flow 2=0;Addit						
Pulse Cour : : : : : 0000;						
	$i = 1$	$i = 2$...		$i = d$	
Time	27Al	31P	44Ca	48Ti	57Fe	60Ni
	dwel tim	dwel tim	dwel tim	dwel tim	dwel tim	dwel tim
0.02234	500.01	1000.04	1666.778	350.0049	700.0196	200.0016
0.31559	850.0289	833.3611	3333.778	100.0004	1250.063	350.0049
0.60897	250.0025	0	1500.09	200.0016	300.0036	350.0049
0.90213	600.0144	1333.404	3667.205	100.0004	650.0169	150.0009
1.19535	350.0049	833.3611	3167.068	350.0049	450.0081	100.0004
1.48861	400.0064	1000.04	2000.16	250.0025	850.0289	300.0036
	Data					

Figure B.3: Raw data structure in csv files from the quadrupole MS.

for each of the M raster lines with N data points per line. A screenshot of the data structure resulting from the command

```
[d,hdrtxt] = readfiles;
```

is shown in Fig. B.4.

Since development of most recent standard operating procedure for MIMS sequence acquisition in 2015, the newest version of `readfiles.m` (version 10) also parses out header information from the quadrupole ICP-MS raw data files and provides this information as an $M + 1 \times 86$ cell variable `hdrtxt` for each line of the M scanned lines. This variable is used to differentiate the distinct MIMS maps in a sequence. The function `divMIMSstruct.m` takes `hdrtxt` as an input and identifies unique line labels in the first column of the cell (see Fig. B.5).

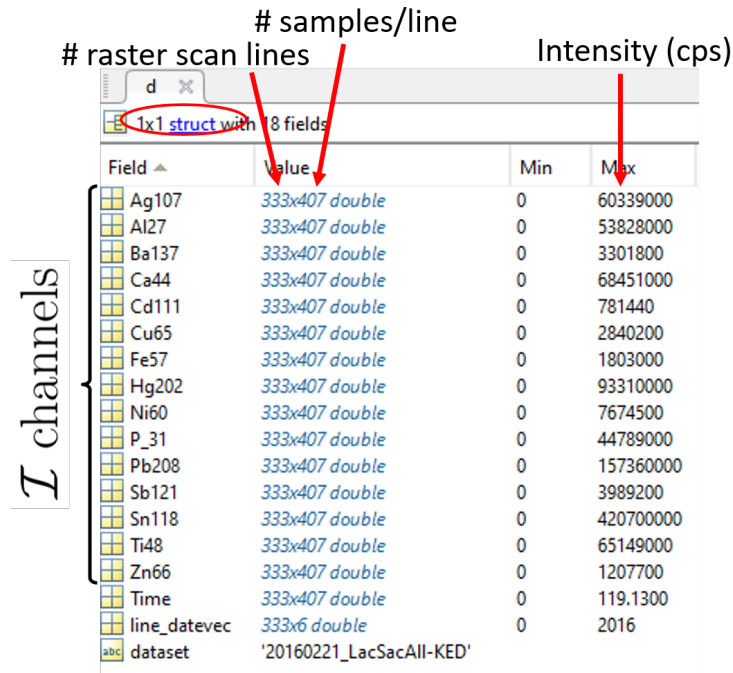


Figure B-4: Data structure provided by readfiles.m in MATLAB workspace.

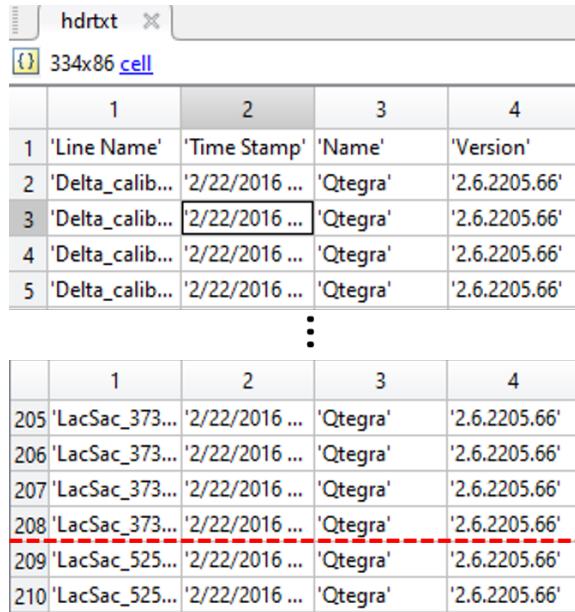


Figure B-5: Quadrupole header file information provided by readfiles.m in MATLAB workspace.

B.2 List of MATLAB Functions

The list of MATLAB functions below is not comprehensive of all functions written to support this thesis, but includes the most relevant original^I functions. If the function is used for the results pertaining to a specific chapter, that chapter is indicated. If the function is used widely for multiple chapters (as are most of the functions developed for MIMS), no chapter will be specified.

B.2.1 Chapter 3 Functions

- HSVtrackingKF
Kalman filtering for tracking position, velocity and acceleration of mouse noise in high speed videos.
Supportive functions: detectHSVobject, CVcentroidPerFrame, computeImageCentroid
- (1) EB_brainimg_processing, (2) EB_brainimg_buildpdfs, (3) EB_brainimg_classifyimgs
These functions support the semi-supervised pathology classification of EB-injected surface macroscopic images. (1) uses a file-specific naming structure (file name includes the string “mask”) to identify images for which tissue class examples are available. (2) and (3) are sequentially executed to ultimately build the probability density function $p(c|\vec{i})$ and classify pixels in each image respectively.
Supportive functions: build_rgbpdf

B.2.2 MIMS Functions

- readfiles
Extracts raw MIMS data into a structure in MATLAB. This structure is the basic data variable required by most of the functions developed.
- reshape_OEScorr
Restructures raw data from the optical emission spectrometer which contains multiple horizontal lines in a single data line (described in Section 4.1.3).

^IParts of these functions may require either MATLAB licensed or publicly available MATLAB functions.

- `labelMIMSstruct`
Uses outputs from `readfiles.m` to automatically segment the parts of a MIMS map (described in Section 4.2).
Supportive functions: `divMIMSstruct`, `bimodalHistMask`
- `MIMSmve`
Transforms data into a normalized domain using mean-variance equalization (described in Section 4.4).
Supportive functions: `labelMIMSstruct`

B.2.3 MMMCIR Functions

- `manualregGUI`
GUI which provides the user with real-time visualization of applying different affine transformation parameters to a moving image.
- `simannealGeneral`
Simulated annealing optimization function which relies heavily on MATLAB's `simulannealbnd.m`. It's important to know that this function uses `twoimgMIkde.m` (personally implemented) to compute the multi-variate mutual information.
Supportive functions: `computeCost`, `twoimgMIkde`
- Accessory Functions: `transform_image`, `alpha2tmat`, `change_alpha_dim`, `find_inv_alpha`
Functions containing relevant affine transformation parameter adjustments.
- `MIMSregSequence`, `regresultPlots`
Performs all processing required for image registration procedure described in Chapter 5
Supportive functions: `simannealGeneral`

B.2.4 Image Visualization Functions

- `plot_heatmap`
MIMS data structure-specific plotting function. A variety of property options have been embedded which afford the user a high degree of custom visualization options including channel overlaying, selection of pseudo coloring map, spatial scaling of axes, title and colorbar properties, etc. A full list of the available properties can be found in the header of the function.
Supportive functions: `auto_thresh`
- `imoverlay`
Various dual image visualization methods (transparent overlay, checkering, edge display, etc.) for visualizing image registration results.

Appendix C

Derivation of Physical Parameters for Inverse Affine Transformation

Recall the following definitions from Section 4.5.2 and Eqn. 4.16:

Physical Transformation Parameters

$$\vec{\mu} = \{t_x, t_y, \theta, s_x, s_y, s_k\}$$

Affine Transformation Parameters

$$\vec{a} = [a_1, a_2, a_3, a_4, a_5, a_6]^T$$

Affine Transformation Matrix

$$\begin{aligned}
 A_{\vec{\mu}} &= \left(\underbrace{\begin{bmatrix} 1 & 0 & t_x \\ 0 & 1 & t_y \\ 0 & 0 & 1 \end{bmatrix}}_{\text{translation}} \cdot \underbrace{\begin{bmatrix} \cos(\theta) & -\sin(\theta) & 0 \\ \sin(\theta) & \cos(\theta) & 0 \\ 0 & 0 & 1 \end{bmatrix}}_{\text{rotation}} \cdot \left(\underbrace{\begin{bmatrix} 1 & s_k & 0 \\ 0 & 1 & 0 \\ 0 & 0 & 1 \end{bmatrix}}_{\text{skew}} \cdot \underbrace{\begin{bmatrix} s_x & 0 & 0 \\ 0 & s_y & 0 \\ 0 & 0 & 1 \end{bmatrix}}_{\text{scaling}} \right) \right) \\
 &= \begin{bmatrix} s_x \cos(\theta) & s_y(s_k \cos(\theta) - \sin(\theta)) & t_x \\ s_x \sin(\theta) & s_y(s_k \sin(\theta) + \cos(\theta)) & t_y \\ 0 & 0 & 1 \end{bmatrix} = \begin{bmatrix} a_1 & a_2 & a_3 \\ a_4 & a_5 & a_6 \\ 0 & 0 & 1 \end{bmatrix}
 \end{aligned}$$

where

t_x = positive value shifts image to the left

t_y = positive value shifts image up

θ = rotation angle, measured counter-clockwise from the x -axis

s_x = change of scale in x direction

s_y = change of scale in y direction

s_k = shear factor along the x -axis = $\tan(\omega)$

(ω = the skew angle, measured clockwise from the y -axis)

Generally, the relationship between affine transformation parameters, \vec{a} and physical transformation parameters, $\vec{\mu}$, can be derived using the six equations:

$$(1) \quad a_1 = s_x \cos \theta \quad (2) \quad a_2 = s_y (s_k \cos \theta - \sin \theta) \quad (3) \quad a_3 = t_x$$

$$(4) \quad a_4 = s_x \sin \theta \quad (5) \quad a_5 = s_y (s_k \sin \theta + \cos \theta) \quad (6) \quad a_6 = t_y$$

Given an affine transformation matrix A , the goal is to determine the physical transformation parameters as a function of \vec{a} . This can be done solving the system of equations:

Equations (1) and (4) can be used to solve for $\theta(\vec{a})$:

$$s_x = \frac{a_1}{\cos \theta} \quad \Rightarrow \quad a_4 = a_1 \frac{\sin \theta}{\cos \theta} \quad \Rightarrow \quad \boxed{\theta = \tan^{-1} \left(\frac{a_4}{a_1} \right)}$$

Equations (2) and (5) are equal and can be used to solve for $s_k(\vec{a})$

$$\frac{a_5}{(s_k \sin \theta + \cos \theta) s_y} = \frac{a_2}{(s_k \cos \theta - \sin \theta) s_y}$$

$$a_5 s_k \cos \theta - a_5 \sin \theta = a_2 s_k \sin \theta + a_2 \cos \theta$$

$$s_k (a_5 \cos \theta - a_2 \sin \theta) = a_2 \cos \theta + a_5 \sin \theta$$

$$s_k = \frac{a_2 \cos \theta + a_5 \sin \theta}{a_5 \cos \theta - a_2 \sin \theta}$$

Resulting $\vec{\mu}(\vec{a})$:

$$t_x = a_3$$

$$t_y = a_6$$

$$\theta = \tan^{-1} \left(\frac{a_4}{a_1} \right)$$

$$s_x = \frac{a_1}{\cos \theta} = \frac{a_4}{\sin \theta}$$

$$s_y = \frac{a_5}{(s_k \sin \theta + \cos \theta)}$$

$$s_k = \frac{a_2 \cos \theta + a_5 \sin \theta}{a_5 \cos \theta - a_2 \sin \theta}$$

Note that s_y is expressed as a function of s_k . One could either substitute the expression for $s_k(\vec{a})$ into the expression for $s_y(\vec{a})$, or one could solve for $s_k(\vec{a})$, then use this value to solve for $s_y(\vec{a})$.

Using these expressions and noting that $A_{\vec{\mu}}^{-1} = B_{\vec{\mu}'}$ is also a 3×3 matrix with six non-zero affine transformation parameters \vec{b} , the physical transformation parameters for the inverse affine transformation can be solved using the equations above and the values if the inverse transformation matrix $B_{\vec{\mu}'}$.

This procedure is implemented in the function `find_inv_alpha.m`.

Bibliography

- Abdelmoula, W. M., Carreira, R. J., Shyti, R., Balluff, B., van Zeijl, R. J. M., Tolner, E. A., Lelieveldt, B. F. P., van den Maagdenberg, A. M. J. M., McDonnell, L. A., and Dijkstra, J. (2014). Automatic Registration of Mass Spectrometry Imaging Data Sets to the Allen Brain Atlas. Analytical Chemistry, 86(8):3947–3954.
- Anderson, N. G., Wojno, T. H., and Grossniklaus, H. E. (2003). Clinicopathologic findings from lacrimal sac biopsy specimens obtained during dacryocystorhinostomy. Ophthalmic Plastic and Reconstructive Surgery, 19(3):173–176.
- Andreou, P. and Rose, G. E. (2002). Clinical presentation of patients with dacryolithiasis. Ophthalmology, 109(8):1573 – 1574.
- Atlas, A. B. (2013). Allen reference atlas: interactive atlas viewer.
- Avants, B. B., Duda, J. T., Zhang, H., and Gee, J. C. (2007). Multivariate normalization with symmetric diffeomorphisms for multivariate studies, volume 10, pages 359–366.
- Avants, B. B., Epstein, C. L., Grossman, M., and Gee, J. C. (2008). Symmetric diffeomorphic image registration with cross-correlation: evaluating automated labeling of elderly and neurodegenerative brain. Medical Image Analysis, 12(1):26–41.
- Avants, B. B., Tustison, N. J., Song, G., Cook, P. A., Klein, A., and Gee, J. C. (2011). A reproducible evaluation of ANTs similarity metric performance in brain image registration. Neuroimage, 54(3):2033–2044.
- Barkhoudarian, G., Hovda, D. A., and Giza, C. C. (2011). The molecular pathophysiology of concussive brain injury. Clinics in Sports Medicine, 30:33–48.
- Becker, J., Matusch, A., and Wu, B. (2014). Bioimaging mass spectrometry of trace elements - recent advance and applications of LA-ICP-MS: A review. Analytica Chimica Acta, 835:1 – 18.
- Becker, J. S. and Salber, D. (2010). New mass spectrometric tools in brain research. Trends in Analytical Chemistry, 29(9):966 – 979.

- Becker, J. S., Zoriy, M., Becker, J. S., Dobrowolska, J., and Matusch, A. (2007). Laser ablation inductively coupled plasma mass spectrometry (LA-ICP-MS) in elemental imaging of biological tissues and in proteomics. Journal of Analytical Atomic Spectrometry, 22:736–744.
- Becker, J. S., Zoriy, M., Matusch, A., Wu, B., Salber, D., Palm, C., and Becker, J. S. (2010). Bioimaging of metals by laser ablation inductively coupled plasma mass spectrometry (LA-ICP-MS). Mass Spectrometry Reviews, 29(1):156–175.
- Beni-Adani, L., Gozes, I., Cohen, Y., Assaf, Y., Steingart, R. A., Breneman, D. E., Eizenberg, O., Trembolter, V., and Shohami, E. (2001). A peptide derived from activity-dependent neuroprotective protein (ADNP) ameliorates injury response in closed head injury in mice. Journal of Pharmacology and Experimental Therapeutics, 296(1):57–63.
- Benzinger, T. L. S., Brody, D., Cardin, S., Curley, K. C., Mintun, M. A., Mun, S. K., Wong, K. H., and Wrathall, J. R. (2009). Blast-related brain injury: imaging for clinical and research applications: report of the 2008 St. Louis workshop. Journal of Neurotrauma, 26.
- Bishop, C. M. (2006). Pattern Recognition and Machine Learning (Information Science and Statistics). Springer-Verlag New York, Inc., Secaucus, NJ, USA.
- Brenner, L. A., Ivins, B. J., Schwab, K., Warden, D., Nelson, L. A., Jaffee, M., and Terrio, H. (2010). Traumatic brain injury, posttraumatic stress disorder, and postconcussive symptom reporting among troops returning from Iraq. The Journal of Head Trauma Rehabilitation, 25:307–12.
- Cantu, R. C. (2007). Chronic traumatic encephalopathy in the national football league. Neurosurgery, 61(2):223.
- Caprioli, R. M., Farmer, T. B., and Gile, J. (1997). Molecular imaging of biological samples: localization of peptides and proteins using MALDI-TOF MS. Analytical Chemistry, 69(23):4751–4760.
- Caselles, V., Kimmel, R., and Sapiro, G. (1997). Geodesic active contours. International Journal of Computer Vision, 22(1):61–79.
- Cernak, I. and Noble-Haeusslein, L. J. (2010). Traumatic brain injury: an overview of pathobiology with emphasis on military populations. Journal of Cerebral Blood Flow and Metabolism, 30:255–266.
- Chan, T. and Vese, L. (2001). Active contours without edges. IEEE Transactions on Image Processing, 10(2):266–277.

- Chen, S. and Luk, B. (1999). Adaptive simulated annealing for optimization in signal processing applications. Signal Processing, 79(1):117 – 128.
- Chen, Y., Constantini, S., Trembovler, V., Weinstock, M., and Shohami, E. (1996). An experimental model of closed head injury in mice: pathophysiology, histopathology, and cognitive deficits. Journal of Neurotrauma, 13:557–68.
- Cornett, D. S., Reyzer, M. L., Chaurand, P., and Caprioli, R. M. (2007). MALDI imaging mass spectrometry: molecular snapshots of biochemical systems. Nature Methods, 4(10):828–833.
- DeKosky, S. T., Blennow, K., Ikonovic, M. D., and Gandy, S. (2013). Acute and chronic traumatic encephalopathies: pathogenesis and biomarkers. Nature Reviews Neurology, 9(4):192–200.
- del Valle, J., Camins, A., Pallas, M., Vilaplana, J., and Pelegri, C. (2008). A new method for determining blood-brain barrier integrity based on intracardiac perfusion of an Evans Blue-Hoechst cocktail. Journal of Neuroscience Methods, 174(1):42–49.
- Electron Microscopy Sciences (2016). Grids for Electron Microscopy. [Online; accessed 20-May-2016].
- Fischl, B. (2012). FreeSurfer. Neuroimage, 62(2):774–781.
- Fisher, A. (2017). Modeling acute and chronic effects of blast- and impact-related neurotrauma in mice. PhD thesis, Boston University.
- Frieden, T. R., Houry, D., and Baldwin, G. (2015). Report to Congress on Traumatic Brain Injury In the United States: Epidemiology and Rehabilitation. [Online; accessed 20-March-2017].
- Gavett, B. E., Stern, R. A., and McKee, A. C. (2011). Chronic traumatic encephalopathy: A potential late effect of sport-related concussive and subconcussive head trauma. Clinics in Sports Medicine, 30(1):179 – 188. Concussion in Sports.
- Goldstein, L. E., Fisher, A. M., Tagge, C. A., Zhang, X.-L., Velisek, L., Sullivan, J. A., Upreti, C., Kracht, J. M., Ericsson, M., Wojnarowicz, M. W., Goletiani, C. J., Maglakelidze, G. M., Casey, N., Moncaster, J. A., Minaeva, O., Moir, R. D., Nowinski, C. J., Stern, R. A., Cantu, R. C., Geiling, J., Blusztajn, J. K., Wolozin, B. L., Ikezu, T., Stein, T. D., Budson, A. E., Kowall, N. W., Chargin, D., Sharon, A., Saman, S., Hall, G. F., Moss, W. C., Cleveland, R. O., Tanzi, R. E., Stanton, P. K., and McKee, A. C. (2012). Chronic Traumatic Encephalopathy in Blast-Exposed Military Veterans and a Blast Neurotrauma Mouse Model. Science Translational Medicine, 4(134):134ra60.

- Guo, H. (2011). A simple algorithm for fitting a gaussian function [dsp tips and tricks]. IEEE Signal Processing Magazine, 28(5):134–137.
- Hansen, B. (2009). Lecture notes on nonparametrics. ECON 718.
- Hare, D. J., Kysenius, K., Paul, B., Knauer, B., Hutchinson, R. W., O’Connor, C., Fryer, F., Hennessey, T. P., Bush, A. I., Crouch, P. J., and Doble, P. A. (2017). Imaging Metals in Brain Tissue by Laser Ablation - Inductively Coupled Plasma - Mass Spectrometry (LA-ICP-MS). Journal of Visualized Experiments, (119).
- Hare, D. J., Lee, J. K., Beavis, A. D., van Gramberg, A., George, J., Adlard, P. A., Finkelstein, D. I., and Doble, P. A. (2012). Three-dimensional atlas of iron, copper, and zinc in the mouse cerebrum and brainstem. Analytical Chemistry, 84(9):3990–3997. PMID: 22462591.
- Hare, D. J., Raven, E. P., Roberts, B. R., Bogeski, M., Portbury, S. D., McLean, C. A., Masters, C. L., Connor, J. R., Bush, A. I., Crouch, P. J., and Doble, P. A. (2016). Laser ablation-inductively coupled plasma-mass spectrometry imaging of white and gray matter iron distribution in alzheimer’s disease frontal cortex. NeuroImage, 137:124 – 131.
- Hawes, M. J. (1988). The dacryolithiasis syndrome. Ophthalmic Plastic and Reconstructive Surgery, 4(2):87–90.
- Head and Neck Cancer Guide (2017). Orbital tumors. [Online; accessed 17-March-201y].
- Heinrich, M. P., Jenkinson, M., Bhushan, M., Matin, T., Gleeson, F. V., Brady, S. M., and Schnabel, J. A. (2012). Mind: Modality independent neighbourhood descriptor for multi-modal deformable registration. Medical Image Analysis, 16(7):1423 – 1435. <ce:title>Special Issue on the 2011 Conference on Medical Image Computing and Computer Assisted Intervention</ce:title>.
- Hero, A., Ma, B., Michel, O., and Gorman, J. (2002). Applications of entropic spanning graphs. IEEE Signal Processing Magazine, 19(5):85–95.
- Hicks, R. R., Fertig, S. J., Desrocher, R. E., Koroshetz, W. J., and Pancrazio, J. J. (2010). Neurological effects of blast injury. Journal of Trauma, 68:1257–63.
- Hoge, C. W., McGurk, D., Thomas, J. L., Cox, A. L., Engel, C. C., and Castro, C. A. (2008). Mild Traumatic Brain Injury in U.S. Soldiers Returning from Iraq. New England Journal of Medicine, 358(5):453–463.
- Hutchinson, R. W., Cox, A. G., McLeod, C. W., Marshall, P. S., Harper, A., Dawson, E. L., and Howlett, D. R. (2005). Imaging and spatial distribution of beta-amyloid peptide and metal ions in Alzheimer’s plaques by laser ablation-inductively coupled plasma-mass spectrometry. Analytical Biochemistry, 346(2):225–233.

- Ingber, L. (1993). Simulated annealing: Practice versus theory. Mathematical and Computer Modelling, 18:29–57.
- Jaffer, H., Adjei, I. M., and Labhasetwar, V. (2013). Optical imaging to map blood-brain barrier leakage. Scientific Reports, 3:3117.
- Jay, J. L. and Lee, W. R. (1976). Dacryolith formation around an eyelash retained in the lacrimal sac. British Journal of Ophthalmology, 60(10):722–725.
- Kabu, S., Jaffer, H., Petro, M., Dudzinski, D., Stewart, D., Courtney, A., Courtney, M., and Labhasetwar, V. (2015). Blast-associated shock waves result in increased brain vascular leakage and elevated ros levels in a rat model of traumatic brain injury. PLoS ONE, 10(5):e0127971.
- Kern, J. P. and Pattichis, M. S. (2007). Robust multispectral image registration using mutual-information models. IEEE Transactions on Geoscience and Remote Sensing, 45(5):1494–1505.
- Kindness, A., Sekaran, C. N., and Feldmann, J. (2003). Two-dimensional mapping of copper and zinc in liver sections by laser ablation inductively coupled plasma mass spectrometry. Clinical Chemistry, 49(11):1916–1923.
- Kirkpatrick, S., Gelatt, C. D., and Vecchi, M. P. (1983). Optimization by simulated annealing. Science, 220:671–680.
- Klein, S., Staring, M., Murphy, K., Viergever, M., and Pluim, J. (2010). elastix: A toolbox for intensity-based medical image registration. IEEE Transactions on Medical Imaging, 29(1):196–205.
- Lein, E. S., Hawrylycz, M. J., Ao, N., Ayres, M., Bensinger, A., Bernard, A., Boe, A. F., Boguski, M. S., Brockway, K. S., Byrnes, E. J., Chen, L., Chen, L., Chen, T.-M., Chin, M. C., Chong, J., Crook, B. E., Czaplinska, A., Dang, C. N., Datta, S., Dee, N. R., Desaki, A. L., Desta, T., Diep, E., Dolbeare, T. A., Donelan, M. J., Dong, H.-W., Dougherty, J. G., Duncan, B. J., Ebbert, A. J., Eichele, G., Estin, L. K., Faber, C., Facer, B. A., Fields, R., Fischer, S. R., Fliss, T. P., Frensley, C., Gates, S. N., Glattfelder, K. J., Halverson, K. R., Hart, M. R., Hohmann, J. G., Howell, M. P., Jeung, D. P., Johnson, R. A., Karr, P. T., Kawal, R., Kidney, J. M., Knapik, R. H., Kuan, C. L., Lake, J. H., Laramée, A. R., Larsen, K. D., Lau, C., Lemon, T. A., Liang, A. J., Liu, Y., Luong, L. T., Michaels, J., Morgan, J. J., Morgan, R. J., Mortrud, M. T., Mosqueda, N. F., Ng, L. L., Ng, R., Orta, G. J., Overly, C. C., Pak, T. H., Parry, S. E., Pathak, S. D., Pearson, O. C., Puchalski, R. B., Riley, Z. L., Rockett, H. R., Rowland, S. A., Royall, J. J., Ruiz, M. J., Sarno, N. R., Schaffnit, K., Shapovalova, N. V., Sivisay, T., Slaughterbeck, C. R., Smith, S. C., Smith, K. A., Smith, B. I., Sodt, A. J., Stewart, N. N., Stumpf, K.-R., Sunkin, S. M., Sutram, M., Tam, A., Teemer, C. D., Thaller, C., Thompson,

- C. L., Varnam, L. R., Visel, A., Whitlock, R. M., Wohnoutka, P. E., Wolkey, C. K., Wong, V. Y., Wood, M., Yaylaoglu, M. B., Young, R. C., Youngstrom, B. L., Yuan, X. F., Zhang, B., Zwingman, T. A., and Jones, A. R. (2007). Genome-wide atlas of gene expression in the adult mouse brain. Nature, 445:168–176.
- Ling, G., Armonda, R., Grant, G., and Ecklund, J. (2009). Explosive blast neurotrauma. Journal of Neurotrauma, 26:815–25.
- Mac Donald, C. L., Johnson, A. M., Cooper, D., Nelson, E. C., Werner, N. J., Shimony, J. S., Snyder, A. Z., Raichle, M. E., Witherow, J. R., Fang, R., Flaherty, S. F., and Brody, D. L. (2011). Detection of Blast-Related Traumatic Brain Injury in U.S. Military Personnel. New England Journal of Medicine, 364(22):2091–2100. PMID: 21631321.
- Maes, F., Collignon, A., Vandermeulen, D., Marchal, G., and Suetens, P. (1997). Multimodality image registration by maximization of mutual information. IEEE Transactions on Medical Imaging, 16(2):187–198.
- Manaenko, A., Chen, H., Kammer, J., Zhang, J. H., and Tang, J. (2011). Comparison evans blue injection routes: Intravenous versus intraperitoneal, for measurement of blood-brain barrier in a mice hemorrhage model. Journal of Neuroscience Methods, 195(2):206 – 210.
- Marchi, N., Bazarian, J. J., Puvenna, V., Janigro, M., Ghosh, C., Zhong, J., Zhu, T., Blackman, E., Stewart, D., Ellis, J., Butler, R., and Janigro, D. (2013). Consequences of repeated blood-brain barrier disruption in football players. PLoS ONE, 8(3):1–11.
- Matusch, A. and Becker, J. S. (2012). Bio-imaging of metals in a mouse model of Alzheimer’s disease by laser ablation inductively coupled plasma mass spectrometry. Biomedical Spectroscopy and Imaging, 1:57–65.
- McKee, A. C., Cantu, R. C., Nowinski, C. J., Hedley-Whyte, E. T., Gavett, B. E., Budson, A. E., Santini, V. E., Lee, H.-S., Kubilus, C. A., and Stern, R. A. (2009). Chronic traumatic encephalopathy in athletes: Progressive tauopathy after repetitive head injury. Journal of Neuropathology and Experimental Neurology, 68(7):709 – 735.
- McKee, A. C., Gavett, B. E., Stern, R. A., Nowinski, C. J., Cantu, R. C., Kowall, N. W., Perl, D. P., Hedley-Whyte, E. T., Price, B., Sullivan, C., Morin, P., Lee, H.-S., Kubilus, C. A., Daneshvar, D. H., Wulff, M., and Budson, A. E. (2010). Tdp-43 proteinopathy and motor neuron disease in chronic traumatic encephalopathy. Journal of Neuropathology and Experimental Neurology, 69:918 – 929.

- McKee, A. C., Stein, T. D., Nowinski, C. J., Stern, R. A., Daneshvar, D. H., Alvarez, V. E., Lee, H.-S., Hall, G., Wojtowicz, S. M., Baugh, C. M., Riley, D. O., Kubilus, C. A., Cormier, K. A., Jacobs, M. A., Martin, B. R., Abraham, C. R., Ikezu, T., Reichard, R. R., Wolozin, B. L., Budson, A. E., Goldstein, L. E., Kowall, N. W., and Cantu, R. C. (2013). The spectrum of disease in chronic traumatic encephalopathy. Brain, 136(1):43–64.
- Meaney, D. F., Morrison, B., and Dale Bass, C. (2014). The mechanics of traumatic brain injury: a review of what we know and what we need to know for reducing its societal burden. Journal of Biomechanical Engineering, 136(2):021008.
- National Institute of Standards and Technology (2016). SRM 612 - Trace Elements in Glass. [Online; accessed 19-May-2016].
- Neemuchwala, H. and Hero, A. (2005). Entropic graphs for registration. In Blum, R. and Liu, Z., editors, Multi-Sensor Image Fusion and Its Applications, Signal Processing and Communications, chapter 6, pages 185–263. Taylor & Francis.
- Neuwelt, E. A., Bauer, B., Fahlke, C., Fricker, G., Iadecola, C., Janigro, D., Leybaert, L., Molnar, Z., O'Donnell, M. E., Povlishock, J. T., Saunders, N. R., Sharp, F., Stanimirovic, D., Watts, R. J., and Drewes, L. R. (2011). Engaging neuroscience to advance translational research in brain barrier biology. Nature Reviews Neuroscience, 12(3):169–182.
- Niehaus, R., Sperling, M., and Karst, U. (2015). Study on aerosol characteristics and fractionation effects of organic standard materials for bioimaging by means of LA-ICP-MS. Journal of Analytical Atomic Spectrometry, 30:2056–2065.
- Ojo, J. O., Mouzon, B. C., and Crawford, F. (2016). Repetitive head trauma, chronic traumatic encephalopathy and tau: Challenges in translating from mice to men. Experimental Neurology, 275, Part 3:389 – 404. Traumatic Brain Injury.
- Omalu, B. I., DeKosky, S. T., Hamilton, R. L., Minster, R. L., Kamboh, M. I., Shakir, A. M., and Wecht, C. H. (2006). Chronic traumatic encephalopathy in a national football league player: part ii. Neurosurgery, 59(5):1086–1093.
- Omalu, B. I., DeKosky, S. T., Minster, R. L., Kamboh, M. I., Hamilton, R. L., and Wecht, C. H. (2005). Chronic traumatic encephalopathy in a national football league player. Neurosurgery, 57(1):128–134.
- Pacholski, M. and Winograd, N. (1999). Imaging with mass spectrometry. Chemical Reviews, 99(10):2977–3006.
- Peskind, E. R., Petrie, E. C., Cross, D. J., Pagulayan, K., McCraw, K., Hoff, D., Hart, K., Yu, C.-E., Raskind, M. A., Cook, D. G., and Minoshima, S. (2011).

- Cerebrocerebellar hypometabolism associated with repetitive blast exposure mild traumatic brain injury in 12 Iraq war Veterans with persistent post-concussive symptoms. Neuroimage, 54 Suppl 1:S76–82.
- Portbury, S. D., Hare, D. J., Sgambelloni, C. J., Bishop, D. P., Finkelstein, D. I., Doble, P. A., and Adlard, P. A. (2017). Age modulates the injury-induced metallic profile in the brain. Metallomics, 9(4):402–410.
- Pugh, J. A. T., Cox, A. G., McLeod, C. W., Bunch, J., Writer, M. J., Hart, S. L., Bienemann, A., White, E., and Bell, J. (2012). Elemental imaging of MRI contrast agents: benchmarking of LA-ICP-MS to MRI. Analytical and Bioanalytical Chemistry, 403(6):1641–1649.
- Rawson, R. A. (1943). The binding of t-1824 and structurally related diazo dyes by the plasma proteins. American Journal of Physiology – Legacy Content, 138(5):708–717.
- Repp, D. J., Burkat, C. N., and Lucarelli, M. J. (2009). Lacrimal excretory system concretions: Canalicular and lacrimal sac. Ophthalmology, 116(11):2230 – 2235.
- Rizzardi, A. E., Johnson, A. T., Vogel, R. I., Pambuccian, S. E., Henriksen, J., Skubitz, A. P., Metzger, G. J., and Schmechel, S. C. (2012). Quantitative comparison of immunohistochemical staining measured by digital image analysis versus pathologist visual scoring. Diagnostic Pathology, 7:42.
- Robertson, J. (2006). Iraq War’s Signature Wound: Brain Injury. The Associated Press.
- Robichaud, G., Garrard, K. P., Barry, J. A., and Muddiman, D. C. (2013). MSiReader: an open-source interface to view and analyze high resolving power MS imaging files on Matlab platform. Journal of The American Society for Mass Spectrometry, 24(5):718–721.
- Sabuncu, M. R. and Ramadge, P. (2008). Using spanning graphs for efficient image registration. IEEE Transactions on Image Processing, 17(5):788–797.
- Sawyer, A. J. and Kyriakides, T. R. (2013). Nanoparticle-based evaluation of blood-brain barrier leakage during the foreign body response. Journal of Neural Engineering, 10(1):016013.
- Shenton, M. E., Hamoda, H. M., Schneiderman, J. S., Bouix, S., Pasternak, O., Rathi, Y., Vu, M.-A., Purohit, M. P., Helmer, K., Koerte, I., Lin, A. P., Westin, C.-F., Kikinis, R., Kubicki, M., Stern, R. A., and Zafonte, R. (2012). A review of magnetic resonance imaging and diffusion tensor imaging findings in mild traumatic brain injury. Brain Imaging and Behavior, 6(2):137–192.

- Špiclin, Ž., Likar, B., and Pernuš, F. (2011). Information-Theoretic Multi-modal Image Registration Based on the Improved Fast Gauss Transform: Application to Brain Images, pages 135–142. Springer Berlin Heidelberg, Berlin, Heidelberg.
- Sricharan, K. and Hero, A. O. (2012). Ensemble weighted kernel estimators for multivariate entropy estimation. In Pereira, F., Burges, C. J. C., Bottou, L., and Weinberger, K. Q., editors, Advances in Neural Information Processing Systems 25, pages 566–574. Curran Associates, Inc.
- Stahel, P. F., Shohami, E., Younis, F. M., Kariya, K., Otto, V. I., Lenzlinger, P. M., Grosjean, M. B., Eugster, H.-P., Trentz, O., Kossmann, T., and Morganti-Kossmann, M. C. (2000). Experimental closed head injury: Analysis of neurological outcome, blood-brain barrier dysfunction, intracranial neutrophil infiltration, and neuronal cell death in mice deficient in genes for pro-inflammatory cytokines. Journal Cerebral Blood Flow and Metabolism, 20:369–380.
- Tagge, C. A. (2016). Effects of Concussive Impact Injury Assess in a New Murine Neurotrauma Model. PhD thesis, Boston University.
- Tagge, C. A., Fisher, A. M., Minaeva, O. V., Gaudreau-Balderrama, A., Moncaster, J. A., Zhang, X.-L., Wojnarowicz, M. W., Casey, N., Lu, H., Kokiko-Cochran, O. N., Saman, S., Ericsson, M., Onos, K. D., Veksler, R., Jr., V. V. S., Kondo, A., Zhou, X. Z., Miry, O., Vose, L. R., Gopaul, K. R., Upreti, C., Nowinski, C. J., Cantu, R. C., Alvarez, V. E., Konrad, J., Hamilton, J. A., Hua, N., Tripodis, Y., Anderson, A. T., Howell, G. R., Kaufer, D., Hall, G. F., Lu, K. P., Ransohoff, R. M., Cleveland, R. O., Kowall, N. W., Huber, B. R., Stein, T. D., Lamb, B. T., Moss, W. C., Friedman, A., Stanton, P. K., McKee, A. C., and Goldstein, L. E. ([under review] 2017). Concussion, Microvascular Injury, and Early Tauopathy in Young Athletes after Impact Head Injury and an Impact Concussion Mouse Model. Brain.
- Tanielian, T., Jaycox, L., and Corporation, R. (2008). Invisible Wounds of War: Psychological and Cognitive Injuries, Their Consequences, and Services to Assist Recovery. Number v. 1-2 in G - Reference, Information and Interdisciplinary Subjects Series. RAND.
- Teasdale, G. and Jennett, B. (1974). Assessment of coma and impaired consciousness. a practical scale. The Lancet, 304(7872):81 – 84.
- Teledyne CETAC Technologies (2014). LSX-213 G2+ Laser Ablation System. <http://www.teledynecetac.com/product/laser-ablation/lxs-213-g2+>. [Online; accessed 3-May-2016].
- Terrio, H., Brenner, L. A., Ivins, B. J., Cho, J. M., Helmick, K., Schwab, K., Scally, K., Bretthauer, R., and Warden, D. (2009). Traumatic brain injury screening:

- Preliminary findings in a us army brigade combat team. The Journal of Head Trauma Rehabilitation, 24.
- Thermo Fisher Scientific (2010). Rapid, simple, interference-free analysis of environmental samples using the Thermo Scientific XSERIES 2 ICP-MS. Technical Report 40852, Thermo Fisher Scientific. [Online; accessed 4-March-2017].
- Thévenaz, P. and Unser, M. (2000). Optimization of mutual information for multiresolution image registration. IEEE Transactions on Image Processing, 9(12):2083–2099.
- Uerlings, R., Matusch, A., and Weiskirchen, R. (2016a). Reconstruction of laser ablation inductively coupled plasma mass spectrometry (LA-ICP-MS) spatial distribution images in Microsoft Excel 2007. International Journal of Mass Spectrometry, 395:27 – 35.
- Uerlings, R., Matusch, A., and Weiskirchen, R. (2016b). Standardization and normalization of data from laser ablation inductively coupled plasma mass spectrometry. In Yang, D., editor, Applications of Laser Ablation - Thin Film Deposition, Nanomaterial Synthesis and Surface Modification, chapter 18. InTech.
- Uyama, O., Okamura, N., Yanase, M., Narita, M., Kawabata, K., and Sugita, M. (1988). Quantitative evaluation of vascular permeability in the gerbil brain after transient ischemia using evans blue fluorescence. Journal of Cerebral Blood Flow and Metabolism, 8:282 – 284.
- VA and DoD (2016). Management of Concussion-mild Traumatic Brain Injury (mTBI). In VA/DoD Clinical Practice Guideline. Department of Veterans Affairs and Department of Defense.
- Van de Plas, R., Yang, J., Spraggins, J., and Caprioli, R. M. (2015). Image fusion of mass spectrometry and microscopy: a multimodality paradigm for molecular tissue mapping. Nature Methods.
- Vasterling, J., Verfaellie, M., and Sullivan, K. (2009). Mild traumatic brain injury and posttraumatic stress disorder in returning veterans: perspectives from cognitive neuroscience. Clinical Psychology Review, 29:674–84.
- Viola, P. and Wells III, W. M. (1997). Alignment by maximization of mutual information. International Journal of Computer Vision, 24:137–154.
- Wachinger, C. and Navab, N. (2012). Entropy and laplacian images: Structural representations for multi-modal registration. Medical Image Analysis, 16(1):1 – 17.
- Weissberg, I., Veksler, R., Kamintsky, L., Saar-Ashkenazy, R., Milikovsky, D. Z., Shelef, I., and Friedman, A. (2014). Imaging blood-brain barrier dysfunction in football players. JAMA Neurology, 71(11):1453–1455.

- Wells, W. M. I., Viola, P., Atsumi, H., Nakajima, S., and Kikinis, R. (1996). Multi-modal volume registration by maximization of mutual information. Medical Image Analysis, 1(1):35 – 51.
- Winkler, E. A., Bell, R. D., and Zlokovic, B. V. (2011). Central nervous system pericytes in health and disease. Nature Neuroscience, 14:1398–405.
- Wu, Y. (2009). Chan vese active contours without edges.
- Xiong, Y., Mahmood, A., and Chopp, M. (2013). Animal models of traumatic brain injury. Nature Reviews Neuroscience, 14:128–142.
- Yazici, B., Hammad, A. M., and Meyer, D. R. (2001). Lacrimal sac dacryoliths: Predictive factors and clinical characteristics. Ophthalmology, 108(7):1308 – 1312.
- Yoo, T. S., Ackerman, M. J., Lorensen, W. E., Schroeder, W., Chalana, V., Aylward, S., Metaxas, D., and Whitaker, R. (2002). Engineering and algorithm design for an image processing Api: a technical report on ITK—the Insight Toolkit. Studies in Health Technology and Informatics, 85:586–592.
- Zoroya, G. (2005). Key iraq wound: Brain trauma. USA Today.

CURRICULUM VITAE



Amanda Gaudreau-Balderrama

100 N Whisman Rd #2211, Mountain View, CA, 94043

amandagbalderrama@gmail.com

US Citizen

SUMMARY

My interest is in using machine learning and probabilistic modeling techniques to solve real world problems in data analytics and inference.

EDUCATION

Doctor of Philosophy, Boston University *2010 – 2017*

- Electrical and Computer Engineering. GPA: 3.97/4
- Dissertation: “Methods and Algorithms for Quantitative Analysis of Metal-
Iomic Images to Assess Traumatic Brain Injury”
- Research advisors: Professor Janusz Konrad (BU ECE), Dr. Lee Goldstein
(BU Medical School)

Master of Eng., Massachusetts Institute of Technology *2009 – 2010*

- Electrical Engineering. VI-A Industrial Master’s Program with Medtronic.
GPA: 5/5
- Thesis: “Adaptive Therapy Learning Algorithm for Spinal Cord Simulation”
- Research advisors: Professor Collin Stultz (MIT EECS), Eric Panken
(Medtronic)

Bachelor of Science, Massachusetts Institute of Technology *2005 – 2009*

- Electrical Engineering. GPA: 4.5/5

EXPERIENCE

Research Assistant, Dr. Goldstein & Dr. Konrad, Boston University, MA *2011 – 2017*

- Developed a suite of image extraction and analysis functions for metallomic imaging mass spectroscopy and fluorescent imaging microscopy. Contributions include custom functions for image visualization, normalization, segmentation, statistical modeling and feature selection
- Implemented a multi-modal, multi-channel image registration algorithm. Model parameters are estimated by maximizing multi-dimensional mutual information using simulated annealing
- Tracked head motion in video using active contours for position measurements and Kalman Filtering for tracking
- Assessed injury severity in RGB-images via semi-supervised clustering

Intern, MIT Lincoln Labs, Wideband Tactical Networking, Lexington, MA *2010/06 – 08*

- Used Simulink to model the performance of a complete satellite communication link
- Designed and parameterized a control system for open loop antenna pointing in the presence of severe motion disturbance

Intern, Medtronic, Inc., Neuromodulation, Minneapolis, MN *2009/06 – 2010/01*

- Developed an algorithm that learns patient preferred spinal cord stimulation parameters for improving therapy efficacy in an existing spinal cord stimulation product
- Characterized pain patient posture behavior by clustering accelerometer data and visualizing their 2-D/3-D distributions
- Developed tools in MATLAB to assess classification performance of an algorithm for posture detection using accelerometer data *2008/06 – 2008/08*

Intern, General Electric – Transportation, Control Electronics, Erie, PA *2007/06 – 08*

- Performed failure mode analysis by simulating locomotive electric motor panel
- Calculated panel reliability by assessing worst case load on each circuit component

Research Assistant, Dr. Mike Zody, The Broad Institute, Cambridge, MA 2005/06 –
2005/12

- Collected data to test whether CpG mutations are a time-dependent or a replication-dependent process using human and dog model species
- Developed Perl script which extracted desired data from large genome files

AWARDS & PUBLICATIONS

- National Institute of Health (NIH) F31 Fellowship (NINDS) 2012 – 2015
- Posture State Classification for a Medical Device (Issued Patent US8388555) 2013
- Graduate Teaching Fellow of the Year Award from Boston University 2010 – 2011
- J. Francis Reintjes Excellence in VI-A Industrial Practice Award from MIT 2010
- Tagge, C. A., Fisher, A. M., Minaeva, O. V., Gaudreau-Balderrama, A., *et al.* ([under review] 2017). Concussion, Microvascular Injury, and Early Tauopathy in Young Athletes after Impact Head Injury and an Impact Concussion Mouse Model. Brain.
- A. Gaudreau-Balderrama, N. Casey, J. Konrad, and L. Goldstein. “Multi-modal Image Registration for Evaluating Traumatic Brain Injury Neuropathology,” Gordon Research Conference on Image Science, June 2014. (Poster)
- M. Yip, D. He, E. Winokur, A. Gaudreau-Balderrama, “A Flexible Pressure Monitoring System for Pressure Ulcer Prevention,” IEEE Engineering in Medicine and Biology Conference, Sept. 2009. (**2nd Place Student Paper Award**)

SKILLS

Digital signal processing, machine learning, computer vision, data visualization, multi-dimensional data analysis & modeling, optimization, regularization, image reconstruction, MATLAB, Perl, \LaTeX

REFERENCES

Available upon request